

# The nature of the quasiparticles in two benchmark transition metal oxides: A spectroscopic study of anatase $\text{TiO}_2$ and tetragonal $\text{CuO}$ .

THÈSE N° 6383 (2014)

PRÉSENTÉE LE 5 DÉCEMBRE 2014  
À LA FACULTÉ DES SCIENCES DE BASE  
LABORATOIRE DE SPECTROSCOPIE ÉLECTRONIQUE  
PROGRAMME DOCTORAL EN PHYSIQUE

ÉCOLE POLYTECHNIQUE FÉDÉRALE DE LAUSANNE

POUR L'OBTENTION DU GRADE DE DOCTEUR ÈS SCIENCES

PAR

Simon Karl MOSER

acceptée sur proposition du jury:

Prof. F. Mila, président du jury  
Prof. M. Grioni, directeur de thèse  
Prof. J. H. Dil, rapporteur  
Prof. D. Malterre, rapporteur  
Prof. D. Van der Marel, rapporteur



ÉCOLE POLYTECHNIQUE  
FÉDÉRALE DE LAUSANNE

Suisse  
2014



Science is the great antidote to the poison of enthusiasm and superstition.  
— Adam Smith

To my father Karl. J. Moser.





# Acknowledgements

I would like to thank my thesis advisor Prof. Marco Grioni for the great opportunity to prove myself in a challenging new field and to emancipate myself as a person and as a scientist. The freedom I had to follow my own interests and ideas was very stimulating and opened a broad range of opportunities. I am really grateful for the chance of an extended research stay at the ALS Berkeley, where I was welcomed by Dr. Luca Moreschini. Luca taught me all the finesses of the ARPES experiment and showed me how to still take it easy after a 36 hours shift. The turbulent interplay in between Italian temperament and German thoroughness made a quite complementary team hopefully to be continued in the future.

I would further like to thank the whole beamline team at the ALS Berkeley for their trust. Dr. Young Jun Chang patiently taught me everything about the PLD. Dr. Aaron Bostwick remained serene even after I confessed to have dropped a dozen user samples – one blocking a UHV valve – while simultaneously announcing my immediate departure into Christmas Holidays. Dr. Eli Rotenberg adopted me in his team and his lunch group with incredible leap of faith, invited me to his unforgettable house parties, and gave me the great opportunity to join his group as a postdoc.

I would like to thank the people who helped to realize the T-CuO project: Dr. Davide Innocenti managed the frustrating initial stage of T-CuO PLD growth. Franziska Fuchs and Nis-Hauke Hansen characterized the thin films. Prof. Frédéric Mila and Dr. HongYu Yang made a great effort to help me understand the electronic and magnetic structure of T-CuO. In collaboration with Dr. Debakanta Samal we are now realizing the first RIXS measurements on T-CuO.

I would like to thank Dr. Jaćim Jaćimović who introduced me to the fascinating subject of TiO<sub>2</sub>. My great acknowledgements go to Helmuth Berger, Philippe Bugnon and Dr. Arnaud Magrez for their tireless passion to develop crystals of higher and higher quality, and for their support of my work. I would like to thank Dr. Osor Barišić for modeling the polaron spectral function and for many great discussions we had on polaronic effects. Many thanks to Prof. Peter Krüger for his MCMS calculations and for many wonderful discussions we had on XAS, RIXS and resPES. Further, I would like to thank Prof. Yoshihisa Harada for many valuable discussions on symmetry selectivity in XAS and RIXS.

I would like to thank Afsoon Ebrahimi for her great contributions to the work on Iridates, and for the pleasure of having her as my office mate. Many thanks also to my friend and officemate Dr.

## Acknowledgements

---

Cédric Tournier-Colletta, who taught me precision and scientific modesty, and most importantly how to rock on stage. A great appreciation to my collaborator and synchrotron companion Sara Fatale for her reliability and support. Many thanks to Dr. Alberto Crepaldi for the “ongoing strong ties” (he promised in his thesis’ acknowledgements), and for being there when I needed him. My acknowledgements also to Edoardo Baldini for many great discussions on TiO<sub>2</sub> and time resolved spectroscopies. Many thanks to Jens Johannsen, who one day will save the planet with graphene based technologies.

Moreover, I would like to thank Dr. Andrea Crottini for all his trust and support concerning the patenting of our invention. Many thanks to Dr. Elodie Dahan for all her advice related to that matter.

I greatly appreciate the accurate work and reliability of our technicians Claude Amendola, Gérald Beney, Philippe Cuanillon, Martial Doy, Gilles Grandjean, José Grandjean, Philippe Guex, Olivier Haldimann, Primo Locatelli and Philippe Zürcher. Many thanks to our organizing angles Claire-Lise Bandelier, Nadja Favre and Chantal Roulin.

Further acknowledgements are addressed to people who crossed my path during some important time within the past: Dr. Kamel Aït-Mansour, Prof. Harald Brune, Dr. Alberto Cavallin, Prof. Johan Chang, Dr. Fabio Donati, Dr. Quentin Dubout, Marie Dufour, Noée Galès, Dr. Luca Gagnaniello, Dr. Marco Guarise, Dr. Martin Heiss, Dr. Fabian Natterer, Giulia Pacchioni, Dr. François Patthey, Dr. Marina Pivetta, Dr. Bastien Dalla Piazza, Dr. Stéphane Pons, Daniel Rüffer, Dr. Stephano Rusponi, Massimo Spina, Maja Varga, Dr. Sergio Vlaic and Chongqi Yu.

Many thanks are directed to my former roommates Dr. Cédric Cortijo, Anuschka Ferrari, Elodie Bouvier and Madame Monique Cassard. Thanks to my friends Simon, Sunshine and Leonardo, to Adrian, to Clementine and to Caro.

Special thanks go to my family Maja and Tara (and Moritz the cat) for *not at all* sharing my passion for physics but taking me out for completely different adventures. Many many thanks to my mother Beate, my brother Korbinian and my sisters Amelie and Luise for being there for me no matter what decisions I take in life.

A great thank you goes to my grandmas Käth and Marianne and to my grandpa Alois, who always – no matter what – supported me the best they possibly could. Most people of their generation did not have the supreme opportunity of getting higher education like I did. It is therefore only appropriate to appreciate the achievement of *free education open to anybody*, from which I profit so much and which I strongly believe is the base of prosperity and peace.

Lausanne, 25 August 2014

S. M.

# Abstract

Transition metal oxides (TMOs) are emerging strong players in many domains, ranging from superconductivity, to microelectronics to spintronics to light harvesting for photovoltaics. Beyond their non-toxicity, low corrosiveness and low price, they exhibit a whole range of exciting electronic properties, which could be realistically exploited in new devices. Typically, TMOs are governed by strong correlation of its  $3d$  electrons, often dressed by lattice or magnetic excitations and thus leading to complex electronic behavior. This work is focused on the electronic structure of two benchmark TMOs – anatase  $\text{TiO}_2$  and tetragonal  $\text{CuO}$  – spectroscopically investigated by angle resolved photoemission (ARPES) and resonant inelastic x-ray scattering (RIXS).

Anatase  $\text{TiO}_2$ , a  $3d^0$  system, has been proposed for many applications from transparent conducting layers to photovoltaic- and photocatalytic- devices, as well as memristors. For the performance of these devices, the charge carrier lifetime and their control is of primordial importance. By means of ARPES, the possibility to achieve a fine control of the mobile charge carrier concentration through x-ray beam doping is demonstrated. We show that the conduction electrons in anatase, and their nature, is determined by significant electron-phonon-coupling and by the number of oxygen defects. At low defect densities, charge carriers behave as a gas of weakly interacting large polarons. At larger densities, the polarons spatially overlap and dissolve into a weakly correlated Fermi liquid. The role of the electron-lattice coupling is further resolved by RIXS. The spectral signatures of phonons hint towards isotropic electron-phonon-coupling in anatase. Phonon frequency and electron-phonon coupling both show low doping sensitivity.

The cupric oxide  $\text{CuO}$ , a  $3d^9$  system, exhibits an insulating ground state with a correlation-induced charge-transfer gap and antiferromagnetism. It is, in principle, the most straightforward parent compound of the doped cuprates, and therefore has been theoretically studied as a model material for high temperature superconductivity. Bulk  $\text{CuO}$  crystallizes in a low-symmetry monoclinic form, in contrast to the rocksalt structure typical of late  $3d$  transition metal monoxides. In this work,  $\text{CuO}$  was synthesized by epitaxial growth on  $\text{SrTiO}_3$  substrates in a higher symmetry tetragonal structure (T- $\text{CuO}$ ) much closer to the one observed in most cuprates. ARPES identifies its first ionization state as a Zhang Rice Singlet (ZRS). This is the first observation of the ZRS on a quasi 2D *edge-sharing* cuprate system with possible implications for magnetism and potential superconductivity in the doped phase.

**Keywords:** ARPES, RIXS, anatase  $\text{TiO}_2$ , polarons, oxygen vacancies, beam doping, tetragonal

## **Acknowledgements**

---

CuO, strong correlation, Zhang-Rice-Singlet, cuprates, magnons

# Zusammenfassung

Übergangsmetalloxide gewinnen in vielen Bereichen an zunehmender Bedeutung, angefangen von der Supraleitung, über die Mikroelektronik und Spintronik bis zur Lichtausbeutung in der Photovoltaik. Neben ihrer gesundheitlichen Unbedenklichkeit, ihrer geringen Korrosivität und den geringen Materialkosten, weisen sie eine ganze Reihe von spannenden elektronischen Eigenschaften auf, die in realistischer Hinsicht zu neuen Anwendungen führen könnten. Üblicherweise sind die Übergangsmetalloxide durch starke Korrelation ihrer  $3d$  Elektronen beherrscht, die oft mit Gitter- oder magnetischen Anregungen wechselwirken und damit zu komplexem elektronischen Verhalten führen können. Die vorliegende Arbeit konzentriert sich auf die elektronische Struktur zweier exemplarischer Übergangsmetalloxide – Anatas -  $\text{TiO}_2$  und tetragonales  $\text{CuO}$  – die hier spektroskopisch mittels winkelaufgelöster Photoelektronenspektroskopie (ARPES) und resonanter inelastischer Röntgenstreuung (RIXS) untersucht werden.

Anatas- $\text{TiO}_2$  ist ein  $3d^0$ -System, das für viele Anwendungen angefangen bei transparent-leitfähigen Schichten über Photovoltaik- und photo-katalytische Bauteile bis hin zu Memristoren in Frage kommt. Für deren Effizienz ist die Lebensdauer der Ladungsträger und deren Kontrolle von erheblicher Bedeutung. Mittels ARPES wird hier die Möglichkeit zur Feineinstellung der beweglichen Ladungsträgerkonzentration in Anatas durch Röntgenstrahldotierung demonstriert. Es wird gezeigt, dass die Leitungselektronen in Anatas und ihre Eigenschaften durch maßgebliche Elektron-Phonon-Wechselwirkung und die Anzahl der Sauerstoff-Fehlstellen bestimmt ist. Bei niedrigen Defektkonzentrationen verhalten sich die Ladungsträger als Gas schwach wechselwirkender großer Polarone. Bei höheren Dichten überlappen die Polarone räumlich und lösen sich in einer schwach korrelierten Fermi-Flüssigkeit auf. Des weiteren wird die Bedeutung der Elektronen-Phonon-Wechselwirkung mittels RIXS aufgezeigt. Die Signatur der Phononen im RIXS Spektrum deutet in Richtung einer isotropen Elektron-Phonon-Wechselwirkung in Anatas. Die Frequenz als auch die Interaktion der Phononen mit den Elektronen zeigen eine geringe Abhängigkeit von der Dotierung.

Das Kupferoxid  $\text{CuO}$ , ein  $3d^9$  System, ist ein korrelations- bedingter Ladungstransfer-Isolator mit anti-ferromagnetischem Grundzustand. Im Prinzip ist es das einfachste Ausgangsmaterial der dotierten Cuprate, und wurden daher theoretisch als Modellsystem für die Hochtemperatursupraleitung studiert. Kristallines  $\text{CuO}$  wächst in einer monoklinen Gitterstruktur mit niedriger Symmetrie, im Gegensatz zur typischen Steinsalz Struktur der  $3d$  Übergangsmetalloxide. In dieser Arbeit wurde  $\text{CuO}$  in einer höher-symmetrischen tetragonalen Struktur (T- $\text{CuO}$ ) epitaktisch

## Acknowledgements

---

auf SrTiO<sub>3</sub> Substraten gewachsen, welche der Struktur der Cuprate viel näher kommt. ARPES identifiziert den ersten Ionisierungszustand als so genanntes Zhang-Rice-Singulett (ZRS). Dies ist die erste Beobachtung eines ZRS auf einem quasi zwei-dimensionalem Kuprat-System, bei dem sich benachbarte CuO<sub>4</sub> Plaketten jeweils eine Kante teilen, und was möglicherweise Auswirkungen auf Magnetismus und Supraleitung in der dotierten Phase hat.

**Schlagwörter:** ARPES, RIXS, Anatas TiO<sub>2</sub>, Polarone, Sauerstoff Störstellen, Strahldotierung, tetragonales CuO, starke Korrelation, Zhang-Rice-Singulett, Kuprate, Magnonen

# Contents

<b>Acknowledgements</b>	<b>v</b>
<b>Abstract</b>	<b>vii</b>
<b>Zusammenfassung</b>	<b>ix</b>
<b>Contents</b>	<b>xi</b>
<b>Introduction</b>	<b>1</b>
<b>1 Angle resolved photoemission</b>	<b>3</b>
1.1 Summary . . . . .	3
1.2 Motivation . . . . .	3
1.3 The photoemission cross section . . . . .	4
1.4 The spectral function . . . . .	6
1.5 The one-electron matrix element . . . . .	8
1.5.1 Matrix elements without surface . . . . .	8
1.5.2 Matrix elements in the presence of a surface . . . . .	12
1.5.3 The electron escape depth $\lambda$ . . . . .	14
1.5.4 The photoelectron escape . . . . .	15
1.5.5 Matrix elements in tight binding approximation . . . . .	17
1.5.6 Rotation of atomic orbitals . . . . .	25
1.6 Appendix . . . . .	27
1.6.1 Matrix elements of a rotated Bloch Wave . . . . .	27
1.6.2 Explicit rotation of atomic orbitals . . . . .	29
<b>2 Resonant inelastic x-ray scattering</b>	<b>33</b>
2.1 Summary . . . . .	33
2.2 Introduction . . . . .	33
2.3 The RIXS cross section . . . . .	34
2.4 Momentum transfer . . . . .	37
2.5 Basis functions of the tetrahedral system . . . . .	39
2.6 Dipole approximation in RIXS . . . . .	40
2.6.1 Symmetry selectivity in the RIXS excitation process . . . . .	42

## Contents

---

2.6.2	Symmetry selectivity in the re-emission process . . . . .	46
2.6.3	Intermediate state selection . . . . .	51
2.7	Selfabsorption . . . . .	52
2.7.1	Selfabsorption in a bulk material . . . . .	53
2.7.2	Selfabsorption in a thin film . . . . .	54
<b>3</b>	<b>Anatase TiO<sub>2</sub> – a polaronic semiconductor investigated by ARPES</b>	<b>57</b>
3.1	Summary . . . . .	57
3.2	Motivation . . . . .	57
3.3	Crystal growth and preparation . . . . .	59
3.4	Film growth and characterization . . . . .	62
3.5	Anatase TiO <sub>2</sub> – a large polaron system . . . . .	62
3.6	<i>k</i> -space mapping in anatase . . . . .	68
3.6.1	<i>k<sub>y</sub>k<sub>x</sub></i> CE-maps . . . . .	68
3.6.2	<i>k<sub>x</sub>k<sub>z</sub></i> CE-maps . . . . .	71
3.6.3	Matrilelements in anatase TiO <sub>2</sub> . . . . .	71
3.7	Oxygen vacancy formation . . . . .	73
3.8	Doping dependence of the electron pocket . . . . .	77
3.8.1	Along <i>k<sub>  </sub></i> . . . . .	77
3.8.2	Along <i>k<sub>z</sub></i> . . . . .	79
3.9	Temperature dependence of the pocket . . . . .	79
3.10	Derivation of the polaron spectral function . . . . .	82
3.10.1	Model . . . . .	82
3.10.2	Low doping . . . . .	83
3.10.3	<i>l</i> = 1 contribution to the ARPES spectral weight . . . . .	84
3.10.4	<i>l</i> = 2 contribution to the ARPES spectral weight . . . . .	86
3.10.5	High doping . . . . .	87
3.11	Some quantitative estimates . . . . .	89
3.11.1	Electrical properties . . . . .	89
3.11.2	Electron phonon coupling . . . . .	92
<b>4</b>	<b>Anatase TiO<sub>2</sub> – a polaronic semiconductor investigated by RIXS</b>	<b>95</b>
4.1	Summary . . . . .	95
4.2	Motivation . . . . .	95
4.3	Methods . . . . .	96
4.4	Excitation energy dependence . . . . .	97
4.5	The fluorescence . . . . .	98
4.6	RIXS symmetry selection in anatase . . . . .	99
4.7	Doping dependence of the elastic contributions . . . . .	104
4.8	Doping dependence and nature of the phonons . . . . .	106
4.9	A generalized Franck Condon model . . . . .	107
4.10	Phonons at the oxygen K-edge . . . . .	109



<b>5</b>	<b>T-CuO – a 2D edge-sharing cuprate investigated by ARPES</b>	<b>113</b>
5.1	Summary . . . . .	113
5.2	Motivation . . . . .	113
5.3	Methods . . . . .	114
5.4	Film characterization . . . . .	114
5.5	From tenorite to T-CuO . . . . .	115
5.6	The electronic structure of cuprates . . . . .	120
5.7	Core level spectra . . . . .	121
5.8	Valence band spectra . . . . .	123
5.9	X-ray absorption . . . . .	125
5.10	ARPES overview . . . . .	126
5.11	<i>c</i> -axis dispersion . . . . .	131
5.12	Angle resolved photoemission - beyond the ZRS . . . . .	131
5.13	Matrilements in T-CuO . . . . .	133
5.14	The generalized <i>t</i> - <i>J</i> model . . . . .	135
5.15	Speculations about the doped system . . . . .	138
<b>6</b>	<b>T-CuO – a 2D edge-sharing cuprate investigated by RIXS</b>	<b>141</b>
6.1	Summary . . . . .	141
6.2	Motivation . . . . .	141
6.3	Methods . . . . .	143
6.4	RIXS along $\Gamma X$ . . . . .	144
6.5	RIXS along $\Gamma X'$ . . . . .	145
6.6	$\sigma$ vs $\pi$ -polarization . . . . .	147
6.7	Comparison to the antiferromagnetic cuprates . . . . .	148
6.8	What's next . . . . .	148
<b>A</b>	<b>Iridates – spin-orbit induced Mott insulators investigated by ARPES</b>	<b>151</b>
A.1	Monolayer perovskite iridate $\text{Ba}_2\text{IrO}_4$ . . . . .	151
A.2	Bilayer perovskite iridate $\text{Sr}_3\text{Ir}_2\text{O}_7$ . . . . .	165
	<b>Bibliography</b>	<b>171</b>
	<b>Curriculum Vitae</b>	<b>189</b>
	<b>Publication List</b>	<b>191</b>



# Introduction

Society as we know it today is widely based on a model assuming unlimited supply of natural resources [1]. This resource problem is known and nowadays widely accepted to be at the cause of severe social unrest and national conflicts [2–4]. Even though most people in this context naturally think of phenomena like “peak-oil” and the energy crisis, serious problems also arise from society’s current consumption behavior of electronic devices. For example, cell phones, laptops, tablets or televisions all depend on fast switching capacitor technology based on tantalum, a rare earth element gained from Coltan (columbite-tantalite), which by definition is a rare resource. This rareness and associated economic risks puts society into a longstanding dependence of a scarce good, and causes severe social, political and ecological problems all over the planet.

Trying to solve the central challenge of a transition from limited to unlimited resources at constant standard, society requires *abundant* materials with useful electronic properties [5, 6]. Besides the replacement of existing technologies, grand challenges in the generation and storage of energy - e.g. via water splitting and hydrogen storage - drives research into advanced solar energy generation and the search for hydrogenated materials [7]. The capacity and efficiency of energy grids could be significantly increased using high temperature superconductors [8]. The drive to miniaturize electronics beyond the foreseen limits of silicon leads to research in molecular-scale electronics [9].

Transition metal oxides (TMOs) are prospective candidates in many of these domains. They are typically non-toxic, show low corrosiveness (since they are already oxidized), are typically available in “unlimited” quantities and therefore low in price. Besides, they exhibit a whole range of exciting electronic properties interesting for applications.

Typically, TMOs are governed by strong correlation of their  $3d$  electrons, leading to a complex electronic behavior. In a technological sense, complexity is derived from the manipulation of many length scales and degrees of freedom in the structure and composition of materials to lead to new and useful properties. For example, fabrication of patterned materials from the micron to the atomic scales can simultaneously control the photon, phonon, and electron density of states and is expected to play a key role in the development of new solar energy technologies [10]. In a mathematical sense, complexity emerges from the inherently non-linear interactions between the microscopic parts of a system. This nonlinearity leads to intricate dynamical behavior in time and

space that cannot be easily predicted by a “bottom-up” consideration of the local interactions.

The problem thus amounts to understand the collective behavior of up to  $\sim 10^{23}$  free electrons in a shifting landscape of nuclei and bound electrons from their experimental spectra. The electrons in the system are perturbed – e.g. by x-rays – and advanced detection tools and modeling measure and interpret their response. From these insights, further predictions on similar or even more complex systems can be made. In this work, we focus on two binary oxides with conceivably simplest stoichiometry but high importance for modern applications: anatase  $\text{TiO}_2$  and tetragonal  $\text{CuO}$ .

We start the discussion by introducing the experimental techniques. In Ch. 1, a consistent introduction to the basic concepts of angle resolved photoemission (ARPES) is given. A special focus is put on the so called “one electron matrix element”, which can be directly related to the local properties of the groundstate wavefunction.

In Ch. 2, the main concepts of resonant inelastic x-ray scattering (RIXS) are summarized. Some useful tools to exploit the local symmetries of the ground state wavefunction are developed to optimize the RIXS experimental geometry and to interpret the data.

In Chs. 3 and 4, entire focus is put on  $\text{TiO}_2$  anatase, investigated by ARPES and RIXS. We will discuss the role of electron phonon coupling and oxygen defect concentration in this polar material for the re-normalization of the charge carriers and test the theoretical concepts developed in Chs. 1 and 2. We further propose a new industrial method to manipulate the charge carrier concentration in  $\text{TiO}_2$  based devices.

In Ch. 5, we introduce tetragonal  $\text{CuO}$  (T- $\text{CuO}$ ), a new high symmetry form of  $\text{CuO}$  – proxy structure for the high temperature superconducting cuprate parent compounds – and discuss its low energy electronic structure based on ARPES results. The preliminary RIXS data presented in Ch. 6 will deliver some unexpected surprises.

# 1 Angle resolved photoemission

## 1.1 Summary

In this chapter, a pedagogical introduction to the basic principles of angle resolved photoemission is given. Based on a simple model, we derive the most important properties exploited in a modern ARPES experiment, introduce the concepts of the spectral function and the single electron transition matrix element. From a simple tight binding model we will estimate how ARPES intensity varies as a function of the experimental configuration and the crystal symmetry. The tools developed will prove useful for the data interpretation in the chapters to follow.

## 1.2 Motivation

Angle resolved photoemission spectroscopy (ARPES) is a many-body spectroscopy with the potential to answer some of the deepest questions in condensed-matter physics, especially in correlated electron systems like Mott insulators or high temperature superconductors [11]. It is the only tool that can give direct information on energy, momentum, and scattering processes of the least-bound valence electrons near the Fermi level - those electrons that determine all the fundamental properties of the solid [12, 13]. In its simplest incarnation, ARPES measures the bandstructure, i.e. the energy-momentum relationship  $E$  vs  $\mathbf{k}$  that is the fundamental electronic property of all crystals.

With sufficient energy and momentum resolution, ARPES also measures the spectral function  $A(\mathbf{k}, \omega)$ , which encodes the single-particle bandstructure, the scattering lifetime and the mass re-normalization accompanying many-body interactions. From these quantities one can determine various transport properties, the self-energy, and the many-body coupling constants [14–22]. The latter quantities are very important to understand effects such as superconductivity, colossal magnetoresistance or spin-charge separation. As such, the spectral function serves as the *lingua franca* between many-body theorists and experimentalists.

## Chapter 1. Angle resolved photoemission

---

Photoemission spectroscopy is an old and well established technique, dating back to the discovery of the photoelectric effect by Albert Einstein in 1905 [23]. Many of the theoretical concepts and models used to interpret our today's experimental observations therefore have been developed many years ago and summarized in reviews and textbooks [12, 24].

With the advent of 3rd generation synchrotrons in the 1990ies, improvements in resolution and 2D detectors however came a dramatic increase in the throughput of ARPES experiments, enabling much more elegant and thorough experiments. An explosion of results in the study of magnetic, quantum-confined and correlated materials followed [21]. The ability to efficiently sample large volumes in energy-momentum space with polarized light gave access to experimental parameters often not considered rigorously in the data interpretation. One example is the variation of ARPES intensity throughout  $k$ -space, often times rationalized by hand-waving symmetry arguments. It is therefore useful to return and build on concepts developed during the "early days" of photoemission and try a more rigorous treatment of these effects.

The aim of this chapter is to consistently introduce the most important concepts of ARPES guided by a simple model. We will put a special focus on the one electron transition matrix elements<sup>1</sup> and their relationship to the experimental geometry, typically strongly varied throughout the scope of one experiment. We will further show a method to simulate matrix elements for systems that are well described by their local molecular orbitals in the tight binding approximation.

### 1.3 The photoemission cross section

Photoemission measures the transition probability  $w_{fi}$  for an optical excitation between an  $N$ -electron ground state  $\Psi_i^N$  and one of the available final states  $\Psi_f^N$  with one photoelectron. Assuming the interaction between incoming light and matter to be weak, this process can be conveniently described by Fermi's Golden rule for first order processes

$$w_{if} = \frac{2\pi}{\hbar} |\langle \Psi_f^N | H_{int} | \Psi_i^N \rangle|^2 \delta(E_f^N - E_i^N - h\nu), \quad (1.1)$$

where  $E_i^N$  and  $E_f^N$  are the initial and final state energies of the  $N$ -particle system, respectively, and  $h\nu$  is the photon energy.

In the nonrelativistic limit, the light matter interaction can be treated as

---

<sup>1</sup>The term *matrix element* in the following refers to the simplified picture of a transition from a Bloch state to a plane wave final state. The complex behavior of the final state is therefore neglected.

$$H_{int} = \sum_{i=1}^N \left[ \frac{e}{m} \mathbf{A}(\mathbf{r}_i) \cdot \hat{\mathbf{p}}_i + \frac{e^2}{2m} \mathbf{A}^2(\mathbf{r}_i) + \frac{e\hbar}{2m} \hat{\boldsymbol{\sigma}}_i \cdot \nabla \times \mathbf{A}(\mathbf{r}_i) - \frac{e^2\hbar}{(2mc)^2} \hat{\boldsymbol{\sigma}}_i \cdot \frac{\partial \mathbf{A}_i(\mathbf{r}_i)}{\partial t} \times \mathbf{A}(\mathbf{r}_i) \right], \quad (1.2)$$

where  $\hat{\mathbf{p}}_i$  is the momentum operator and  $\mathbf{r}_i$  the position of electron  $i$ . The  $\hat{\boldsymbol{\sigma}}_i$  are the Pauli spin matrices. Neglecting the spin dependent parts and the terms quadratic in the vector potential  $\mathbf{A}$ , we remain with

$$H_{int} \sim \frac{e}{m} \sum_{i=1}^N \mathbf{A}(\mathbf{r}_i) \cdot \hat{\mathbf{p}}_i = \frac{e}{mc} \sum_{i=1}^N e^{i\mathbf{k}_{h\nu} \cdot \mathbf{r}_i} \boldsymbol{\epsilon} \cdot \hat{\mathbf{p}}_i = -i \frac{\hbar e}{mc} \sum_{i=1}^N e^{i\mathbf{k}_{h\nu} \cdot \mathbf{r}_i} \boldsymbol{\epsilon} \cdot \nabla_i, \quad (1.3)$$

where  $\boldsymbol{\epsilon}$  is the polarization vector and  $\mathbf{k}_{h\nu}$  the momentum vector of the incoming light.<sup>2</sup> In second quantization, this Hamiltonian can be expressed as

$$H_{int} = \sum_{\mathbf{k}_f, \mathbf{k}} M_{\mathbf{k}_f \mathbf{k}} \hat{c}_{\mathbf{k}_f}^\dagger \hat{c}_{\mathbf{k}}, \quad (1.4)$$

where  $\hat{c}_{\mathbf{k}}$  destroys an electron in Bloch state  $|\Psi_{n\mathbf{k}}\rangle$  and  $\hat{c}_{\mathbf{k}_f}^\dagger$  creates a free electron  $|\mathbf{k}_f\rangle$ . The matrix element  $M_{\mathbf{k}_f \mathbf{k}}$  hereby is defined as  $M_{\mathbf{k}_f \mathbf{k}} = -i \frac{\hbar e}{mc} \langle \mathbf{k}_f | e^{i\mathbf{k}_{h\nu} \cdot \mathbf{r}} \boldsymbol{\epsilon} \cdot \nabla | \Psi_{n\mathbf{k}} \rangle$ .

Within the ‘‘sudden approximation’’, we can assume the ionization process to be very rapid and the photoelectron to be decoupled from the  $N - 1$  electron state. The final state thus factorizes into the  $(N - 1)$  electron wave function  $|\Psi_f^{N-1}\rangle$  and the wave function  $|\mathbf{k}_f\rangle$  of the photoemitted electron with momentum  $\mathbf{k}_f$  and kinetic energy  $E_{kin}$ .

$$|\Psi_f^N\rangle \sim \hat{A}(|\mathbf{k}_f\rangle \otimes |\Psi_f^{N-1}\rangle) = \hat{c}_{\mathbf{k}_f}^\dagger |\Psi_f^{N-1}\rangle. \quad (1.5)$$

<sup>2</sup>This expression for  $H_{int}$  accounts mainly for bulk direct transitions. In general, this term has to be complemented by a surface photoemission term accounting for the discontinuity of the vector potential at the surface and a term depending explicitly on spin [25].

## Chapter 1. Angle resolved photoemission

---

The operator  $\hat{\mathcal{A}}$  assures the proper anti-symmetrization of the  $N$  electron wave functions. Eq. 1.1 can so be rewritten as

$$\begin{aligned}
 w_{if} &= \frac{2\pi}{\hbar} \left| \langle \Psi_f^{N-1} | \hat{c}_{\mathbf{k}_f} \sum_{\mathbf{k}'_f, \mathbf{k}} M_{\mathbf{k}'_f \mathbf{k}} \hat{c}_{\mathbf{k}'_f}^\dagger \hat{c}_{\mathbf{k}} | \Psi_i^N \rangle \right|^2 \delta(E_f^{N-1} + E_{kin} - E_i^N - h\nu) \\
 &= \frac{2\pi}{\hbar} \left| \sum_{\mathbf{k}} M_{\mathbf{k}_f \mathbf{k}} \langle \Psi_f^{N-1} | \hat{c}_{\mathbf{k}} | \Psi_i^N \rangle \right|^2 \delta(E_f^{N-1} + E_{kin} - E_i^N - h\nu) \quad (1.6)
 \end{aligned}$$

Neglecting interference effects, i.e. assuming there is only one channel  $\hat{c}_{\mathbf{k}}$  connecting the initial state  $|\Psi_i^N\rangle$  with the final state  $|\Psi_f^{N-1}\rangle$ , we can approximate

$$w_{if} = \frac{2\pi}{\hbar} \sum_{\mathbf{k}} |M_{\mathbf{k}_f \mathbf{k}}|^2 \underbrace{\left| \langle \Psi_f^{N-1} | \hat{c}_{\mathbf{k}} | \Psi_i^N \rangle \right|^2 \delta(E_f^{N-1} + E_{kin}^N - E_i^N - h\nu)}_{\sum_f \Rightarrow A(\mathbf{k}, \omega)} . \quad (1.7)$$

The spectral function

$$A(\mathbf{k}, \omega) = \sum_f |\langle \Psi_f^{N-1} | \hat{c}_{\mathbf{k}} | \Psi_i^N \rangle|^2 \delta(E_f^{N-1} + E_{kin}^N - E_i^N - h\nu) \quad (1.8)$$

contains all the many body effects of the  $N$  particle system, whereas the one-electron matrix element  $M_{\mathbf{k}_f \mathbf{k}} \propto \langle \mathbf{k}_f | e^{i\mathbf{k}_{h\nu} \cdot \mathbf{r}} \boldsymbol{\epsilon} \cdot \nabla | \Psi_{n\mathbf{k}} \rangle$  depends largely on geometrical factors like photon momentum  $\mathbf{k}_{h\nu}$ , the polarization  $\boldsymbol{\epsilon}$  and the momentum  $\mathbf{k}_f$  of the photoelectron.

### 1.4 The spectral function

The spectral function  $A(\mathbf{k}, \omega)$  relates directly to the single - particle Green's function

$$A(\mathbf{k}, \omega) = -\frac{1}{\pi} \text{Im} [G(\mathbf{k}, \omega)] , \quad (1.9)$$



where  $G(\mathbf{k}, \omega)$  is expressed as in terms of the noninteracting one-electron energy  $E_{\mathbf{k}}^0$

$$G(\mathbf{k}, \omega) = \frac{1}{\omega - E_{\mathbf{k}}^0 - \Sigma(\mathbf{k}, \omega)}. \quad (1.10)$$

The self energy  $\Sigma(\mathbf{k}, \omega) = \text{Re}[\Sigma(\mathbf{k}, \omega)] + i\text{Im}[\Sigma(\mathbf{k}, \omega)]$  describes the interaction of the electrons and encodes the energy and the lifetime of the re-normalized QP within its real and imaginary part, respectively.

The spectral function so reads

$$A(\mathbf{k}, \omega) = \frac{1}{\pi} \frac{\text{Im}[\Sigma(\mathbf{k}, \omega)]}{(\omega - E_{\mathbf{k}}^0 - \text{Re}[\Sigma(\mathbf{k}, \omega)])^2 + (\text{Im}[\Sigma(\mathbf{k}, \omega)])^2} \quad (1.11)$$

In the noninteracting case,  $\Sigma(\mathbf{k}, \omega) = 0$  and we obtain the ideal case of a particle with infinite lifetime

$$\lim_{\Sigma \rightarrow 0} A(\mathbf{k}, \omega) = \lim_{\epsilon \rightarrow 0} \frac{1}{\pi} \frac{\epsilon}{(\omega - E_{\mathbf{k}}^0 - \epsilon)^2 + (\epsilon)^2} = \delta(\omega - E_{\mathbf{k}}^0). \quad (1.12)$$

Equally useful, the concept of the Fermi-liquid describes interacting particles which themselves can be mapped on a system of noninteracting particles. The self energy of a Fermi liquid in the limit  $\omega \rightarrow E_F = 0$  is  $\Sigma(\mathbf{k}, \omega) = \alpha\omega + i\beta\omega^2$  and the spectral function reduces to

$$A(\mathbf{k}, \omega) = \frac{1}{\pi} \frac{\beta\omega^2}{(\omega - E_{\mathbf{k}}^0)^2 + (\beta\omega^2)^2}. \quad (1.13)$$

Now, the lifetime of the quasi-particle (QP) is determined by its interaction with the Fermi liquid  $(\beta\omega^2)^2$ . For  $\omega \rightarrow E_F = 0$  however,  $(\beta\omega^2)^2 \rightarrow 0$  and the lifetime of the QP is again infinite.

The discussion of the spectral function for more complex systems can be very complicated and is a research topic in itself. We thus refer the interested reader to the literature [26].

### 1.5 The one-electron matrix element

The one-electron matrix element has been subject to longstanding interest. Historically, important contributions were made by authors such as Schaich, Ashcroft, Gadzuk and Mahan in the 1970ies [27–31]. These were followed by important work by Goldberg *et al.*, calculating in detail the atomic orbital cross sections in fixed orientation [32].

The advent of modern third generation synchrotron light sources gave access to polarized photons with high flux over typically large intervals of photon energies. The rising performance of state of the art photoemission end stations further has enabled detailed access to complete sets of photoemission data over a wide range of reciprocal space. Consequently, matrix element effects varying over broad ranges of  $k$ -space become systematically accessible. Especially in systems with high purity of the orbital character, matrix element effects can lead to severe ARPES intensity modulation [33–36].

In the following, we will illustrate a simple but effective model to estimate the contribution of the matrix element to bulk photoemission. As a byproduct, we will directly derive the basic kinematic relations of photoemission.

#### 1.5.1 Matrix elements without surface

We first consider the simplest situation conceivable: excitation of an electron from an initial Bloch state  $|\Psi_{n\mathbf{k}}\rangle$  into a plane wave final state  $|\mathbf{k}_f\rangle$  inside the solid. A sketch of this situation is shown in Fig. 1.1 (a), where we assume an infinitely extending solid without any influence of the surface. To calculate the matrix element, it is helpful to rewrite  $\Psi_{n\mathbf{k}}$  in terms of its Fourier components – the maximally localized Wannier functions [37]

$$|\mathbf{R}n\rangle = \frac{V}{(2\pi)^3} \int_{BZ} d^3\mathbf{k} e^{-i\mathbf{k}\cdot\mathbf{R}} |\Psi_{n\mathbf{k}}\rangle. \quad (1.14)$$

$\mathbf{R}$  is a real space lattice vector,  $V$  the real-space primitive cell volume and the integral is carried out over the entire Brillouin zone. The Wannier function  $|\mathbf{R}n\rangle$  is in general exponentially localized to lattice site  $\mathbf{R}$  and can be interpreted as the equivalent of a localized molecular orbital in a solid.

The Bloch functions

$$|\Psi_{n\mathbf{k}}\rangle = e^{i\mathbf{k}\cdot\mathbf{r}} u_{n\mathbf{k}}(\mathbf{r}) \quad (1.15)$$

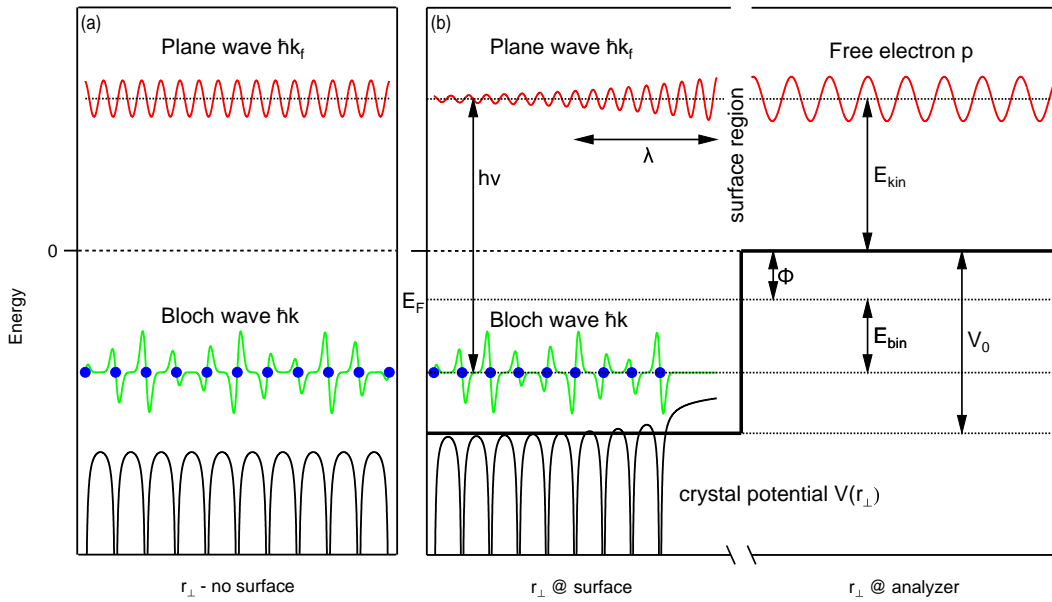


Figure 1.1: **(a)** Photoemission from an initial Bloch state  $\hbar k$  into a final state plane  $\hbar k_f$  wave without taking into account the surface. Translation invariance requires full momentum conservation. **(b)** Photoemission in the presence of a surface from an initial Bloch  $\hbar k$  state into a damped final state plane  $\hbar k_f$  wave inside the solid. Along the surface normal, translation symmetry is broken. The surface now acts as a source of out of plane momentum  $k_{\perp}$ .

## Chapter 1. Angle resolved photoemission

---

so can be written as an inverse Fourier transform

$$|\Psi_{n\mathbf{k}}\rangle = \sum_{\mathbf{R}} e^{i\mathbf{k}\cdot\mathbf{R}} |\mathbf{R}n\rangle, \quad (1.16)$$

where the sum runs over all lattice sites  $\mathbf{R}$  and

$$u_{n\mathbf{k}} = e^{-i\mathbf{k}\cdot\mathbf{r}} \sum_{\mathbf{R}} e^{i\mathbf{k}\cdot\mathbf{R}} |\mathbf{R}n\rangle. \quad (1.17)$$

A simple example of how Bloch- and Wannier functions transform into each other is shown in Fig. 1.2.

The matrix element  $M_{\mathbf{k}_f\mathbf{k}}$  of Eq. 1.6 now can be written as

$$\begin{aligned} M_{\mathbf{k}_f\mathbf{k}} &\propto \langle \mathbf{k}_f | e^{i\mathbf{k}_{h\nu}\cdot\mathbf{r}} \boldsymbol{\epsilon} \cdot \nabla | \Psi_{n\mathbf{k}} \rangle \\ &= \langle \mathbf{k}_f | e^{i\mathbf{k}_{h\nu}\cdot\mathbf{r}} \boldsymbol{\epsilon} \cdot \nabla \sum_{\mathbf{R}} e^{i\mathbf{k}\cdot\mathbf{R}} |\mathbf{R}n\rangle \\ &= \boldsymbol{\epsilon} \cdot \sum_{\mathbf{R}} e^{i\mathbf{k}\cdot\mathbf{R}} \langle \mathbf{k}_f | e^{i\mathbf{k}_{h\nu}\cdot\mathbf{r}} \nabla | \mathbf{R}n \rangle \\ &= \boldsymbol{\epsilon} \cdot \sum_{\mathbf{R}} e^{i\mathbf{k}\cdot\mathbf{R}} \int d^3\mathbf{r} e^{-i(\mathbf{k}_f - \mathbf{k}_{h\nu})\cdot\mathbf{r}} \nabla \Phi_n(\mathbf{r} - \mathbf{R}) \\ &= -\boldsymbol{\epsilon} \cdot \sum_{\mathbf{R}} e^{i\mathbf{k}\cdot\mathbf{R}} \int d^3\mathbf{r} \Phi_n(\mathbf{r} - \mathbf{R}) \nabla e^{-i(\mathbf{k}_f - \mathbf{k}_{h\nu})\cdot\mathbf{r}} \\ &= i\boldsymbol{\epsilon} \cdot (\mathbf{k}_f - \mathbf{k}_{h\nu}) \sum_{\mathbf{R}} e^{i\mathbf{k}\cdot\mathbf{R}} \int d^3\mathbf{r} \Phi_n(\mathbf{r} - \mathbf{R}) e^{-i(\mathbf{k}_f - \mathbf{k}_{h\nu})\cdot\mathbf{r}} \\ &= i\boldsymbol{\epsilon} \cdot \mathbf{k}_f \sum_{\mathbf{R}} e^{i\mathbf{k}\cdot\mathbf{R}} \int d^3\mathbf{r} \Phi_n(\mathbf{r} - \mathbf{R}) e^{-i(\mathbf{k}_f - \mathbf{k}_{h\nu})\cdot\mathbf{r}} \end{aligned} \quad (1.18)$$

where we defined

$$\Phi_n(\mathbf{r} - \mathbf{R}) = \langle \mathbf{r} | \mathbf{R}n \rangle, \quad (1.19)$$

and made use of  $\epsilon \cdot \mathbf{k}_{h\nu} = 0$  and  $\nabla^\dagger = -\nabla$ .<sup>3</sup>

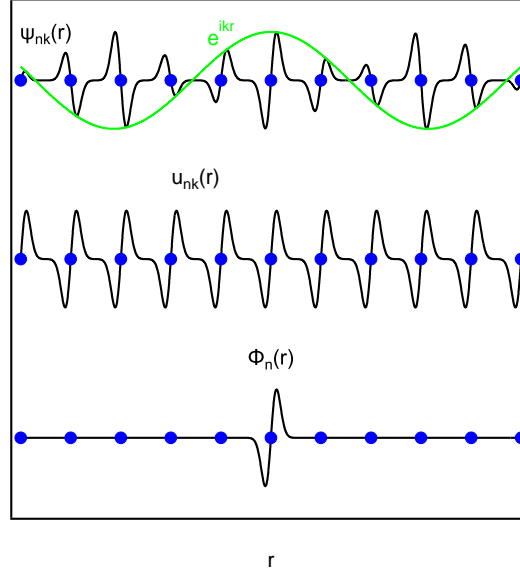


Figure 1.2: Transformation from Bloch functions (top) to Wannier functions (bottom). **(Top)** Real-space representation of a Bloch function  $\Psi_{nk}(r) = e^{ikr}u_k(r)$  associated with a single band in 1D for one value of the wave vector  $k$ . Filled circles indicate lattice atoms, and the green line indicates the  $e^{ikr}$  envelope. **(Middle)** Lattice periodic function  $u_k(r)$  associated with the same band, forming periodic images of one another. **(Bottom)** Single site Wannier function  $\Phi_n(r) = \langle r|\mathbf{0}n\rangle$ .

Introducing the coordinate transformation  $\mathbf{r} \rightarrow \mathbf{x} = \mathbf{r} - \mathbf{R}$  and  $d^3\mathbf{r} = d^3\mathbf{x}$  and approximating  $\sum_{\mathbf{R}}$  as an integral  $\sum_{\mathbf{R}} \rightarrow \frac{N}{V} \int d^3\mathbf{R}$ , with the total sample volume  $V$  and number of lattice sites  $N$ , we find

<sup>3</sup>We assume that  $\Phi_n(\mathbf{r} - \mathbf{R})$  is exponentially localized at lattice site  $\mathbf{R}$  and thus  $\lim_{r \rightarrow \infty} \Phi_n(\mathbf{r} - \mathbf{R}) = 0$ . By partial integration we obtain  $\int \Psi^*(\mathbf{r}) \nabla \phi_n(\mathbf{r} - \mathbf{R}) = [\Psi^*(\mathbf{r}) \Phi_n(\mathbf{r} - \mathbf{R})]_{-\infty}^{\infty} - \int \nabla \Psi^*(\mathbf{r}) \Phi_n(\mathbf{r} - \mathbf{R}) = - \int \nabla \Psi^*(\mathbf{r}) \Phi_n(\mathbf{r} - \mathbf{R})$  and thus  $\nabla^\dagger = -\nabla$ .

$$\begin{aligned}
 M_{\mathbf{k}_f \mathbf{k}} &\propto i \frac{N}{V} \boldsymbol{\epsilon} \cdot \mathbf{k}_f \int d^3 \mathbf{R} e^{i\mathbf{k} \cdot \mathbf{R}} \int d^3 \mathbf{x} \Phi_n(\mathbf{x}) e^{-i(\mathbf{k}_f - \mathbf{k}_{h\nu}) \cdot (\mathbf{x} + \mathbf{R})} \\
 &= i \frac{N}{V} \boldsymbol{\epsilon} \cdot \mathbf{k}_f \int d^3 \mathbf{R} e^{i\mathbf{k} \cdot \mathbf{R}} \underbrace{e^{i\mathbf{G} \cdot \mathbf{R}}}_{\equiv 1} \int d^3 \mathbf{x} \Phi_n(\mathbf{x}) e^{-i(\mathbf{k}_f - \mathbf{k}_{h\nu}) \cdot (\mathbf{x} + \mathbf{R})} \\
 &= i \frac{N}{V} \boldsymbol{\epsilon} \cdot \mathbf{k}_f \underbrace{\int d^3 \mathbf{R} e^{i(\mathbf{k} + \mathbf{G} - \mathbf{k}_f + \mathbf{k}_{h\nu}) \cdot \mathbf{R}}}_{\delta(\mathbf{k} + \mathbf{G} - \mathbf{k}_f + \mathbf{k}_{h\nu})} \underbrace{\int d^3 \mathbf{x} \Phi_n(\mathbf{x}) e^{-i(\mathbf{k}_f - \mathbf{k}_{h\nu}) \cdot \mathbf{x}}}_{\langle \mathbf{k}_f - \mathbf{k}_{h\nu} | \mathbf{0}n \rangle} \\
 &= i(2\pi)^{3/2} \frac{N}{V} \boldsymbol{\epsilon} \cdot \mathbf{k}_f \delta(\mathbf{k} + \mathbf{G} - \mathbf{k}_f + \mathbf{k}_{h\nu}) \langle \mathbf{k}_f - \mathbf{k}_{h\nu} | \mathbf{0}n \rangle,
 \end{aligned} \tag{1.20}$$

where we took into account the translation invariance  $e^{i\mathbf{G}\mathbf{R}} = 1$  with respect to some arbitrary reciprocal lattice vector  $\mathbf{G}$ . We can see that the well known momentum conservation is a property of the one-electron matrix element, and therefore reasonably independent of the multibody effects in the solid. More interestingly, we find the total matrix element to be well approximated by the Fourier transform  $\langle \mathbf{k}_f - \mathbf{k}_{h\nu} | \mathbf{0}n \rangle \sim \langle \mathbf{k}_f | \mathbf{0}n \rangle$  of one localized Wannier function. In other words, the matrix element related ARPES intensity distribution is a direct measure of the real space distribution of the local Wannier function, i.e. the local molecular orbital.

### 1.5.2 Matrix elements in the presence of a surface

Photoemission is a surface process. This mirrors in two important facts: For one, the penetration depth of the incoming photon beam is finite ( $\mathcal{O}(100 \text{ nm})$ ). Second and important for our considerations, the outgoing electrons interact with the solid through electron-electron and electron-phonon interaction. Consequently, the electrons only possess a limited lifetime and thus are strongly damped with characteristic mean free paths of  $\lambda \sim \mathcal{O}(5 \text{ \AA})$ .<sup>4</sup> In the presence of a surface, the final state so needs to be expressed more properly as inverse LEED state, phenomenologically described by an evanescent plane wave

$$\langle \mathbf{r} | \mathbf{k}_f \rangle = e^{i\mathbf{k}_f \mathbf{r}} e^{r_{\perp} / \lambda}, \tag{1.21}$$

for  $r_{\perp}$  within reach of the crystal potential. The mean free path  $\lambda$  can so be interpreted as the penetration depth of the inverse LEED state which characterizes the damping of the evanescent

---

<sup>4</sup>The electrons which lose energy on their way out of the solid are typically termed “secondary electrons”. Their number as a function of binding energy increases in an integral manner [38].

wave inside the solid.<sup>5</sup>

Eq. 1.18 now reads

$$\begin{aligned}
 M_{\mathbf{k}_f \mathbf{k}} &\propto \epsilon \cdot \sum_{\mathbf{R}, R_\perp < 0} e^{i\mathbf{k} \cdot \mathbf{R}} \int d^3 \mathbf{r} e^{-i\mathbf{k}_f \cdot \mathbf{r}} e^{r_\perp / \lambda} e^{i\mathbf{k}_{h\nu} \cdot \mathbf{r}} \nabla \Phi_n(\mathbf{r} - \mathbf{R}) \\
 &= -\epsilon \cdot \sum_{\mathbf{R}, R_\perp < 0} e^{i\mathbf{k} \cdot \mathbf{R}} \int d^3 \mathbf{r} \Phi_n(\mathbf{r} - \mathbf{R}) \nabla e^{-i(\mathbf{k}_f - \mathbf{k}_{h\nu}) \cdot \mathbf{r}} e^{r_\perp / \lambda} \\
 &= \epsilon \cdot (i\mathbf{k}_f - i\mathbf{k}_{h\nu} - \frac{1}{\lambda} \mathbf{e}_\perp) \sum_{\mathbf{R}, R_\perp < 0} e^{i\mathbf{k} \cdot \mathbf{R}} \int d^3 \mathbf{r} \Phi_n(\mathbf{r} - \mathbf{R}) e^{-i(\mathbf{k}_f - \mathbf{k}_{h\nu}) \cdot \mathbf{r}} e^{r_\perp / \lambda} \\
 &= \epsilon \cdot (i\mathbf{k}_f - \frac{1}{\lambda} \mathbf{e}_\perp) \sum_{\mathbf{R}, R_\perp < 0} e^{i\mathbf{k} \cdot \mathbf{R}} \int d^3 \mathbf{x} \Phi_n(\mathbf{x}) e^{-i(\mathbf{k}_f - \mathbf{k}_{h\nu}) \cdot (\mathbf{x} + \mathbf{R})} e^{(x_\perp + R_\perp) / \lambda} \\
 &= \epsilon \cdot (i\mathbf{k}_f - \frac{1}{\lambda} \mathbf{e}_\perp) \sum_{\mathbf{R}, R_\perp < 0} e^{i(\mathbf{k} - \mathbf{k}_f + \mathbf{k}_{h\nu}) \cdot \mathbf{R}} e^{R_\perp / \lambda} \int d^3 \mathbf{x} \Phi_n(\mathbf{x}) e^{-i(\mathbf{k}_f - \mathbf{k}_{h\nu}) \cdot \mathbf{x}} e^{x_\perp / \lambda} \\
 &= \epsilon \cdot (i\mathbf{k}_f - \frac{1}{\lambda} \mathbf{e}_\perp) \sum_{\mathbf{R}, R_\perp < 0} e^{i(\mathbf{k} - \mathbf{k}_f + \mathbf{k}_{h\nu}) \cdot \mathbf{R}} e^{R_\perp / \lambda} \langle \mathbf{k}_f - \mathbf{k}_{h\nu} + \frac{i}{\lambda} \mathbf{e}_\perp | \mathbf{0}n \rangle, \quad (1.22)
 \end{aligned}$$

where  $\mathbf{e}_\perp$  is the sample surface unit vector and where we again used the coordinate transformation  $\mathbf{r} \rightarrow \mathbf{x} = \mathbf{r} - \mathbf{R}$  with  $r_\perp \rightarrow x_\perp = r_\perp - R_\perp$ . Writing  $\sum_{\mathbf{R}, R_\perp < 0}$  in terms of integrals parallel and perpendicular to the crystal surface  $\frac{N}{V} \int dR_\parallel \int_{-\infty}^0 dR_\perp$  and assuming explicitly, that the Wannier function decays exponentially faster as  $e^{r_\perp / \lambda}$  rises, the total matrix element becomes

$$\begin{aligned}
 M_{\mathbf{k}_f \mathbf{k}} &\propto \frac{N}{V} \epsilon \cdot (i\mathbf{k}_f - \frac{1}{\lambda} \mathbf{e}_\perp) \langle \mathbf{k}_f - \mathbf{k}_{h\nu} + \frac{i}{\lambda} \mathbf{e}_\perp | \mathbf{0}n \rangle \\
 &\times \int dR_\parallel e^{i(\mathbf{k}_\parallel - \mathbf{k}_{f\parallel} + \mathbf{k}_{h\nu\parallel}) R_\parallel} \underbrace{e^{i\mathbf{G}_\parallel R_\parallel}}_{\equiv 1} \int_{-\infty}^0 dR_\perp e^{(i(k_\perp - k_{f\perp} + k_{h\nu\perp}) + \frac{1}{\lambda}) R_\perp} \\
 &= 2\pi \frac{N}{V} \epsilon \cdot (i\mathbf{k}_f - \frac{1}{\lambda} \mathbf{e}_\perp) \langle \mathbf{k}_f - \mathbf{k}_{h\nu} + \frac{i}{\lambda} \mathbf{e}_\perp | \mathbf{0}n \rangle \\
 &\times \delta(\mathbf{k}_\parallel + \mathbf{G}_\parallel - \mathbf{k}_{f\parallel} + \mathbf{k}_{h\nu\parallel}) \frac{1}{i(k_\perp - k_{f\perp} + k_{h\nu\perp}) + 1/\lambda}. \quad (1.23)
 \end{aligned}$$

<sup>5</sup> It is important to emphasize here that we intentionally do not define a strict surface (e.g.  $r_\perp = 0$ ) but rather expect the exponential factor  $e^{r_\perp / \lambda}$  to be active within reach of the crystal potential. Since the Wannier function is assumed to decay exponentially “faster” than the divergent term  $e^{r_\perp / \lambda}$  of the evanescent wave, this allows for a smooth convergence of the integrals in the following.

## Chapter 1. Angle resolved photoemission

---

In the presence of the surface, only the in plane components of the electron momentum are strictly conserved within some in plane reciprocal lattice vector  $\mathbf{G}_{\parallel}$ . For the out of plane component, we find a Lorentzian “pseudo momentum conservation”  $|M_{\mathbf{k}_f \mathbf{k}}|^2 \propto \frac{1}{(k_{\perp} - k_{f\perp} + k_{h\nu\perp})^2 + 1/\lambda^2} \xrightarrow{\lambda \rightarrow \infty} \pi \delta(k_{\perp} - k_{f\perp} + k_{h\nu\perp})$ , which becomes sharper and sharper with larger penetration depth  $\lambda$  of the final state.

We further find the angular distribution of photoelectrons still to be determined by the Fourier transform  $\langle \mathbf{k}_f - \mathbf{k}_{h\nu} + \frac{i}{\lambda} \mathbf{e}_{\perp} | \mathbf{0}n \rangle$  of the local Wannier function  $|\mathbf{0}n\rangle$ , with a  $\lambda$  – dependent phase shift in the argument. Since  $1/\lambda \sim \mathcal{O}(0.2 \text{ \AA}^{-1})$  and  $k_{h\nu} = 2\pi\nu/c \sim \mathcal{O}(0.05 \text{ \AA}^{-1})$  are small with respect to  $k_f \sim \sqrt{2mE_{kin}} \sim \mathcal{O}(5 \text{ \AA}^{-1})$  in UV- and soft x-ray photoemission with  $h\nu \sim \mathcal{O}(100 \text{ eV})$ ,  $\langle \mathbf{k}_f - \mathbf{k}_{h\nu} + \frac{i}{\lambda} \mathbf{e}_{\perp} | \mathbf{0}n \rangle$  will be typically well approximated by  $\langle \mathbf{k}_f | \mathbf{0}n \rangle$ .

### 1.5.3 The electron escape depth $\lambda$

It is - once again - important to note that the integrals in the model above only converge if the Wannier functions decay faster than the divergent term  $e^{r_{\perp}/\lambda}$  of the evanescent wave rises. It has been theoretically shown however, that it is always possible to construct exponentially localized Wannier functions in dimensions  $D \leq 3$  which fulfil this criterion for sufficiently high  $\lambda$  [37, 39].

For a quick estimate and in analogy to an atomic orbital with quantum number  $n$ , we can assume the radial part of a Wannier function to decay exponentially as  $e^{-r/(an)}$ , where  $a$  is the spatial extension (typically the size of one unit cell) of this “molecular orbital”. The integrals of Eq. 1.23 hence converge only if  $\lambda > an$ , i.e. if the evanescent wave covers at least one unit cell. In many cases of photoemission however,  $\lambda$  is actually quite close to  $a$  and discussed model therefore at risk.

Mostly, the photoelectron escape depth  $\lambda$  is determined by electron-electron interaction. In the energy range of  $E_{kin} \sim \mathcal{O}(100 \text{ eV})$ , the electrons involved in the scattering process can be considered a free electron gas and their bonding to the solid is no longer important. The electron-electron interaction is therefore largely determined by the plasma frequency of the solid, which is only a function of electron density  $\rho$  and therefore largely independent of the constituents of the solid. Consequently, the overall attenuation length  $\lambda$  is well described by a “universal curve” which only depends on the kinetic energy of the photoelectron  $E_{kin}$  and which can be empirically described as

$$\lambda[\text{\AA}] \sim c_1 (E_{kin}[\text{eV}] + \Phi[\text{eV}])^{-2} + c_2 \sqrt{a[nm](E_{kin}[\text{eV}] + \Phi[\text{eV}])}, \quad (1.24)$$

where  $c_1 \sim 538$  and  $c_2 \sim 0.41$  are good parameters to describe elements, 2170 and 0.72 good for inorganic compounds [40].  $E_{kin}$  and  $\Phi$  are kinetic energy and workfunction as defined in Fig. 1.2.



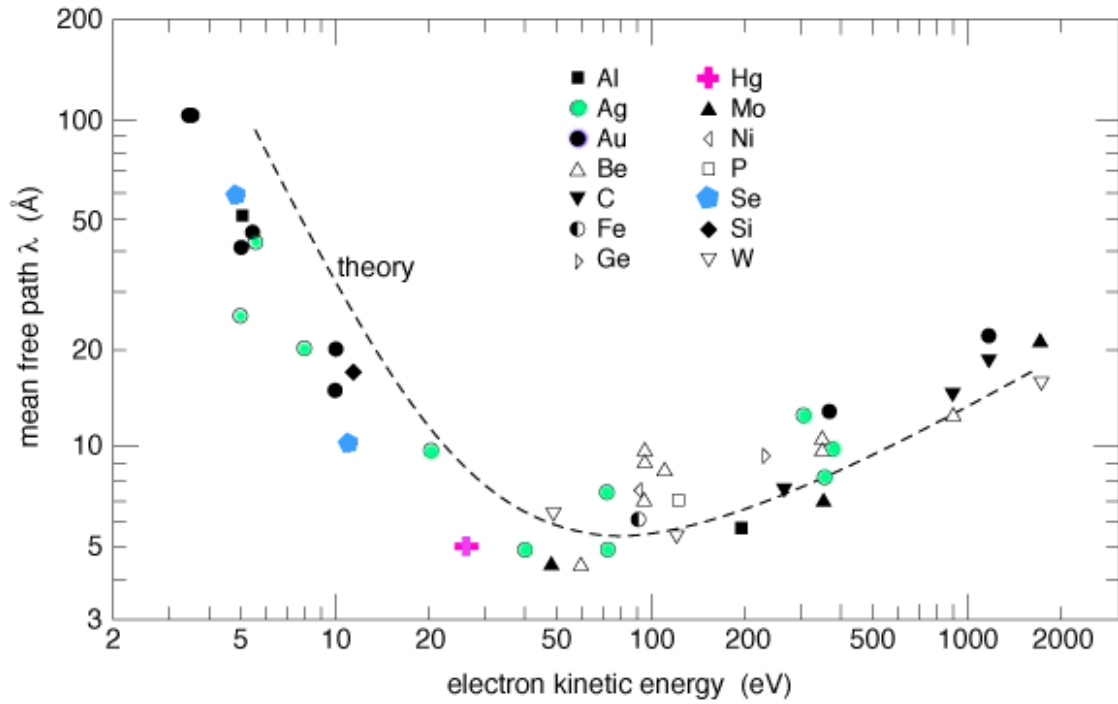


Figure 1.3: Universal curve describing the electron mean free path  $\lambda$  as a function of energy (above the Fermi level). The graph was taken from the internet [41].

Fig. 1.3 reproduces the original data by Seah et al. [40]. Clearly,  $\lambda$  is of the order of few  $\text{\AA}$ , which demonstrates the high importance of the surface in photoemission. The very thin surface layer sampled by ARPES hence requires for atomically clean surfaces prepared under ultra high vacuum conditions.

#### 1.5.4 The photoelectron escape

To understand how the “pseudo momentum conservation” shown in previous sections is reflected in the actual measurement of the photoelectron momentum  $\mathbf{p}$ , it is instructive to recall the propagation of an unbound free electron across a step potential as illustrated in Fig. 1.1 (b).

$$V(\mathbf{r}) = \begin{cases} -V_0 & r_{\perp} < 0 \\ 0 & r_{\perp} > 0 \end{cases} \quad (1.25)$$

where  $V_0$  is the inner potential of the solid.

Energy conservation during the emission process requires that  $E(r_{\perp} < 0) = E(r_{\perp} > 0)$  and

## Chapter 1. Angle resolved photoemission

---

thus

$$\frac{\hbar^2 \mathbf{k}_f^2}{2m} = \frac{\mathbf{p}^2}{2m} + V_0 \quad (1.26)$$

Since the in plane momentum  $\hbar \mathbf{k}_{f\parallel} = \mathbf{p}_{\parallel}$  remains conserved due to translation symmetry, the out of plane momentum has to absorb the effect of the inner potential and we find

$$\frac{\hbar^2 k_{f\perp}^2}{2m} = \frac{p_{\perp}^2}{2m} + V_0. \quad (1.27)$$

In photoemission, one typically measures the emission angles  $(\phi_k, \theta_k)$  and the kinetic energy  $E_{kin}$  of the photoelectron, which are related to the photoelectron momenta as

$$p_x = \sqrt{2mE_{kin}} \sin \theta_k \cos \phi_k, \quad p_y = \sqrt{2mE_{kin}} \sin \theta_k \sin \phi_k, \quad p_z = \sqrt{2mE_{kin}} \cos \theta_k. \quad (1.28)$$

We thus have

$$\begin{aligned} \hbar^2 \mathbf{k}_{f\parallel}^2 &= \mathbf{p}_{\parallel}^2 = p_x^2 + p_y^2 = 2mE_{kin} \sin^2 \theta_k \\ \hbar^2 k_{f\perp}^2 &= p_{\perp}^2 + 2mV_0 = 2m(E_{kin} \cos^2 \theta_k + V_0), \end{aligned} \quad (1.29)$$

and finally

$$\begin{aligned} k_{f\parallel} &= \frac{1}{\hbar} \sqrt{2mE_{kin}} \sin \theta_k \\ k_{f\perp} &= \frac{1}{\hbar} \sqrt{2m(E_{kin} \cos^2 \theta_k + V_0)}. \end{aligned} \quad (1.30)$$

According to Fig. 1.1, the kinetic energy  $E_{kin}$  further is related to the binding energy  $E_B$  of the electron via photon energy  $h\nu$  and the workfunction  $\Phi$  of the solid:  $E_{kin} = h\nu - E_B - \phi$ .<sup>6</sup>

---

<sup>6</sup>Note that in the experiment, the photoelectron has to be “absorbed” by the electron analyzer. The analyzer is in electrical equilibrium with the sample and thus the quantity  $\Phi$  which enters here is the actually workfunction of the analyzer  $\Phi_{Ana}$ .

### 1.5.5 Matrix elements in tight binding approximation

As we saw, the total matrix element  $M_{\mathbf{k}_f \mathbf{k}}$  is to a large extent determined by the Fourier Transform  $\langle \mathbf{k}_f | 0n \rangle$  of the localized Wannier function  $|0n\rangle$ . In complex systems, the determination of the Wannier function can be a tedious task and is typically subject to the vast field of density functional theory.

In certain cases however, the groundstate electron wave function can be well approximated by a linear combination of generalized atomic orbitals  $|0n\rangle \sim \sum_{\mathbf{R}_i} \sum_{nlm} c_{inlm} |\mathbf{R}_i, nlm\rangle$  located at each lattice site.  $|\mathbf{R}_i, nlm\rangle$  are atomic wave functions  $|nlm\rangle$  centered at coordinates  $\mathbf{R}_i$  within one unit cell. The coefficients  $c_{inlm}$  need to be adapted to the unit cell's local point group. In other words, the linear combination of atomic orbitals needs to respect the symmetry properties of the crystal.<sup>7</sup>

The Bloch function  $|\Psi_{\mathbf{k}}\rangle$  has now the same form as the Bloch-sum formula in tight-binding theory, where the Wannier functions are replaced by molecular orbitals

$$|\Psi_{\mathbf{k}}\rangle = \sum_{\mathbf{R}} e^{i\mathbf{k}\cdot\mathbf{R}} \sum_{\mathbf{R}_i} \sum_{nlm} c_{inlm} |\mathbf{R}_i, nlm\rangle, \quad (1.31)$$

where  $\mathbf{R}$  labels all lattice sites in the solid and  $\mathbf{R}_i$  again labels all the atoms within one unit cell. Omitting the terms for ‘pseudo momentum conservation’ in Eq. 1.23, the total matrix element can be written as the Fourier transform

$$\begin{aligned} M_{\mathbf{k}_f \mathbf{k}} &\propto \boldsymbol{\epsilon} \cdot \left( i\mathbf{k}_f - \frac{1}{\lambda} \mathbf{e}_{\perp} \right) \langle \mathbf{k}_f - \mathbf{k}_{h\nu} + \frac{i}{\lambda} \mathbf{e}_{\perp} | \sum_{\mathbf{R}_i} \sum_{nlm} c_{inlm} |\mathbf{R}_i, nlm\rangle \\ &= \boldsymbol{\epsilon} \cdot \left( i\mathbf{k}_f - \frac{1}{\lambda} \mathbf{e}_{\perp} \right) \sum_{\mathbf{R}_i} \sum_{nlm} c_{inlm} \langle \mathbf{k}_f - \mathbf{k}_{h\nu} + \frac{i}{\lambda} \mathbf{e}_{\perp} | \mathbf{R}_i, nlm\rangle \\ &= \boldsymbol{\epsilon} \cdot \left( i\mathbf{k}_f - \frac{1}{\lambda} \mathbf{e}_{\perp} \right) \sum_{\mathbf{R}_i} \sum_{nlm} c_{inlm} e^{i(\mathbf{k}_f - \mathbf{k}_{h\nu} + \frac{i}{\lambda} \mathbf{e}_{\perp}) \cdot \mathbf{R}_i} \langle \mathbf{k}_f - \mathbf{k}_{h\nu} + \frac{i}{\lambda} \mathbf{e}_{\perp} | \mathbf{0}, nlm\rangle \\ &= \sum_{\mathbf{R}_i} \sum_{nlm} c_{inlm} e^{i(\mathbf{k}_f - \mathbf{k}_{h\nu} + \frac{i}{\lambda} \mathbf{e}_{\perp}) \cdot \mathbf{R}_i} M^{nlm}(\mathbf{k}_f, \mathbf{k}_{h\nu}, \lambda), \end{aligned} \quad (1.32)$$

<sup>7</sup>For an instructive example refer to Sec: 5.13.

## Chapter 1. Angle resolved photoemission

---

where

$$M^{nlm}(\mathbf{k}_f, \mathbf{k}_{h\nu}, \lambda) \propto \boldsymbol{\epsilon} \cdot \left( i\mathbf{k}_f - \frac{1}{\lambda} \mathbf{e}_\perp \right) \langle \mathbf{k}_f - \mathbf{k}_{h\nu} + \frac{i}{\lambda} \mathbf{e}_\perp | \underbrace{\mathbf{0}, nlm}_{\equiv |nlm\rangle} \rangle . \quad (1.33)$$

The main task is hence to calculate the Fourier transform  $\langle \mathbf{k}_f - \mathbf{k}_{h\nu} + \frac{i}{\lambda} \mathbf{e}_\perp | nlm \rangle$  of the atomic orbitals.

### The radial cross section

Already in 1929, B. Podolsky and L. Pauling have shown that wave functions of the form [42]

$$|\Phi(\mathbf{r})\rangle = |nlm\rangle = R_{nl}(r)|l, m\rangle \quad (1.34)$$

with radial part  $R_{nl}$  and  $\mathbf{r} = \{r, \theta_r, \phi_r\}$  possess a Fourier transform

$$|\tilde{\Phi}(\mathbf{k}_f)\rangle = f_{nl}(k_f)|l, m\rangle \quad (1.35)$$

with  $\mathbf{k}_f = \{k_f, \theta_k, \phi_k\}$ .

Whereas the Fourier transform of the spherical harmonics  $|lm\rangle$  is just the spherical harmonics itself, the Fourier transform of radial part  $R_{nl}(r)$  transforms to

$$f_{nl}(k_f) = 4\pi(-i)^l \int_0^\infty dr r^2 j_l(k_f r) R_{nl}(r) , \quad (1.36)$$

where  $j_l(k_f r)$  is a Bessel function. Fig. 1.4 shows  $|f_{nl}(k_f)|$  calculated for different radial atomic functions

$$R_{nl}(r) = \sqrt{\left(\frac{2}{na}\right)^3 \frac{(n-l-1)!}{2n(n+l)!}} e^{-r/na} \left(\frac{2r}{na}\right)^l L_{n-l-1}^{2l+1} \left(\frac{2r}{na}\right) , \quad (1.37)$$

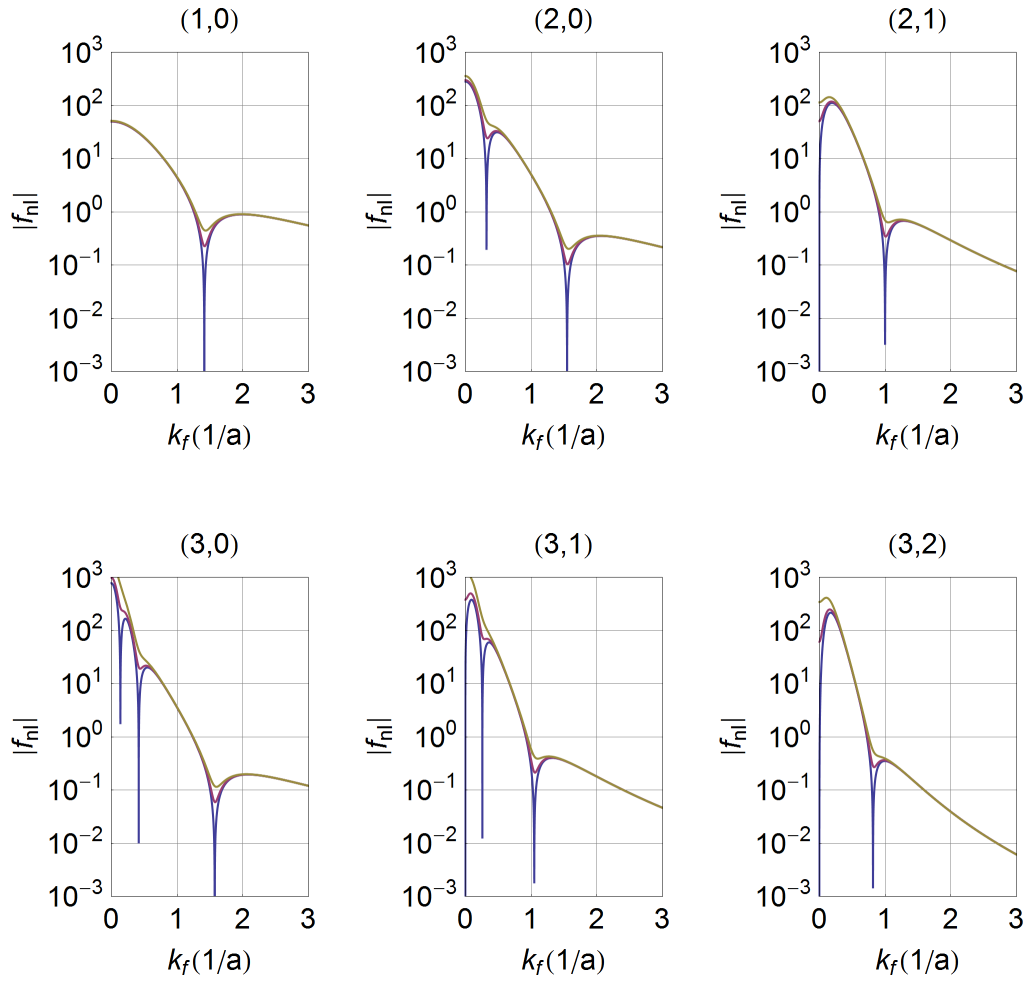


Figure 1.4: The radial contribution to the matrix element  $|f_{nl}(k_f)|$  calculated for several radial atomic wave functions  $(n, l)$  with **(blue)**  $\lambda \rightarrow \infty$ , **(red)**  $\lambda = 20a$ , **(yellow)**  $\lambda = 10a$ . At distinct values of  $k_f$ , sharp “Cooper minima” are observed, which are softened for finite penetration depths  $\lambda$ .

## Chapter 1. Angle resolved photoemission

---

where  $a$  is the characteristic radius of the orbital. Overall,  $|f_{nl}(k_f)|$  falls off with increasing  $k_f \propto \sqrt{E_{kin}}$ . Depending on the quantum numbers  $n$  and  $l$ ,  $|f_{nl}(k_f)|$  develops additional sharp minima, which leads to a severe suppression of photoemission intensity for certain orbitals at distinct photon energies. These minima are the so called ‘‘Cooper minima’’ [43]:

With increasing  $k_f$ , the final state plane wave – represented by the Bessel function in the integral of Eq. 1.36 – oscillates more rapidly in space. This leads to more cancelation effects for increasing  $k_f$ , and  $|f_{nl}(k_f)|$  consequently diminishes. The Cooper minima form at low  $k_f$ , where the Bessel function  $j_l(k_f r)$  changes its sign on a length scale of  $\mathcal{O}(a)$ . On the same length scale,  $R_{nl}(r)$  decays and likewise exhibits a total of  $n - l - 1$  sign changes. The interplay of sign changes of both function so leads to a complete suppression of the integral  $|f_{nl}(k_f)|$  at distinct momenta  $k_f$ , or equivalently at distinct kinetic energies  $E_{kin}$ .

To qualitatively test the effect of the surface penetration depth  $\lambda$  on  $f_{nl}(k_f)$ , we develop  $|\mathbf{k}_f + i/\lambda \mathbf{e}_\perp|$  in terms of small values  $1/\lambda$ :

$$\begin{aligned}
 \left| \mathbf{k}_f + \frac{i}{\lambda} \mathbf{e}_\perp \right| &= \sqrt{k_{f\parallel}^2 + \left( k_{f\perp} + \frac{i}{\lambda} \right)^2} \\
 &\sim \sqrt{k_{f\parallel}^2 + k_{f\perp}^2} + \frac{ik_{f\perp}}{\sqrt{k_{f\parallel}^2 + k_{f\perp}^2}} \frac{1}{\lambda} + \mathcal{O}(\lambda^{-2}) \\
 &= k_f + \frac{ik_{f\perp}}{k_f} \frac{1}{\lambda} + \mathcal{O}(\lambda^{-2})
 \end{aligned} \tag{1.38}$$

At normal emission,  $k_{f\parallel} = 0$  and the result collapses to

$$\left| \mathbf{k}_f + \frac{i}{\lambda} \mathbf{e}_\perp \right| \sim k_{f\perp} + \frac{i}{\lambda} + \mathcal{O}(\lambda^{-2}) . \tag{1.39}$$

Fig. 1.4 additionally plots the results of  $f_{nl}(k_f + \frac{i}{\lambda})$  for  $\lambda = 20a$  and  $\lambda = 10a$ . Interestingly, the imaginary phase  $i/\lambda$ , only softens the Cooper minima, but does not change the overall envelope of the curve. It should however be noted that according to the ‘‘universal Curve’’ of Eq. 1.24 and Fig. 1.3,  $\lambda$  varies as a function of  $E_{kin} \propto k_f^2$  and a more realistic result would therefore be in between the extremes shown in this plot.

## 1.5. The one-electron matrix element

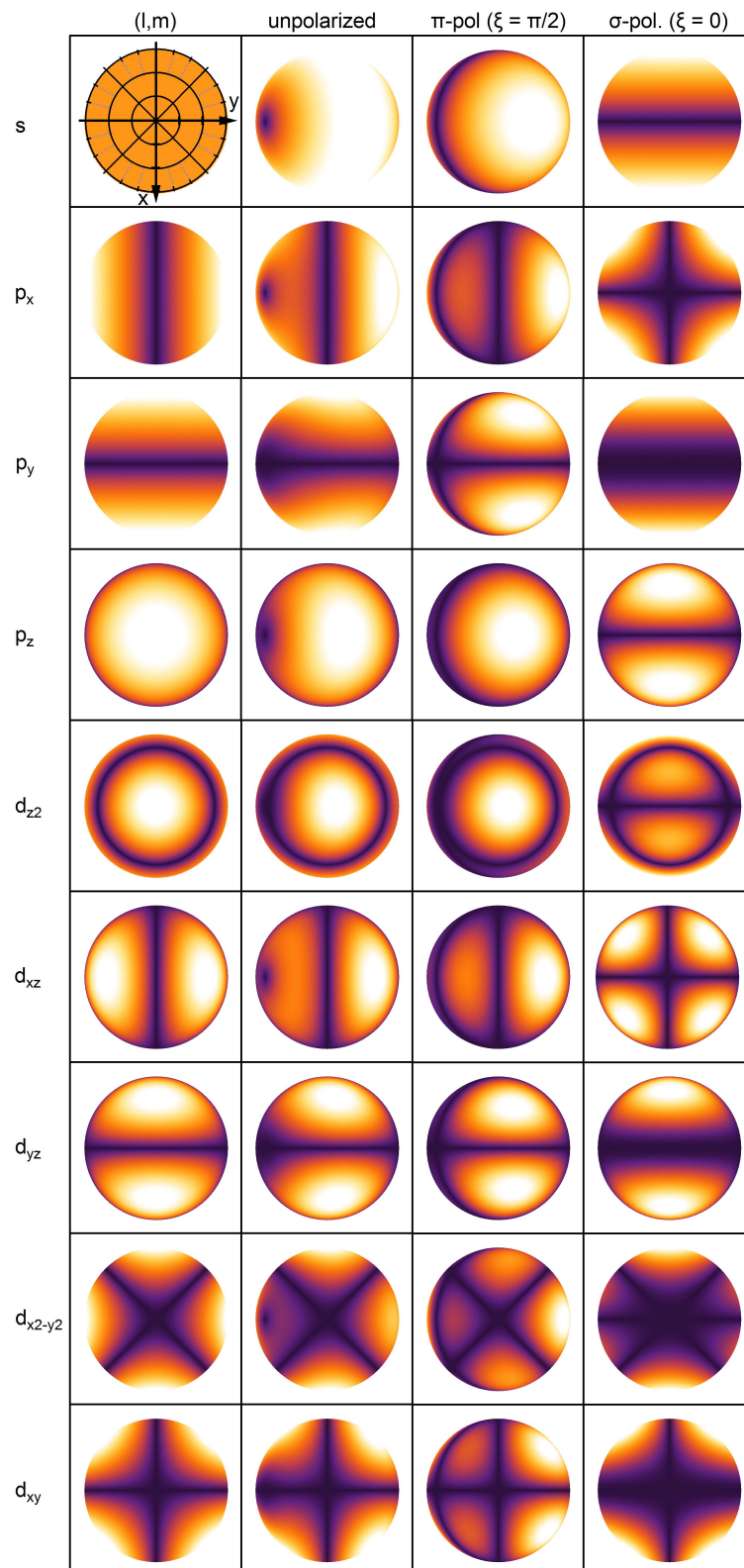


Figure 1.5: Angular distribution  $|M(\theta_k, \phi_k)|$  of matrix elements for different polarizations  $\xi$  and an incident light angle of  $\alpha = 60^\circ$  (light coming from left).

### The angular cross section

As we saw, the angular part of an atomic orbital is basically invariant under Fourier transformation. The influence of the experimental geometry for the distribution of spectral weight relies on the projection of the polarization vector  $\epsilon$  onto the wavevector  $\mathbf{k}_f$  of the outgoing photoelectron  $\epsilon \cdot \mathbf{k}_f$ . In a hypothetical experimental configuration with isotropically unpolarized light, the matrix element will consequently cancel out all variations of  $\epsilon \cdot \mathbf{k}_f$  and express the same angular distribution as the Wannier function.

In a linearly polarized configuration, the polarization vector  $\epsilon$  can be written as

$$\epsilon = \begin{pmatrix} \epsilon_x \\ \epsilon_y \\ \epsilon_z \end{pmatrix} = \epsilon \begin{pmatrix} 1 & 0 & 0 \\ 0 & \cos \alpha & -\sin \alpha \\ 0 & \sin \alpha & \cos \alpha \end{pmatrix} \cdot \begin{pmatrix} \cos \xi \\ \sin \xi \\ 0 \end{pmatrix} = \epsilon \begin{pmatrix} \cos \xi \\ \cos \alpha \sin \xi \\ \sin \alpha \sin \xi \end{pmatrix} \quad (1.40)$$

where  $\alpha$  is the angle in between incoming x-ray beam and analyzer, and  $\xi$  is the polarization as defined in Fig. 1.6 and 1.7 ( $\xi = 0$ :  $\sigma$ -polarized;  $\xi = \pi/2$ :  $\pi$ -polarized).

$\epsilon \cdot (i\mathbf{k}_f - \frac{1}{\lambda}\mathbf{e}_\perp)$  so simplifies to

$$\epsilon \cdot (i\mathbf{k}_f - \frac{1}{\lambda}\mathbf{e}_\perp) = i\epsilon \left( \cos \xi k_x + \cos \alpha \sin \xi k_y + \sin \alpha \sin \xi \left( k_z + \frac{i}{\lambda} \right) \right) \quad (1.41)$$

In a typical experimental geometry with  $\alpha = \pi/3$ , this quantity vanishes if  $k_y = -\sqrt{3}(k_z + i/\lambda)$  in  $\pi$ -polarization, which is impossible to fulfil if  $\lambda$  is finite. In  $\sigma$ -polarization, it will always vanish for  $k_x = 0$ .

Exemplary plots of the angular distribution of matrix elements calculated according to Eq. 1.33 are shown in Fig. 1.5 for the  $s$ ,  $p$  and  $d$  orbitals. The effect of a finite penetration depth  $\lambda$  to the angular distribution of the matrix element was found to be minor and was therefore not taken into account.<sup>8</sup>

The left column “ $(lm)$ ” shows the angular distribution of the orbital  $|lm\rangle$  which is identical to matrix elements obtained in an isotropic light configuration. This distribution is essentially captured by matrix elements obtained in an unpolarized light configuration (“unpolarized”).<sup>9</sup> Further we show the angular distribution of spectral weight in  $\sigma$ - and  $\pi$ -polarization in the third

<sup>8</sup>We will see however in Ch. 3, that taking into account a finite  $\lambda$  may change the intensity distribution on a small angular scale.

<sup>9</sup>Isotropic light refers to light with polarizations distributed isotropically along all directions of 3D space. Unpolarized light refers to the physical situation of light with polarization vectors distributed along the 2D polarization plane, perpendicular to the incoming light direction.



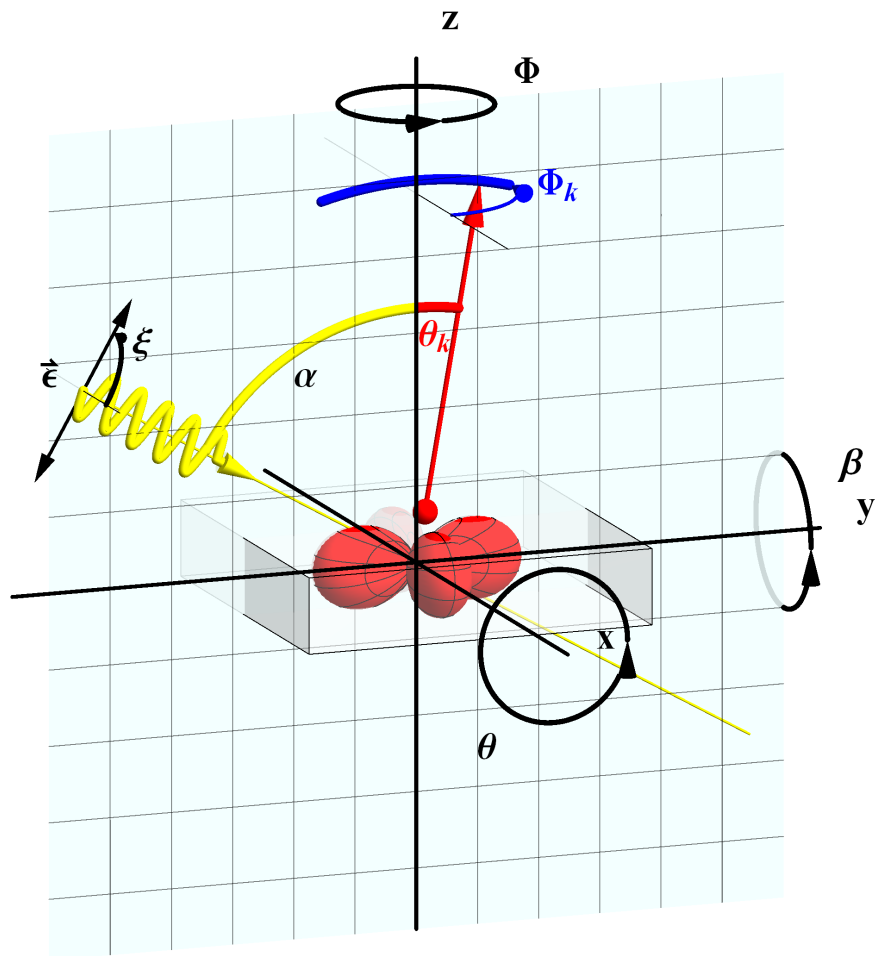


Figure 1.6: Typical geometry of an ARPES setup with  $\pi$ -polarized light (yellow wiggles,  $\xi = \pi/2$ ) and  $\pi$ -polarized analyzer slits (blue curve,  $\phi_k = \pi/2$ ). All possible sample rotations are indicated by arrow-headed circles. The sample in this example can be rotated around  $x$ -,  $y$ - and  $z$ -axis by dependent angles  $\theta$ ,  $\beta$  and  $\phi$ , respectively. At most synchrotrons, the polarization  $\xi$  can be chosen as well. The orientation of the analyzer slit  $\phi_k$  is typically fixed.

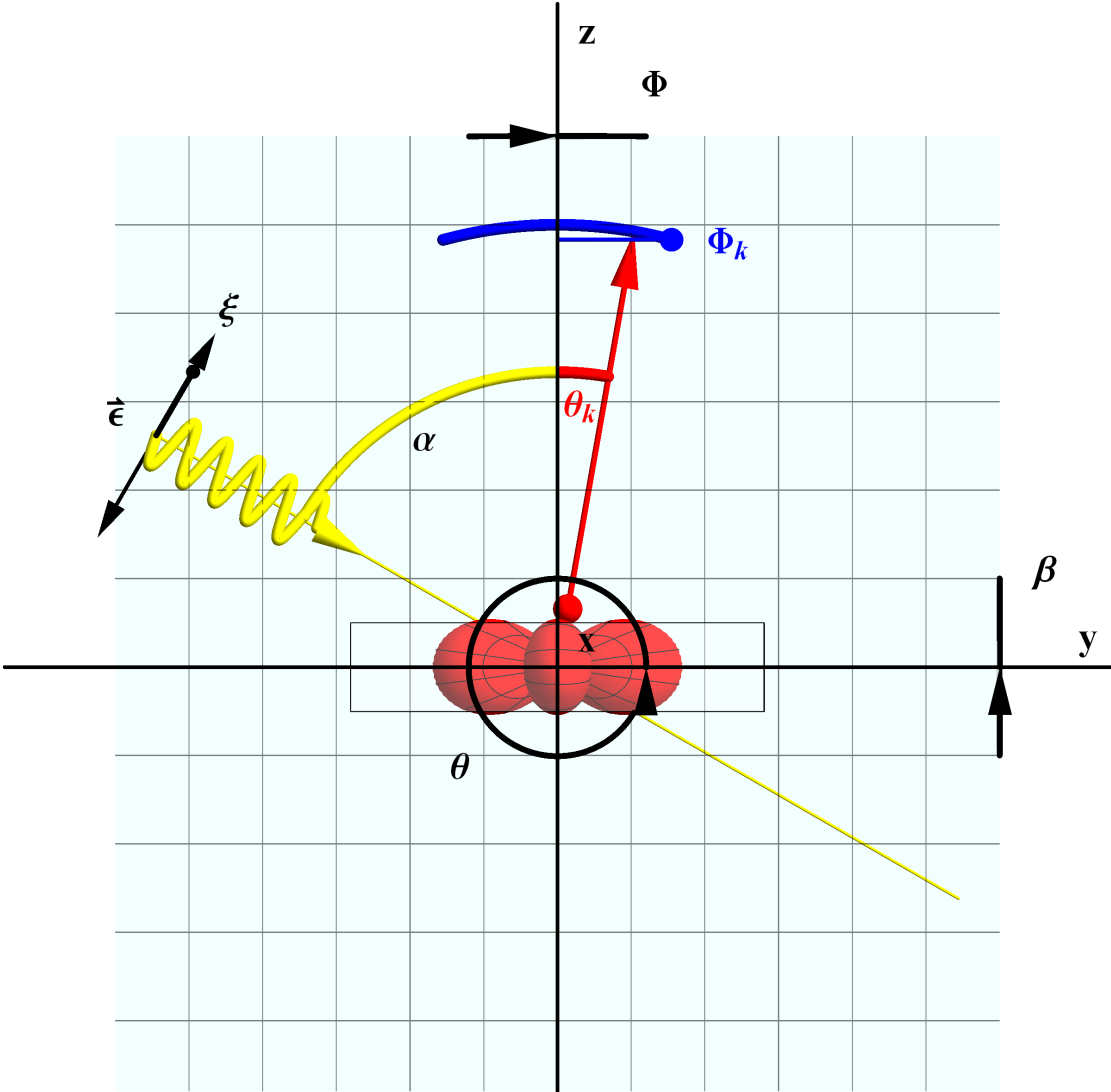


Figure 1.7: Sideview of the ARPES geometry of Fig. 1.6.

and fourth column.

Let us exemplarily discuss the most simple case of an  $s$ -orbital. The left column shows its angular distribution which is of course isotropic and basically the same result of the matrix element in an isotropic light configuration. The second column shows the unpolarized case, namely the light polarization isotropically distributed within the incoming polarization plane. The third column shows the result of  $\pi$ -polarized light. The polarization vector now suppresses all components along the incoming light direction and the resulting intensity distribution conforms with a linear combination of  $p_y$ - and  $p_z$  orbital. In  $\sigma$ -polarization, this node is along the  $yz$  plane and the distribution of spectral weight consequently  $p_x$ -like.

It is also interesting to quickly discuss the circular polarized configurations. In analogy to Eq. 1.40, the polarization vector  $\epsilon^\pm$  for right and left handed circular polarization can be written as

$$\epsilon^\pm = \begin{pmatrix} 1 \\ \pm i \cos \alpha \\ \pm i \sin \alpha \end{pmatrix}. \quad (1.42)$$

The polarization dependent term of the matrix element  $\epsilon^\pm \cdot (i\mathbf{k}_f - \frac{1}{\lambda}\mathbf{e}_\perp)$  so becomes

$$M^\pm \propto i\epsilon \left( k_x \pm i \cos \alpha k_y \pm i \sin \alpha \left( k_z + \frac{i}{\lambda} \right) \right). \quad (1.43)$$

Calculating circular dichroism we find

$$|M^+|^2 - |M^-|^2 \propto -\frac{4k_x \sin \alpha}{\lambda}, \quad (1.44)$$

which is clearly non zero for finite penetration depths  $\lambda$  and thus has to be taken into account as geometric side effect even in systems without spin polarization.

### 1.5.6 Rotation of atomic orbitals

In a typical ARPES experiment with a 2D detector, only a certain interval of angles  $\theta_k$  at a given  $\phi_k$  can be sampled at a time, determined by the acceptance angle of the analyzer and the orientation  $\phi_k$  of the entrance slits of the analyzer. Analogous to the terminology for light polarization, slits oriented along the  $x$ -axis and  $\phi_k = 0$  are referred to as  $\sigma$ -configuration, whereas

## Chapter 1. Angle resolved photoemission

---

slits oriented along  $y$ -axis and  $\phi_k = \pi/2$  are referred to as  $\pi$ -configuration.

For the experimental geometry of the ARPES setup used in this work, beamline 7 of the Advanced light source (Fig. 1.6 and 1.7), the scattering plane  $yz$  is fixed and contains the polarization vector  $\epsilon$  as well as the analyzer slits. The angle between the incident light and the spectrometer's axis ( $z$ -axis) is  $60^\circ$  and the photoelectrons are collected within an angular range  $-15^\circ < \theta_k < 15^\circ$  and  $\phi_k = 0$ . Due to this limitation, the sample has to be rotated to access the complete  $k$ -space information.

The rotation of the sample by angles  $\theta$ ,  $\beta$  and  $\phi$  around the  $x$ -,  $y$ - and  $z$ -axis, can be expressed in terms of a unitary transformation  $U(\theta, \phi, \beta)$  which rotates the orbitals according to a rotation matrix  $\mathcal{R}(\theta, \phi, \beta)$ .<sup>10</sup> At normal emission,  $\beta = \theta = \phi = 0$  and the sample normal coincides with the  $z$  axis. In a typical  $k_x k_y$  ARPES measurement,  $\beta$  is changed, while  $\theta$  and  $\phi$  remain constant.

The total matrix element  $M^{nlm}(\mathbf{k}_f)$  thus becomes a function of  $\theta$ ,  $\phi$  and  $\beta$  and consequently transforms as<sup>11</sup>

$$\begin{aligned}
 M^{nlm}(\mathbf{k}_f, \mathbf{k}_{h\nu}, \lambda) &\rightarrow M^{nlm'}(\mathbf{k}_f, \mathbf{k}_{h\nu}, \lambda, \theta, \phi, \beta) \\
 &= \langle \mathbf{k}_f | (e^{i\mathbf{k}_{h\nu} \cdot \mathbf{r}} \boldsymbol{\epsilon} \cdot \nabla) U(\theta, \phi, \beta) | n, l, m \rangle \\
 &= \sum_{m'=-l}^l \langle \mathbf{k}_f | e^{i\mathbf{k}_{h\nu} \cdot \mathbf{r}} \boldsymbol{\epsilon} \cdot \nabla | n, l, m' \rangle \langle n, l, m' | U(\theta, \phi, \beta) | n, l, m \rangle \\
 &= \sum_{m'=-l}^l D_{m',m}^l(\theta, \phi, \beta) \langle \mathbf{k}_f | e^{i\mathbf{k}_{h\nu} \cdot \mathbf{r}} \boldsymbol{\epsilon} \cdot \nabla | n, l, m' \rangle \\
 &= \sum_{m'=-l}^l D_{m',m}^l(\theta, \phi, \beta) M^{nlm'}(\mathbf{k}_f, \mathbf{k}_{h\nu}, \lambda), \tag{1.45}
 \end{aligned}$$

where the  $D_{m',m}^l(\theta, \phi, \beta)$  are the coefficients of the Wigner D-matrix which are given explicitly for  $s$ -,  $p$ - and  $d$ -orbitals in appendix 1.6.2.<sup>12</sup>

---

<sup>10</sup>The order of the angles  $\phi$ ,  $\theta$  and  $\beta$  represents the order of rotation. At BL7, the only independent angle is  $\theta$  which rotates the manipulator. The rotation stage  $\phi$  sits on the manipulator and is therefore dependent on  $\theta$ . Likewise,  $\beta$  depends on both  $\theta$  and  $\phi$ .

<sup>11</sup>In the appendix we show that the matrix element of a rotated Bloch wave can be reduced to the matrix element of the rotated the Wannier function.

<sup>12</sup>Typically, the Wigner D-Matrix is expressed in the  $z$ - $x$ - $z$  convention namely a first rotation  $\alpha_{z_0}$  about the  $z$ -axis, a second rotation  $\alpha_x$  about the  $x$ -axis and another rotation  $\alpha_{z_1}$  about the  $z$ -axis. In general, great care has to be taken to express  $\alpha_{z_0}$ ,  $\alpha_x$  and  $\alpha_{z_1}$  in terms of an arbitrary rotation (e.g.  $\beta, \theta, \phi$  as given in the particular experimental case). Such a transformation of rotation  $R(\theta, \phi, \beta)$  into a rotation around Euler angles  $R(\alpha_{z_1}, \alpha_x, \alpha_{z_0})$  can be difficult. For a detailed demonstration on this topic see Ref. 44.

In less mathematical words, the rotation of the sample in an otherwise fixed experimental geometry of course rotates the orbitals of the sample as well. These rotated orbitals however are now no good representation of basis functions in the reference frame of analyzer and polarization vector anymore. In fact, these orbitals now have to be considered -depending on the rotation - as a linear combination of proper representations in the experimental frame. For example, if we probe a pure  $d_{xy}$  state at normal emission and we start to rotate the sample around the  $x$ -axis we will intermix more and more  $d_{xz}$  and  $d_{yz}$  components to the initial state. Likewise, the angular distribution of matrix elements will become a superposition of contributions from  $d_{xy}$  and  $d_{xz}/d_{yz}$ .

## 1.6 Appendix

### 1.6.1 Matrix elements of a rotated Bloch Wave

Let us define a unitary transformation  $U$  which rotates the Bloch function  $\Psi_{n\mathbf{k}}$  according to an arbitrary rotation matrix  $\mathcal{R}$ . Expressing  $\Psi_{n\mathbf{k}}$  in terms of Wannier functions  $\phi_n(\mathbf{r} - \mathbf{R})$

$$\begin{aligned} U\Psi_{n\mathbf{k}}(\mathbf{r}) &= \sum_{\mathbf{R}} e^{i\mathbf{k}\cdot\mathbf{R}} U\Phi_n(\mathbf{r} - \mathbf{R}) \\ &= \sum_{\mathbf{R}} e^{i\mathbf{k}\cdot\mathbf{R}} \Phi_n(\mathcal{R}\mathbf{r} - \mathbf{R}) \end{aligned} \quad (1.46)$$

Analogue to Eq. 1.23 we so get

$$\begin{aligned} \langle \mathbf{k}_f | (e^{i\mathbf{k}_{h\nu}\cdot\mathbf{r}} \boldsymbol{\epsilon} \cdot \nabla) U | \Psi_{n\mathbf{k}} \rangle &= \boldsymbol{\epsilon} \cdot \sum_{\mathbf{R}, R_{\perp} < 0} e^{i\mathbf{k}\cdot\mathbf{R}} \int d^3\mathbf{r} e^{-i(\mathbf{k}_f - \mathbf{k}_{h\nu})\cdot\mathbf{r}} e^{r_{\perp}/\lambda} \nabla \Phi_n(\mathcal{R}\mathbf{r} - \mathbf{R}) \\ &= -\boldsymbol{\epsilon} \cdot \sum_{\mathbf{R}, R_{\perp} < 0} e^{i\mathbf{k}\cdot\mathbf{R}} \int d^3\mathbf{r} \Phi_n(\mathcal{R}\mathbf{r} - \mathbf{R}) \nabla e^{-i(\mathbf{k}_f - \mathbf{k}_{h\nu})\cdot\mathbf{r}} e^{r_{\perp}/\lambda} \\ &= \boldsymbol{\epsilon} \cdot (i\mathbf{k}_f - \frac{1}{\lambda} \mathbf{e}_{\perp}) \\ &\times \sum_{\mathbf{R}, R_{\perp} < 0} e^{i\mathbf{k}\cdot\mathbf{R}} \int d^3\mathbf{r} \Phi_n(\mathcal{R}\mathbf{r} - \mathbf{R}) e^{-i(\mathbf{k}_f - \mathbf{k}_{h\nu})\cdot\mathbf{r}} e^{r_{\perp}/\lambda} \end{aligned} \quad (1.47)$$

We now perform a coordinate transformation  $\mathbf{r} \rightarrow \mathbf{x} = \mathcal{R}\mathbf{r} - \mathbf{R}$ . The Jacobian of this transformation is just the rotation matrix  $\mathcal{R}$  itself, its determinant therefore 1 and we have  $d^3\mathbf{x} = d^3\mathbf{r}$ .  $\mathbf{r}$  can be expressed in terms of a back rotation  $\mathbf{r} = \mathcal{R}^{-1}(\mathbf{x} + \mathbf{R}) = \mathcal{R}^{-1}\mathbf{x} + \mathcal{R}^{-1}\mathbf{R}$  and

## Chapter 1. Angle resolved photoemission

---

$r_{\perp} = (\mathcal{R}^{-1}(\mathbf{x} + \mathbf{R}))_{\perp} = (\mathcal{R}^{-1}\mathbf{x})_{\perp} + (\mathcal{R}^{-1}\mathbf{R})_{\perp}$  and we have

$$\begin{aligned} \langle \mathbf{k}_f | (e^{i\mathbf{k}_{h\nu}\cdot\mathbf{r}} \boldsymbol{\epsilon} \cdot \nabla) U | \Psi_{n\mathbf{k}} \rangle &= \boldsymbol{\epsilon} \cdot \left( i\mathbf{k}_f - \frac{1}{\lambda} \mathbf{e}_{\perp} \right) \sum_{\mathbf{R}, R_{\perp} < 0} e^{i\mathbf{k}\cdot\mathbf{R}} \\ &\times \int d^3\mathbf{x} \Phi_n(\mathbf{x}) e^{-i(\mathbf{k}_f - \mathbf{k}_{h\nu})\cdot\mathcal{R}^{-1}(\mathbf{x} + \mathbf{R})} e^{(\mathcal{R}^{-1}(\mathbf{x} + \mathbf{R}))_{\perp}/\lambda} \end{aligned} \quad (1.48)$$

Now we make use of a property of the dot product  $(\mathbf{k}_f - \mathbf{k}_{h\nu}) \cdot \mathcal{R}^{-1}(\mathbf{x} + \mathbf{R}) = \mathcal{R}(\mathbf{k}_f - \mathbf{k}_{h\nu}) \cdot (\mathbf{x} + \mathbf{R})$  and  $(\mathcal{R}^{-1}(\mathbf{x} + \mathbf{R}))_{\perp}/\lambda = (\mathbf{e}_{\perp} \cdot (\mathcal{R}^{-1}(\mathbf{x} + \mathbf{R}))) = (\mathcal{R}\mathbf{e}_{\perp}) \cdot (\mathbf{x} + \mathbf{R})/\lambda$ , where  $\mathbf{e}_{\perp}$  is the surface unit vector, and find

$$\begin{aligned} \langle \mathbf{k}_f | (e^{i\mathbf{k}_{h\nu}\cdot\mathbf{r}} \boldsymbol{\epsilon} \cdot \nabla) U | \Psi_{n\mathbf{k}} \rangle &= \boldsymbol{\epsilon} \cdot \left( i\mathbf{k}_f - \frac{1}{\lambda} \mathbf{e}_{\perp} \right) \sum_{\mathbf{R}, R_{\perp} < 0} e^{i(\mathbf{k} - \mathcal{R}(\mathbf{k}_f - \mathbf{k}_{h\nu}))\cdot\mathbf{R}} e^{\mathcal{R}\mathbf{e}_{\perp}\cdot\mathbf{R}/\lambda} \\ &\times \int d^3\mathbf{x} \Phi_n(\mathbf{x}) e^{-i\mathcal{R}(\mathbf{k}_f - \mathbf{k}_{h\nu})\cdot\mathbf{x}} e^{\mathcal{R}\mathbf{e}_{\perp}\cdot\mathbf{x}/\lambda} \\ &= \boldsymbol{\epsilon} \cdot \left( i\mathbf{k}_f - \frac{1}{\lambda} \mathbf{e}_{\perp} \right) \sum_{\mathbf{R}, R_{\perp} < 0} e^{i(\mathbf{k} - \mathcal{R}(\mathbf{k}_f - \mathbf{k}_{h\nu}))\cdot\mathbf{R}} e^{\mathcal{R}\mathbf{e}_{\perp}\cdot\mathbf{R}/\lambda} \\ &\times \int d^3\mathbf{x} e^{-i(\mathbf{k}_f - \mathbf{k}_{h\nu})\cdot\mathcal{R}^{-1}\mathbf{x}} e^{\mathbf{e}_{\perp}\cdot\mathcal{R}^{-1}\mathbf{x}/\lambda} \Phi_n(\mathbf{x}) \\ &= \boldsymbol{\epsilon} \cdot \left( i\mathbf{k}_f - \frac{1}{\lambda} \mathbf{e}_{\perp} \right) \sum_{\mathbf{R}, R_{\perp} < 0} e^{i(\mathbf{k} - \mathcal{R}(\mathbf{k}_f - \mathbf{k}_{h\nu}))\cdot\mathbf{R}} e^{\mathcal{R}\mathbf{e}_{\perp}\cdot\mathbf{R}/\lambda} \\ &\times \int d^3\mathbf{x} e^{-i(\mathbf{k}_f - \mathbf{k}_{h\nu})\cdot\mathbf{x}'} e^{\mathbf{e}_{\perp}\cdot\mathbf{x}'/\lambda} \Phi_n(\mathcal{R}^{-1}\mathbf{x}) \\ &= \boldsymbol{\epsilon} \cdot \left( i\mathbf{k}_f - \frac{1}{\lambda} \mathbf{e}_{\perp} \right) \sum_{\mathbf{R}, R_{\perp} < 0} e^{i(\mathbf{k} - \mathcal{R}(\mathbf{k}_f - \mathbf{k}_{h\nu}))\cdot\mathbf{R}} e^{\mathcal{R}\mathbf{e}_{\perp}\cdot\mathbf{R}/\lambda} \\ &\times \langle \mathbf{k}_f - \mathbf{k}_{h\nu} + \frac{i}{\lambda} \mathbf{e}_{\perp} | U^{\dagger} | \mathbf{0}_n \rangle \end{aligned} \quad (1.49)$$

Writing  $\sum_{\mathbf{R}, R_{\perp} < 0}$  in terms of in and out of plane integrals  $\frac{N}{V} \int dR_{\parallel} \int_{-\infty}^0 dR_{\perp}$  and assuming explicitly, that the Wannier function decays exponentially faster as  $e^{r_{\perp}/\lambda}$  rises, the total matrix element becomes

$$\begin{aligned}
 \langle \mathbf{k}_f | (e^{i\mathbf{k}_{h\nu} \cdot \mathbf{r}} \boldsymbol{\epsilon} \cdot \nabla) U | \Psi_{n\mathbf{k}} \rangle &= \frac{N}{V} \boldsymbol{\epsilon} \cdot (i\mathbf{k}_f - \frac{1}{\lambda} \mathbf{e}_\perp) \langle \mathbf{k}_f - \mathbf{k}_{h\nu} + \frac{i}{\lambda} \mathbf{e}_\perp | U^\dagger | \mathbf{0}n \rangle \\
 &\times \int dR_\parallel e^{i(\mathbf{k}_\parallel - \mathcal{R}(\mathbf{k}_f - \mathbf{k}_{h\nu} - i\mathbf{e}_\perp/\lambda))_\parallel \cdot R_\parallel} \underbrace{e^{i\mathcal{R}\mathbf{G}_\parallel \cdot \mathbf{R}_\parallel}}_{\equiv 1} \\
 &\times \int_{-\infty}^0 dR_\perp e^{i(k_\perp - \mathcal{R}(\mathbf{k}_f - \mathbf{k}_{h\nu} - i\mathbf{e}_\perp/\lambda))_\perp \cdot R_\perp} \underbrace{e^{i\mathcal{R}\mathbf{G}_\parallel \cdot \mathbf{R}_\perp}}_{\equiv 1} \\
 &= 2\pi \frac{N}{V} \boldsymbol{\epsilon} \cdot (i\mathbf{k}_f - \frac{1}{\lambda} \mathbf{e}_\perp) \langle \mathbf{k}_f - \mathbf{k}_{h\nu} + \frac{i}{\lambda} \mathbf{e}_\perp | U^\dagger | \mathbf{0}n \rangle \\
 &\times \delta \left( \mathbf{k}_\parallel - (\mathcal{R}(\mathbf{k}_f + \mathbf{G}_\parallel - \mathbf{k}_{h\nu} - \frac{i}{\lambda} \mathbf{e}_\perp))_\parallel \right) \\
 &\times \frac{1}{(\mathcal{R}\mathbf{e}_\perp)_\perp / \lambda + i(k_\perp - (\mathcal{R}(\mathbf{k}_f + \mathbf{G}_\parallel - \mathbf{k}_{h\nu}))_\perp)} \quad (1.50)
 \end{aligned}$$

The rotation  $\mathcal{R}$  now implies that some of the momentum created along the surface normal necessarily has to be absorbed by in the in plane momentum of the photoelectron  $k_{f\parallel}$  and the in plane momentum conservation reads  $\delta(\mathbf{k}_\parallel - (\mathcal{R}(\mathbf{k}_f + \mathbf{G}_\parallel - \mathbf{k}_{h\nu} - i\mathbf{e}_\perp/\lambda))_\parallel)$ .

For the out of plane component, we again find a Lorentz distributed ‘‘pseudo momentum conservation’’  $|\langle \mathbf{k}_f | (e^{i\mathbf{k}_{h\nu} \cdot \mathbf{r}} \boldsymbol{\epsilon} \cdot \nabla) U | \Psi_{n\mathbf{k}} \rangle|^2 \propto \frac{1}{(\mathcal{R}\mathbf{e}_\perp)_\perp^2 / \lambda^2 + (k_\perp - (\mathcal{R}(\mathbf{k}_f + \mathbf{G}_\parallel - \mathbf{k}_{h\nu}))_\perp)^2}$ , which becomes sharper with increasing penetration depth  $\lambda$  of the final state. We interestingly also find the effect of the rotation  $(\mathcal{R}\mathbf{e}_\perp)_\perp^2$ , which is zero if the sample is rotated by  $90^\circ$ . In such a configuration, the momentum component  $k_{f\perp}$  of the photoelectron only contains in plane components  $k_\parallel$  of the Bloch wave momentum, which is of course completely conserved.

Most importantly however, the angular distribution of the matrix element of a rotated Bloch wave is determined by  $\langle \mathbf{k}_f | (e^{i\mathbf{k}_{h\nu} \cdot \mathbf{r}} \boldsymbol{\epsilon} \cdot \nabla) U | \Psi_{n\mathbf{k}} \rangle \propto \langle \mathbf{k}_f - \mathbf{k}_{h\nu} + \frac{i}{\lambda} \mathbf{e}_\perp | U^\dagger | \mathbf{0}n \rangle$ . This is the Fourier transform of the Wannier function rotated back into the experimental reference frame.

### 1.6.2 Explicit rotation of atomic orbitals

Rotations in the ARPES experiments performed in this work can be expressed in terms of angles  $\beta$ ,  $\theta$  and  $\phi$  corresponding to rotations around the  $x$ -, the  $y$ - and the  $z$ -axis:

$$\mathcal{R}(\theta, \phi, \beta) = \begin{pmatrix} 1 & 0 & 0 \\ 0 & \cos \beta & -\sin \beta \\ 0 & \sin \beta & \cos \beta \end{pmatrix} \begin{pmatrix} \cos \phi & -\sin \phi & 0 \\ \sin \phi & \cos \phi & 0 \\ 0 & 0 & 1 \end{pmatrix} \begin{pmatrix} \cos \theta & 0 & -\sin \theta \\ 0 & 1 & 0 \\ \sin \theta & 0 & \cos \theta \end{pmatrix} \quad (1.51)$$

## Chapter 1. Angle resolved photoemission

---

or in general

$$\mathcal{R} = \begin{pmatrix} a & b & c \\ d & e & f \\ g & h & o \end{pmatrix} \quad (1.52)$$

Under such a rotation, the atomic orbitals  $|nlm\rangle$  transform according to the coefficients  $D_{m',m}^l = \langle n, l, m' | \mathcal{R}(\theta, \phi, \beta) | n, l, m \rangle$ . Rather than calculating these coefficients explicitly, we perform the transformation directly to the adapted orbital basis sets  $\{s\}$ ,  $\{p_x, p_y, p_z\}$  and  $\{d_{x^2-y^2}, d_{xz}, d_{z^2}, d_{yz}, d_{xy}\}$  [45].

The trivial case of a spherical  $s$ -orbital under rotation simply transforms as

$$s_{x^2+y^2+z^2} \rightarrow s'_{x^2+y^2+z^2} = D_{ss} \cdot s_{x^2+y^2+z^2} = 1 \cdot s_{x^2+y^2+z^2}$$

The  $p$ -orbitals, transform as functions  $x$ ,  $y$  and  $z$  and the coefficients  $D_{p',p}$  transforming orbitals  $p$  to  $p'$  hence simply can be expressed in terms of the rotation matrix:

$$\begin{pmatrix} p_x \\ p_y \\ p_z \end{pmatrix} \rightarrow \begin{pmatrix} p'_x \\ p'_y \\ p'_z \end{pmatrix} = \begin{pmatrix} a & b & c \\ d & e & f \\ g & h & o \end{pmatrix} \cdot \begin{pmatrix} p_x \\ p_y \\ p_z \end{pmatrix}$$

For the  $d$ -orbitals, the situation is not so easy anymore and we have to calculate the matrix element  $\langle d' | \mathcal{R} | d \rangle$  explicitly. We demonstrate the method for one example and give the full result down below:

Let us calculate  $\langle d_{x^2-y^2} | \mathcal{R} | d_{x^2-y^2} \rangle$  for demonstration. Calculating  $\mathcal{R}(x^2 - y^2)$  we find

$$\begin{aligned} \mathcal{R}(x^2 - y^2) &= a^2x^2 + 2abxy + 2acxz + b^2y^2 + 2bcyz + c^2z^2 \\ &\quad - d^2x^2 + 2dexy + 2dfxz + e^2y^2 + 2efyz + f^2z^2 \\ &= (a^2 - d^2)x^2 + 2(ab - de)xy + 2(ac - df)xz \\ &\quad + (b^2 - e^2)y^2 + 2(bc - ef)yz + (c^2 - f^2)z^2 \end{aligned} \quad (1.53)$$



The matrix elements with odd terms in  $x$ ,  $y$  and  $z$  will vanish and we remain with:

$$\begin{aligned} \langle d_{x^2-y^2} | \mathcal{R} | d_{x^2-y^2} \rangle &= \langle x^2(a^2 - d^2)x^2 \rangle + \langle x^2(b^2 - e^2)y^2 \rangle + \langle x^2(c^2 - f^2)z^2 \rangle \\ &\quad - \langle y^2(a^2 - d^2)x^2 \rangle - \langle y^2(b^2 - e^2)y^2 \rangle - \langle y^2(c^2 - f^2)z^2 \rangle \end{aligned} \quad (1.54)$$

Integrals of the form  $\langle x^4 \rangle$  give the same as  $\langle x^4 \rangle$ . Similarly,  $\langle x^2y^2 \rangle$  give the same as  $\langle x^2z^2 \rangle$  and so forth. Collecting together all terms of type  $\langle x^4 \rangle$  gives  $(a^2 - d^2 - b^2 + e^2)$  and collecting terms of the type  $\langle x^2y^2 \rangle$  gives  $(b^2 - e^2 + c^2 - f^2 - a^2 + d^2 - c^2 + f^2) = -(a^2 - d^2 - b^2 + e^2)$

and we finally have

$$\begin{aligned} \langle d_{x^2-y^2} | \mathcal{R} | d_{x^2-y^2} \rangle &= (a^2 - d^2 - b^2 + e^2) (\langle x^4 \rangle - \langle x^2y^2 \rangle) \\ &= (a^2 - d^2 - b^2 + e^2) \frac{1}{2} (\langle x^4 \rangle - 2\langle x^2y^2 \rangle + \langle y^4 \rangle) \\ &= \frac{1}{2} (a^2 - d^2 - b^2 + e^2) \underbrace{\langle (x^2 - y^2)^2 \rangle}_{\equiv 1} \end{aligned} \quad (1.55)$$

The full result is

$$\begin{pmatrix} d_{x^2-y^2} \\ d_{xz} \\ d_{z^2} \\ d_{yz} \\ d_{xy} \end{pmatrix} \rightarrow \begin{pmatrix} d'_{x^2-y^2} \\ d'_{xz} \\ d'_{z^2} \\ d'_{yz} \\ d'_{xy} \end{pmatrix} = \begin{pmatrix} \frac{a^2-d^2-b^2+e^2}{2} & (ac-df) & \frac{2c^2-b^2-a^2-2f^2+e^2+d^2}{\sqrt{12}} & (bc-ef) & (ab-de) \\ ag-bh & ao+cg & \frac{2co-bh-ag}{\sqrt{3}} & bo+ch & ah+bg \\ \frac{2q^2-d^2-a^2-2h^2+e^2+b^2}{\sqrt{12}} & \frac{2go-df-ac}{\sqrt{3}} & \frac{4o^2-2(h^2+g^2+f^2+e^2)+e^2+d^2+b^2+a^2}{6} & \frac{2ho-ef-cb}{\sqrt{3}} & \frac{2gh-ed-ab}{\sqrt{3}} \\ dg-eh & do+fg & \frac{2of-eh-dg}{\sqrt{3}} & eo+fh & dh+eg \\ ad-be & af+cd & \frac{2ef-eh-ad}{\sqrt{3}} & bf+ce & ae+bd \end{pmatrix} \cdot \begin{pmatrix} d_{x^2-y^2} \\ d_{xz} \\ d_{z^2} \\ d_{yz} \\ d_{xy} \end{pmatrix} \quad (1.56)$$



# 2 Resonant inelastic x-ray scattering

## 2.1 Summary

In the following chapter, we give a brief introduction to resonant inelastic x-ray scattering (RIXS) in the framework of the Kramer-Heisenberg formalism. We show that the spectral weight of RIXS can be reduced to matrix elements mostly sensitive to the on site properties of the wave functions involved. Based on this finding and the Wigner-Eckart theorem, we develop a formalism to estimate the relative spectral weight of transitions to final states with different total symmetries. We further briefly address the problem of self absorption in bulk systems and thin films.

## 2.2 Introduction

During the past decade, resonant inelastic x-ray scattering (RIXS) became increasingly popular, especially in the domain of correlated electron physics [46]. Even if more and more spectrometers with higher and higher resolution are under construction all over the planet,<sup>1</sup> the available machine time cannot satisfy the increasing demand for experimental shifts. E.g. “the overbooking factor (i.e., the ratio of requested shifts to available shifts) at each station of the ADDRESS beamline is typically  $> 4$ ” [48]. For a researcher, every minute of granted beam time is obviously precious and the experiment should thus be subject to a careful preparation. In contrast to ARPES, RIXS is a second order process and the underlying cross sections thus very low, which results in typical data acquisition times on the order of hours - with respect to minutes in ARPES - for one spectrum. Performing time consuming  $k$ -space mapping experiments therefore requires an optimized experimental geometry with respect to the sample *and* the desired effect. The experimentalist should be able to perform an “educated guess” of what geometry - e.g. what polarization - and what excitation energy to use to observe the desired effect.

Similar to RAMAN spectroscopy, careful consideration of the experimental geometry with

---

<sup>1</sup>E.g. high resolution spectrometer “Centurion” ( $R = 100000$ ) and a high throughput spectrometer “Viking” ( $R = 5000$ ) are currently under construction at NSLS II, [47].

respect to the the point group symmetry of the sample therefore is important. So is the detailed knowledge about the final state properties of the related x-ray absorption spectra.

Even if these fundamental considerations sound trivial, the situation becomes less obvious for the “less experienced” researcher typically carrying out the experiment. Rather than resuming a complete theory of RIXS, the following chapter aims to depict some useful tools to find a promising geometry.<sup>2</sup>

### 2.3 The RIXS cross section

In the Kramers–Heisenberg picture, the RIXS amplitude is described as [51]

$$F(h\nu, h\nu') = \sum_f \left| \sum_i \frac{\langle f | \hat{T}_2 | i \rangle \langle i | \hat{T}_1 | g \rangle}{E_i - E_g - h\nu - i\Gamma_i} \right|^2 \delta(h\nu - h\nu' + E_g - E_f), \quad (2.1)$$

where  $\hat{T}_{1/2} = \epsilon_{1/2} \cdot \hat{p} e^{\pm i\mathbf{k}_2 \cdot \mathbf{r}}$  is the transition operator for absorption (emission) of a photon with polarization  $\epsilon_1$  ( $\epsilon_2$ ), energy  $h\nu$  ( $h\nu'$ ) and wavevector  $\mathbf{k}_1$  ( $\mathbf{k}_2$ ).  $|g\rangle$ ,  $|i\rangle$  and  $|f\rangle$  are the ground-, the intermediate and the final state in the RIXS process and  $E_g$ ,  $E_i$  and  $E_f$  their corresponding energies.

In the absorption process, a core electron is excited above the Fermi level, forming an excited core-hole electron state  $|i\rangle$ . In the subsequent de-excitation process, an electron refills the core-hole, leaving the system either in its groundstate  $|f\rangle = |g\rangle$  (resonant elastic scattering) or in some excited state  $|f\rangle \neq |g\rangle$  (resonant inelastic scattering).

From Eq. 2.1 we immediately can see the main difference between RIXS and non-resonant x-ray scattering  $\langle f | H_{int} | g \rangle$ : only the atoms absorbing the photon  $h\nu$ , are directly involved in the resonance process and contribute coherently to the RIXS amplitude. This intimate connection between the excitation and de-excitation process will be the main justification for the symmetry selectivity of both absorption and re-emission process exploited in the following sections.

We now assume that an electron interacts with only one photon at a time and that Coulomb interaction does not significantly perturb the other electrons during the excitation and de-excitation process. This “frozen core approximation” is valid only in case the excited charge carriers are sufficiently delocalized and therefore screening effects only marginally affect the other electrons, i.e. if the excitations concern valence states. The many particle wave functions  $|g\rangle$  and  $|f\rangle$  can thus be approximated as single particle wave functions. In an ordered system, initial and final states are naturally described by Bloch functions of the form

---

<sup>2</sup>For a more thorough introduction to RIXS, the reader is referred to refs. 49 and 50.

$$\begin{aligned} |g\rangle &= e^{i\mathbf{k}_i \cdot \mathbf{r}} v_{\mathbf{k}_i}(\mathbf{r}) \\ |f\rangle &= e^{i\mathbf{k}_f \cdot \mathbf{r}} c_{\mathbf{k}_f}(\mathbf{r}) \end{aligned} \quad (2.2)$$

where  $v_{\mathbf{k}_i}$  and  $c_{\mathbf{k}_i}$  denote lattice periodic functions of the valence and conduction band, respectively. The intermediate state – strongly localized by the Coulomb force in between core-hole and electron – may be represented by an atomic wave function with core level index  $n$  and centered at atomic position  $\mathbf{R}_j$

$$|i\rangle = \Psi_n(\mathbf{r} - \mathbf{R}_j). \quad (2.3)$$

We now can calculate the matrix elements of Eq. 2.1 more explicitly. Making use of the periodicity of  $v_{\mathbf{k}_i}$  and  $c_{\mathbf{k}_i}$  and performing a coordinate transformation  $\mathbf{r} \rightarrow \mathbf{x} - \mathbf{R}_j$  and  $d^3\mathbf{x} = d^3\mathbf{r}$ , we obtain

$$\begin{aligned} \langle f | \hat{T}_2 | i \rangle &= \int e^{-i\mathbf{k}_f \cdot \mathbf{r}} c_{\mathbf{k}_f}^*(\mathbf{r}) \epsilon_2 \cdot \hat{\mathbf{p}}_2 e^{-i\mathbf{k}_2 \cdot \mathbf{r}} \Psi_n(\mathbf{r} - \mathbf{R}_j) d^3\mathbf{r} \\ &= \int e^{-i\mathbf{k}_f \cdot (\mathbf{x} + \mathbf{R}_j)} c_{\mathbf{k}_f}^*(\mathbf{x}) \epsilon_2 \cdot \hat{\mathbf{p}}_2 e^{-i\mathbf{k}_2 \cdot (\mathbf{x} + \mathbf{R}_j)} \Psi_n(\mathbf{x}) d^3\mathbf{x} \\ &= e^{-i(\mathbf{k}_f + \mathbf{k}_2) \cdot \mathbf{R}_j} \int e^{i\mathbf{k}_f \cdot \mathbf{x}} c_{\mathbf{k}_f}^*(\mathbf{x}) \epsilon_2 \cdot \hat{\mathbf{p}}_2 e^{-i\mathbf{k}_2 \cdot \mathbf{x}} \Psi_n(\mathbf{x}) d^3\mathbf{x} \end{aligned} \quad (2.4)$$

and in a similar way

$$\langle i | \hat{T}_1 | g \rangle = e^{i(\mathbf{k}_i + \mathbf{k}_1) \cdot \mathbf{R}_j} \int \Psi_n(\mathbf{x}) \epsilon_1 \cdot \hat{\mathbf{p}}_1 e^{i\mathbf{k}_1 \cdot \mathbf{x}} e^{i\mathbf{k}_i \cdot \mathbf{x}} v_{\mathbf{k}_i}(\mathbf{x}) d^3\mathbf{x} \quad (2.5)$$

Carrying out the sum  $\sum_i$  partially over all intermediate state lattice sites  $\mathbf{R}_j$  in Eq. 2.1 and

## Chapter 2. Resonant inelastic x-ray scattering

---

approximating  $\sum_{\mathbf{R}}$  as an integral  $\sum_{\mathbf{R}} \rightarrow \frac{N}{V} \int d^3\mathbf{R}$ , we can simplify

$$\sum_{\mathbf{R}_j} e^{i(\mathbf{k}_i + \mathbf{k}_1 - \mathbf{k}_f - \mathbf{k}_2) \cdot \mathbf{R}_j} = \frac{N}{V} \delta(\mathbf{k}_i + \mathbf{k}_1 - \mathbf{k}_f - \mathbf{k}_2), \quad (2.6)$$

and find the conservation of total momentum. This important finding is especially exploited in RIXS experiments used to determine the dispersion relation of low energy excitations like spinwaves [52, 53].

We now write the periodic functions  $v_{\mathbf{k}_i}$  and  $c_{\mathbf{k}_i}$  in terms of maximally localized Wannier functions  $\Phi_n(\mathbf{r} - \mathbf{R})$

$$v_{\mathbf{k}_i} = e^{-i\mathbf{k}_i \cdot \mathbf{r}} \sum_{\mathbf{R}} e^{i\mathbf{k}_i \cdot \mathbf{R}} \Phi_n(\mathbf{r} - \mathbf{R}) \quad (2.7)$$

$$c_{\mathbf{k}_f}^* = e^{-i\mathbf{k}_f \cdot \mathbf{r}} \sum_{\mathbf{R}} e^{i\mathbf{k}_f \cdot \mathbf{R}} \Phi_n(\mathbf{r} - \mathbf{R}) \quad (2.8)$$

and find the remaining integrals to be of the form

$$\begin{aligned} & \int e^{i\mathbf{k}_f \cdot \mathbf{x}} c_{\mathbf{k}_f}^*(\mathbf{x}) \epsilon_2 \cdot \hat{\mathbf{p}}_2 e^{-i\mathbf{k}_2 \cdot \mathbf{x}} \Psi_n(\mathbf{x}) d^3\mathbf{x} = \\ & \int e^{i\mathbf{k}_f \cdot \mathbf{x}} e^{-i\mathbf{k}_f \cdot \mathbf{x}} \sum_{\mathbf{R}} e^{i\mathbf{k}_f \cdot \mathbf{R}} \Phi_n(\mathbf{x} - \mathbf{R}) \epsilon_2 \cdot \hat{\mathbf{p}}_2 e^{-i\mathbf{k}_2 \cdot \mathbf{x}} \Psi_n(\mathbf{x}) d^3\mathbf{x} = \\ & \sum_{\mathbf{R}} e^{i\mathbf{k}_f \cdot \mathbf{R}} \int \Phi_n(\mathbf{x} - \mathbf{R}) \epsilon_2 \cdot \hat{\mathbf{p}}_2 e^{-i\mathbf{k}_2 \cdot \mathbf{x}} \Psi_n(\mathbf{x}) d^3\mathbf{x} \end{aligned} \quad (2.9)$$

and

$$\begin{aligned} & \int \Psi_n(\mathbf{x}) \epsilon_1 \cdot \hat{\mathbf{p}}_1 e^{i\mathbf{k}_1 \cdot \mathbf{x}} e^{i\mathbf{k}_i \cdot \mathbf{x}} v_{\mathbf{k}_i}(\mathbf{x}) d^3\mathbf{x} = \\ & \sum_{\mathbf{R}} e^{i\mathbf{k}_i \cdot \mathbf{R}} \int \Psi_n(\mathbf{x}) \epsilon_1 \cdot \hat{\mathbf{p}}_1 e^{i\mathbf{k}_1 \cdot \mathbf{x}} \Phi_n(\mathbf{x} - \mathbf{R}) d^3\mathbf{x} \end{aligned} \quad (2.10)$$

Assuming that the intermediate state wave function is strongly localized by the core-hole electron attraction, the major contribution of the sum  $\sum_{\mathbf{R}}$  is covered by the on site term  $\mathbf{R} = \mathbf{0}$ . We further notice that the matrix elements of the RIXS process - as similar to ARPES - can again be written in terms of local integrals. We will thus in the following make use of the symmetry properties of the local Hamiltonian to obtain an “educated guess” of the expected RIXS amplitude.

## 2.4 Momentum transfer

The typical experimental geometry (e.g. SAXES at SLS or BL07LSU at SPring 8) is shown in Fig. 2.1. The wavevector of the ingoing light  $\mathbf{k}_1$  can be expressed as a function of its energy  $h\nu$  and the angles of incidence  $\alpha$  and  $\phi$  and we find

$$\begin{aligned} \mathbf{k}_1 &= -\frac{h\nu}{\hbar c} \begin{pmatrix} \cos \phi & -\sin \phi & 0 \\ \sin \phi & \cos \phi & 0 \\ 0 & 0 & 1 \end{pmatrix} \cdot \begin{pmatrix} 1 & 0 & 0 \\ 0 & \cos(\alpha) & -\sin(\alpha) \\ 0 & \sin(\alpha) & \cos(\alpha) \end{pmatrix} \cdot \begin{pmatrix} 0 \\ 0 \\ 1 \end{pmatrix} \\ &= \frac{h\nu}{\hbar c} \begin{pmatrix} -\sin(\alpha) \sin \phi \\ \sin(\alpha) \cos \phi \\ -\cos(\alpha) \end{pmatrix}. \end{aligned} \quad (2.11)$$

The outgoing light direction is related to the incoming light direction  $\alpha$  and  $\phi$  and the scattering angle  $\tau$ . By replacing  $\alpha$  with  $\tau + \alpha - \pi$  in above formula we find

$$\mathbf{k}_2 = \frac{h\nu}{\hbar c} \begin{pmatrix} -\sin(\tau + \alpha) \sin \phi \\ \sin(\tau + \alpha) \cos \phi \\ -\cos(\tau + \alpha) \end{pmatrix}. \quad (2.12)$$

Assuming  $h\nu \sim h\nu'$ , the momentum transfer to the sample  $\mathbf{q} = \mathbf{k}_f - \mathbf{k}_i = \mathbf{k}_1 - \mathbf{k}_2$  is expressed as

$$\mathbf{q} = \frac{h\nu}{\hbar c} \begin{pmatrix} -\sin \phi (\sin \alpha - \sin(\tau + \alpha)) \\ \cos \phi (\sin \alpha - \sin(\tau + \alpha)) \\ -\cos \alpha + \cos(\tau + \alpha) \end{pmatrix}. \quad (2.13)$$

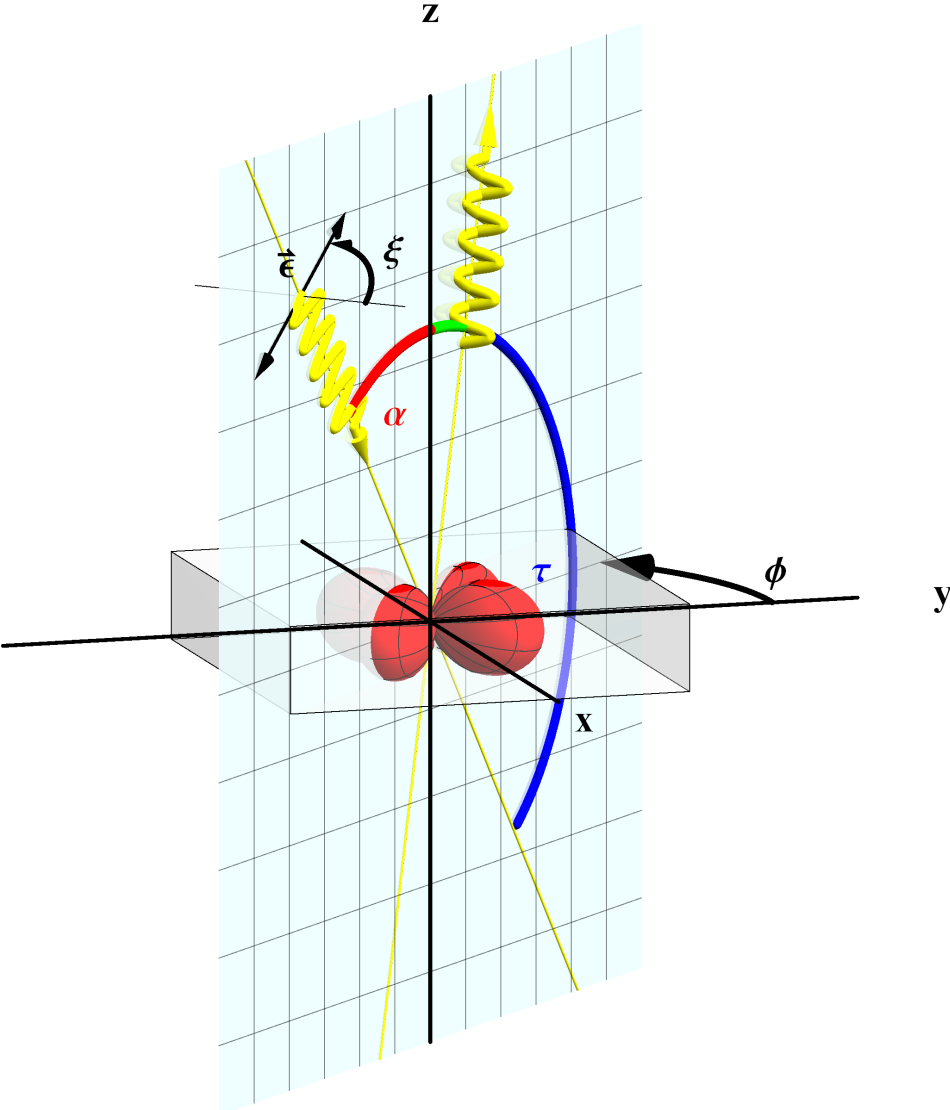


Figure 2.1: Typical RIXS experimental configuration as employed at SAXES at SLS or BL07LSU at SPring 8. The sample is represented by its natural coordinate system. The scattering angle  $\tau$  is kept fixed while the momentum transfer direction is varied by changing  $\alpha$ .



## 2.5. Basis functions of the tetrahedral system

The in plane momentum  $q_{\parallel} = |\sin \alpha - \sin(\tau + \alpha)|$  is zero for  $\alpha = \arccos\left(\frac{1 - \cos \tau}{\sqrt{2 - 2 \cos \tau}}\right)$ , which is  $\alpha = 45^\circ$  for a scattering geometry  $\tau = 90^\circ$  and  $\alpha = 25^\circ$  for a scattering geometry  $\tau = 130^\circ$ , i.e. the specular geometries. Since  $\alpha$  is confined by the sample surface, the out of plane component  $q_{\perp} = |-\cos \alpha + \cos(\tau + \alpha)|$  is always nonzero.

## 2.5 Basis functions of the tetrahedral system

The systems studied in this work, anatase  $\text{TiO}_2$  as well as T-CuO are both systems with tetrahedral point group symmetry. The following concepts are consequently demonstrated for  $D_{4h}$ . The irreducible representations and standard basis functions  $|\Gamma, \gamma\rangle$  of  $D_{4h}$  are tabulated in Tab. 2.1 [54].

stand.	$\gamma$		1	2
	$\Gamma$			
$A_{1g}$	1		$x^2 + y^2 + z^2$	
$A_{2g}$	2		$xp_y - yp_x$	
$B_{1g}$	3		$x^2 - y^2$	
$B_{2g}$	4		$xy$	
$E_g$	5		$yp_z - zp_y$	$zp_x - xp_z$
$A_{1u}$	1		$(x^2 - y^2)xyz$	
$A_{2u}$	2		$z$	
$B_{1u}$	3		$xyz$	
$B_{2u}$	4		$(x^2 - y^2)z$	
$E_u$	5		$x$	$y$

Table 2.1: Definition of the irreducible representations and standard basis functions  $|\Gamma, \gamma\rangle$  of  $D_{4h}$ . For example, the component of irreducible representation  $E_u$  transforming as  $y$  is labeled  $|5, 1\rangle$  in Griffith notation.

The basis functions are labeled in Griffith's notation  $|\Gamma, \gamma\rangle$  as used later in this work [55]. The usefulness of this notation will become obvious by analogy to a spherical system: its basis functions (e.g. of an atomic Hamiltonian), are given by the spherical harmonics  $|l, m\rangle$ , where  $m = \{-l \dots l\}$ . All spherical harmonics with a fixed  $l$  belong to the same irreducible representation of the symmetry group of rotations around a fixed point. Varying  $m$  selects distinct components, i.e. the basis function of this representation.

In a non spherical system,  $|l, m\rangle$  are no proper basis functions anymore. Their place is now taken by the irreducible representations of the point group in focus, labeled by  $\Gamma$ . Their components - which can be transformed into one another by the symmetry operations of the group - are labeled by  $\gamma$ .

In  $D_{4h}$  for example, the function  $x$  is a component of irreducible representation  $E_u$ . In Griffith's notation this corresponds to  $|5, 1\rangle^-$  where the “-” sign indicates the parity. By a simple symmetry

operation, e.g. a rotation of  $90^\circ$  around the  $z$ -axis,  $x$  can be transformed into function  $y$ , in Griffith's notation  $|5, 2\rangle^-$ , and therefore a component of the same irreducible representation. One can thus use  $\Gamma$  and  $\gamma$  analogously to the orbital quantum numbers  $l$  and  $m$  of atomic physics.

## 2.6 Dipole approximation in RIXS

The wavelength of the soft x-rays we use in this work is large compared to the typical extension of the excited core-hole (e.g.  $100 \text{ eV} \sim 12.4 \text{ \AA}$ ). The transition operator  $\hat{T}$  can thus be approximated as the leading order term of a Taylor series

$$\hat{T} = \frac{e}{mc} e^{i\mathbf{k}\mathbf{r}} \boldsymbol{\epsilon} \cdot \hat{\mathbf{p}} \sim \frac{e}{mc} \boldsymbol{\epsilon} \cdot \hat{\mathbf{p}} + \dots = -i \frac{\hbar e}{mc} \boldsymbol{\epsilon} \cdot \hat{\nabla} \quad (2.14)$$

The components  $T_x \propto \partial/\partial x$ ,  $T_y \propto \partial/\partial y$ ,  $T_z \propto \partial/\partial z$  of this dipole operator  $\hat{T}$  transform like the functions  $x$ ,  $y$  and  $z$ . In analogy to the work of Matsubara et al. [56–59] and following the group theoretical algebra developed by Tanabe and Sugano [60], Tanabe and Kamimura [61], Griffith [55] as well as Fano and Racah [62], we will now make use of these symmetry properties to reduce the matrix elements in Eq. 2.1.<sup>3</sup>

We start from the Wigner-Eckart theorem, which in Griffith's notation [55] takes the form

$$\langle \Gamma\gamma | \hat{O}_{\bar{\gamma}}^{\bar{\Gamma}} | \Gamma'\gamma' \rangle = \langle \Gamma || \hat{O}^{\bar{\Gamma}} || \Gamma' \rangle \begin{pmatrix} \Gamma & \Gamma' & \bar{\Gamma} \\ \gamma & \gamma' & \bar{\gamma} \end{pmatrix} \quad (2.15)$$

where the matrix element of the operator  $\hat{O}$  transforming as component  $\bar{\gamma}$  of representation  $\bar{\Gamma}$  connects states transforming as components  $\gamma$  and  $\gamma'$  of the representations  $\Gamma$  and  $\Gamma'$  respectively. Relation 2.15 holds strictly only for real components. The double-bar reduced matrix element  $\langle \dots || \dots || \dots \rangle$  is independent of the component labels  $\gamma$ ,  $\gamma'$  and  $\bar{\gamma}$  and can be conveniently defined as [55]

$$\langle \Gamma || \hat{O}^{\bar{\Gamma}} || \Gamma' \rangle \equiv c_{\gamma\gamma'\bar{\gamma}}^{\Gamma\Gamma'\bar{\Gamma}} \delta_{\Gamma,\Gamma'\otimes\bar{\Gamma}} := \begin{cases} c_{\gamma\gamma'\bar{\gamma}}^{\Gamma\Gamma'\bar{\Gamma}} & \forall \Gamma \in \{\bar{\Gamma} \otimes \Gamma'\} \\ 0 & \text{otherwise} \end{cases}, \quad (2.16)$$

---

<sup>3</sup>Note that the following concepts are neither restricted to the point group symmetry  $D_{4h}$ , nor to the dipole approximation. In certain situations, it may be useful to estimate the quadrupole terms contributing to the RIXS cross section. In this case the components of the quadrupole operator have to be considered. In  $D_{4h}$ , these are transforming as  $z^2$ ,  $x^2 - y^2$ ,  $xy$  and  $xz/yz$ , and thus represented by irreducible representations  $A_{1g}$ ,  $B_{1g}$ ,  $B_{2g}$  and  $E_g$ .

where  $c_{\gamma\gamma'\bar{\gamma}}^{\Gamma\Gamma'\bar{\Gamma}}$  are arbitrary coefficients adapted to the explicit problem to solve. In other words,  $\langle \dots | \dots | \dots \rangle$  can only be nonzero if the total symmetry is conserved, i.e. if the final state has a symmetry which is contained in the direct product of initial state symmetry and the symmetry of the operator  $\hat{O}$ .

The tensor  $\left( \begin{smallmatrix} \Gamma & \Gamma' & \bar{\Gamma} \\ \gamma & \gamma' & \bar{\gamma} \end{smallmatrix} \right)$  contains coupling coefficients determined by the point group of the system – analogous to the Wigner 3- $j$  symbols ( $\propto$  Clebsch Gordan coefficients) in spherical symmetry  $SO_3$ . For the most common point groups, these are tabulated e.g. in Refs. 55 and 54 or online [63].

As discussed in the previous section, the group representations  $\Gamma$ ,  $\Gamma'$  and  $\bar{\Gamma}$  “act” as the orbital quantum number  $l$  and their components  $\gamma$ ,  $\gamma'$  and  $\bar{\gamma}$  as the magnetic quantum number  $m$ . Let us illustrate this concept on a simple example: photon absorption in a single atom. The basis function of this problem are the spherical harmonics  $|l, m\rangle$ , where  $m$  runs from  $-l$  to  $l$ . The dipole operator  $\hat{O} = \hat{T}$  is represented by  $|l_T, m_T\rangle = |1, 0\rangle$  for linear polarized light and  $|1, \pm 1\rangle$  for circular polarized light. The transition propability to excite the initial state electron  $|l_g, m_g\rangle$  into a final state  $|l_f, m_f\rangle$ , is given by the dipole matrix element  $\langle l_f, m_f | T | l_g, m_g \rangle$ . The addition of angular momentum imposes that adding angular momentum  $l_T = 1$  to  $l_g$  can only give final state results  $l_f = l_g - 1, l_g$  and  $l_g + 1$ . Further, the total parity  $w = (-1)^l$  has to be conserved, i.e.  $w_f = (-1)^{l_f} = (-1)^{l_T} (-1)^{l_g} = -w_g$  and therefore  $l_f \neq l_g$ . These arguments describe the action of the reduced matrix element  $\langle \dots | \dots | \dots \rangle$ . The remaining component  $m_g$  depends on the Clebsch Gordon coefficients, which give non-zero contributions only if  $m_f = m_g + m_T$ . We thus recover the well known selection rules

$$\Delta l = \pm 1$$

$$\Delta m = 0, \pm 1 . \tag{2.17}$$

$$\tag{2.18}$$

In a non-spherical system, the matrix element of Eq. 2.15 analogously will only be non-zero, if  $\Gamma$  is contained in the direct product  $\bar{\Gamma} \otimes \Gamma'$  and if the coefficients  $\left( \begin{smallmatrix} \Gamma & \Gamma' & \bar{\Gamma} \\ \gamma & \gamma' & \bar{\gamma} \end{smallmatrix} \right)$  are nonzero. Given that in a general experimental configuration, the dipole operator  $\hat{T}$  can have components of several different irreducible representations, the total matrix element can be expressed as the weighted sum of all independent partial components of the operator  $\hat{T}$ . The total transition matrix element therefore involves all nonzero projections of the final state onto a linear combination of the form

$$\begin{aligned}
 |\Gamma\gamma\rangle &= \hat{O}_{\bar{\gamma}}^{\bar{\Gamma}}|\Gamma'\gamma'\rangle \\
 &= \underbrace{\sum_{\Gamma'',\gamma''} |\Gamma''\gamma''\rangle \langle \Gamma''\gamma''|}_{\equiv 1} \hat{O}_{\bar{\gamma}}^{\bar{\Gamma}}|\Gamma'\gamma'\rangle \\
 &= \sum_{\Gamma'',\gamma''} |\Gamma''\gamma''\rangle \langle \Gamma''\gamma''|\hat{O}_{\bar{\gamma}}^{\bar{\Gamma}}|\Gamma'\gamma'\rangle \begin{pmatrix} \Gamma'' & \Gamma' & \bar{\Gamma} \\ \gamma'' & \gamma' & \bar{\gamma} \end{pmatrix} \\
 &= \sum_{\Gamma'',\gamma''} |\Gamma''\gamma''\rangle c_{\gamma''\gamma'\bar{\gamma}}^{\Gamma''\Gamma'\bar{\Gamma}} \delta_{\Gamma'',\bar{\Gamma}\otimes\Gamma'} \begin{pmatrix} \Gamma'' & \Gamma' & \bar{\Gamma} \\ \gamma'' & \gamma' & \bar{\gamma} \end{pmatrix}, \tag{2.19}
 \end{aligned}$$

where the completeness of the orthonormal basis set  $\{|\Gamma\gamma\rangle\}$  is exploited.

### 2.6.1 Symmetry selectivity in the RIXS excitation process

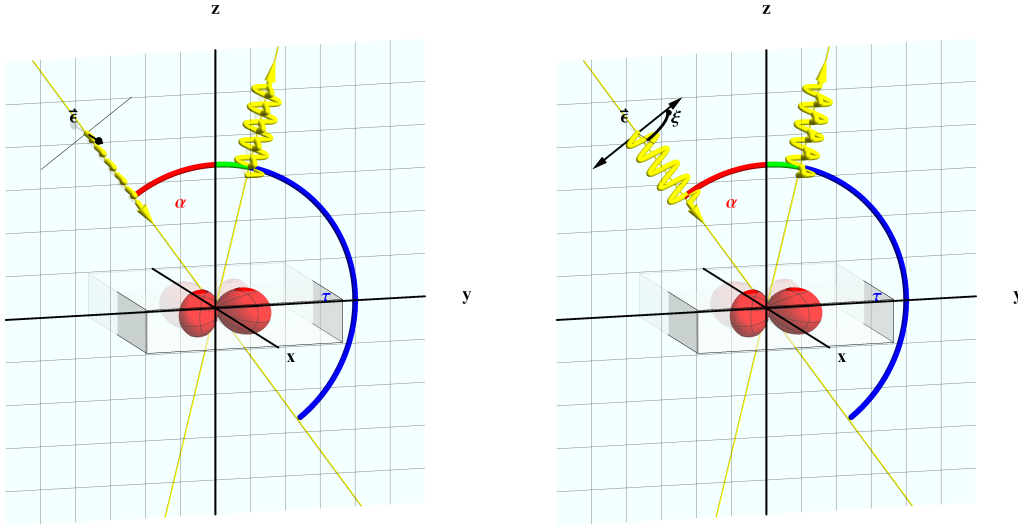


Figure 2.2: Typical RIXS experimental configuration as employed at SAXES at SLS or BL07LSU at SPring 8. The sample is represented by its natural coordinate system. The scattering angle  $\tau$  is kept fixed while the momentum transfer direction is varied by changing  $\alpha$ . **(left)**  $\sigma$ -polarized configuration (polarized,  $\xi = 0$ ), **(right)**  $\pi$ -polarized configuration (depolarized,  $\xi = \pi/2$ ). Note that the polarization of the outgoing light in general can contain polarized and depolarized components. The azimuthal orientation  $\phi$  is typically fixed once the sample is mounted.

Let us now apply the above findings to a RIXS experiment done on a system of  $D_{4h}$  point group

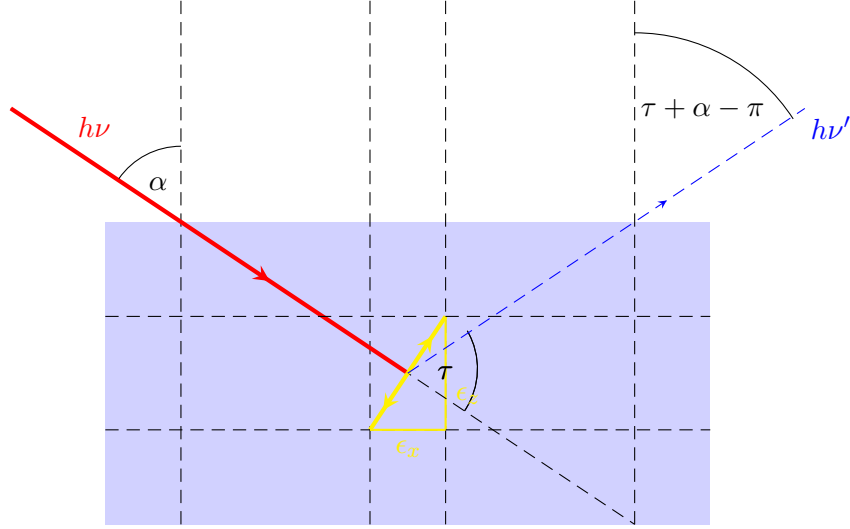


Figure 2.3: Projections of a  $\pi$ -polarization vector onto its principal components  $\epsilon_x$  and  $\epsilon_z$ .

symmetry, like the perovskite oxides, the cuprates or titanates discussed in this thesis. The typical experimental geometry (e.g. SAXES at SLS or BL07LSU at SPring 8) is again shown in Fig. 2.2, for simplicity, we keep the scattering plane fixed in  $yz$ . The coordinate system is adapted to the basis functions describing the sample, i.e. the  $z$  axis is oriented along its surface normal.

The Kramer Heisenberg formula of Eq. 2.1 involves two dipole matrix elements, one for the photon absorption and one for the photon emission process. For the absorption, we are primarily interested in the relative orientation of the incident polarization with respect to the symmetry planes of the sample as sketched in Fig. 2.3. Assuming linear polarization, the vector potential of the incoming light can be written as

$$\begin{aligned} \epsilon_1 &= \begin{pmatrix} \epsilon_x \\ \epsilon_y \\ \epsilon_z \end{pmatrix} = \epsilon \begin{pmatrix} \cos \phi & -\sin \phi & 0 \\ \sin \phi & \cos \phi & 0 \\ 0 & 0 & 1 \end{pmatrix} \cdot \begin{pmatrix} 1 & 0 & 0 \\ 0 & \cos \alpha & -\sin \alpha \\ 0 & \sin \alpha & \cos \alpha \end{pmatrix} \cdot \begin{pmatrix} \cos \xi \\ \sin \xi \\ 0 \end{pmatrix} \\ &= \epsilon \begin{pmatrix} \cos \phi \cos \xi - \cos \alpha \sin \phi \sin \xi \\ \sin \phi \cos \xi + \cos \alpha \cos \phi \sin \xi \\ \sin \alpha \sin \xi \end{pmatrix}, \end{aligned} \quad (2.20)$$

where  $\alpha$  is the angle in between the surface normal  $z$  and the incoming light, and  $\xi$  is the polarization angle.  $\phi$  is the azimuthal rotation angle of the sample, which will be typically fixed once the sample is mounted. Depending on  $(\phi, \alpha, \xi)$ , the dipole operator can have projections

## Chapter 2. Resonant inelastic x-ray scattering

onto  $x$ ,  $y$  and  $z$  components and according to Tab. 2.1 is contained both in the  $E_u(x, y)$  and  $A_{2u}(z)$  irreducible representations of  $D_{4h}$ .

To simplify the discussion, we now keep the scattering plane oriented along a high symmetry plane  $yz$  with  $\phi = 0$ , but give the general results in the associated tables. We identify two important experimental configurations: in the  $\sigma$ -polarized configuration ( $\xi = 0$ ), the polarization vector  $\epsilon$  is along  $x$  and perpendicular to the scattering plane  $yz$ . The dipole operator  $\hat{T}_1^\sigma$  representing the incident light thus is contained solely in the  $E_u(x)$  ( $\rightarrow |51\rangle^-$ ) representation of  $D_{4h}$ . In the  $\pi$ -polarized configuration ( $\xi = \pi/2$ ), the polarization vector lies in the scattering plane  $yz$ . Now, a fraction  $\cos \alpha$  of the photons represented by  $\hat{T}_1^\pi$  involve transitions of  $E_u(y)$  ( $\rightarrow |52\rangle^-$ ), whereas a fraction  $\sin \alpha$  involve transitions of  $A_{2u}(z)$  ( $\rightarrow |21\rangle^-$ ) symmetry.

$ g\rangle$				$T_1$	$\Gamma''\gamma''$					
$\Gamma'\gamma'$	$\times$	$\bar{\Gamma}\bar{\gamma}$		$\times$	$A_1$  11>	$A_2(z)$  21>	$B_1(x^2 - y^2)$  31>	$B_2(xy)$  41>	$E(x)$  51)	$E(y)$  52)
$A_1(x)$  11>	1	$E(x)$  51)		$\sqrt{(\cos \phi \cos \xi - \cos \alpha \sin \phi \sin \xi)^2}$	0	0	0	0	1	0
		$E(y)$  52)		$\sqrt{\sin \phi \cos \xi + \cos \alpha \cos \phi \sin \xi)^2}$	0	0	0	0	0	1
		$A_2(z)$  21)		$\sqrt{(\sin \alpha \sin \xi)^2}$	0	1	0	0	0	0

Table 2.2: Symmetry selectivity in the RIXS excitation process from an  $A_{1g}$  groundstate in  $D_{4h}$  symmetry. The use of this table is explained in detail in the caption of Tab. 2.5.

### Absorption from an $A_{1g}$ groundstate

In undoped anatase  $\text{TiO}_2$ , the  $d^0$  groundstate of the system  $|g\rangle$  is of spherical  $A_{1g}$  symmetry and thus can be labeled by basis function  $|11\rangle^+$  in Griffith notation. Now we apply the Wigner-Eckart theorem to the absorption process in  $\sigma$ -polarization in order to calculate the linear combination  $|i^\sigma\rangle$  associated to all symmetry allowed XAS final state projections  $|\Gamma, \gamma\rangle$  with non zero matrix elements.

$$\begin{aligned}
 |i^\sigma\rangle &= \sum_{\Gamma'', \gamma''} c_{\gamma''11}^{\Gamma''15} \delta_{\Gamma'', 5} \begin{pmatrix} \Gamma'' & 1 & 5 \\ \gamma'' & 1 & 1 \end{pmatrix} |\Gamma''\gamma''\rangle \\
 &= c_{111}^{515} |51\rangle^- \\
 &= |51\rangle^-
 \end{aligned} \tag{2.21}$$

The coefficient  $c_{111}^{515}$  is determined by the orientation of the dipole operator  $\epsilon_1$  with respect to the crystal coordinates, or in other words by the fraction of photons polarized along  $x$ , namely  $c_{111}^{515} = \sqrt{(\cos \phi \cos \xi - \cos \alpha \sin \phi \sin \xi)^2} = 1$  for  $\phi = \xi = 0$ .

In an analogous way, we yield

$$\begin{aligned}
 |i^\pi\rangle &= \sum_{\Gamma'', \gamma''} \left( c_{\gamma''12}^{\Gamma''15} \delta_{\Gamma'',5} \begin{pmatrix} \Gamma'' & 1 & 5 \\ \gamma'' & 1 & 2 \end{pmatrix} + c_{\gamma''11}^{\Gamma''12} \delta_{\Gamma'',2} \begin{pmatrix} \Gamma'' & 1 & 2 \\ \gamma'' & 1 & 1 \end{pmatrix} \right) |\Gamma'' \gamma''\rangle \\
 &= c_{212}^{515} |52\rangle^- + c_{111}^{212} |21\rangle^- \\
 &= \cos \alpha |52\rangle^- + \sin \alpha |21\rangle^-
 \end{aligned} \tag{2.22}$$

in  $\pi$ -polarization  $\xi = \pi/2$ . Whereas we only find spectral weight from  $E_u$  total symmetry final states in  $\sigma$ -polarization, we can find additional final states of  $A_{2u}$  symmetry in  $\pi$ -polarization. The general result of an arbitrary experimental configuration is presented in Tab. 2.2.

### Absorption from a $B_{2g}$ groundstate

$ g\rangle$		$T_1$		$\Gamma'' \gamma''$						
$\Gamma' \gamma'$	$\times$	$\bar{\Gamma} \bar{\gamma}$	$\times$	$A_1$  11>	$A_2(z)$  21>	$B_1(x^2 - y^2)$  31>	$B_2(xy)$  41>	$E(x)$  51>	$E(y)$  52)	
$B_2(xy)$	41)	1	$\begin{matrix} E(x) &  51) \\ E(y) &  52) \\ A_2(z) &  21) \end{matrix}$	$\begin{matrix} \sqrt{(\cos \phi \cos \xi - \cos \alpha \sin \phi \sin \xi)^2} \\ \sqrt{\sin \phi \cos \xi + \cos \alpha \cos \phi \sin \xi)^2} \\ \sqrt{(\sin \alpha \sin \xi)^2} \end{matrix}$	0	0	0	0	0	1
				0	0	0	0	1	0	
				0	0	0	0	0	0	

Table 2.3: Symmetry selectivity in the excitation process from a ground state  $B_{2g}$  in  $D_{4h}$  symmetry. The use of this table is explained in detail in the caption of Tab. 2.5.

Doping anatase  $\text{TiO}_2$  with oxygen vacancies introduces  $\text{Ti}^{3+}$  sites with  $d_{xy}^1$  character. Locally, the system now can be described by a  $3d_{xy}$  ground state with ground state symmetry  $B_{2g}$  ( $|41\rangle^+$ ).

Again, we apply the Wigner-Eckart theorem to the absorption process in  $\sigma$ - and  $\pi$ -polarization in order to calculate all symmetry allowed XAS final states:

$$\begin{aligned}
 |i^\sigma\rangle &= \sum_{\Gamma'', \gamma''} c_{\gamma''11}^{\Gamma''45} \delta_{\Gamma'',5} \begin{pmatrix} \Gamma'' & 4 & 5 \\ \gamma'' & 1 & 1 \end{pmatrix} |\Gamma'' \gamma''\rangle \\
 &= c_{211}^{545} |52\rangle^-
 \end{aligned} \tag{2.23}$$

where the weight  $c_{211}^{545}$  is determined by the fraction of photons causing the transition, namely  $c_{211}^{545} = 1$ .

In an analogous way, we have

$$\begin{aligned}
 |i^\pi\rangle &= \sum_{\Gamma'', \gamma''} \left( c_{\gamma''12}^{\Gamma''45} \delta_{\Gamma'',5} \begin{pmatrix} \Gamma'' & 4 & 5 \\ \gamma'' & 1 & 2 \end{pmatrix} + c_{\gamma''11}^{\Gamma''42} \delta_{\Gamma'',2} \underbrace{\begin{pmatrix} \Gamma'' & 4 & 2 \\ \gamma'' & 1 & 1 \end{pmatrix}}_{=0} \right) |\Gamma'' \gamma''\rangle \\
 &= c_{112}^{545} |51\rangle^- = \cos \alpha |51\rangle^-.
 \end{aligned} \tag{2.24}$$

### Absorption from a $B_{1g}$ groundstate

$ g\rangle$	$\times$	$T_1$		$\Gamma'' \gamma''$						
				$A_1$	$A_2(z)$	$B_1(x^2 - y^2)$	$B_2(xy)$	$E(x)$	$E(y)$	
$\Gamma' \gamma'$	$\times$	$\bar{\Gamma} \bar{\gamma}$	$\times$	$ 11\rangle$	$ 21\rangle$	$ 31\rangle$	$ 41\rangle$	$ 51\rangle$	$ 52\rangle$	
$B_1(x^2 - y^2)$	$ 31\rangle$	1	$\begin{array}{ c c } \hline E(x) &  51\rangle \\ E(y) &  52\rangle \\ A_2(z) &  21\rangle \\ \hline \end{array}$	$\begin{array}{ c } \hline \sqrt{(\cos \phi \cos \xi - \cos \alpha \sin \phi \sin \xi)^2} \\ \sqrt{\sin \phi \cos \xi + \cos \alpha \cos \phi \sin \xi)^2} \\ \sqrt{(\sin \alpha \sin \xi)^2} \\ \hline \end{array}$	0	0	0	0	0	1
				0	0	0	0	1	0	
				0	0	0	0	0	0	

Table 2.4: Symmetry selectivity in the excitation process from a  $B_{1g}$  ground state in  $D_{4h}$  symmetry. The use of this table is explained in detail in the caption of Tab. 2.5.

In tetragonal CuO, the hole of the  $d^9$  groundstate mostly occupies the  $d_{x^2-y^2}$  orbital. Tab. 2.4 therefore summarizes the same consideration starting from a  $B_{1g}$  groundstate. We immediately see that the result is equivalent to the result obtained for  $B_{2g}$ .

It is important to note that a high exchange coupling  $J$  in the correlated cuprates leads to antiferromagnetic ordering. The ground state wave function therefore necessarily needs to take into account the spin and the ground state symmetry is more appropriately described by the according magnetic (Shubnikov) point group.

### 2.6.2 Symmetry selectivity in the re-emission process

In the de-excitation process, the system will create photons represented by the dipole operator  $\hat{T}_2$ . The principal components of  $\hat{T}_2$  are  $E_u(x)$ ,  $E_u(y)$  and  $A_{2u}(z)$  as exemplarily demonstrated in Fig. 2.4. However, only photons with principal components that have a non-zero projections perpendicular to the outgoing light direction will be measured. In order to calculate the number of photons escaping along the outgoing light direction  $\mathbf{k}_2$ , we therefore need to calculate the projections of  $\mathbf{e}_x = \{1, 0, 0\}$ ,  $\mathbf{e}_y = \{0, 1, 0\}$  and  $\mathbf{e}_z = \{0, 0, 1\}$  onto the polarization plane. The outgoing light direction is



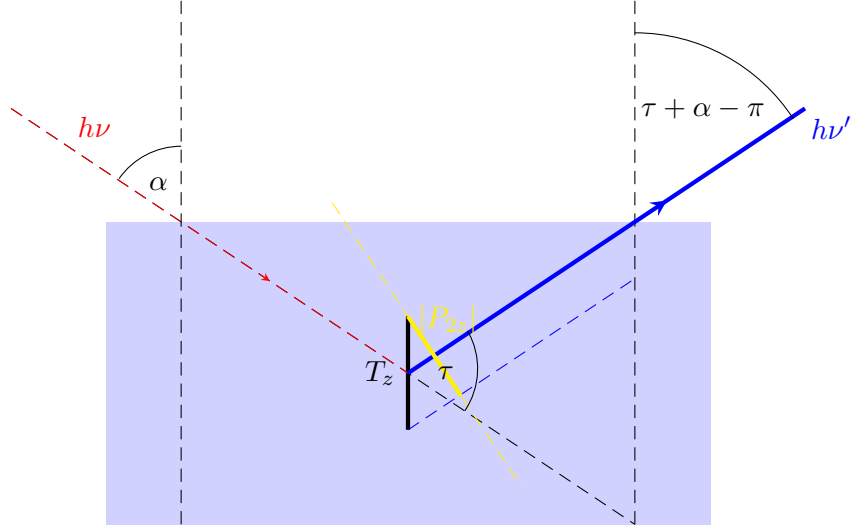


Figure 2.4: Projection  $|P_{2z}|$  of the principal component  $T_z$  onto the polarization plane of the emitted light.

$$\frac{\hbar c}{h\nu} \mathbf{k}_2 = \begin{pmatrix} -\sin(\tau + \alpha) \sin \phi \\ \sin(\tau + \alpha) \cos \phi \\ -\cos(\tau + \alpha) \end{pmatrix}, \quad (2.25)$$

The projection of an arbitrary vector  $\mathbf{v}$  onto the polarization plane perpendicular to  $\mathbf{k}_2$  is given by

$$\mathbf{P}_2 = \mathbf{v} - (\mathbf{v} \cdot \frac{\mathbf{k}_2}{k_2}) \frac{\mathbf{k}_2}{k_2}. \quad (2.26)$$

The absolute projections  $|P_{2x}|$ ,  $|P_{2y}|$ ,  $|P_{2z}|$  of  $\mathbf{e}_x = \{1, 0, 0\}$ ,  $\mathbf{e}_y = \{0, 1, 0\}$  and  $\mathbf{e}_z = \{0, 0, 1\}$  onto the outgoing polarization plane can therefore be easily calculated as

$$\begin{pmatrix} |P_{2x}| \\ |P_{2y}| \\ |P_{2z}| \end{pmatrix} = \begin{pmatrix} \frac{1}{2} \sqrt{3 + \cos(2\phi) + 2 \cos[2(\alpha + \tau)] \sin^2 \phi} \\ \frac{1}{2} \sqrt{3 - \cos(2\phi) + 2 \cos[2(\alpha + \tau)] \cos^2 \phi} \\ \sqrt{\sin^2(\alpha + \tau)} \end{pmatrix}. \quad (2.27)$$

## Chapter 2. Resonant inelastic x-ray scattering

$\Gamma'\gamma'$	$ i\rangle$	$\times$	$T_2$			$\Gamma''\gamma''$					
						$A_1$	$A_2(z)$	$B_1(x^2 - y^2)$	$B_2(xy)$	$E(x)$	$E(y)$
			$\bar{\Gamma}\bar{\gamma}$	$\times$	$ 11\rangle$	$ 21\rangle$	$ 31\rangle$	$ 41\rangle$	$ 51\rangle$	$ 52\rangle$	
$E(x)$	$ 51\rangle$	$\sqrt{(\cos\phi\cos\xi - \cos\alpha\sin\phi\sin\xi)^2}$	$E(x)$	$ 51\rangle$	$\frac{1}{2}\sqrt{3 + \cos(2\phi) + 2\cos[2(\alpha + \tau)]\sin^2\phi}$	$1/\sqrt{2}$	0	$1/\sqrt{2}$	0	0	0
			$E(y)$	$ 52\rangle$	$\frac{1}{2}\sqrt{3 - \cos(2\phi) + 2\cos[2(\alpha + \tau)]\cos^2\phi}$	0	$1/\sqrt{2}$	0	$1/\sqrt{2}$	0	0
			$A_2(z)$	$ 21\rangle$	$\sqrt{\sin^2(\alpha + \tau)}$	0	0	0	0	0	0
$E(y)$	$ 52\rangle$	$\sqrt{(\sin\phi\cos\xi + \cos\alpha\cos\phi\sin\xi)^2}$	$E(x)$	$ 51\rangle$	$\frac{1}{2}\sqrt{3 + \cos(2\phi) + 2\cos[2(\alpha + \tau)]\sin^2\phi}$	0	$-1/\sqrt{2}$	0	$1/\sqrt{2}$	0	0
			$E(y)$	$ 52\rangle$	$\frac{1}{2}\sqrt{3 - \cos(2\phi) + 2\cos[2(\alpha + \tau)]\cos^2\phi}$	$1/\sqrt{2}$	0	$-1/\sqrt{2}$	0	0	0
			$A_2(z)$	$ 21\rangle$	$\sqrt{\sin^2(\alpha + \tau)}$	0	0	0	0	0	0
$A_2(z)$	$ 21\rangle$	$\sqrt{(\sin\alpha\sin\xi)^2}$	$E(x)$	$ 51\rangle$	$\frac{1}{2}\sqrt{3 + \cos(2\phi) + 2\cos[2(\alpha + \tau)]\sin^2\phi}$	0	0	0	0	0	-1
			$E(y)$	$ 52\rangle$	$\frac{1}{2}\sqrt{3 - \cos(2\phi) + 2\cos[2(\alpha + \tau)]\cos^2\phi}$	0	0	0	0	1	0
			$A_2(z)$	$ 21\rangle$	$\sqrt{\sin^2(\alpha + \tau)}$	0	0	0	0	0	0

Table 2.5: Symmetry selectivity in the re-emission process after absorption from a spherical ground state  $A_{1g}$  in  $D_{4h}$  symmetry. Note that parity is omitted. The table consists of three major parts. The left part, here marked by  $|i\rangle$ , marks the initial state of the transition. The column indicated by “ $\times$ ” gives the relative weight of initial state  $\Gamma'\gamma'$ . The middle part, here indicated by  $T_2$ , gives the relevant transitions  $\bar{\Gamma}\bar{\gamma}$  and their relative weight indicated by “ $\times$ ”. The right part summarizes all coupling coefficients between initial state and transition operator. To find the spectral weight of a certain final state  $|\Gamma'', \gamma''\rangle$ , one has to sum over all non zero components of the associated column multiplied by the weights “ $\times$ ” of the same row. For final state  $|5, 2\rangle$  this would be e.g.  $\left(-\frac{1}{2}\sqrt{3 + \cos(2\phi) + 2\cos[2(\alpha + \tau)]\sin^2\phi}\sqrt{(\sin\alpha\sin\xi)^2}\right)^2$ .

### Re-emission after absorption from an $A_{1g}$ groundstate

The dipole allowed intermediate states of the RIXS process calculated in 2.6.1 will now be used to apply the Wigner-Eckart theorem a second time, corresponding to the emission process in the RIXS process. The calculation is completely analogous - except that coefficients  $c_{\gamma\gamma'\bar{\gamma}}^{\Gamma\Gamma'\bar{\Gamma}}$  are now determined by  $\{|P_x\rangle, |P_y\rangle, |P_z\rangle\}$  - and itemized in detail in Tab. 2.5.

We find that dipole allowed contributions to the final state in  $\sigma$ -polarized ( $\xi = 0$ ) are described by the linear combination

$$|f^\sigma\rangle = \frac{1}{\sqrt{2}} \left[ |11\rangle^+ + \cos(\tau + \alpha)|21\rangle^+ + |31\rangle^+ + \cos(\tau + \alpha)|41\rangle^+ \right]$$

and for  $\pi$ -polarization ( $\xi = \pi/2$ )

$$|f^\pi\rangle = \frac{1}{\sqrt{2}} \left[ \cos\alpha\cos(\tau + \alpha)|11\rangle^+ - \cos\alpha|21\rangle^+ - \cos\alpha\cos(\tau + \alpha)|31\rangle^+ + \cos\alpha|41\rangle^+ \right. \\ \left. + \sin\alpha\cos(\tau + \alpha)|51\rangle^+ - \sin\alpha|52\rangle^+ \right].$$

## 2.6. Dipole approximation in RIXS

Note that we again kept  $\phi = 0$  for ease of discussion. The spectral weight of an isolated final state  $|\Gamma, \gamma\rangle$  is finally given by  $I \propto |\langle \Gamma, \gamma | f \rangle|^2$  and summarized in Tab. 2.6.

$\phi$	pol	$A_{1g}$	$A_{2g}$	$B_{1g}$	$B_{2g}$	$E_g(yz)$	$E_g(xz)$
0	$\sigma$	$\frac{1}{2}$	$\frac{1}{2} \cos^2(\alpha + \tau)$	$\frac{1}{2}$	$\frac{1}{2} \cos^2(\alpha + \tau)$	0	0
0	$\pi$	$\frac{1}{2} \cos^2 \alpha \cos^2(\alpha + \tau)$	$\frac{1}{2} \cos^2 \alpha$	$\frac{1}{2} \cos^2 \alpha \cos^2(\alpha + \tau)$	$\frac{1}{2} \cos^2 \alpha$	$\cos^2(\alpha + \tau) \sin^2 \alpha$	$\sin^2 \alpha$
$\pi/4$	$\sigma$	$\frac{1}{4}(3 + \cos[2(\alpha + \tau)])$	0	0	$\frac{1}{4}(3 + \cos[2(\alpha + \tau)])$	0	0
$\pi/4$	$\pi$	$\frac{1}{4} \cos^2 \alpha (3 + \cos[2(\alpha + \tau)])$	0	0	$\frac{1}{4} \cos^2 \alpha (3 + \cos[2(\alpha + \tau)])$	$\frac{1}{4} \sin^2 \alpha (3 + \cos[2(\alpha + \tau)])$	$\frac{1}{4} \sin^2 \alpha (3 + \cos[2(\alpha + \tau)])$

Table 2.6: Spectral weight of the final states as a function of scattering angle  $\tau$  and the incoming light direction  $\alpha$  starting from a  $A_{1g}$  groundstate.

The expected dependence of all dipole allowed final states on the incidence angle  $\alpha$  for  $\sigma$  and  $\pi$ -polarization is plotted in Fig. 2.5. For  $\phi = 0$ , final states of  $A_{1g}$  and  $B_{1g}$  symmetry, behave in the same way. So behave final states of  $A_{2g}$  and  $B_{2g}$  symmetry. For  $\phi = 45^\circ$ ,  $A_{1g}$  groups with  $B_{2g}$  and  $A_{2g}$  with  $B_{1g}$ . Apart from these “degeneracies”, the behavior of the branches is quite complex, and it is often possible suppress certain final state symmetries with respect to others.

### Re-emission after absorption from a $B_{1g}$ or $B_{2g}$ groundstate

$\Gamma'\gamma'$	$ i\rangle$	$\times$	$\bar{\Gamma}\bar{\gamma}$	$T_2$	$\Gamma''\gamma''$					
					$A_1$	$A_2(z)$	$B_1(x^2 - y^2)$	$B_2(xy)$	$E(x)$	$E(y)$
$E(x)$	51)	$\sqrt{\sin \phi \cos \xi + \cos \alpha \cos \phi \sin \xi}^2$	$E(x)$  51)	$\frac{1}{2} \sqrt{3 + \cos(2\phi) + 2 \cos[2(\alpha + \tau)] \sin^2 \phi}$	$1/\sqrt{2}$	0	$1/\sqrt{2}$	0	0	0
$E(y)$	52)	$\sqrt{\sin \phi \cos \xi + \cos \alpha \cos \phi \sin \xi}^2$	$E(y)$  52)	$\sqrt{\sin \phi \cos \xi + \cos \alpha \cos \phi \sin \xi}^2$	0	$1/\sqrt{2}$	0	$1/\sqrt{2}$	0	0
$E(z)$	21)	$\sqrt{\sin^2(\alpha + \tau)}$	$A_2(z)$  21)	$\sqrt{\sin^2(\alpha + \tau)}$	0	0	0	0	0	0
$E(x)$	51)	$\sqrt{(\cos \phi \cos \xi - \cos \alpha \sin \phi \sin \xi)^2}$	$E(x)$  51)	$\frac{1}{2} \sqrt{3 + \cos(2\phi) + 2 \cos[2(\alpha + \tau)] \sin^2 \phi}$	0	$-1/\sqrt{2}$	0	$1/\sqrt{2}$	0	0
$E(y)$	52)	$\sqrt{(\cos \phi \cos \xi - \cos \alpha \sin \phi \sin \xi)^2}$	$E(y)$  52)	$\sqrt{\sin \phi \cos \xi + \cos \alpha \cos \phi \sin \xi}^2$	$1/\sqrt{2}$	0	$-1/\sqrt{2}$	0	0	0
$A_2(z)$	21)	$\sqrt{\sin^2(\alpha + \tau)}$	$A_2(z)$  21)	$\sqrt{\sin^2(\alpha + \tau)}$	0	0	0	0	0	0

Table 2.7: Symmetry selectivity in the re-emission process from a ground state  $B_{1g}$  or  $B_{2g}$  in  $D_{4h}$  symmetry. The use of this table is explained in detail in the caption of Tab. 2.5.

From the absence of spectral weight for  $A_{2u}$  contributions to the RIXS intermediate state (see Tabs. 2.3 and 2.4) we can immediately infer that the  $E_g$  states must be suppressed in the final state. However, the  $c$ -coefficients in  $\sigma$  and  $\pi$ -polarization exchange according to Tab. 2.7 and we find

$$|f^\sigma\rangle = \frac{1}{\sqrt{2}} [\cos(\tau + \alpha)|11\rangle^+ - |21\rangle^+ - \cos(\tau + \alpha)|31\rangle^+ + |41\rangle^+]$$

as well as

$$|f^\pi\rangle = \frac{1}{\sqrt{2}} [\cos \alpha |11\rangle^+ + \cos \alpha \cos(\tau + \alpha) |21\rangle^+ + \cos \alpha |31\rangle^+ + \cos \alpha \cos(\tau + \alpha) |41\rangle^+].$$

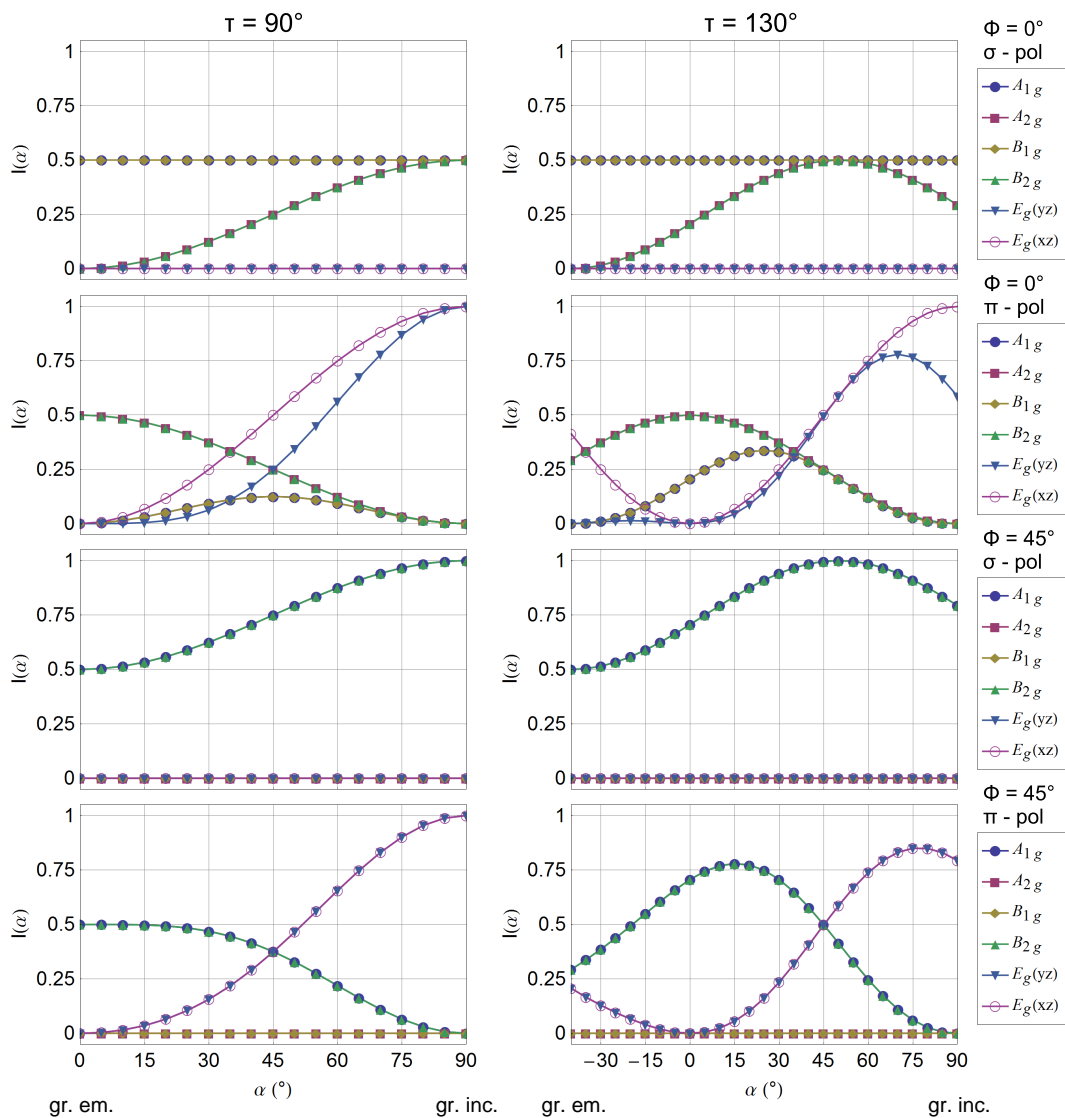


Figure 2.5: Angular dependence of all dipole allowed final states from a  $A_{1g}$  ground state in  $\sigma$ - and  $\pi$ -polarized configuration. The results are shown **(left)** for scattering angles  $\tau = 90^\circ$  and **(right)**  $130^\circ$  as used throughout the scope of this thesis.

## 2.6. Dipole approximation in RIXS

$\phi$	pol	$A_{1g}$	$A_{2g}$	$B_{1g}$	$B_{2g}$	$E_g(yz)$	$E_g(xz)$
0	$\sigma$	$\frac{1}{2} \cos^2(\alpha + \tau)$	$\frac{1}{2}$	$\frac{1}{2} \cos^2(\alpha + \tau)$	$\frac{1}{2}$	0	0
0	$\pi$	$\frac{1}{2} \cos^2 \alpha$	$\frac{1}{2} \cos^2 \alpha \cos^2(\alpha + \tau)$	$\frac{1}{2} \cos^2 \alpha$	$\frac{1}{2} \cos^2 \alpha \cos^2(\alpha + \tau)$	0	0
$\pi/4$	$\sigma$	$\frac{1}{4}(3 + \cos[2(\alpha + \tau)])$	0	0	$\frac{1}{4}(3 + \cos[2(\alpha + \tau)])$	0	0
$\pi/4$	$\pi$	$\frac{1}{4} \cos^2 \alpha (3 + \cos[2(\alpha + \tau)])$	0	0	$\frac{1}{4} \cos^2 \alpha (3 + \cos[2(\alpha + \tau)])$	0	0

Table 2.8: Spectral weight of the final states as a function of scattering angle  $\tau$  and the incoming light direction  $\alpha$  starting from a  $B_{1g}$  or  $B_{2g}$  groundstate.

Clearly, having started from a  $B_{1g}$  or  $B_{2g}$  ground state flips the  $\alpha$ -dependence in between  $A_{1g}$  and  $A_{2g}$  as well as  $B_{1g}$  and  $B_{2g}$  states with respect to a  $A_{1g}$  groundstate. Except of the inverted labeling, Fig. 2.5 therefore stays valid. Turning the system  $\phi = 45^\circ$  about the  $z$  axis gives identical results to the  $A_{1g}$  groundstate except for the suppression of  $E_g$  states in the former case. Going from  $\phi = 0$  to  $\phi = 45^\circ$ , we thus can expect a complete suppression of states  $A_{2g}$  and  $B_{1g}$ .

It is important however that our estimation only gives information on the *total* symmetry. Assuming that close to zero energy loss, the electronic wave function will hardly have changed. The total symmetry so has to be decomposed into the symmetry of the electronic wave function  $B_{1g}$  or  $B_{2g}$  and the symmetry of the excitation remaining in the crystal.

It is necessary to note again that formally above method should apply equally for the cuprates. However, previous considerations did not take into account the full symmetry of the wavefunction, which explicitly includes the spin. In order to obtain a reliable result, the ground state symmetry – including magnetic long range order – must be known and described by the appropriate magnetic (Shubnikov) point group and *not* by the ordinary point groups. Given that the magnetic ground state of T-CuO (compare Ch. 6) is not known to date, we forbear from doing such a treatment in this work.<sup>4</sup> A careful consideration of symmetry selectivity in the antiferromagnetic cuprates has been done in detail in refs. 69 and 217.

### 2.6.3 Intermediate state selection

In some cases, we find the resonance of a distinct RIXS signal at excitation energies that correspond to a certain orbital configuration of the intermediate or in other words the XAS final state. In Ch. 4, we e.g. find a phonon resonance in anatase  $\text{TiO}_2$  at XAS peaks relating to electronic transitions into  $d_{x^2-y^2}$  and  $d_{z^2}$  orbitals. Such a situation can in principle help to further narrow the criteria for final state selection. Given this orbital selectivity, the intermediate state must be contained in the representations of the possible core hole state. In Tab. 2.9 we apply this idea to a  $2p^5 3d^1$  state and show the multiplication table of the according subspace of  $D_{4h}$ .

The intermediate states with the electron in a  $d_{x^2-y^2}$  or  $d_{z^2}$  orbital can contain both the  $E_u$  and  $A_{2u}$  representations. Therefore, all possible final state symmetries – discussed in Tab. 2.5 – can be expected in the RIXS experiment.

<sup>4</sup>The coupling coefficients for the magnetic point groups are tabulated in refs. 64–67 and an application of magnetic point groups to symmetry selection rules is given in Ref. 68.

“ $O_h$ ”	“ $e_g$ ”		“ $t_{2g}$ ”	
$D_{4h}$	$B_{1g}(d_{x^2-y^2})$	$a_{1g}(d_{z^2})$	$b_{2g}(d_{xy})$	$e_g(d_{yz}/d_{xz})$
$E_u(p_x/p_y)$	$E_u$	$E_u$	$E_u$	$A_{1u}, A_{2u}, B_{1u}, B_{2u}$
$A_{2u}(p_z)$	$B_{2u}$	$A_{2u}$	$B_{1u}$	$E_u$

Table 2.9: Intermediate state selection for a  $p \rightarrow d$  transition. In a  $d^0$  system like  $\text{TiO}_2$ , the excited electron can occupy “ $t_{2g}$ ” and “ $e_g$ ” states. Thus all direct product intermediate states are possible. In a  $d^9$  system like  $\text{CuO}$ , the excited electron can only occupy the  $B_{1g}(x^2 - y^2)$  orbital. Intermediate state selection thus allows only the  $E_u$  and  $B_{2u}$  states of which only the  $E_u$  can be reached in XAS.

## 2.7 Selfabsorption

So far, we neglected the angular dependent effect of selfabsorption for the modulation of the RIXS intensity. A thorough correction method has been presented in [71]. Here, we will reduce the treatment to a very simple model. Incident x-rays  $h\nu$  traveling a distance  $l$  in the solid will exponentially lose intensity

$$I(h\nu, l) \propto e^{-\mu(h\nu)l}, \quad (2.28)$$

where  $\mu(h\nu)$  is the absorption cross section.<sup>5</sup> Consequently, the quantity  $-dI \propto \mu(h\nu)e^{-\mu(h\nu)l}dl$  will be absorbed along the infinitesimal path length  $[l, l + dl]$ . Some fraction of this number – e.g. determined by the symmetry considerations discussed in the last chapter – will cause the RIXS transition of Eq. 2.1 and create photons  $h\nu'$ . On their way  $l'(l, \alpha, \tau)$  out of the solid, these x-rays will lose intensity as well, resulting in an effect called self-absorption. According to Fig. 2.6, the law of sines gives

$$\frac{l}{\cos(\tau + \alpha - \pi)} = \frac{l'}{\cos(\alpha)}. \quad (2.29)$$

and we therefore find

$$dI_{\text{RIXS}}(h\nu, h\nu', l) \propto \mu(h\nu)e^{-\left(\mu(h\nu) + \mu(h\nu')\frac{\cos(\alpha)}{\cos(\tau + \alpha - \pi)}\right)l}dl. \quad (2.30)$$

---

<sup>5</sup>In general,  $\mu(h\nu)$  depends on the orientation of the polarization vector with respect to the crystal orientation. In titanates like  $\text{TiO}_2$ , dichroism effects are typically weak and  $\mu(h\nu)$  thus can be treated isotropically. In the non-isotropic case, the absorption cross section  $\mu(h\nu)$  becomes a function of experimental geometry  $\alpha$  and  $\phi$  and the polarization  $\xi$ .  $\mu(h\nu')$  additionally depends on the scattering angle  $\tau$ .

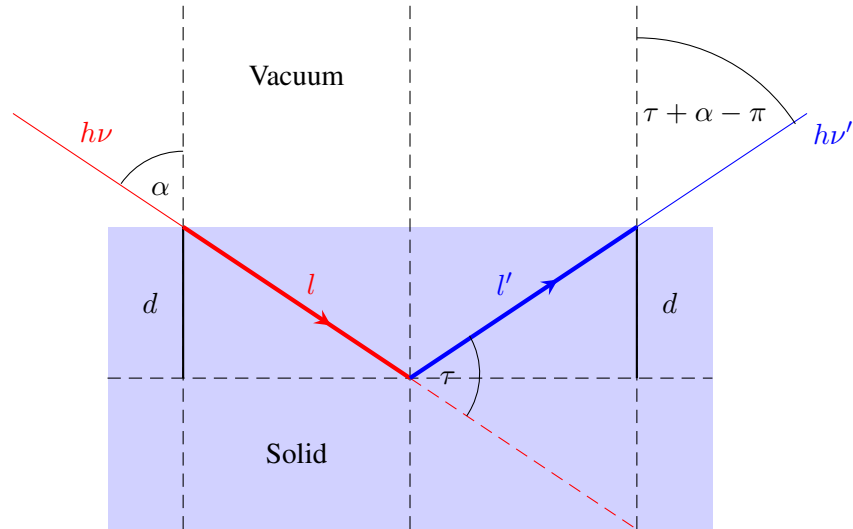


Figure 2.6: Self absorption geometry in RIXS.

### 2.7.1 Selfabsorption in a bulk material

To obtain the total RIXS signal in a bulk material, we need to integrate over the half-space  $\int_0^\infty dI_{RIXS}$  and obtain

$$I_{RIXS}(h\nu, h\nu') \propto \frac{1}{1 + \frac{\mu(h\nu')}{\mu(h\nu)} \frac{\cos(\alpha)}{\cos(\tau + \alpha)}}. \quad (2.31)$$

Fig. 2.7 shows the results of Eq. 2.31 for scattering angles  $\tau = 90^\circ$  and  $130^\circ$  and different ratios  $\mu(h\nu')/\mu(h\nu)$  of the absorption coefficient of out and ingoing x-rays. Clearly, self absorption is not symmetric around the specular angle. Towards grazing incidence, suppression is mostly determined by the absorption of the incident beam. Towards grazing emission however, the traveling distance of the outgoing light is long and suppression of RIXS signal high. Additionally, outgoing photons of different energy are subject to the energy dependence of the absorption cross section  $\mu(h\nu')$ , which modifies the spectra in an inhomogeneous way.

For  $\mu(h\nu') \gg \mu(h\nu)$  – which can be the case when exciting with an energy higher than the main absorption feature in XAS – significant spectral weight can only be expected close to grazing incidence. If  $\mu(h\nu')$  can be neglected however – as can be the case for RIXS features far away from the absorption edge probed – signal will only be significantly reduced close to grazing emission. If absorption coefficients of incident light and RIXS signal are comparable, the RIXS intensity to some approximation goes linear for scattering angles  $\tau = 90^\circ$ . Towards larger scattering angles  $\tau$ , this trend flattens considerably and intensity would remain constant for a broad interval of  $\alpha$  in backscattering geometry. Experimental configurations with large scattering

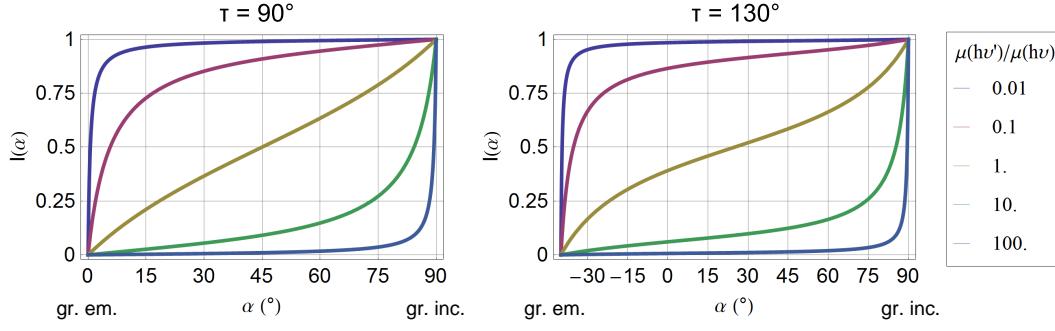


Figure 2.7: Self absorption in bulk samples. Results are shown for two experimental geometries with **(left)**  $\tau = 90^\circ$  and **(right)**  $\tau = 130^\circ$  scattering angle in units of the total RIXS signal created in the solid. The characteristic parameter  $\mu(h\nu')/\mu(h\nu)$  is varied over 4 orders of magnitude.

angle therefore not only provide a wider range of momentum transfer vectors but considerably improve the “dynamic range” of angles to work with.

### 2.7.2 Selfabsorption in a thin film

In case of a thin film – like the thin films of T-CuO we present in Ch. 6 – one can neglect the contribution of the bulk and needs to integrate Eq. 2.30 only over film thickness  $d$ :

$$\int_0^{d/\cos\alpha} dI_{RIXS} = \frac{\cos(\alpha + \tau) \left( e^{\mu(h\nu) \frac{d}{\cos\alpha} \left( \frac{\mu(h\nu')}{\mu(h\nu)} \frac{\cos\alpha}{\cos(\alpha+\tau)} - 1 \right)} - 1 \right)}{\frac{\mu(h\nu')}{\mu(h\nu)} \cos\alpha - \cos(\alpha + \tau)} \quad (2.32)$$

The results for  $\tau = 90$  and  $130^\circ$  scattering geometry obtained for several normalized film thicknesses  $d \times \mu(h\nu) = 0.1, 1$  and  $10$  are shown in Fig. 2.8. For small film thicknesses, selfabsorption is quite insensitive to the ratio  $\mu(h\nu')/\mu(h\nu)$ . The RIXS intensity suppression so remains largely independent on  $h\nu'$  and the spectra are modified in a homogeneous way. In the limit of a thick film we approach the bulk result shown in Fig. 2.7.



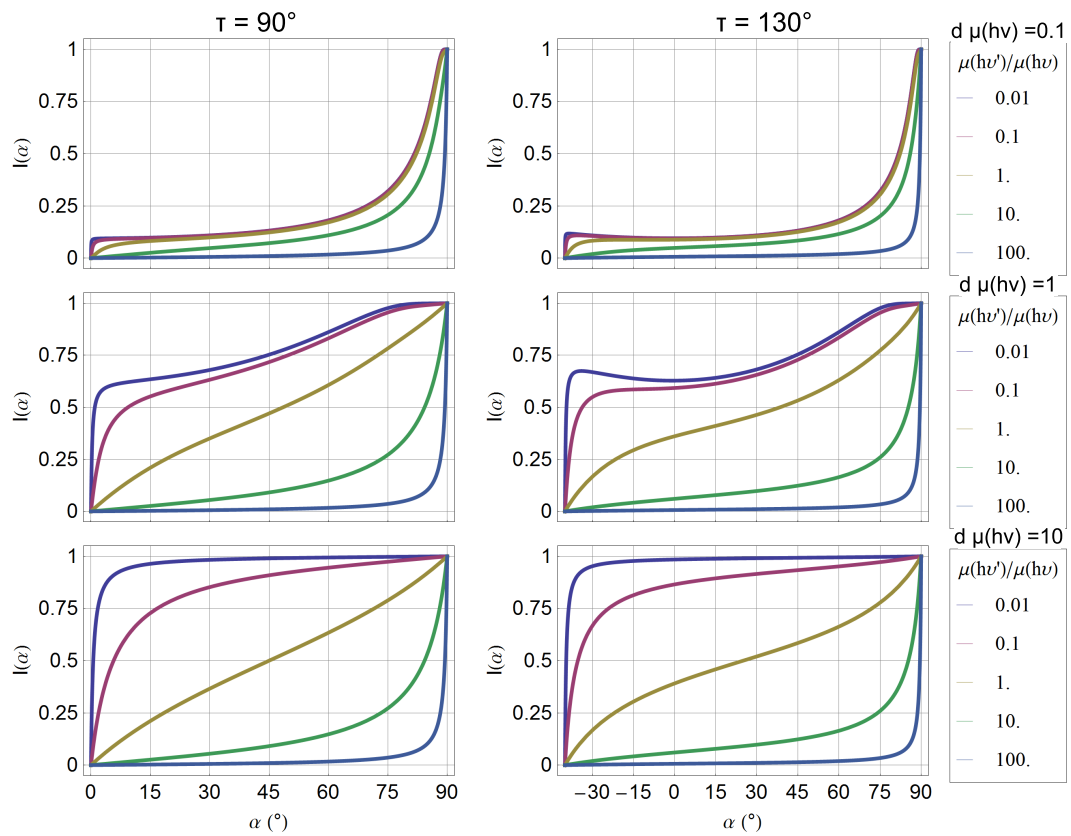


Figure 2.8: Self absorption in thin film samples. Results are shown for two experimental geometries with **(left)**  $\tau = 90^\circ$  and **(right)**  $\tau = 130^\circ$  scattering angle in units of the total RIXS signal created in the solid. The characteristic parameter  $\mu(h\nu')/\mu(h\nu)$  is varied over 4 orders of magnitude for three different normalized film thicknesses  $d \times \mu(h\nu)$ .



# 3 Anatase TiO<sub>2</sub> – a polaronic semiconductor investigated by ARPES

## 3.1 Summary

In this chapter, we investigate the electronic structure of anatase TiO<sub>2</sub> (001) surfaces on both *in situ* prepared thin films and bulk single crystals by means of ARPES. We demonstrate the possibility to fine tune electron doping through the amount of oxygen vacancies created in the x-ray beam spot - which can be exploited in applications. We reveal the bottom of the conduction band, a bulk  $d_{xy}$  state similar to the conduction state observed previously in SrTiO<sub>3</sub>, which is subject to significant e-ph coupling. The “peak-dip hump” signature of the ARPES spectra are indicative for the formation of so called large polarons, and points out the importance of distinct longitudinal optical (LO) phonons for charge renormalization in this material. In the high doping limit, the single polaron wavefunctions start to overlap and a weakly correlated Fermi liquid picture becomes more adequate.

## 3.2 Motivation

The anatase polymorph of TiO<sub>2</sub> is a celebrated candidate for many innovative applications in photo-catalysis [72–74] and photo-voltaics [75–77]. The crucial quantity for the figure of merit in these devices is the valence exciton lifetime, and it is therefore of major interest to understand and control the electronic properties of pristine and doped anatase, both in bulk and nano-crystalline form.

Pristine anatase is a classic band insulator with a band gap of  $E_{gap} \sim 3.2$  eV. As depicted in Fig. 3.1, the valence band is mostly O  $2p$  derived and completely filled whereas the conduction band is mostly Ti  $3d$  derived and completely empty. In the bulk, mobile charge carriers can be obtained by creation of oxygen defects, the natural dopants of TiO<sub>2</sub>. The mobility of these charge carriers is determined by the defect concentration and by the e-ph coupling.

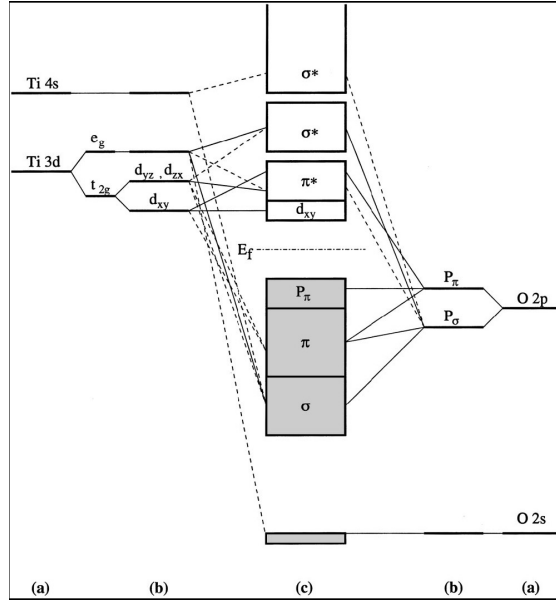


Figure 3.1: Electronic structure of anatase TiO<sub>2</sub>. (a) atomic levels, (b) crystal-field split levels, and (c) final interaction states. Solid lines indicate strong, dashed lines weak hybridization. The picture was taken from Ref. 78.

Resistivity measurements over a temperature range from 4.2 to 300 K<sup>1</sup> (Fig. 3.2) clearly reveal the presence of two distinct temperature regimes. In the 300 - 60 K interval, the sample is a relatively good conductor ( $\sim 1 \Omega\text{cm}$ ) and surprisingly exhibits a metal-like temperature dependence  $d\rho/dT > 0$ , despite the large band gap  $E_{gap} \sim 3.2 \text{ eV}$  of the pristine phase [79]. In contrast to what is expected for a typical semiconductor, resistivity rises by more than 5 times from 60 to 300 K which speaks in favor of non-conventional transport of charge carriers, determined by the interaction with thermally activated phonons.

Below 60 K, an insulating phase characterized by a rapid increase of the resistivity emerges, in line with the semiconductor picture. From this temperature region one can extract an activation energy  $E_a \sim E_{gap}/2$  for charge transport of about 10 meV, as previously shown in Ref. 80. This energy corresponds to shallow donor states resulting from oxygen vacancies, which electron dope the system by the following relationship:  $\text{Ti}^{4+}\text{O}_2^{2-} \rightarrow \text{Ti}_{1-x}^{4+}\text{Ti}_x^{3+}(\text{O}_{2-x}^{2-}) + xe^-$  [80–82]. In the very low doping regime  $\sim 10^{17} \text{ cm}^{-3}$ , defect states are localized, and the Fermi level aligns between donor ( $E_d$ ) and the conduction band level  $E_{CB}$ . Thus, temperature promotes charge carriers into the conduction band following a Boltzmann distribution factor  $\exp[-(E_{CB} - E_d)/k_B T]$ . For significantly higher doping concentrations, one expects donor states to form an impurity band which eventually merges with the conduction band.

Consequently, charge carriers will be found at the Fermi level even at very low temperatures and

<sup>1</sup>Transport experiments were carried out by Jaćim Jaćimović for samples with carrier densities in the  $7 \times 10^{17} \text{ cm}^{-3}$  regime. The carrier density was determined independently from Hall measurements not shown here.

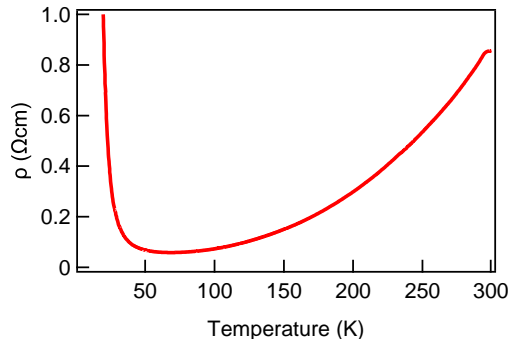


Figure 3.2: Resistivity as a function of temperature, measured on a single crystal of anatase  $\text{TiO}_2$ . The steep increase of  $\rho$  above 60 K suggests enhanced e-ph scattering. Below 60 K, carriers are deactivated and resistivity rises exponentially.

the resistivity is expected to saturate at a minimal value. These expectations are in agreement with independent transport measurements on Nb-,F- and oxygen vacancy doped anatase [83, 84, 105]. However, transport is very bulk sensitive and may integrate over a variety of different effects. In order to get a complete picture on the nature and behavior of these donor states, we investigate anatase in a much more direct way by APRES applied to oxygen vacancy doped anatase thin films and single crystals.

### 3.3 Crystal growth and preparation

The three polymorphs of  $\text{TiO}_2$  are rutile, anatase, and brookite. Whereas rutile in general is the most studied phase, anatase has the highest efficiency among the three in many applications and is used almost exclusively in nanoparticle form [75]. The origin of differences in performance is still unclear. The lack of information on the details of the electronic structure of anatase is partially due to the difficulty of synthesizing both bulk single-crystals and stoichiometric films.

Anatase has a body centered tetragonal ( $bct2$ ) lattice reflected in a  $D_{4h}^{19}$  symmetry with lattice parameters  $a = 3.782 \text{ \AA}^{-1}$  and  $c = 9.502 \text{ \AA}^{-1}$  [85]. Locally, titanium atoms are coordinated tetrahedrally, almost octahedrally by the oxygen atoms. Transparent single crystals were grown by a chemical transport method, similarly to the one described by Berger *et al.* [86]. 0.5 g of high purity anatase powder were sealed in a 3 mm thick, 2 cm large and 20 cm long quartz ampule together with 150 mg of  $\text{NH}_4\text{Cl}$ , previously dried at  $60 \text{ }^\circ\text{C}$  under dynamic vacuum for one night, and 400 mbar of electronic grade HCl. Both HCl and  $\text{NH}_4\text{Cl}$  serve as transport agent. The ampules were placed in a horizontal tubular two-zone furnace and heated very slowly to  $740 \text{ }^\circ\text{C}$  at the source, and  $610 \text{ }^\circ\text{C}$  at the deposition zone. After two weeks, millimeter-sized crystals with a bi-pyramidal shape were collected and cut into rectangular bars (typically  $0.8 \times 0.6 \times 0.15 \text{ mm}^3$ ).

Transport measurements shown in the introduction were performed by a standard four point technique. The electrical leads were gold wires, glued onto pre-evaporated gold pads by means

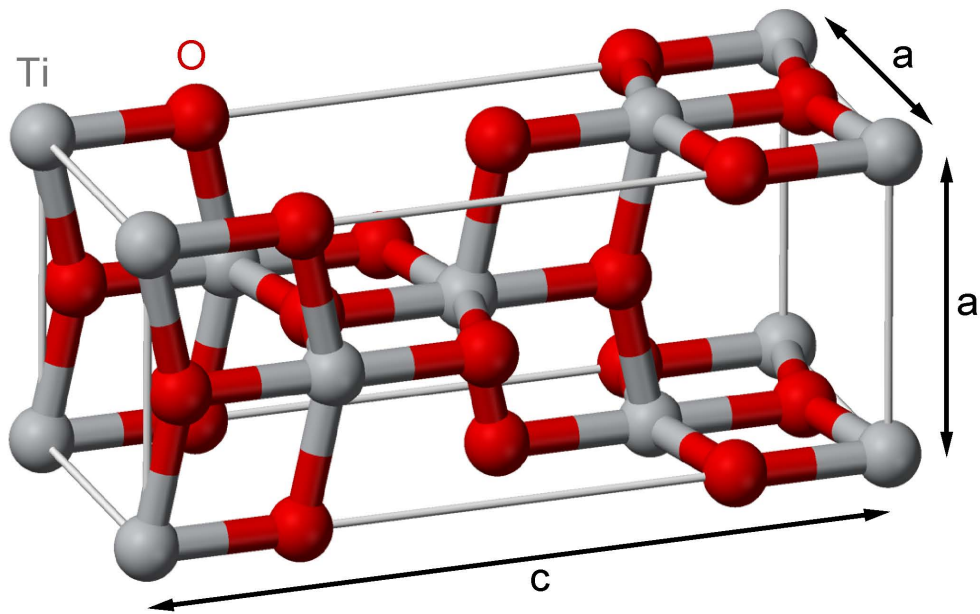


Figure 3.3: Crystal structure of anatase  $\text{TiO}_2$ . Grey and red balls indicate titanium and oxygen atoms, respectively. Locally, titanium atoms are coordinated tetrahedrally (almost octahedrally) by 6 oxygen atoms.

### 3.3. Crystal growth and preparation

of silver paste, which ensured stable electrical contacts.

For ARPES measurements, a crystal was polished and cleaned in a buffered 5% fluoridic acid solution before introducing it into the UHV system ( $< 10^{-10}$  mbar). Several cycles of sputtering with 1.5 kV argon ions and annealing at 500 °C were performed to obtain a clean, ordered surface. In order to compensate oxygen loss caused by the sputtering process, the crystal was annealed in 35 mbar of oxygen at 400 °C for 30 minutes before the ARPES experiments. A reflective high energy electron diffraction (RHEED) pattern is shown in Fig. 3.4 (a). Besides the expected 2D signature, we clearly observe 3D spots indicative of some surface roughness (e.g. terraces and steps), but no sign of additional phases.

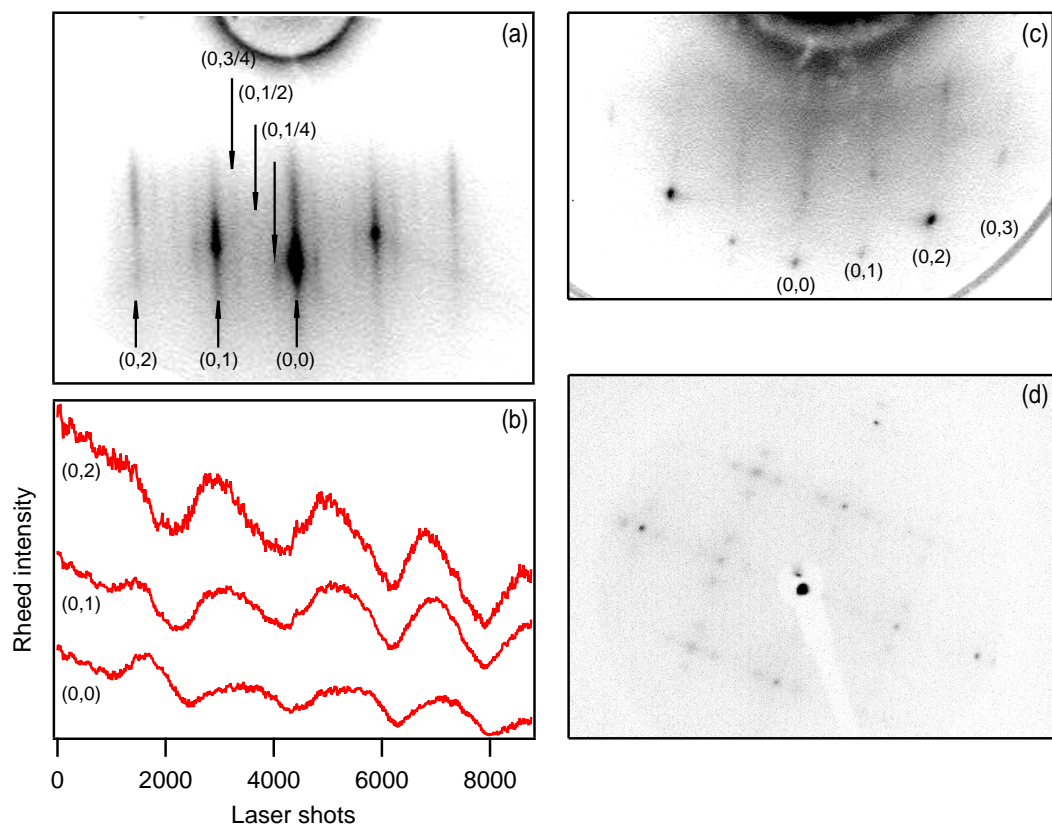


Figure 3.4: (a) RHEED image of an anatase (001) surface grown by PLD. Traces of the two-domain  $4 \times 1$  surface reconstruction indicate high surface quality. (b) RHEED intensity oscillations of the (0,0), (0,1) and (0,2) streak during film growth of anatase (001) (c) RHEED image of the polished anatase single crystal (001) surface. 3D spots indicate residual surface roughness. (d) LEED image of the anatase single crystal (001) surface reveals traces of the two-domain  $4 \times 1$  surface reconstruction.

### 3.4 Film growth and characterization

Thin films were grown *in situ* at the electronic structure factory end station at beamline 7 of the Advanced Light Source, Lawrence Berkeley National Laboratory. Anatase thin films were grown by means of pulsed laser deposition (PLD) on (001) oriented 0.5 % Nb-doped SrTiO<sub>3</sub> and undoped LaAlO<sub>3</sub>. Films grown on Nb:STO yielded somewhat sharper spectral features in ARPES, possibly reflecting a better surface quality, the good electrical conductivity of the substrate, or both. During deposition, the substrate was kept at 650 °C in  $7 \times 10^{-4}$  mbar O<sub>2</sub> atmosphere. PLD was performed from a monocrystalline TiO<sub>2</sub> rutile target using a 248 nm Coherent Complex Pro 205 F Excimer Laser. The sample was grown at a repetition rate of 10 Hz with about 20 mJ per pulse. Film growth was monitored by *in situ* RHEED and film thickness was estimated through corresponding RHEED oscillations. We have measured films of varying thickness between 5 and 20 ML, with no detectable change in the ARPES signal. A typical example of a RHEED image and oscillations of an anatase (001) surface are shown in Fig. 3.4 (a) and (b). Clearly visible are traces of the two-domain  $4 \times 1$  surface reconstruction reported by several authors [87–89]. Additionally, we show a RHEED image on a polished anatase single crystal in Fig. 3.4 (c) and a LEED image on a single crystal with a natural atomically flat surface which was used in the experiment of Ch. 4.

### 3.5 Anatase TiO<sub>2</sub> – a large polaron system

ARPES experiments on anatase single crystals and *in situ* grown thin films show surprising results: even though the system is expected to be a band insulator, we observe significant dispersive spectral weight at the Fermi level for samples that are sufficiently oxygen vacancy doped. The number of oxygen vacancies in the (sub-)surface region thereby can be increased through x-ray beam exposure and decreased through subsequent re-oxidation, which allows to control the charge carrier concentration in between  $\sim 10^{18}$  to  $\sim 10^{20}$  cm<sup>-3</sup>. Due to the polarity of the lattice, these doped in charge carriers are strongly interacting with the LO phonon background, forming so called large polaron quasi-particles (QPs). An overview over these findings is presented in the following paper [90]. Additional in depth information will be given from Sec. 3.6.





## Tunable Polaronic Conduction in Anatase TiO<sub>2</sub>

S. Moser,<sup>1,2</sup> L. Moreschini,<sup>1</sup> J. Jaćimović,<sup>2</sup> O. S. Barišić,<sup>3</sup> H. Berger,<sup>2</sup> A. Magrez,<sup>2</sup> Y. J. Chang,<sup>1,4</sup> K. S. Kim,<sup>1</sup>  
A. Bostwick,<sup>1</sup> E. Rotenberg,<sup>1</sup> L. Forró,<sup>2</sup> and M. Grioni<sup>2</sup>

<sup>1</sup>Advanced Light Source (ALS), Berkeley, California 94720, USA

<sup>2</sup>Ecole Polytechnique Fédérale de Lausanne (EPFL), Institut de Physique des Nanostructures, CH-1015 Lausanne, Switzerland

<sup>3</sup>Institute of Physics, Bijenička c. 46, HR-10000 Zagreb, Croatia

<sup>4</sup>Department of Physics, University of Seoul, Seoul, 130-743, Korea

(Received 26 February 2013; published 7 May 2013)

Oxygen vacancies created in anatase TiO<sub>2</sub> by UV photons (80–130 eV) provide an effective electron-doping mechanism and induce a hitherto unobserved dispersive metallic state. Angle resolved photoemission reveals that the quasiparticles are large polarons. These results indicate that anatase can be tuned from an insulator to a polaron gas to a weakly correlated metal as a function of doping and clarify the nature of conductivity in this material.

DOI: [10.1103/PhysRevLett.110.196403](https://doi.org/10.1103/PhysRevLett.110.196403)

PACS numbers: 71.38.Fp, 79.60.Bm

The anatase structural phase of titanium dioxide (TiO<sub>2</sub>) can be the key element in novel applications. Whereas extensive work has been focused on its famous photocatalytic behavior [1–3], more and more proposed devices, such as memristors [4], spintronic devices [5], and photovoltaic cells [6–8], rely on its less well-known electronic properties. In particular, anatase has been recently suggested as a candidate for replacing the In-based technology for transparent conducting oxides [9] in a wide range of applications from solar cell elements, to light-emitting devices, to flat panels, to touch-screen controls [10]. The crucial quantity for the figure of merit in these devices is conductivity, and it is therefore of major interest to understand and control the electronic properties of pristine and doped anatase.

Stoichiometric anatase is an insulator with a 3.2 eV band gap [11] but oxygen vacancies, typically present with concentrations in the 10<sup>17</sup> cm<sup>-3</sup> range [12,13], create a shallow donor level ~10 meV below the conduction band (CB) [14]. Since large single crystals became available for transport studies, a better insight has been gained on the influence of these donors on the electronic response of anatase. Above ~60 K, the electrons thermally excited into the CB give rise to metalliclike transport. At lower temperatures, the anomalous increase of resistivity indicates that the charge carriers are not bare electrons but polarons [14], i.e., electrons coherently coupled to a lattice distortion induced by the Coulomb interaction. Understanding the properties of such composite particles in anatase is important to better engineer the material for targeted applications, where the low electron mobility often represents the overall performance bottleneck. We will also demonstrate that, from the point of view of fundamental physics, anatase represents an excellent model compound to study the behavior of the “rare” large polaron quasiparticles (QPs), intermediate between localized small polarons and free electrons.

We performed angle resolved photoemission (ARPES) measurements on TiO<sub>2</sub> single crystals [Fig. 1(a)] and thin films grown *in situ* on insulating LaAlO<sub>3</sub> and conducting Nb-doped SrTiO<sub>3</sub> (Nb:STO) substrates. Clean (001) surfaces were prepared as described in the Supplemental Material [15]. The results presented have been obtained consistently both for single crystals and thin films, and therefore reflect intrinsic properties of the anatase phase, independent of the sample preparation method. The thin film samples grown on Nb:STO yielded somewhat sharper spectral features, reflecting a better surface quality [15]. While oxygen defects are always present to some extent after the surface preparation, exposure to UV photons induces a much larger amount of vacancies, and provides a substantial electron doping [16]. Hence, we could tune the electron density over more than 2 orders of magnitude by varying the beam intensity and the oxygen partial pressure during the ARPES experiment, and explore samples with carrier densities in the 10<sup>18</sup>–10<sup>20</sup> cm<sup>-3</sup> range.

Figures 1(c) and 1(d) show two ARPES constant energy maps measured at the Fermi level in two perpendicular sections of momentum space, parallel (c) and perpendicular (d) to the (001) surface. The two planes completely define the three-dimensional (3D) Fermi surface (FS) of an ellipsoidal electron pocket, elongated in the  $k_z$  direction and centered at the  $\Gamma$  point, center of the 3D Brillouin zone (BZ) [Fig. 1(b)]. The data are in agreement with theoretical calculations for the bottom of the conduction band of anatase TiO<sub>2</sub> [17], and more importantly, they establish the existence of conduction electrons with a well-defined FS in electron-doped anatase. Note that the closed FS contour proves the 3D nature of the electronic dispersion, in contrast with the two-dimensional character of the metallic states observed at the surface of SrTiO<sub>3</sub> [18,19] and KTaO<sub>3</sub> [20].

The ARPES intensity map of Fig. 1(e) illustrates the energy-momentum dispersion of the conduction states for a sample with electron density  $n_e \sim 3.5 \times 10^{19}$  cm<sup>-3</sup>, as

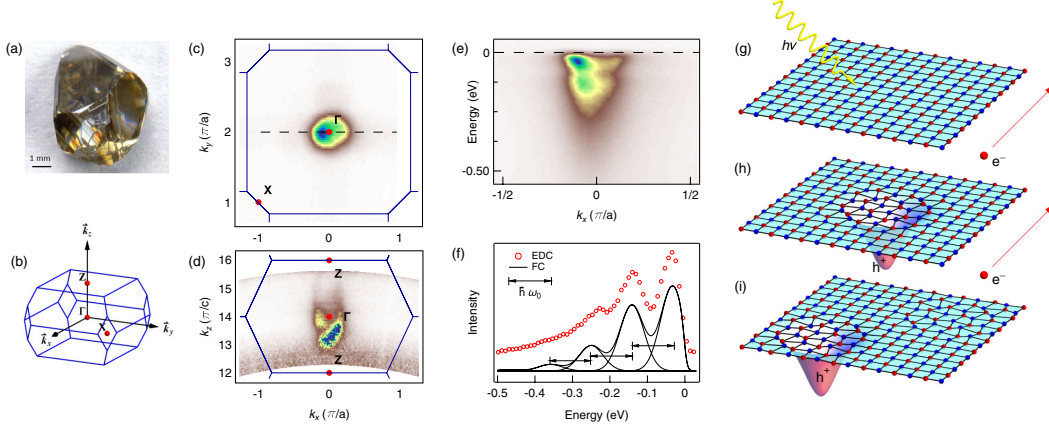


FIG. 1 (color online). (a) An as-grown anatase single crystal. (b) The BZ of anatase. (c),(d) constant energy maps at  $E_F$  ( $T = 20$  K,  $h\nu = 85$  eV) of electron-doped anatase (001) in the  $k_x k_y$  (c) and  $k_x k_z$  (d) planes, respectively. The blue lines outline the boundaries of the 3D BZs. (e)  $E$  vs  $k$  dispersion of the bottom of the conduction band for a sample with  $n_e \approx 3.5 \times 10^{19}$  cm<sup>-3</sup>. (f) ARPES intensity measured at  $k = k_F$  for a sample with  $n_e \approx 5 \times 10^{18}$  cm<sup>-3</sup>. The solid line is a Frank-Condon line shape. Voigt peaks of width  $\Delta E = 90$  meV (FWHM) are separated by 108 meV, while intensities follow a Poisson distribution. (g)–(i) Cartoon of the polaron formation induced by the photoemission process, showing the solid in its ground state (g) and two possible final states (h),(i) of ARPES.

determined from the volume of the electron pocket. It consists of a shallow QP band with the minimum at  $-40$  meV, which crosses the Fermi level  $E_F$  at  $k_F = \pm 0.12 \text{ \AA}^{-1}$ . Remarkably, the QP band is followed by a satellite with a similar dispersion at  $\sim 100$  meV higher binding energy, and by a broad tail. The satellite is more clearly resolved in samples with lower carrier densities, e.g., in the spectrum of panel (f) measured on a sample with  $n_e \sim 5 \times 10^{18}$  cm<sup>-3</sup>, where also a weaker replica is visible  $\sim 100$  meV below the first satellite.

The intensity distribution of Fig. 1(e) reveals the clearly dispersive nature of the states, but also a substantial renormalization of the spectral function, incompatible with a simple scenario of a metal with weakly interacting electrons. A parabolic fit yields an effective mass of  $m_{xy}^* = (0.7 \pm 0.05)m_e$ , where  $m_e$  is the bare electron mass. A comparison with  $m_{xy} = 0.42m_e$  from a band structure calculation [21], yields a mass renormalization ( $m_{xy}^*/m_{xy}$ )  $\sim 1.7$ . Indeed, at these carrier densities ( $n_e \sim 10^{18}$ – $10^{19}$  cm<sup>-3</sup>) the low energy states appear to fit in the intermediate regime of the so-called large polarons. The electron-phonon ( $e$ -ph) coupling induced by the ionic anatase lattice causes the QP dressing and the mass enhancement, but the polaron wave functions extend over several lattice constants. We stress here that, although similar claims are valid for the rutile phase of TiO<sub>2</sub> [22], the same ARPES experiment repeated on several (001) rutile surfaces failed to show any trace of a metallic edge, even after a long exposure to the photon beam.

The well-known Franck-Condon scenario for an electron coupled to a vibrational mode provides a schematic

but instructive guideline to interpret the data [23]. In the electron-removal spectrum, the main “zero phonon” peak is followed by a progression of vibronic satellites, separated by the phonon energy  $\hbar\omega_0$ , with peak intensities following the Poisson distribution [24]. A Franck-Condon line shape indeed provides a good qualitative description of the spectrum of Fig. 1(f) for a phonon energy of  $\hbar\omega_0 = 108$  meV, the energy of a longitudinal optical (LO)  $E_u$  phonon mode observed by Raman spectroscopy [25]. Within the photoemission literature, the series of distinct satellites is hardly observable, and the distinctive sign of a polaronic system is the characteristic “peak-dip-hump” spectrum [26–29]. Figures 1(g)–1(i) illustrate the physical picture underlying the polaron state as measured by ARPES. After absorbing a photon (g), the solid is left with a photohole coherently coupled to a phonon cloud, moving through the lattice in its ground state (h), or in one of its vibrational excited states (i). The case (h) corresponds to the QP band, while (i) corresponds to the satellite replica(s).

In order to get more quantitative information on the effect of  $e$ -ph coupling in this (unusual) regime, we consider, as appropriate for a polar material, a Fröhlich polaron model. It is characterized by the nonlocal interaction between the electron and a LO phonon branch [24]:

$$\hat{H}_{e\text{-ph}} = \frac{1}{\sqrt{V}} \sum_{\vec{k}, \vec{q}} \frac{M}{|q|} c_{\vec{k}+\vec{q}}^\dagger c_{\vec{k}} (b_{\vec{q}} + b_{-\vec{q}}^\dagger),$$

$$M^2 = \frac{4\pi\alpha\hbar(\hbar\omega_0)^{3/2}}{\sqrt{2m_b}}.$$

$c_{\vec{k}}^{\dagger}$  and  $b_{\vec{q}}^{\dagger}$  create, respectively, an electron with wave vector  $\vec{k}$  and a phonon with wave vector  $\vec{q}$ .  $m_b$  is the band mass of the uncoupled electron and the dimensionless constant  $\alpha$  defines the  $e$ -ph coupling strength. For sufficiently small dopings, a single-polaron approach is appropriate, since the effective polaron-polaron interaction is weak in this limit.

The ARPES spectrum is proportional, via dipole matrix elements, to the one-particle spectral function  $A(\vec{k}, E)$ . For a Fröhlich polaron it takes the form  $A(\vec{k}, E) = A_c^{(0)}(\vec{k}, E) + A_{\text{inc}}^{(l>0)}(\vec{k}, E)$ . The coherent QP spectrum  $A_c^{(0)}(\vec{k}, E)$  corresponds to transitions to an excited state where the lattice remains unperturbed. It follows the renormalized band dispersion  $E^{(0)}(\vec{k}) = \hbar^2 k^2 / 2m^* - \mu$ , where  $\mu$  is the chemical potential. The remaining  $l > 0$  contributions are the incoherent parts of the spectrum, and involve  $l$  phonon excitations in the final state. The leading  $l = 1$  term can be calculated analytically. It exhibits a logarithmic singularity at energy  $E^{(1)}(\vec{k}) = E^{(0)}(\vec{k}) - \hbar\omega_0$ , i.e., the same dispersion as the QP band, and increased broadening [15]. The  $l > 1$  terms yield a fairly homogeneous background in the energy ranges  $-\hbar\omega_0 - \mu < E < -\hbar\omega_0$ . Figure 2 compares the experimental spectra extracted from the intensity map of Fig. 1(e) with the calculated spectral function, including the  $l = 0$  and  $l = 1$  terms, with  $\hbar\omega_0 = 108$  meV. A Gaussian broadening (85 meV full width at half maximum—FWHM) was applied to the theory. It accounts for the coupling to low-energy phonons and other scattering mechanisms, and for the instrumental resolution (30 meV). The overall agreement between theory and experiment is very satisfactory, considering that the theory does not include the background tail of the  $l > 1$  terms.

The above calculation is too simple to provide an accurate estimation on the strength of the  $e$ -ph coupling. We can assess it more reliably analyzing the intensity distribution of the ARPES signal between the two branches. Quite generally, spectral weight is transferred from the QP band to the incoherent satellites as the  $e$ -ph coupling is increased. The coherent fraction  $Z(k_F)$  of the total spectral weight can be inferred from the experimental spectrum of

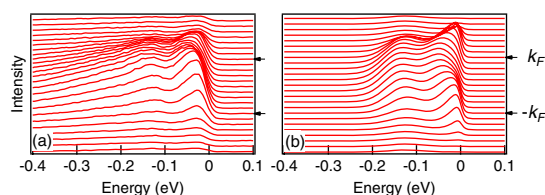


FIG. 2 (color online). (a) Spectra extracted from the intensity map of Fig. 1(e) in the range  $-0.25 < k_x < 0.25 \text{ \AA}^{-1}$ . (b) Spectral function  $A(k, E)$  for the Fröhlich polaron, including the QP term and the leading  $l = 1$  incoherent contribution, corresponding to the first phonon satellite.

Fig. 1(f), yielding  $Z(k_F) = 0.36$ . For this value, diagrammatic quantum Monte Carlo simulations of the electron addition spectrum deduce an  $e$ -ph coupling constant  $\alpha \approx 2$  [30], in a regime of intermediate coupling. Using as a starting point the experimentally observed mass renormalization factor of 1.7, the same numerical calculations predict  $\alpha \approx 2.5$ , in fairly good agreement and in the same coupling regime.

The size of the  $e$ -ph coupling also has an influence on the energy broadening of the photoemission signal. This is illustrated by the spectra in Fig. 3(a), measured between 20 K and 300 K on a sample with  $n_e \approx 5 \times 10^{18} \text{ cm}^{-3}$ . The spectral line shape exhibits a temperature dependence besides the trivial broadening of the Fermi cutoff. The intrinsic (Lorentzian) FWHM  $\Delta E_L$  of the QP peak, extracted from the spectra after removal of an experimental (Gaussian) broadening, is shown in Fig. 3(b).  $\Delta E_L$  exhibits an approximately linear  $T$  dependence above  $T = 150$  K, and saturates below  $T = 50$ –60 K to a value  $\sim 55$  meV, which includes contributions from impurity scattering and from the finite photoelectron lifetime. The data are well described by the Bloch-Grüneisen curve modeling resistivity in metals [31]. From its high temperature limit  $\Delta E_L = 2\pi\lambda k_B T$  one can extract the mass-enhancement parameter  $\lambda \approx 0.7$ , which again yields  $(m_{xy}^*/m_{xy}) = 1 + \lambda = 1.7$ . This  $\lambda$  accounts for the electron interaction with all the phonons, in particular with the low-energy acoustic modes, and should not be confused with  $\alpha$  introduced above, which embodies the coupling with the single LO mode at 108 meV.

We now turn to the doping dependence of the spectra. During the ARPES measurement, oxygen vacancies are

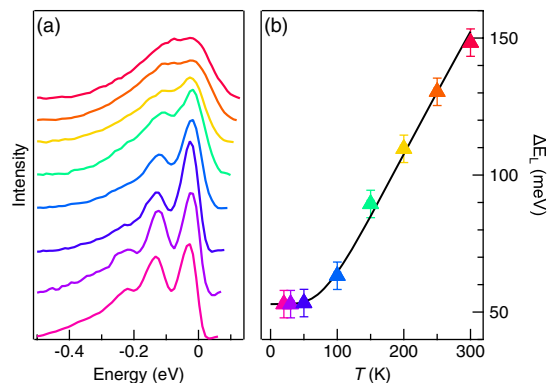


FIG. 3 (color online). (a) Spectra measured between  $T = 20$  K and  $T = 300$  K on a sample with  $n_e \approx 5 \times 10^{18} \text{ cm}^{-3}$ , showing a progressive broadening with increasing temperature. The signal extracted from the shallow electron pocket was integrated over a momentum range of  $-k_F < k_x < k_F$ . (b) Temperature-dependent intrinsic QP line width. Colors of the symbols correspond to those of the spectra in (a). The line is a Bloch-Grüneisen curve.

created by the photon beam in a thin layer below the surface. If the sample is at the same time exposed to a small O<sub>2</sub> partial pressure, a competing reoxidation process takes place. A dynamic equilibrium is reached, which depends on the photon flux at the sample. This offers a unique opportunity to study the electronic states of anatase at various electron densities, without changing *ex situ* the stoichiometry or adding extrinsic impurities. In the following experiment, we kept the photon flux on the sample constant, and varied the oxygen pressure between  $2 \times 10^{-10}$  and  $5 \times 10^{-8}$  mbar. The corresponding electron densities, estimated from the volume of the electron pocket at the bottom of the CB, varied between  $\sim 5 \times 10^{20} \text{ cm}^{-3}$  and  $10^{18} \text{ cm}^{-3}$ , respectively. At constant oxygen pressure, data could be collected for several hours without appreciable changes.

Figure 4 shows spectra of the CB for various doping levels. Panel (a) for  $n_e = 5 \times 10^{18} \text{ cm}^{-3}$  shows a very shallow electron pocket and well-defined satellites. At  $T = 20 \text{ K}$ , the momentum width  $\Delta k$  of the ARPES spectral function at  $k_F$  gives a QP coherence length  $l = 1/\Delta k = 7 \text{ \AA}$ . Therefore, in this low-density limit the polaronic QPs cannot move freely for more than  $\sim 2$  unit cells. Increasing

the carrier density to  $n_e = 3 \times 10^{19} \text{ cm}^{-3}$  in (b) and to  $n_e = 1 \times 10^{20} \text{ cm}^{-3}$  in (c), one observes that (i) the QP band dispersion deviates from a parabola, and (ii) near the bottom of the band, the QP intensity is reduced and the satellite spreads into the background. At  $n_e = 3.5 \times 10^{20} \text{ cm}^{-3}$  the QP band is visible only near the Fermi level crossings at  $\pm k_F$ . For smaller wave vectors, the QP intensity is strongly suppressed, with most of the spectral weight spread over a broad energy range (the ‘‘hump’’).

The dispersion seen in Figs. 4(d1) and (d2) in the vicinity of  $E = \hbar\omega_0$  is reminiscent of the characteristic kink structure encountered in several Fermi liquids with more moderate *e*-ph coupling. The evolution of the CB states with doping indeed suggests a breakdown of the single-polaron picture, as charges added to the CB progressively screen the *e*-ph interaction. Polarons, which are well-defined QPs at low density, eventually lose coherence and dissociate into an electron liquid coupled to the phonon(s). The spectral weight distribution for high dopings can be reproduced by standard perturbation theory [24] (Supplemental Material [15]).

Our observations shed light on the conduction mechanisms taking place in anatase-based devices, and in particular on the role of the *e*-ph coupling, which has been shown to represent the dominant scattering process at typical operating temperatures in pristine and doped films [9]. The tunability of the doping level by UV (or *e*-beam) illumination over a very broad range is attractive for numerous applications, and in particular in the field of transparent conductors. Carrier densities  $>10^{20} \text{ cm}^{-3}$ , necessary for thin film operation, can be reached without extrinsic metal dopants, which are additional scattering centers [10]. Moreover, the possibility of after-growth patterning of conductive paths could yield important practical advantages. Namely, the initial growth conditions could be set independently of the required final conductivity, and etching processes often involved in oxide structuring could potentially be avoided.

Finally, the present study is likewise relevant for anatase-based devices employing nanostructured materials, where the overall transport properties depend on inter- as well as intraparticle processes. The crossover from a polaronic to a diffusive regime is expected to occur when the overlap between the polaron clouds becomes significant. The ARPES data of Fig. 4 suggest that this happens around  $n_e^* \approx 10^{19} \text{ cm}^{-3}$ . Estimating the polaron radius  $r_p$  from the average separation between polarons  $d \sim n^{-1/3} = 2r_p$ , gives  $r_p \sim 20 \text{ \AA}$ . By comparison, Fröhlich’s model in the intermediate coupling regime yields  $r_p = \sqrt{\hbar/2m^*\omega_0} \approx 10 \text{ \AA}$ . Both values are much smaller than the typical dimensions (few nm) of anatase nanoparticles considered for applications. Therefore, the polaronic nature of the QPs and their evolution upon electron doping must necessarily be taken into account when modeling transport in actual devices.

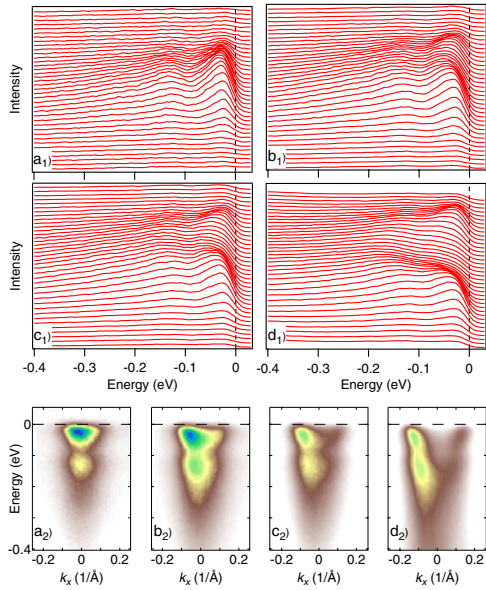


FIG. 4 (color online). Evolution of the CB states with doping. The ARPES spectra ( $\hbar\nu = 85 \text{ eV}$ ) were measured at  $T = 20 \text{ K}$  along the dashed line ( $k_y = 2\pi/a$ ) of Fig. 1(c) for samples with  $n_e = 5 \times 10^{18} \text{ cm}^{-3}$  (a1),  $n_e = 3 \times 10^{19} \text{ cm}^{-3}$  (b1),  $n_e = 1 \times 10^{20} \text{ cm}^{-3}$  (c1), and  $n_e = 3.5 \times 10^{20} \text{ cm}^{-3}$  (d1). The same data are also presented as  $E$  vs  $k_x$  image plots in the bottom panels (a2)–(d2). A doping scan with finer steps is presented as a movie with the Supplemental Material [15].



We acknowledge support by the Swiss NSF, namely through Grant No. PA00P2-136420 (L.M.). We thank N. Mannella, A. Petrozza, C. Tournier-Colletta, and A. Crepaldi for discussions. The Advanced Light Source is supported by the Director, Office of Science, Office of Basic Energy Sciences, of the U.S. Department of Energy under Contract No. DE-AC02-05CH11231. S.M., L.M., and J.J. contributed equally to this work.

- [1] R. Asahi, T. Morikawa, T. Ohwaki, K. Aoki, and Y. Taga, *Science* **293**, 269 (2001).
- [2] Y. He, A. Tilocca, O. Dulub, A. Selloni, and U. Diebold, *Nat. Mater.* **8**, 585 (2009).
- [3] A. Fujishima and K. Honda, *Nature (London)* **238**, 37 (1972).
- [4] D.B. Strukov, G.S. Snider, D.R. Stewart, and R.S. Williams, *Nature (London)* **459**, 1154 (2009).
- [5] H. Toyosaki, T. Fukumura, Y. Yamada, K. Nakajima, T. Chikyow, T. Hasegawa, H. Koinuma, and M. Kawasaki, *Nat. Mater.* **3**, 221 (2004).
- [6] B. O'Regan and M. Grätzel, *Nature (London)* **353**, 737 (1991).
- [7] D. Kuang, J. Brilliet, P. Chen, M. Takata, S. Uchida, H. Miura, K. Sumioka, S.M. Zakeeruddin, and M. Grätzel, *ACS Nano* **2**, 1113 (2008).
- [8] O.K. Varghese, M. Paulose, and C.A. Grimes, *Nat. Nanotechnol.* **4**, 592 (2009).
- [9] Y. Furubayashi, T. Hitosugi, Y. Yamamoto, K. Inaba, G. Kinoda, Y. Hirose, T. Shimada, and T. Hasegawa, *Appl. Phys. Lett.* **86**, 252101 (2005).
- [10] R.G. Gordon, *MRS Bull.* **25**, 52 (2000).
- [11] H. Tang, H. Berger, P.E. Schmid, F. Lévy, and G. Burri, *Solid State Commun.* **87**, 847 (1993).
- [12] L. Forró, O. Chauvet, D. Emin, L. Zuppiroli, H. Berger, and F. Lévy, *J. Appl. Phys.* **75**, 633 (1994).
- [13] A. Kitada, S. Kasahara, T. Terashima, K. Yoshimura, Y. Kobayashi, and H. Kageyama, *Appl. Phys. Express* **4**, 035801 (2011).
- [14] J. Jačimović, C. Vaju, A. Magrez, H. Berger, L. Forró, R. Gaál, V. Cerovski, and R. Žikić, *Europhys. Lett.* **99**, 57005 (2012).
- [15] See Supplemental Material at <http://link.aps.org/supplemental/10.1103/PhysRevLett.110.196403> for experimental details, complementary ARPES data including a movie of the doping dependence, and a detailed description of the theoretical model.
- [16] A. Locatelli, T. Pabisiak, A. Pavloska, T.O. Mendes, L. Aballe, A. Kiejna, and E. Bauer, *J. Phys. Condens. Matter* **19**, 082202 (2007).
- [17] L. Chiodo, J.M. García-Lastra, A. Iacomino, S. Ossicini, J. Zhao, H. Petek, and A. Rubio, *Phys. Rev. B* **82**, 045207 (2010).
- [18] A.F. Santander-Syro, O. Copie, T. Kondo, F. Fortuna, S. Pailhès, R. Weht, X.G. Qiu, F. Bertran, A. Nicolaou, A. Taleb-Ibrahimi, P. Le Fèvre, G. Herranz, M. Bibes, N. Reyren, Y. Apertet, P. Lecoeur, A. Barthélémy, and M.J. Rozenberg, *Nature (London)* **469**, 189 (2011).
- [19] W. Meevasana, P.D.C. King, R.H. He, S.-K. Mo, M. Hashimoto, A. Tamai, P. Songsiriritthigul, F. Baumberger, and Z.X. Shen, *Nat. Mater.* **10**, 114 (2011).
- [20] P.D.C. King, R.H. He, T. Eknapakul, P. Buaphet, S.-K. Mo, Y. Kaneko, S. Harashima, Y. Hikita, M.S. Bahrany, C. Bell, Z. Hussain, Y. Tokura, Z.-X. Shen, H. Y. Hwang, F. Baumberger, and W. Meevasana, *Phys. Rev. Lett.* **108**, 117602 (2012).
- [21] T. Hitosugi, H. Kamisaka, K. Yamashita, H. Nogawa, Y. Furubayashi, S. Nakao, N. Yamada, A. Chikamatsu, H. Kumigashira, M. Oshima, Y. Hirose, T. Shimada, and T. Hasegawa, *Appl. Phys. Express* **1**, 111203 (2008).
- [22] E. Hendry, F. Wang, J. Shan, T.F. Heinz, and M. Bonn, *Phys. Rev. B* **69**, 081101 (2004).
- [23] G.A. Sawatzky, *Nature (London)* **342**, 480 (1989).
- [24] G.D. Mahan, *Many-Particle Physics* (Plenum, New York, 1993), 2nd ed.
- [25] R.J. Gonzalez, R. Zallen, and H. Berger, *Phys. Rev. B* **55**, 7014 (1997).
- [26] K.M. Shen, F. Ronning, D.H. Lu, W.S. Lee, N.J.C. Ingle, W. Meevasana, F. Baumberger, A. Damascelli, N.P. Armitage, L.L. Miller, Y. Kohsaka, M. Azuma, M. Takano, H. Takagi, and Z.X. Shen, *Phys. Rev. Lett.* **93**, 267002 (2004).
- [27] N. Mannella, W.L. Yang, X.J. Zhou, H. Zheng, J.F. Mitchell, J. Zaanen, T.P. Devereaux, N. Nagaosa, Z. Hussain, and Z.X. Shen, *Nature (London)* **438**, 474 (2005).
- [28] F. Massee, S. de Jong, Y. Huang, W.K. Siu, I. Santoso, A. Mans, A.T. Boothroyd, D. Prabhakaran, R. Follath, A. Varykhalov, L. Patthey, M. Shi, J.B. Goedkoop, and M.S. Golden, *Nat. Phys.* **7**, 978 (2011).
- [29] W.S. Lee, S. Johnston, B. Moritz, J. Lee, M. Yi, K.J. Zhou, T. Schmitt, L. Patthey, V. Strocov, K. Kudo, Y. Koike, J. van den Brink, T.P. Devereaux, and Z.X. Shen, *arXiv:1301.4267*.
- [30] A.S. Mishchenko, N.V. Prokof'ev, A. Sakamoto, and B.V. Svistunov, *Phys. Rev. B* **62**, 6317 (2000).
- [31] P.B. Allen and N. Chetty, *Phys. Rev. B* **50**, 14855 (1994).

### 3.6 $k$ -space mapping in anatase

The ARPES data of Fig. 3.5 give a more detailed overview of the band structure of anatase. Panel 3.5 (a) is a constant energy (CE) map measured at the Fermi level at  $T = 20$  K with photon energy  $h\nu = 85$  eV. Blue lines are projections of the three-dimensional (3D) Brillouin zone (BZ) onto the (001) surface. The partially resolved circular contours at the centers of the projected BZs correspond to a small electron pocket at the bottom of the conduction band. Changes in the perpendicular wave vector  $k_z$  across the CE map (see Sec. 3.6.1), as well as ARPES matrix elements, explain their unequal intensities in different BZs, *e.g.* the very low intensity around (0, 0). Suppression of emission in the  $k_y = 0$  plane is consistent with the odd parity of the  $d_{xy}$  states that are believed to form the bottom of the conduction band [78, 91] and with our experimental geometry, where the light is  $\pi$ -polarized with respect to the scattering plane. This point will be discussed in more detail in Sec. 3.6.3. Weaker ( $4 \times 1$ ) replicas of the main contours along both  $k_x$  and  $k_y$  reflect a known surface reconstruction [87, 88] and two equivalent domains.

The  $k_x k_z$  CE contour of Fig. 3.5 (b) taken at the Fermi level for  $k_y = 2\pi/a$  (red dashed line in (a)) completely determines the shape, size and position of the electron pocket in  $k$ -space. It is an ellipsoid elongated in the  $c$  direction and centered at the  $\Gamma$  point, the center of the 3D BZ, in agreement with band structure calculations [92–94]. From its volume we determine a carrier density of  $n_e \simeq 2 \times 10^{20}$  cm<sup>-3</sup> for the sample in Fig. 3.5. The top of the valence band (VB) is visible at the  $X$  point of the  $E = -3.3$  eV CE map in panel 3.5 (c), consistent with the theoretical prediction that TiO<sub>2</sub> is an indirect semiconductor [78, 95], and with recent ARPES data [96].

#### 3.6.1 $k_y k_x$ CE-maps

ARPES measurements taken at fixed photon energy  $h\nu$ , as in Fig. 3.5 (a), sample the reciprocal space on the surface of a sphere of radius  $k = 2m/\hbar^2 \sqrt{h\nu - \Phi + V_0}$ , where  $\Phi$  is the work function of the electron analyzer and  $V_0$  is the inner potential of the electrons in the solid. In the center of the second BZ  $(k_x, k_y) = (0, 2\pi/a)$ , this gives a  $k_z$  mismatch of about 1/4th of the unit cell extension  $4\pi/c$ , and at  $(0, 4\pi/a)$ , center of the third BZ, of a whole unit cell. Therefore, care has to be taken when labeling the high symmetry points in a constant energy (CE) cut, especially for large  $k_{||}$  values. In order to illustrate this point, Fig. 3.6 (a-d) show CE maps at four different photon energies. Panels 3.6 (e) and (f) show the  $k_x = -2\pi/a$  and  $k_x = 0$  planes of the reciprocal space, respectively. The curved lines represent the intersections of such planes with the spheres sampled by the energies used in (a-d) for an inner potential  $V_0 = 13$  eV and  $\Phi = 4$  eV.

By matching panels 3.6 (a-d) with panels 3.6 (e) and (f), the metallic state can be located at the  $\Gamma$  points of the BZs. In panel 3.6 (a), the intensity *e.g.* is maximal at  $(0, 2\pi/a)$  and  $(-2\pi/a, 4\pi/a)$ . Here, the measurement sphere cuts the 3D BZ almost exactly at  $\Gamma$ . By contrast, the intensity is weaker at  $(-2\pi/a, 2\pi/a)$  or  $(0, 4\pi/a)$ , where the cut falls between  $\Gamma$  and  $Z$ . Note that since the elongation of the electron pocket along  $k_z$  is comparable to  $c^* = 2\pi/c$  there is always some intensity at  $(k_x, k_y)$  points corresponding to surface projections of the  $\Gamma/Z$  points of the bulk

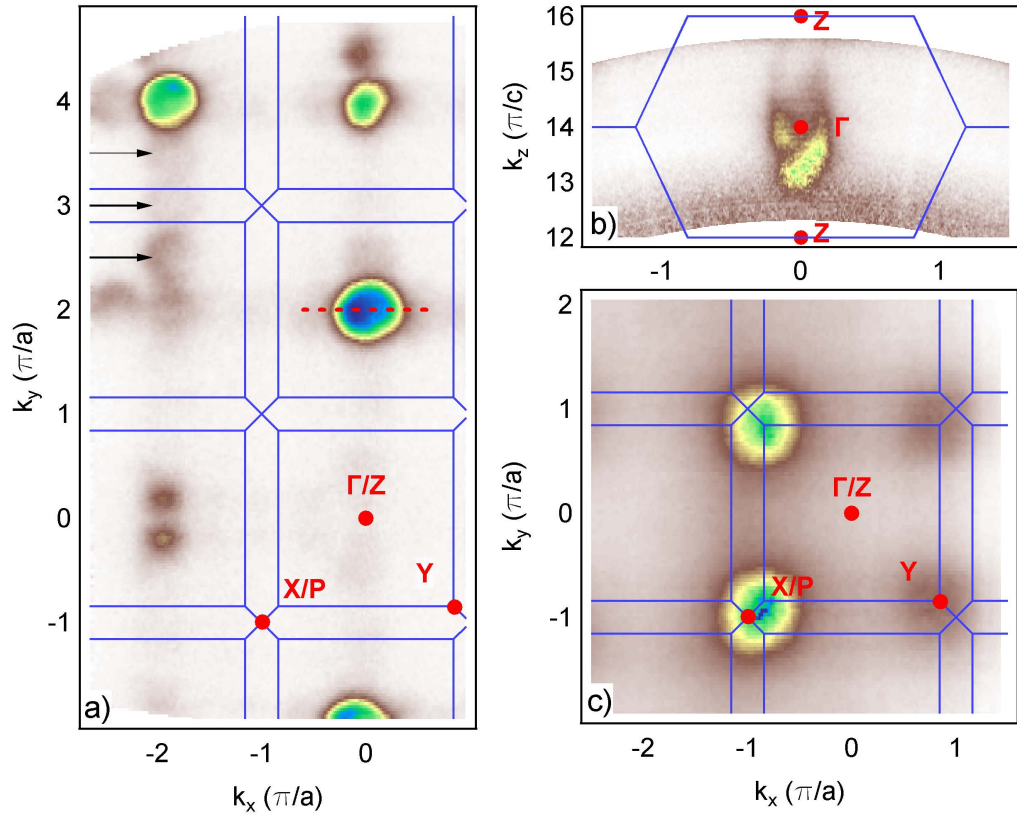


Figure 3.5: **(a)** Fermi surface in the  $k_x k_y$  plane ( $T = 20$  K,  $h\nu = 85$  eV) of oxygen-vacant anatase (001) with  $n_e \simeq 2 \times 10^{20}$  cm $^{-3}$ . Blue dashed lines indicate projections of the 3D BZs. Electron pockets are seen most intense at  $(0, \pm 2\pi/a)$  and  $(-2\pi/a, 4\pi/a)$ , which correspond to  $\Gamma$ -points at this photon energy. Black arrows indicate ARPES signatures of the  $(4 \times 1)$  surface reconstruction. **(b)**  $k_x k_z$  Fermi surface extracted from a photon energy scan for  $k_y = 2\pi/a$  (red dashed line in (a)). The point  $\Gamma = (0, 2\pi/a, 14\pi/c)$  is probed at  $h\nu = 85$  eV. **(c)** CE map ( $h\nu = 128$  eV) at  $E = -3.3$  eV, showing the highest intensity at the  $X$ -points  $(\pm\pi/a, \pm\pi/a, 18\pi/c)$ , the top of the VB.

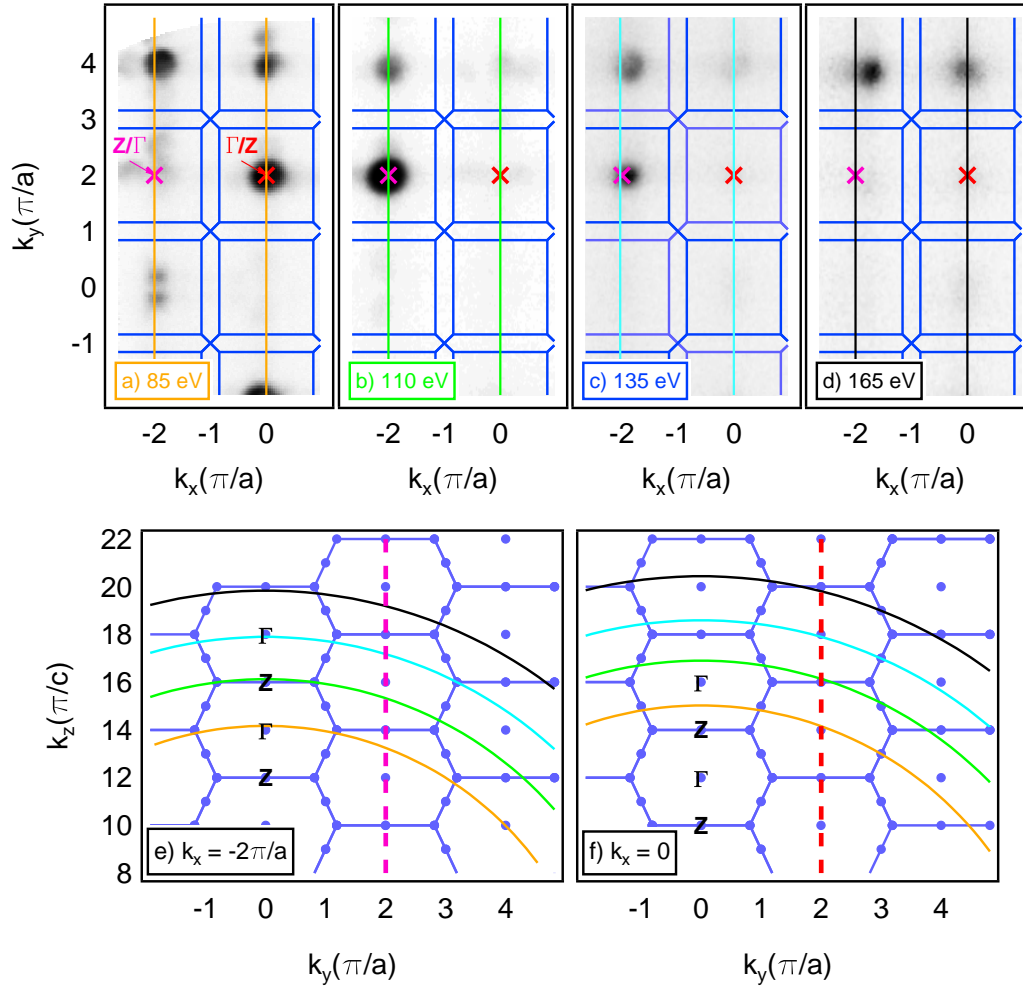


Figure 3.6: **(a-d)**  $k_y k_x$  CE-maps at the Fermi level measured at 85, 110, 135 and 165 eV photon energy. Blue dashed lines indicate the bulk BZ projection. Colored vertical lines mark cuts along which the BZ trajectory is studied. **(e)** Study of the BZ trajectory at  $k_x = -2\pi/a$ . The arcs trace the trajectory through the three dimensional BZ. Their colors correspond to the photon energies in the top panels. **(f)** Study of the BZ trajectory at  $k_x = 0$ . The pink and red vertical lines mark the intersection with the  $k_y = 2\pi/a$  plane. The intersections between each arc and such a plane are indicated as crosses in the top panels.



BZ. An exception is  $(k_x, k_y) = (0, 0)$ , the center of the first BZ, where the intensity is almost completely suppressed by matrix elements because of the  $d_{xy}$  symmetry of the conduction band, as discussed in detail in Sec. 3.6.3.

### 3.6.2 $k_x k_z$ CE-maps

The  $k_x k_z$  CE-map in Fig. 3.5 (b) is built from a series of ARPES images taken at different photon energies. The energies are chosen in such a way as to maintain a constant stepsize  $\Delta k_z = \frac{\partial k_z}{\partial h\nu} \Delta h\nu$ , where  $k_z = \frac{1}{\hbar} \sqrt{2m(E_{kin} \cos^2(\theta) + V_0)}$  and  $E_{kin} = h\nu - \Phi - |E_b|$  with the binding energy  $|E_b|$ . Since  $k_{||} = \frac{1}{\hbar} \sqrt{2mE_{kin}} \sin \theta$  also is a function of  $h\nu$ , the probing angle  $\theta$  has to be adjusted for every photon energy. The inner potential is determined in a self consistent way: starting from a best guess,  $V_0$  is adjusted until the ARPES signal follows the periodicity imposed by the value of  $c^*$ . For anatase  $\text{TiO}_2$  we extract  $V_0 \sim 13$  eV, similar to the value reported by Emori *et al.* [96]

### 3.6.3 Matrixelements in anatase $\text{TiO}_2$

In doped anatase  $\text{TiO}_2$ , the lowest energy state probed by ARPES are conduction band carriers populating the otherwise empty  $3d$  bands. Given the small tetrahedral crystal field and negligible spin orbit interaction of the  $d$ -electrons, the lowest energy band populated by electrons is formed by  $3d_{xy}$  orbitals. The photoemission signal building the spectral weight consequently results from an emitting orbital of  $d_{xy}$  symmetry. The local part of the initial state hence can be approximated as

$$|d_{xy}\rangle = \frac{1}{i\sqrt{2}}(|2, 2\rangle - |2, -2\rangle). \quad (3.1)$$

According to Eq. 1.45 the matrix element so becomes

$$\begin{aligned} M^{d_{xy}}(\mathbf{k}_f, \theta, \phi, \beta) &\propto \frac{1}{i\sqrt{2}} \sum_{m'=-2}^2 \left( D_{m',2}^2(\theta, \phi, \beta) M^{2m'}(\mathbf{k}_f) - D_{m',-2}^2(\theta, \phi, \beta) M^{2m'}(\mathbf{k}_f) \right) \\ &= \frac{1}{i\sqrt{2}} \sum_{m'=-2}^2 M^{2m'}(\mathbf{k}_f) \left( D_{m',2}^2(\theta, \phi, \beta) - D_{m',-2}^2(\theta, \phi, \beta) \right) \end{aligned} \quad (3.2)$$

To simulate the spectral function of the electron pocket, we use a tight binding dispersion

$\varepsilon_{\mathbf{k}} = -8 \cos(ak_x/2) \cos(ak_y/2) \cos(ak_z/2) + \mu$  eV adapted to the periodicity to the *bct2* lattice of anatase where  $\mu = 7.7$  eV is the chemical potential. We further approximate the spectral function of Eq. 1.13 by a Gaussian

$$A(\mathbf{k}, E) \propto \frac{1}{\sqrt{2\pi}\sigma} e^{-\frac{(E-\varepsilon_{\mathbf{k}})^2}{2\sigma^2}} \quad (3.3)$$

with broadening  $\sigma \sim 0.5$  eV.<sup>2</sup>

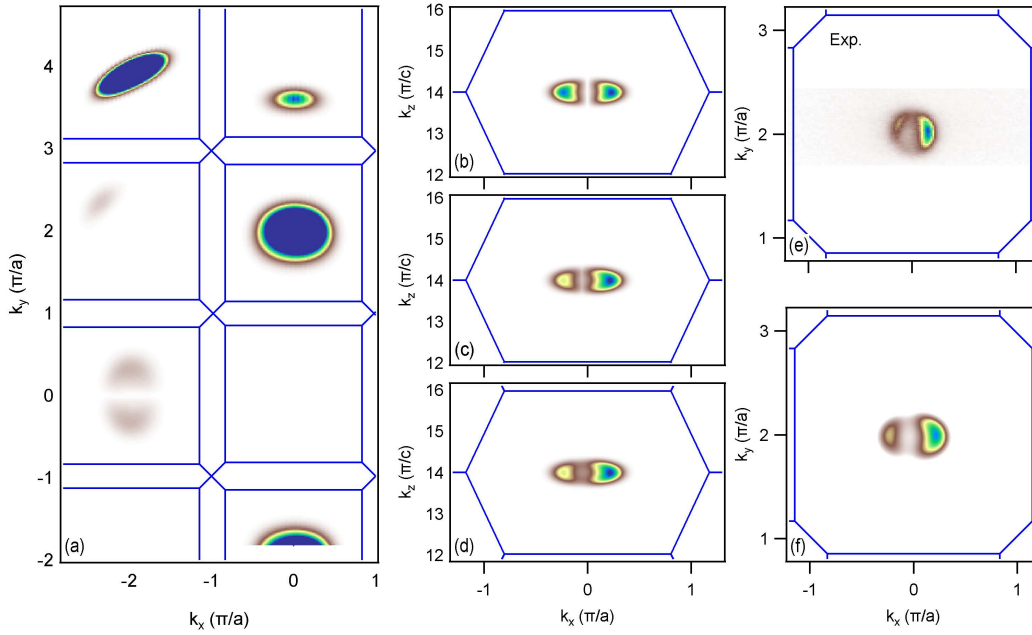


Figure 3.7: Simulated ARPES constant energy maps calculated for 85 eV photon energy and taking into account matrix elements. Blue lines indicate projections of the 3D BZs. **(a)** Simulated  $k_x k_y$  map directly comparable to Fig. 3.5 (a). **(b-d)** Simulated  $k_x k_z$  maps calculated with **(b)**  $\theta = 0^\circ$ ,  $\lambda = 0$ , **(c)**  $\theta = 0.5^\circ$  and  $\lambda = 0$  and **(d)**  $\theta = 0.5^\circ$ ,  $\lambda = 200$  nm. **(e)** Close up measurement of the electron pocket at  $(k_x, k_y) = (0, 2\pi/a)$  compared to the simulation **(f)** with  $\theta = 0.5^\circ$  and  $\lambda = 200$  nm.

Calculation results of the matrix element effect for the  $d_{xy}$  conduction state are shown in Fig. 3.7. Panel 3.7 (a) gives a simulated Fermi surface calculated for 85 eV photon energy, which can be directly compared to the experimental result of Fig. 3.5 (a).

The suppression of spectral weight at normal emission and along  $k_y = 0$  is reproduced. In the BZs

<sup>2</sup>The Gaussian takes into account the experimental broadening and the intrinsic lineshape. For the illustration of the matrix element effect,  $\sigma$  and the doping level of the model dispersion were arbitrarily to reproduce somewhat shape and side of the experimental electron pocket.

centered at  $(-2\pi/a, 2\pi/a)$  and  $(0, 4\pi/a)$ , we find residual spectral weight, similar to the measurement. In contrast to the elliptical Fermisurface of anatase, our simple isotropic band  $\varepsilon_{\mathbf{k}}$  yields a spherical Fermi surface. The ARPES probing sphere with radius  $k = 2m/\hbar^2\sqrt{h\nu - \Phi + V_0}$  consequently cuts the pockets in a different way. This leads to an unrealistic distortion of signal. The effect could be simply compensated by taking into account the significantly higher bandmass  $m_z^* \sim 1.7m_{xy}^*$ , which elongates the pockets along  $k_z$  and by fine tuning of  $\sigma$  and the chemical potential  $\mu$ . However this would over stress the predictive capabilities of this simple model.

3.7 (b-d) show simulated  $k_x k_z$  Fermi surfaces that should be compared to Fig. 3.5 (b). The result calculated for  $\theta = 0$  (b) is symmetric with respect to  $k_x = 0$ , which is at variance with the experimental result. Panel 3.7 (c) takes into account some slight misalignment of  $\theta = 0.5^\circ$ , which produces the asymmetry. Overall, the suppression of spectral weight however is overestimated by the calculation. We therefore take into account a finite mean free path of the electrons  $\lambda = 200$  nm in panel 3.7 (d), which reduces the suppression along  $k_x = 0$ . This value of  $\lambda$  is unrealistic high, a clear deficit of the model which assumes a simple evanescent wave inside the bulk.

A close up of the electron pocket of the BZ centered at  $(0, 2\pi/a)$  measured with  $\theta \sim 0$  is shown in panel 3.7 (e). Again, the intensity distribution can be well reproduced taking into account a small misalignment of  $\theta = 0.5^\circ$  and a finite  $\lambda = 200$  nm in panel 3.7 (f).

### 3.7 Oxygen vacancy formation

In the last chapters, we have shown that oxygen vacancies in anatase  $\text{TiO}_2$  can be created in the intense x-ray beam spot of synchrotron radiation. The underlying mechanism has been studied by Knotek and Feibelman in the late 1970ies [97]: ionizing radiation with energies beyond the Ti M-edge threshold can create Ti  $3p$  core holes. One possible subsequent electron decay channel involves an LVV Auger decay with one valence electron refilling the  $3p$  shell and another one leaving the solid. Due to the large oxygen character of the valence band, this process locally removes two O  $2p$  electrons and thus leads to the formation of unbound  $\text{O}^0$  species. These are not affected by the Coulomb potential of the Ti ions anymore and can desorb before the valence states are refilled. Locally, this leaves titanium in a  $\text{Ti}^{3+}$  state, with a gain of one  $3d$  electron. Unlike in rutile, this excess charge has a strong tendency to delocalize in anatase.

Fig. 3.8 (a) shows a study of the oxygen vacancy formation process while exposing an anatase thin film to 85 eV X-rays in ultra high vacuum  $< 10^{-10}$  mbar. The photon flux was  $\sim 10^{12}$  photons/s focused onto a spot size of  $\sim 100 \mu\text{m} \times 50 \mu\text{m}$ . The photoemission signal is integrated over  $E$ - $k$ -windows of  $E = [-0.6; 0.1] \text{ eV} \times k = [-0.5; 0.5] \text{ \AA}^{-1}$  for the metallic state. Similarly, we integrate over an interval of  $E = [-1.5; -0.6] \text{ eV} \times k = [-1; 1] \text{ \AA}^{-1}$  to monitor a prominent oxygen vacancy in gap state at  $E \sim -1.5 \text{ eV}$  discussed in detail in Sec. 3.8.

At  $t = 0$ , the anatase crystal is nearly stoichiometric. We observe no signal at the Fermi level. With time however, more and more oxygen vacancies are created by the UV radiation. The

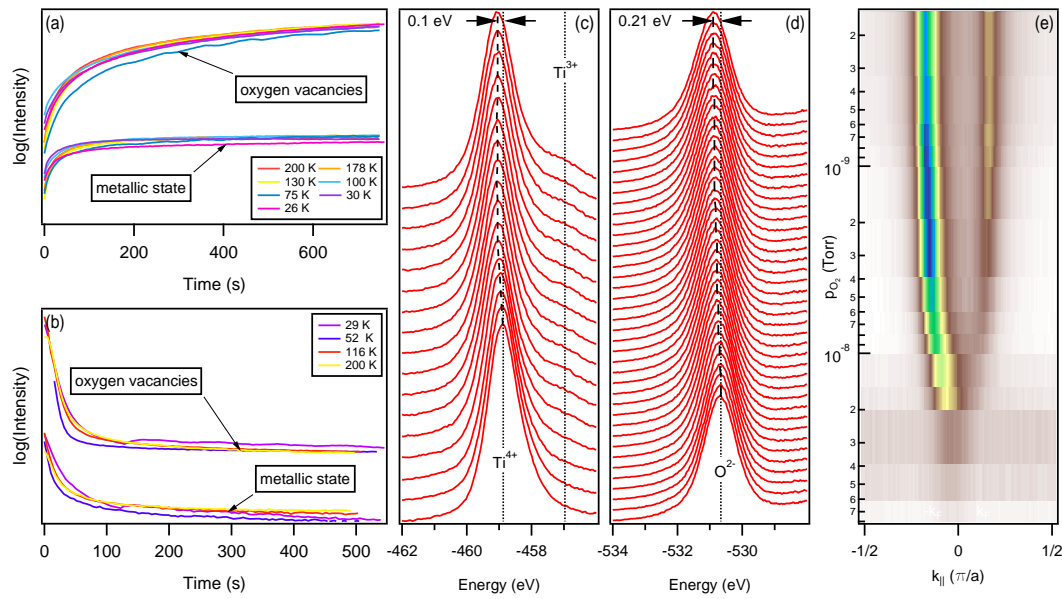


Figure 3.8: **(a)** Time and temperature dependent study of the oxygen vacancy formation in anatase during 85 eV x-ray irradiation. After about 100 s the metallic state saturates while oxygen vacancy formation continues. The effect does not depend on temperature. **(b)** Study of the reverse process. After about 100 s, metallic state and oxygen vacancy signal only diminish slightly due to further re-oxidation of deeper  $\text{TiO}_2$  layers. **(c)** Evolution of the Ti 2p core level peak and **(d)** the O 1s core level peak as a function of oxygen partial pressure. **(e)** Evolution of the Fermi surface as a function of oxygen partial pressure.

additional electrons provided by oxygen vacancies populate the bottom of the conduction band and the signal of the metallic state increases. The increasing amount of conduction band electrons opens up additional LCC Auger channels involving conduction band electrons. With the LVV channel becoming less and less important, oxygen vacancy formation eventually slows down after about 100 s.

While the number of vacancies continues to increase, the signal of the metallic channel saturates and no further population of the conduction band takes place. Presumably, this is due to oxygen vacancy clustering which prevents further delocalization of the doped in charge carriers. The negligible dependence of this effect on temperature shows that  $T = 200$  K is well below the threshold that drives oxygen vacancy diffusion processes in anatase. This is consistent with recent experiments on anatase (101) surfaces by Scheiber *et. al.* [98].

Fig. 3.8 (b) shows a study of the reverse process. Here, the time dependence of a fully saturated metallic state is monitored with a constant oxygen pressure. The oxygen is replenishing the O-vacancy sites which therefore competes with the effect of radiation. The major drop of metallic state and oxygen vacancy state occurs during the first 100 s, indicating surface and subsurface re-oxidation. The ongoing lowering of signal after 100 s may result from re-oxidation of deeper  $\text{TiO}_2$  layers. Again, the effect is not temperature dependent up to 200 K.

Fig. 3.8 (c) shows the effect of increasing oxygen vacancy concentration on the Ti  $2p$  XPS core level peak. Whereas at low concentration, we only identify the signature of  $\text{Ti}^{4+}$  species, a distinct shoulder of  $\text{Ti}^{3+}$  origin develops on its low binding energy side. Besides, the  $\text{Ti}^{4+}$  feature shifts about 100 meV higher in binding energy. Fig. 3.8 (d) shows a similar spectrum of the O  $1s$  XPS core level peak. Whereas we solely identify the signature of  $\text{O}^{2-}$  species, the shift of about 210 meV towards higher binding energies is clearly more pronounced.

The shift in the core level spectra is given by  $\Delta E_B = \Delta\mu + K\Delta Q + \Delta V_M + \Delta\varepsilon_s$ , where  $\Delta Q$  is the change in the number of doped in electrons [12].  $\Delta\mu$  is the associated chemical potential shift,  $K$  describes the Coulomb interaction between core-hole and valence electrons,  $\Delta V_M$  is the change in the Madelung potential and  $\Delta\varepsilon_s$  describes the screening of the core hole potential.

Both  $\text{Ti}^{4+}$  and  $\text{O}^{2-}$  core level peaks shifts towards higher binding energies  $E_B$ . Thus we can assume the Madelung potential  $V_M$  to have no significant effect on  $E_B$ . The increase in the number of the conduction electrons  $\Delta Q$ , scaling with the concentration of  $\text{Ti}^{3+}$  defect sites, is typically on the order of  $\sim 1\%$  and therefore negligible (see Sec. 3.11). We are thus left with  $\Delta E_B \sim \Delta\mu + \Delta\varepsilon_s$ . Since the doped in  $3d$  carriers are primarily located at Ti sites, screening of Ti  $2p$  core holes will be more efficient than screening of O  $1s$  holes, consequently involving a smaller shift. The O  $1s$  core level shift thus gives an estimate of the chemical potential achievable by oxygen vacancy doping  $\mu \sim 210$  meV. Subtracting the shift of Ti  $2p$  yields an estimate for the screening  $\Delta\varepsilon_s \sim (210 - 100)$  meV = 110 meV. Both values are in reasonable agreement with independent estimates in Sec. 3.10.5 ( $\Delta\mu \sim 185$  meV,  $\varepsilon_s \sim 100$  meV), indicating weak screening of O  $1s$  core holes  $\sim \mathcal{O}(10$  meV).

Fig. 3.8 (e) demonstrates how the regulation of oxygen partial pressure vs photon flux can be exploited to achieve a fine regulation of the Fermi surface volume and therefore of the charge carrier concentration. A momentum distribution curve (MDC) cutting the electron pocket centered at  $(0, 2) \pi/a$  along the red dashed line in Fig. 3.5 is plotted as a function of the oxygen partial applied to the sample. Clearly, oxygen dosing allows for a fine tuning of the metallicity of anatase from insulating ( $\sim 10^{17} \text{ cm}^{-3}$ ) to metallic ( $\sim 10^{20} \text{ cm}^{-3}$ ).

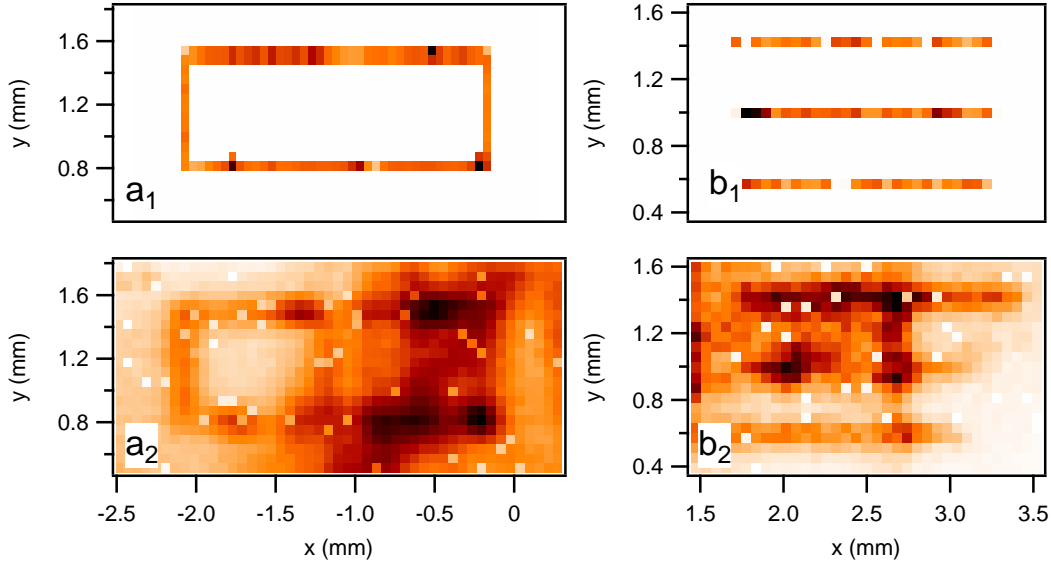


Figure 3.9: Direct lithographic patterning of anatase TiO<sub>2</sub>. The top panels (**a<sub>1</sub>**,**b<sub>1</sub>**) trace paths along which we drag the photon beam. The bottom panels (**a<sub>2</sub>**,**b<sub>2</sub>**) show spectral weight at the Fermi surface as a function of position measured with low photon flux. Clearly, the photons spatially modulate the charge carrier concentration of the sample.

In principle, this allows to directly write charge transport channels into intrinsically insulating oxides without disturbing the crystalline quality of the sample, which lead to the patent application in Ref. 99. The method in principle does not need the development of new infrastructure but can exploit standard UV, EUV (13.5 nm~ 92 eV) and e-beam lithography techniques.

When x-rays or electrons are used to write a certain path, they will – depending on their penetration depth – create oxygen vacancies in a spatially defined way and allow to tune the material from a band insulator to a semiconductor to a metal. As we have seen, the method allows for spatial regulation of the charge carrier concentration in these films from  $10^{17}$  to  $10^{20} \text{ cm}^{-3}$ .

A demonstration of the patterning effect of anatase is shown in Fig. 3.9. In the first step, a stoichiometrically grown anatase thin film is illuminated according to the pattern shown in panels 3.9 (a<sub>1</sub>) and (b<sub>1</sub>). Afterwards, the surface is imaged by scanning the region of interest and measuring the photoemission intensity at the Fermi level with low photon flux. Since this probing step itself also involves x-ray illumination to generate the photoelectron signal, the background

### 3.8. Doping dependence of the electron pocket

---

intensity of the non-patterned region is always nonzero. In the bottom right panel, a vertical streak can be seen that results from RHEED measurements (1.2 keV) during film deposition. This is the indirect indication that e-beam lithography might also be a suitable technique for direct anatase patterning.

Two major problems endanger the stability of metallic anatase regions created by oxygen defects however: first, applications in ambient atmosphere present the risk of refilling the vacancies from the oxygen in air. This effect can in principle be avoided by capping techniques.

A second problem might result from bulk diffusion of oxygen vacancies, which would confine the lifetime of a device to the typical timescale of the defect diffusion process. Our observations indicate that non stoichiometrically grown single crystals remain stable over years at ambient pressure and temperature. A thorough re-oxidation requires annealing these crystals for several days in air at temperatures as high as 600°C, which indicates defect stability. Very few studies treated this problem more systematically at the microscale so far. A recent study on anatase (101) surfaces found oxygen vacancies migrating towards the subsurface for temperatures higher than 200 K, corresponding to a subsurface migration activation energy of about 0.6-1.2 eV. Hence, vacancies are more stable in the bulk than at the surface [81, 98].

## 3.8 Doping dependence of the electron pocket

### 3.8.1 Along $k_{\parallel}$

As demonstrated, subtle regulation of the oxygen partial pressure vs photon flux allows for a fine study of the development of the polaron pocket with doping. Fig. 3.10 (a)-(e) shows energy distribution curve (EDC) stacks measured at oxygen partial pressures from  $6.5 \times 10^{-10}$  to  $6.5 \times 10^{-8}$  mBar applied to an anatase thin film. The re-oxidation process reduces the carrier density from  $\sim 10^{20}$  to about  $\sim 10^{18} \text{ cm}^{-3}$ .

At low doping, we observe stable QPs at the zone center. Injecting more and more carriers, interaction between polarons become significant and the single particle picture breaks down. Thus, the QP continuously smears out at  $k = 0$  towards high doping. Close to  $E_F$  however, the Landau argument holds and the QP remains stable. A thorough theoretical discussion is presented in Sec. 3.10.5. Fig. 3.10 (f) and (g) show a similar, but finer study on the anatase single crystal. EDCs at the zone center  $k = 0$  and the Fermi wave vector  $k = k_F$  are presented in panels 3.10 (f) and (g), respectively and depict the continuous QP breakdown at  $k = 0$  for high doping.

The increasing amount of oxygen vacancies here is reflected in the strong peak at around  $-1.5$  eV which moves towards lower binding energies while doping increases - an effect that to date is hardly understood. In analogy to rutile, one can speculate that low oxygen vacancy concentrations give rise to isolated point defects with well defined defect states. At higher concentrations, stoichiometries intermediate between  $\text{TiO}_2$  and  $\text{Ti}_2\text{O}_3$  can arise forming a variety

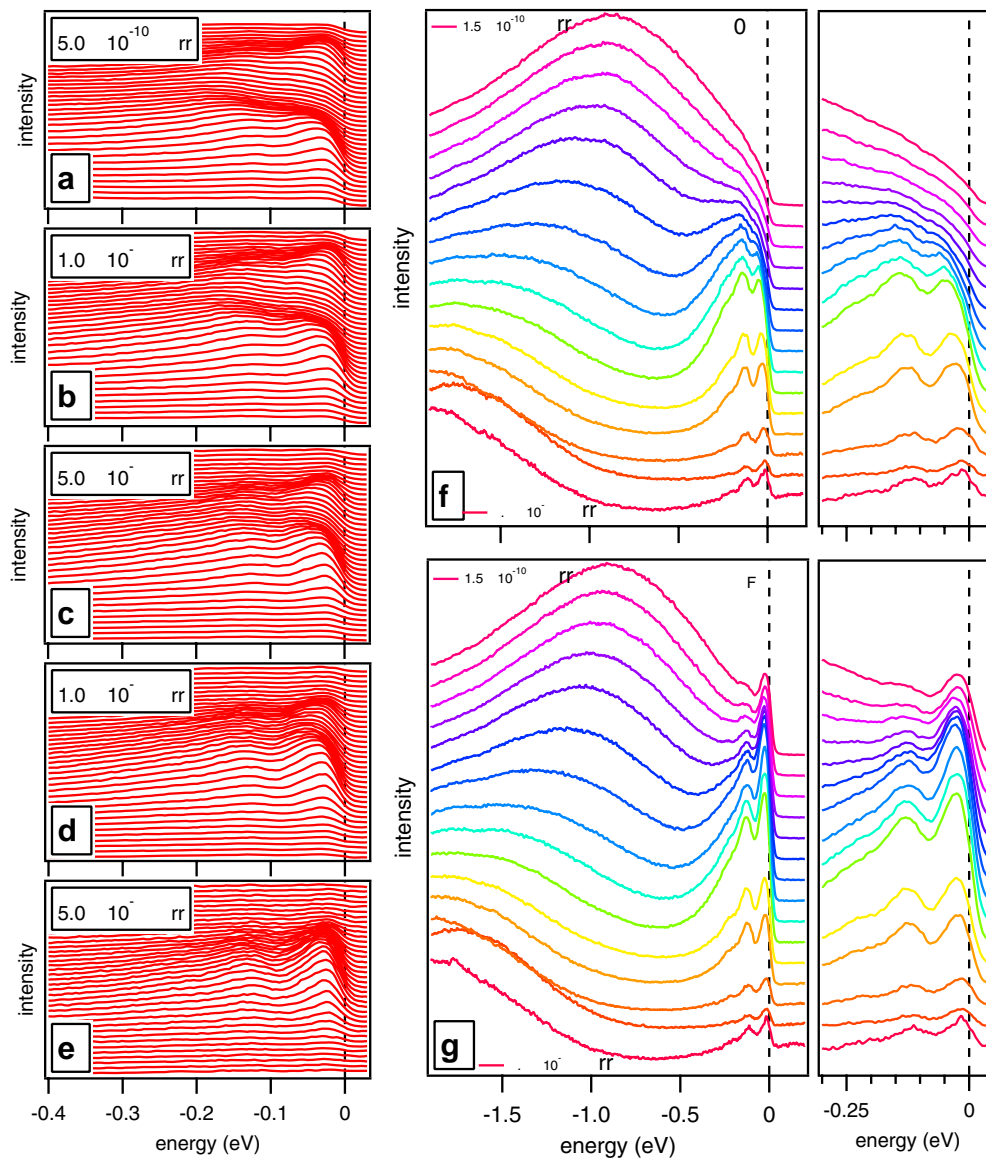


Figure 3.10: Fine study of the development of the polaron pocket with doping. **(a-e)**, EDC stacks measured at oxygen partial pressures from  $6.5 \times 10^{-10}$  to  $6.5 \times 10^{-8}$  mBar on an anatase thin film. Injecting more and more carriers, interaction between polarons cannot be neglected anymore and the single particle breaks down at the zone center. **(f,g)**, Similar study on the anatase single crystal. EDCs are shown at the  $k = 0$  and  $k = k_F$  and demonstrate the continuous QP breakdown at  $k = 0$  for high doping.



of Magnéli phases, i.e. ordered clusters of oxygen defects [100]. Each of these involves a series of spectral contributions. Eventually these defect states merge with the incoherent contribution of the polaron pocket at high concentrations.

In a thin film, the number of Magnéli phases reduces due to the  $c$ -axis confinement, and this effect is much weaker as shown in panels 3.10 (a) to (e).

#### 3.8.2 Along $k_z$

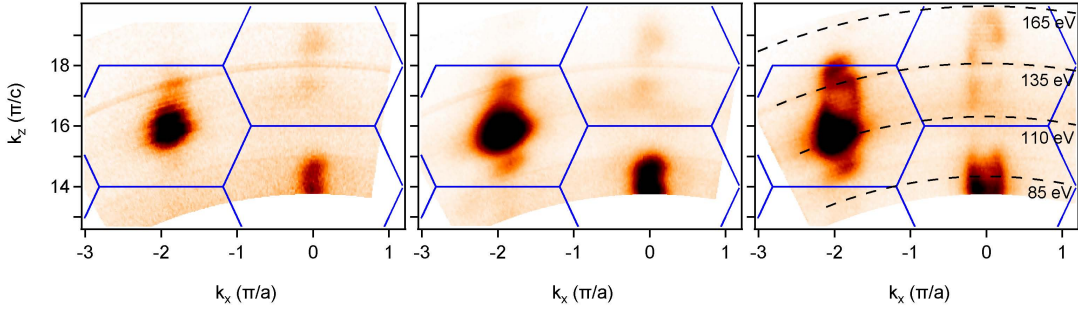


Figure 3.11:  $k_z k_y$  CE-maps over several BZs measured at  $k_y \sim 2\pi/a$  for samples with (a) low doping  $\sim 10^{18} \text{ cm}^{-3}$  (b) medium doping  $\sim 10^{19} \text{ cm}^{-3}$  and (c) high doping  $\sim 10^{20} \text{ cm}^{-3}$ .

$k_x k_z$  CE-maps over several BZs are shown in Fig. 3.11. Panels 3.11 (a), (b) and (c) correspond to low, medium and high doping cases of carriers  $\sim 10^{18} \text{ cm}^{-3}$ ,  $\sim 10^{19} \text{ cm}^{-3}$  and  $\sim 10^{20} \text{ cm}^{-3}$ , respectively, measured at  $k_y \sim 2\pi/a$ . They present ellipsoidal contours, visible in particular at  $k_x = -2\pi/a$ , which grow along all direction going from low to high doping as the conduction band is filled.

A striking feature in Fig. 3.11 (a-c) is the particularly strong intensity enhancement at the BZ center. Whereas at first sight this indicates the presence of a second electronic state, a careful analysis of both EDCs and MDCs rules out the presence of another band. However, this phenomenon can be understood taking again into account the curved ARPES probing sphere with radius  $k = 2m/\hbar^2 \sqrt{\hbar\nu - \Phi + V_0}$ . This sphere can have a large intersection with the ellipsoidal Fermi surface, giving rise to this intensity enhancement.

### 3.9 Temperature dependence of the pocket

Fig. 3.12 shows a detailed study of the temperature dependence of the polaron spectral line shape for samples with carrier densities of (a)  $n_e \simeq 5 \times 10^{18} \text{ cm}^{-3}$ , (b)  $n_e \simeq 3 \times 10^{19} \text{ cm}^{-3}$  and (c)  $n_e \simeq 3.5 \times 10^{20} \text{ cm}^{-3}$ . EDC stacks of the electron pocket are shown as a function of temperature from 20 to 300 K. Below 100 K, the QP as well as first and second incoherent contribution are clearly visible. Above 100 K, the peaks become significantly broader.

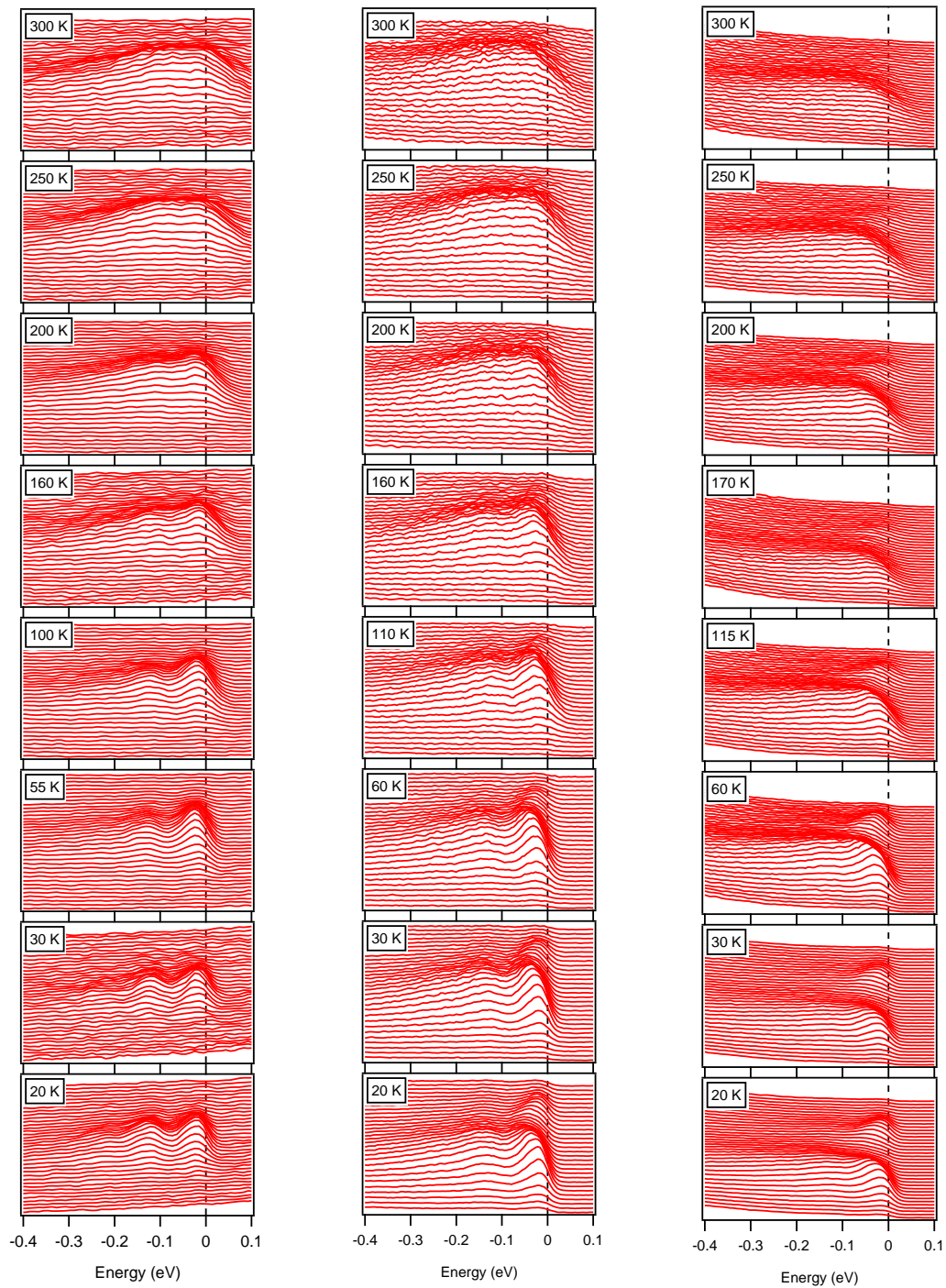


Figure 3.12: Temperature dependence of the polaron pocket. **(left)** low doping  $5 \times 10^{18} \text{ cm}^{-3}$  **(middle)** medium doping  $3 \times 10^{19} \text{ cm}^{-3}$  **(right)** high doping  $3.5 \times 10^{20} \text{ cm}^{-3}$ . Below 100 K, the QP as well as first and second incoherent contribution are clearly visible. Above 100 K, the peaks are broadening significantly.

### 3.9. Temperature dependence of the pocket

To explain this broadening, we need to consider the interactions between electrons and the other phonon modes, especially the acoustic branches of much lower energy. These lattice vibrations are expected to be excited with increasing temperature and hence to affect the lineshape of the spectral function. In the following, electron-phonon scattering theory for metals shall be used to qualitatively discuss the temperature dependent broadening of the spectral function. Well known from Fermi liquid theory, this broadening in energy corresponds to the imaginary part of the self energy and thus to the inverse lifetime of the QP. The spectral width is given by

$$\Delta E = 2Im\Sigma = \frac{\hbar}{\tau}. \quad (3.4)$$

When phonons and impurities dominate the scattering mechanism of a metal, the inverse lifetime can be calculated from Boltzmann theory [101–103]

$$\frac{\hbar}{\tau} = 4\pi k_B T \int_0^{\Omega_{max}} \frac{d\Omega}{\Omega} \beta^2 F(\Omega) \left( \frac{\hbar\Omega/2k_B T}{\sinh(\hbar\Omega/2k_B T)} \right)^2 \quad (3.5)$$

In the 3D Debye approximation  $\Omega(\mathbf{q}) = \Omega_D/V_{BZ}\mathbf{q}$ , the Eliashberg function  $\beta^2 F(\Omega)$  reads

$$\beta^2 F(\Omega) = 2\lambda \left( \frac{\Omega}{\Omega_D} \right)^4 \Theta(\Omega_D - \Omega) \quad (3.6)$$

where  $\Omega_D$  is the effective Debye frequency [103].<sup>3</sup>  $\lambda$  is an effective electron-phonon (e-ph) coupling strength. It describes the coupling of electrons to the (mostly) acoustic phonon background characterized by  $\Omega_D$ . It is not to be confused with  $\alpha$ , which was introduced in Sec. 3.5 to describe the coupling to one distinct LO phonon  $\hbar\omega_0$  in the polaron formation process. Substituting  $dx = \frac{\hbar}{2k_B T} d\Omega$  and using the identity  $\hbar\Omega_D = k_B\Theta_D$ , we obtain the Bloch-Grüneisen formula for resistivity in metals

<sup>3</sup>In general, the Eliashberg function describes strength and spectrum of electron-boson coupling.  $\beta(\Omega, \mathbf{q})$  characterizes the coupling strength whereas  $F(\Omega, \mathbf{q})$  is the boson density of states.  $\beta^2 F$  thus describes the total scattering probability of an electron state  $(E, \mathbf{k})$  to a state  $(E \pm \Omega, \mathbf{k} \pm \mathbf{q})$ .

$$\begin{aligned}
 \frac{\hbar}{\tau} &= 4\pi k_B T \int_0^{\omega_{max}} \frac{d\Omega}{\Omega} 2\lambda \left( \frac{\Omega}{\Omega_D} \right)^4 \left( \frac{\hbar\Omega/2k_B T}{\sinh(\hbar\Omega)/2k_B T} \right)^2 \\
 &= 4\pi k_B T 2\lambda \int_0^{\frac{\hbar\Omega_D}{2k_B T}} \frac{dx}{x} \left( \frac{2k_B T}{\hbar\Omega_D} x \right)^4 \frac{x^2}{\sinh(x)^2} \\
 &= 8\lambda\pi k_B T \left( \frac{2T}{\Theta_D} \right)^4 \int_0^{\frac{\hbar\Omega_D}{2k_B T}} dx \frac{x^5}{\sinh(x)^2} .
 \end{aligned} \tag{3.7}$$

Deconvolving the experimental EDC lineshape by an experimental Gaussian broadening of 25 meV yields the intrinsic Lorentian linewidth as a function of temperature (see Fig. 3 (b) of Sec. 3.5). Fitting these values with Eq. 3.7 and using an experimental value for the Debye temperature  $\Theta_D = 520$  K [104], we obtain  $\lambda = 0.7$  and consequently an effective mass renormalization of  $m_{xy}^*/m_{xy} = 1 + \lambda = 1.7$ . It is interesting to note that for a calculated DFT mass of  $0.42m_e$ , this yields an effective mass of  $m_{xy}^* = 0.71m_e$ , which matches with the effective polaron mass of  $(0.7 \pm 0.05)m_e$  extracted directly from the curvature of the QP dispersion [107].

The line width below 50 K saturates to a value of 55 meV, corresponding to contributions from impurity scattering and the finite photoelectron lifetime. This is in apparent contrast to transport data obtained for carrier densities in the  $10^{17} \text{ cm}^{-3}$  regime of Fig.3.2. However, this can be understood from the fact that ARPES measurements were done for carrier densities typically one to two orders of magnitude higher with respect to the transport measurements. In this regime, donor states merge with the conduction band to form an occupied band even for  $T \rightarrow 0$ . This observation is in agreement with independent transport results on doped samples [83, 84, 105].

## 3.10 Derivation of the polaron spectral function

### 3.10.1 Model

In polar semiconductors, such as TiO<sub>2</sub> anatase, e-ph coupling is often found to be strong. In particular, because of long-range electric fields introduced by LO lattice vibrations, the coupling of electrons to these lattice modes plays the most prominent role. The part of the Fröhlich Hamiltonian describing the interaction between electrons and the LO phonon branch is given by [26]

$$\hat{H}_{\text{e-ph}} = \frac{1}{\sqrt{\nu}} \sum_{\mathbf{q},s} M_q c_{\mathbf{k}+\mathbf{q},s}^\dagger c_{\mathbf{k},s} (b_{-\mathbf{q}}^\dagger + b_{\mathbf{q}}), \quad (3.8)$$

$$M_q = \frac{M_0}{|\mathbf{q}|} = 2\pi e^2 \hbar \omega_0 \left( \frac{1}{\varepsilon_\infty} - \frac{1}{\varepsilon_0} \right) \frac{1}{|\mathbf{q}|}, \quad (3.9)$$

where  $\hbar\omega_0$  is the LO phonon energy,  $\varepsilon_\infty$  and  $\varepsilon_0$  are the low- and the high-frequency dielectric constant, respectively,  $\nu/N$  is the volume of the unit cell, with  $N$  the number of lattice sites. The bare e-ph interaction in Eq. 3.8 is long ranged,  $M_q \propto 1/q$ . However, it is worth noting that by increasing the charge density, the screening of the polar interaction increases, removing the  $q \rightarrow 0$  singularity in Eq. 3.9 as discussed in Sec. 3.10.5. The full Fröhlich Hamiltonian reads

$$\hat{H} = \sum_{\mathbf{k},s} \varepsilon_{\mathbf{k},s} c_{\mathbf{k},s}^\dagger c_{\mathbf{k},s} + \omega_0 \sum_{\mathbf{q}} b_{\mathbf{q}}^\dagger b_{\mathbf{q}} + \hat{H}_{\text{e-ph}}, \quad (3.10)$$

where  $\varepsilon_{\mathbf{k}}$  is the bare electron dispersion.  $c_{\mathbf{k},s}^\dagger$  ( $c_{\mathbf{k},s}$ ) and  $b_{\mathbf{q}}^\dagger$  ( $b_{\mathbf{q}}$ ) are creation (destruction) operators of electrons and phonons, respectively.  $\mathbf{k}$  and  $\mathbf{q}$  denote momenta, while  $s$  is the spin index. In order to simplify the analysis, we consider electrons with an isotropic effective mass. In the nearest-neighbor (NN) approximation with a cubic lattice symmetry, the bare electron dispersion can be written in the tight binding form  $\varepsilon_{\mathbf{k}} = -2t \cos(ak_x/2) \cos(ak_y/2) \cos(ak_z/2)$ , with the electron hopping integral  $t$ . In the long-wavelength limit, such a dispersion takes the form of the free-particle like dispersion,  $\varepsilon_{\mathbf{k}} = ta^2 \mathbf{k}^2 \equiv \hbar^2 \mathbf{k}^2 / 2m$ , with  $m = \hbar^2 / 2ta^2$  being the electron band mass.

### 3.10.2 Low doping

Due to the long-ranged e-ph interaction, electrons doped in the conduction band form large polaron states. For large polarons, lattice discreteness effects are weak, meaning that it is enough to analyze the long-wavelength limit behavior of Eq. 3.8. Due to the phonon cloud, the polarons are characterized by an increased effective mass  $m^*$  compared to the electron band mass  $m$ ,  $t/t^* \propto m^*/m > 1$ , where  $t^*$  and  $m^*$  are the polaron NN-hopping integral and the effective mass, respectively. For small dopings of the conduction band, the effective overlap between polarons is small and can be neglected. Therefore, our starting point for the analysis of the ARPES properties is the gas of noninteracting polarons. It is convenient to introduce  $\xi_{\mathbf{k}}^*$ , representing the polaron energy  $\varepsilon_{\mathbf{k}}^*$  shifted by the Fermi level energy  $\mu$ ,  $\xi_{\mathbf{k}}^* = \varepsilon_{\mathbf{k}}^* - \mu$ . We use the Fermi-Dirac statistics  $n(\mathbf{k})$  assuming that the polaron gas behaves approximately as a gas of fermions, *i.e.*, at  $T=0$  all polaron states are occupied for  $\xi_{\mathbf{k}}^* < 0$ . In the present context, the ARPES intensity is given by the single-electron removal processes, where the initial state is the

ground state  $E_i = \xi_{\mathbf{k}}^*$ . The final state corresponds to a photohole coupled to its phonon dressing, leaving the lattice with or without phonon excitations,  $E_f = \sum_q n_q \hbar\omega_q$ , with  $\hbar\omega_q = \hbar\omega_0$  for LO phonons. Using the standard Lang-Firsov transformation to describe the phonon cloud associated with the polaron, the electron spectral function (ARPES intensity) takes the form  $A(\mathbf{k}, E) = A_c^{(0)}(\mathbf{k}, E) + A_{inc}^{(l>0)}(\mathbf{k}, E)$  [106],

$$\begin{aligned}
 A_c^{(0)}(\mathbf{k}, E) &= \pi Z \bar{n}(\mathbf{k}) \delta(E - \xi_{\mathbf{k}}^*) \\
 A_{inc}^{(l>0)}(\mathbf{k}, E) &= \pi Z \sum_{\mathbf{q}_1, \dots, \mathbf{q}_l} \frac{\prod_{r=1}^l |\gamma(\mathbf{q}_r)|^2}{(2N)^{l!}} \times \bar{n}(\mathbf{k} + \sum_r \mathbf{q}_r) \times \delta(E + \sum_r \hbar\omega_{\mathbf{q}_r} - \xi_{\mathbf{k} + \sum \mathbf{q}_r}^*) \\
 &= \frac{\pi}{2} Z \sum_{\mathbf{q}} \frac{|\gamma(\mathbf{q})|^2}{N} \times \bar{n}(\mathbf{k} + \mathbf{q}) \times \delta(E + \hbar\omega_{\mathbf{q}} - \xi_{\mathbf{k} + \mathbf{q}}^*) \\
 &+ \frac{\pi}{8} Z \sum_{\mathbf{q}_1, \mathbf{q}_2} \frac{|\gamma(\mathbf{q}_1)|^2 |\gamma(\mathbf{q}_2)|^2}{N^2} \times \bar{n}(\mathbf{k} + \mathbf{q}_1 + \mathbf{q}_2) \\
 &\quad \times \delta(E + \hbar\omega_{\mathbf{q}_1} + \hbar\omega_{\mathbf{q}_2} - \xi_{\mathbf{k} + \mathbf{q}_1 + \mathbf{q}_2}^*) \\
 &+ \dots
 \end{aligned} \tag{3.11}$$

where  $Z$  is the QP weight, defined by the projection of the excited polaron wave function onto the free electron state. The first, coherent contribution  $A_c^{(0)}(\mathbf{k}, E)$  in Eq. 3.11 corresponds to a final state of the lattice without phonon excitations. The spectral weight follows the polaron dispersion  $\xi_{\mathbf{k}}^*$ , while the description of its broadening is absent within the single-phonon coupling approach taken in Eq. 3.8. The remaining  $l > 0$  contributions in Eq. 3.11 are incoherent, involving the simultaneous excitation of  $l$  phonons. In Eq. 3.11,  $\gamma_{\mathbf{q}}$  are the amplitudes of coherent states that describe the polaron lattice deformation (polarization) [106]. That is, each amplitude  $\gamma_{\mathbf{q}}$  is the displacement of a given oscillator  $\mathbf{q}$  due to the presence of the electron,  $|\gamma_{\mathbf{q}}|^2 \propto M_q^2/\omega_0^2$ .

### 3.10.3 $l = 1$ contribution to the ARPES spectral weight

Let us analyze in more detail the  $l = 1$  contribution to the incoherent part of the spectral weight in Eq. 3.11. Assuming the low density limit,  $\mu \ll t^*$ , and by recognizing that in this limit the polaron dispersion is parabolic, one may replace the summation over the BZ by the integral,

$$\frac{1}{N} \sum_{\mathbf{q}} |\gamma(\mathbf{q})|^2 = \frac{M_0^2}{\nu (\hbar\omega_0)^2} \sum_{\mathbf{q}} \frac{1}{|\mathbf{q}|^2} \rightarrow \left( \frac{M_0}{\hbar\omega_0} \right)^2 \frac{1}{(2\pi)^3} \int d^3\mathbf{q} \frac{1}{|\mathbf{q}|^2}, \tag{3.12}$$

where  $\nu = Na^3$ ,  $a$  is the lattice unit and  $N$  is the total number of lattice sites. With the change of the integration variable in Eq. 3.11 to  $\mathbf{p} = \mathbf{k} + \mathbf{q}$ , one obtains

### 3.10. Derivation of the polaron spectral function

$$\begin{aligned}
A^{(1)}(\mathbf{k}, E) &= Z \frac{\pi}{2} \frac{1}{N} \sum_{\mathbf{p}} |\gamma(\mathbf{p} - \mathbf{k})|^2 \bar{n}(\mathbf{p}) \delta(E + \hbar\omega_0 - \xi_{\mathbf{p}}^*) \\
&= Z \frac{\pi}{2} \left( \frac{M_0}{\hbar\omega_0} \right)^2 \frac{1}{(2\pi)^3} \int d^3\mathbf{p} \frac{1}{|\mathbf{p} - \mathbf{k}|^2} n(\varepsilon_{\mathbf{p}}) \\
&\quad \times \delta(E + \hbar\omega_0 - \xi_{\mathbf{p}}^*)
\end{aligned} \tag{3.13}$$

Because of the  $\delta$ -function, the integration in Eq. 3.13 is over the spherical surface, given by the condition  $\hbar^2 p^2 / 2m^* = E + \hbar\omega_0 + \mu > 0$ . That is, the radial component of the wavenumber  $\mathbf{p}$  in Eq. 3.13 is fixed by  $E = \hbar\omega$ ,  $p = p(\omega)$ ,

$$\begin{aligned}
&\int d^3\mathbf{p} \frac{1}{|\mathbf{p} - \mathbf{k}|^2} n(p) \delta(E + \hbar\omega_0 - \xi_{\mathbf{p}}^*) \\
&= 2\pi \int_0^\infty p^2 dp \int_{-1}^1 d\nu \frac{1}{p^2 + k^2 - 2\nu pk} n(p) \frac{m^*}{\hbar^2 p} \delta(p - p(\omega)) \\
&= \pi \frac{2m^*}{\hbar^2} n(p(\omega)) p(\omega) \int_{-1}^1 d\nu \frac{1}{p^2(\omega) + k^2 - 2\nu p(\omega)k} \\
&= \pi \frac{2m^*}{\hbar^2} n(p(\omega)) \frac{1}{2k} \ln \left( \frac{p^2(\omega) + k^2 + 2kp(\omega)}{p^2(\omega) + k^2 - 2kp(\omega)} \right) \\
&= \pi \frac{\sqrt{2m^*}}{\hbar} n(E + \hbar\omega_0 + \mu) \frac{1}{\sqrt{\varepsilon_{\mathbf{k}}^*}} \ln \left( \frac{\sqrt{E + \hbar\omega_0 + \mu} + \sqrt{\varepsilon_{\mathbf{k}}^*}}{|\sqrt{E + \hbar\omega_0 + \mu} - \sqrt{\varepsilon_{\mathbf{k}}^*}|} \right)
\end{aligned} \tag{3.14}$$

where  $E \geq -\hbar\omega_0 - \mu$ . Using the Heaviside step function  $\Theta(E)$ , the final result for  $A^{(1)}(\mathbf{k}, E)$  may be expressed as

$$\begin{aligned}
A^{(1)}(\mathbf{k}, E) &= \frac{Z}{32\pi} \left( \frac{M_0}{\hbar\omega_0} \right)^2 \frac{\sqrt{2m^*}}{\hbar} \Theta(E + \hbar\omega_0 + \mu) n(E + \hbar\omega_0 + \mu) \frac{1}{\sqrt{\varepsilon_{\mathbf{k}}^*}} \\
&\quad \times \ln \left( \frac{\sqrt{E + \hbar\omega_0 + \mu} + \sqrt{\varepsilon_{\mathbf{k}}^*}}{|\sqrt{E + \hbar\omega_0 + \mu} - \sqrt{\varepsilon_{\mathbf{k}}^*}|} \right).
\end{aligned} \tag{3.15}$$

This expression diverges logarithmical for  $E = \varepsilon_{\mathbf{k}} - \hbar\omega_0 - \mu$ , i.e. for energies following the

QP dispersion  $\varepsilon_{\mathbf{k}} - \mu$  by one phonon quantum  $\hbar\omega_0$ . The linewidth of  $A^{(1)}(\mathbf{k}, E)$  is therefore intrinsically finite. In distinct contrast to quantum well states, this satellite is subject to a Fermi cutoff at  $E = -\hbar\omega_0 - \mu$ .

### 3.10.4 $l = 2$ contribution to the ARPES spectral weight

For  $A^{(2)}(\mathbf{k}, \omega)$  one has

$$\begin{aligned}
 A^{(2)}(\mathbf{k}, \omega) &= Z \frac{\pi}{8} \sum_{\mathbf{q}_1, \mathbf{q}_2} \frac{|\gamma(\mathbf{q}_1)|^2 |\gamma(\mathbf{q}_2)|^2}{N^2} \times \bar{n}(\mathbf{k} + \mathbf{q}_1 + \mathbf{q}_2) \\
 &\quad \times \delta(\omega + \omega_{\mathbf{q}_1} + \omega_{\mathbf{q}_2} + \mu - \varepsilon_{\mathbf{k} + \mathbf{q}_1 + \mathbf{q}_2}) \\
 A^{(2)}(\mathbf{k}, E) &= Z \frac{\pi}{8} \sum_{\mathbf{q}_1, \mathbf{q}} \frac{|\gamma(\mathbf{q}_1)|^2 |\gamma(\mathbf{q} - \mathbf{k} - \mathbf{q}_1)|^2}{N^2} \times \bar{n}(\mathbf{q}) \times \delta(E - \varepsilon_{\mathbf{q}}) \quad (3.16)
 \end{aligned}$$

where  $E = \omega + 2\omega_0 + \mu \geq 0$ . Using the integration derived for  $A^{(1)}(\mathbf{k}, \omega)$ , we obtain

$$\begin{aligned}
 A^{(2)}(\mathbf{k}, E) &= Z \frac{1}{4N} \sum_{\mathbf{q}_1} |\gamma(\mathbf{q}_1)|^2 \frac{\pi}{2} \frac{1}{N} \sum_{\mathbf{Q}} |\gamma(\mathbf{q} - \mathbf{k} - \mathbf{q}_1)|^2 \times \bar{n}(\mathbf{q}) \times \delta(E - \varepsilon_{\mathbf{q}}) \\
 &= Z \frac{1}{4N} \sum_{\mathbf{q}_1} |\gamma(\mathbf{q}_1)|^2 \frac{\alpha}{8} \frac{\bar{n}(E)}{\hbar\omega_0} \sqrt{\frac{\hbar\omega_0}{\varepsilon_{\mathbf{k} + \mathbf{q}_1}}} \ln \left( \frac{\sqrt{E} + \sqrt{\varepsilon_{\mathbf{k} + \mathbf{q}_1}}}{|\sqrt{E} - \sqrt{\varepsilon_{\mathbf{k} + \mathbf{q}_1}}|} \right) \\
 &= Z \frac{\alpha}{32} \frac{\bar{n}(E)}{\hbar\omega_0} \frac{1}{N} \sum_{\mathbf{q}} |\gamma(\mathbf{q} - \mathbf{k})|^2 \sqrt{\frac{\hbar\omega_0}{\varepsilon_{\mathbf{q}}}} \ln \left( \frac{\sqrt{E} + \sqrt{\varepsilon_{\mathbf{q}}}}{|\sqrt{E} - \sqrt{\varepsilon_{\mathbf{q}}}|} \right) \\
 &= Z \frac{\alpha}{32} \frac{\bar{n}(E)}{\hbar\omega_0} 4\pi\alpha \sqrt{\frac{DJ}{\hbar\omega_0}} a \frac{1}{(2\pi)^3} \\
 &\quad \times \int d^3\mathbf{q} \frac{1}{|\mathbf{q} - \mathbf{k}|^2} \sqrt{\frac{\hbar\omega_0}{\varepsilon_{\mathbf{q}}}} \ln \left( \frac{\sqrt{E} + \sqrt{\varepsilon_{\mathbf{q}}}}{|\sqrt{E} - \sqrt{\varepsilon_{\mathbf{q}}}|} \right) \\
 &= Z\pi \frac{\alpha^2}{8} \frac{\bar{n}(E)}{\hbar\omega_0} \frac{1}{(2\pi)^2} \int q^2 dq \int d\nu \frac{1}{q^2 + k^2 - 2qk\nu} \frac{1}{q} \ln \left( \frac{\sqrt{E} + \sqrt{\varepsilon_{\mathbf{q}}}}{|\sqrt{E} - \sqrt{\varepsilon_{\mathbf{q}}}|} \right) \\
 &= Z\pi \frac{\alpha^2}{8} \frac{\bar{n}(E)}{\hbar\omega_0} \frac{1}{(2\pi)^2} \int dq \frac{1}{k} \ln \left( \frac{k + q}{|k - q|} \right) \ln \left( \frac{p_E + q}{|p_E - q|} \right) \quad (3.17)
 \end{aligned}$$



### 3.10. Derivation of the polaron spectral function

A numerical analysis of this integral yields another singularity at  $E = \varepsilon_{\mathbf{k}} - 2\hbar\omega_0 - \mu$ . Overall, the singularity is less pronounced and the spectral weight of  $A^{(2)}$  distributed more homogeneously between  $-2\hbar\omega_0 - \mu < E < -2\hbar\omega_0$  with respect to  $A^{(1)}$ . We assume the distribution of spectral weight to become more and more homogeneous for spectral contributions  $l > 2$ .

#### 3.10.5 High doping

With more and more charge carriers occupying the conduction band, the single polaron picture can no longer be maintained. Screening of the positively charged ion cores by the electron background becomes important, leading to an effective reduction of e-ph coupling. The polarons, until this point stable QPs, dissociate into an electron-liquid. In this Fermi liquid picture, the self energy of the system is altered. Following the derivation of Ref. 26, the one-phonon self energy then can be written as

$$\Sigma(\mathbf{k}, ik) = -\frac{1}{\beta} \int \frac{d^3\mathbf{q}}{(2\pi)^3} \frac{M_q^2}{\varepsilon(q, i\omega)^2} D(q, i\omega_n) G^{(0)}(\mathbf{k} + \mathbf{q}, ip + i\omega_n), \quad (3.18)$$

where  $G^{(0)}$  is a free-particle electron Green's function and  $D(q, i\omega_n)$  is the renormalized phonon propagator. Assuming here one single Einstein type of LO phonon,  $D(q, i\omega_n)$  takes the form

$$D(q, i\omega_n) = D(i\omega_n) = \frac{-2\omega_0}{\omega_n^2 + \omega_0^2}. \quad (3.19)$$

For a phonon frequency  $\omega_0$  smaller than the plasma frequency, screening may be assumed to be static and the dielectric function  $\varepsilon(q, i\omega)$  can be written in the Thomas-Fermi approximation

$$\varepsilon(q, i\omega) = 1 + \frac{q_{TF}^2}{q^2}, \quad (3.20)$$

where  $q_{TF}$  is the Thomas-Fermi wave vector. The self energy given in Eq. 3.18 describes how the electrons screen and modify phonons and their interactions with the electrons. For electrons  $\varepsilon_{\mathbf{k}} = \hbar^2 \mathbf{k}^2 / 2m$ , the imaginary part of the self energy can be written as

$$\begin{aligned} \text{Im} [\Sigma(\mathbf{k}, E)] &= -\frac{\alpha\omega_0^{3/2}}{4\sqrt{\varepsilon_{\mathbf{k}}}} [\Theta(E - \hbar\omega_0)g_p(E - \hbar\omega_0) + \Theta(-E - \hbar\omega_0)g_p(E + \hbar\omega_0)], \\ g_p(x) &= \ln \left[ \frac{\varepsilon_s + (\sqrt{x + \mu} + \sqrt{\varepsilon_{\mathbf{k}}})^2}{\varepsilon_s + (\sqrt{x + \mu} - \sqrt{\varepsilon_{\mathbf{k}}})^2} \right] \\ &+ \varepsilon_s \left[ \frac{1}{\varepsilon_s + (\sqrt{x + \mu} + \sqrt{\varepsilon_{\mathbf{k}}})^2} - \frac{1}{\varepsilon_s + (\sqrt{x + \mu} - \sqrt{\varepsilon_{\mathbf{k}}})^2} \right], \end{aligned} \quad (3.21)$$

with  $\varepsilon_s = \hbar^2 q_{TF}/2m$ . The real part can be obtained through the Kramers-Kronig relationship

$$\text{Re}[\Sigma(\mathbf{k}, E)] = \int_{-\infty}^{\infty} \frac{dE'}{\hbar\pi} \frac{\text{Im}[\Sigma(\mathbf{k}, E')]}{E' - E}, \quad (3.22)$$

and the spectral function from

$$A(\mathbf{k}, E) = \frac{2}{\pi} \frac{|\text{Im}\Sigma|}{|\hbar\omega - \varepsilon_k - \text{Re}\Sigma|^2 + |\text{Im}\Sigma|^2}. \quad (3.23)$$

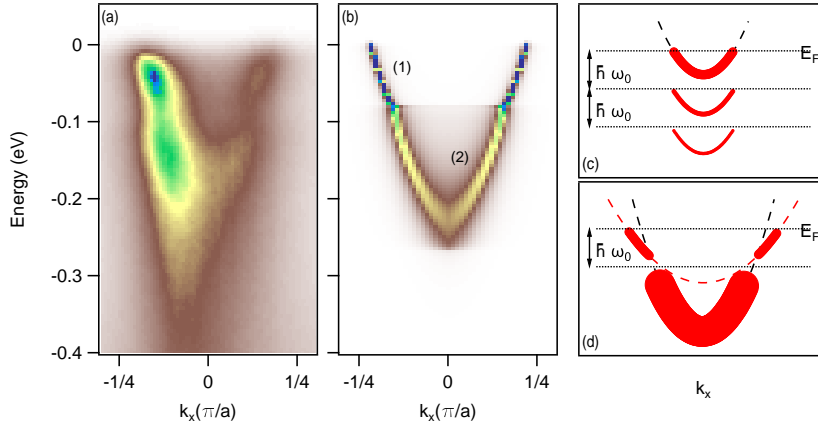


Figure 3.13: **(a)** Measured dispersion of the electronic state at  $(k_x, k_y) = (0, 2\pi/a)$  for the high carrier density limit  $n = 10^{20} \text{ cm}^{-3}$ . Close to  $k_F$ , a significantly renormalized kink structure appears. At the center of the BZ, the QP weight smears into the background resulting in a broad incoherent feature. This incoherent part follows the bare band. **(b)** The renormalized band (1) as well as the dispersion of the incoherent part (2) are well reproduced by the second order perturbation model of Eq. 3.23 for  $\alpha = 2$ . **(c)** Schematics of the low doping case. The polaron parabola is followed by a succession of vibronic satellite bands. **(d)** Schematics of the high doping case. The polaron band crosses the one phonon threshold  $\hbar\omega_0$ . Close to  $\hbar\omega_0$ , the band is strongly renormalized.

Fig. 3.13 (a) shows ARPES results at the high doping limit next to a calculation (b) of Eq. 3.23. To obtain the best possible agreement with ARPES, the phonon frequency was set to  $\omega_0 = 80 \text{ meV}$ , T was set to 20 K and  $t = \hbar^2/2ma^2 = 445 \text{ meV}$  with  $m/m_e = 0.6$  and  $a = 3.782 \text{ \AA}$  [107]. The chemical potential  $\mu$  was calculated from a free electron model

$$n = \frac{8\sqrt{2}\pi m^{3/2}}{h^3} \left( \frac{2}{3}\mu^{3/2} \right) \quad (3.24)$$

and yields  $\mu \sim 185 \text{ meV}$  for  $n = 10^{20} \text{ cm}^{-3}$ . We used a screening  $\varepsilon_s$  of 100 meV and an intrinsic broadening of the spectral function of 10 meV. Our calculations are in good qualitative agreement with the ARPES data for  $\alpha \sim 2$ , which is slightly below the value of 2.5 estimated in the low-density limit. Although this points to a small decrease of the coupling strength, we point

out that besides  $\alpha$ , the band renormalization depends sensitively on  $k$ , the chemical potential  $\mu$  and the band mass  $m$ . For this reason, a derivation of  $\alpha$  solely from the QP dispersion accessed by ARPES has been shown to be inaccurate in this regime [108].

In the vicinity of  $E \sim \hbar\omega_0$ , the dispersion clearly presents a kink (1) and then evolves into the (non renormalized) incoherent branch  $\varepsilon_k$  (2). Fig. 3.13 (c-d) sketches the evolution from the low doping limit to the high doping limit. At low carrier concentration (c), the QPs are polarons and their dispersion above the one phonon threshold  $\hbar\omega_0$ . The QP parabola is followed by a succession of phonon emission lines set of by multiples of  $\hbar\omega_0$ . When the filling is high enough for the QP dispersion to cross the one phonon threshold, the QP becomes unstable in the vicinity of  $\hbar\omega_0$ , and the dispersion strongly renormalizes. Far below the threshold however, carriers follow the unrenormalized dispersion. Carriers in this regime can always de-excite by emitting one or multiple phonons  $\hbar\omega_0$ , their lifetime therefore is low and the ARPES lineshape broad.

## 3.11 Some quantitative estimates

### 3.11.1 Electrical properties

Let us now try to estimate some characteristic properties of the “conductive channels” created by the x-ray beam. The most important parameters we extract from the data is (i) the in plane effective mass  $m_{xy}^*$  of the QP (from the curvature of the QP dispersion), (ii) the Fermi wave vector  $k_f$  (from the MDC at  $E_F$ ) and (iii) its uncertainty  $\Delta k_f$  (from the MDC broadening) as well as (iv) the linewidth of the QP  $\Delta E$  (exploited already in Sec. 3.9).

In the low doping limit, we estimate  $m_{xy}^* \sim 0.7m_e$  from the ARPES data. In the high density limit, the effective mass is further enhanced in the vicinity of  $E = \hbar\omega_0$  (see e.g. Fig. 3.13) and we extract an effective QP mass of about  $(1.2 \pm 0.2)m_e$  close to  $k_F$  for  $n = 10^{20} \text{ cm}^{-3}$ .

Unfortunately, the small band dispersion along the  $c^*$  axis as well as the technical difficulties involved in a  $E$  vs  $k_z$  measurement make an estimation of  $k_{fz}$  and therefore a value for the out of plane effective mass  $m_z^*$  from the data in Fig. 3.5 or Fig. 3.11 unreliable. However, we can estimate  $k_{fz}$  to be in between  $2\pi/3c$  and  $\pi/c$  from Fig. 3.5. From  $\hbar^2 k_{fz}^2 / 2m_z^* \sim 40 \text{ meV}$ , we estimate  $m_z^* \sim 4.7\text{-}10.7m_e$ . The un-renormalized DFT mass obtained in Refs. 107 and 132 is in between  $m_z \sim 2.4m_e$  and  $4.05m_e$ . Assuming isotropic e-ph coupling we so can compare to  $m_z^* \sim 1.7 \times (2.4\text{...}4.05)m_e \sim (4.1\text{...}6.9)m_e$ .

From the Luttinger theorem, we can estimate the charge carrier density by dividing the volume of the electron pocket  $4/3\pi k_f^3$  by the total volume of the BZ  $(2\pi/a)^2(2\pi/c)$  and taking into account in total 2 electrons per state per unit cell. Of course this estimation would be more accurate taking into account the elongation of the pocket along  $k_z$ . Due to the experimental difficulties explained above however, this cannot be done in a reliable way.

We further can estimate the in plane Fermi velocity  $v_F \sim \hbar k_F / m_{xy}^*$ .

From  $\Delta k_F$  we can directly estimate the mean free path of the QP  $l \sim 1/\Delta k_F$  which relates directly to the scattering rate  $\tau \sim l/v_F$  via Drude theory. We consequently yield values of the carrier mobility  $\mu = e\tau/m_{xy}^*$ , the conductivity  $\sigma \sim ne^2\tau/m_{xy}^*$  and the resistivity  $\rho \sim 1/\sigma$ .

Independently, we can obtain the scattering rate  $\tau = \hbar/\Delta E$  from the linewidth of the QP  $\Delta E$ , which relates directly to the mean free path  $l \sim \tau v_F$ . We consequently in a different way again yield the mobility  $\mu = e\tau/m_{xy}^* = e\hbar/\Delta E m_{xy}^*$ , the conductivity  $\sigma = n\mu e$  and resistivity  $\rho = \sigma^{-1}$ .

For the samples discussed in 3.9 we obtain  $\Delta E \sim 50$  meV to 150 meV in the temperature range 20-300 K and find a mobility reduction from  $\mu \sim 33$  cm<sup>2</sup>/Vs at 20 K to  $\mu \sim 11$  cm<sup>2</sup>/Vs at room temperature. The resistivity and conductivity change is summarized in Tab. 3.1.

$n$ (10 <sup>19</sup> cm <sup>-3</sup> )	$\sigma$ (S/cm)	$\rho$ (10 <sup>-3</sup> Ωcm)
0.5	26.5-8.8	40-110
3	160-53	6-19
35	1850-620	0.5-1.6

Table 3.1: Conductivity and resistivity estimates for  $m_{xy}^* = 0.7m_e$  in the temperature range 0-300 K. For comparison, typical conductivities are  $6.3 \times 10^5$  S/cm for copper and up to 10 S/cm for GaAs.

Estimates for different charge carrier concentrations at low temperature ( $T \sim 20$  K) are given in Tab. 3.2.<sup>4</sup> The estimates obtained from  $\Delta k_F$  compare very nicely to the ones obtained from  $\Delta E$  in the low and high doping regimes. In the intermediate doping regime, where the QP is not as well defined and  $m_{xy}^*$  cannot be determined properly, we have slight discrepancies. Nevertheless, we get a good impression of the electric properties of the conductive channel, in good agreement with the transport experiments of Refs. 79, 105 and 109. Interestingly, the conductivity that can be achieved by x-ray beam doping is three orders of magnitude higher than in the pristine case ( $n \sim 10^{17}$  cm<sup>-3</sup>, compare Fig. 3.2).

From the dielectric constants  $\varepsilon_\infty = 5.82$  and  $\varepsilon_0 = 45.1$  obtained in Ref. 110, we can further estimate the plasma frequencies in the low  $\omega_p^- = \sqrt{ne^2/\varepsilon_0 m_{xy}^*}$  and high density limit  $\omega_p^+ = \sqrt{ne^2/\varepsilon_\infty m_{xy}^*}$  [26]. The plasma frequency in the high doping case serves as an indicator for the validity of the Thomas-Fermi approximation exploited in Sec. 3.10.5. At low doping,  $\hbar\omega_p \sim 18-38$  meV  $<$   $\hbar\omega_0 \sim 108$  meV is comparatively low with respect to the phonon frequency indicating that the phonons cannot follow the electrons motion. In the frame of the phonons, the electronic potential can therefore be considered static. In the high doping limit, phonon frequency and plasma frequency become comparable ( $\hbar\omega_p \sim 49 - 135$  meV  $\sim \hbar\omega_0 \sim 108$  meV). This is a

---

<sup>4</sup>Please note that the extraction of the QP linewidth  $\Delta E$  can only be done for low doping samples. Therefore we used an approximate Gaussian fit for the lineshape at  $k = k_F$  to obtain the trend. Obviously, the numbers obtained are much larger than the ones of Sec. 3.9 since they do not take into account the experimental broadening, nor the Fermi cutoff.

### 3.11. Some quantitative estimates

$P_{O_2}$ (mbar)	$5 \times 10^{-8}$	$1 \times 10^{-8}$	$5 \times 10^{-9}$	$1 \times 10^{-9}$	$5 \times 10^{-10}$
$k_F$ ( $\text{\AA}^{-1}$ )	0.05	0.08	0.10	0.13	0.14
$\Delta k_F$ ( $\text{\AA}^{-1}$ )	0.14	0.17	0.18	0.17	0.14
$\Delta E$ (eV)	0.08	0.08	0.10	0.14	0.12
$m_{xy}^*/m_e$ 0.7	0.7	?	?	?	1.2
$10^{-3}e/\mu\text{c}$	0.6	2.3	4.6	10	12
$n$ ( $10^{19}\text{cm}^{-3}$ )	0.42	1.7	3.4	7.4	9.3
$v_F$ ( $10^3\text{m/s}$ )	83	132	165	125	135
derived from MDC					
$l$ ( $\text{\AA}$ )	7.1	5.9	5.6	5.9	7.1
$\tau$ ( $10^{-15}\text{s}$ )	8.6	4.4	3.4	4.7	5.3
$\mu$ ( $\text{cm}^2/\text{Vs}$ )	21.7	11.2	8.4	6.9	7.8
$\rho$ ( $\Omega\text{cm}$ )	0.068	0.030	0.020	0.010	0.009
$\sigma$ (Si/cm)	14.7	30.9	45.7	81.7	115
derived from EDC					
$\tau$ ( $10^{-15}\text{s}$ )	8.2	8.2	6.6	4.7	5.5
$l$ ( $\text{\AA}$ )	6.8	10.9	10.9	5.9	7.4
$\mu$ ( $\text{cm}^2/\text{Vs}$ )	20.6	20.7	16.5	6.9	8.0
$\rho$ ( $\Omega\text{cm}$ )	0.072	0.017	0.011	0.012	0.008
$\sigma$ (Si/cm)	14.0	57.3	89.5	81.9	119.4
derived from dielectric properties					
$\hbar\omega_p^-$ (meV)	14	27	38	43	49
$\hbar\omega_p^+$ (meV)	38	77	107	121	135

Table 3.2: Some quantitative estimates for the electrical and dielectrical properties of beam-doped anatase  $\text{TiO}_2$ .

sign that screening now will gain importance, but not total control over the QP's renormalization.

### 3.11.2 Electron phonon coupling

Let us now estimate the electron phonon coupling strength. We can rewrite Eq. 3.8 in terms of the dimensionless e-ph. coupling strength  $\alpha$ :

$$M_0^2 = \frac{4\pi\alpha\hbar(\hbar\omega_0)^{3/2}}{\sqrt{2m}} \quad (3.25)$$

where  $\alpha$  is defined as

$$\alpha = \frac{e^2}{\hbar} \sqrt{\frac{m}{2\hbar\omega_0}} \left( \frac{1}{\varepsilon_\infty} - \frac{1}{\varepsilon_0} \right). \quad (3.26)$$

With  $m \sim 0.42m_e$ ,  $\hbar\omega_0 \sim 108.7$  meV and using the in plane values  $\varepsilon_\infty = 5.82$  and  $\varepsilon_0 = 45.1$  tabulated for the dielectric constants [110], we find  $\alpha \sim 1.1$  and  $M_0 \sim 0.165$  meV/Å. This value is clearly very low compared to our phenomenological expectation that the number  $\alpha$  should give approximately the number of phonon emission lines in our ARPES spectra, i.e. value around  $\sim 2 - 3$ . We find the origin of this mismatch in the approximations done within the derivation of the Fröhlich Hamiltonian, i.e. that the polarization is proportional to the ionic displacement. More realistically however, the dielectric response is resonantly enhanced close to frequencies of  $\hbar\omega_0$ , resulting in a stronger effect [111].

Fitting the experimental lineshape to the model obtained in Sec. 3.10 yields an unreasonable value of  $\alpha \sim 8$ , for reasons that have not been identified yet.

We thus compare this estimate with a value obtained from the weak coupling limit

$$m^*/m = \frac{1}{1 - \alpha/6} \quad (3.27)$$

which known to work well up to  $\alpha \leq 2$  [112], and find  $\alpha \sim 2.4$ .

In an analogous way, we use the strong coupling limit [113]

$$m^*/m = \alpha^4/48 \tag{3.28}$$

and find  $\alpha = 3$ . These two values give an upper and a lower boundary for the electron phonon coupling to expect in anatase. For more precision, we compare to Diagrammatic Monte Carlo Calculations as discussed in the paper of Sec. 3.5 and obtain a value  $\alpha \sim 2.5$  [112].





# 4 Anatase $\text{TiO}_2$ – a polaronic semiconductor investigated by RIXS

## 4.1 Summary

In this section, we study the role of the electron-lattice coupling in oxygen vacant anatase  $\text{TiO}_2$  by high resolution resonant inelastic x-ray scattering at the Ti  $L_3$ -edge. The spectral signatures of phonon modes of  $A_{1g}$  and  $B_{1g}$  symmetry as well as a fluorescence peak appear for excitation energies corresponding to transitions to delocalized intermediate states. These resonances remain suppressed for intermediate states of excitonic character. We further discuss a progressive emission of well-defined 95 meV Franck-Condon-like loss features indicating intermediate electron-phonon coupling. Phonon frequency and e-ph coupling, both directly probed by RIXS, show low doping sensitivity. We further observed a similar resonance at the O K-edge.

## 4.2 Motivation

Electron-phonon (e-ph) coupling is a key interaction that determines many properties of solids. It is especially important in conventional superconductors, where it mediates the electron pairing [114–116]. In polar semiconductors, e-ph coupling plays a major role in determining the lifetime and effective mass of doped in charge carriers, typically exploited in applications. As discussed in Ch. 3, a benchmark system is anatase  $\text{TiO}_2$  where intermediate range ( $\alpha \sim 2.5$ ) e-ph coupling is believed to be responsible for the formation and dispersion of so called “large polaron” quasiparticles (QPs), i.e. electrons dressed with their self-induced lattice distortion.

The anisotropic nature of anatase further suggests electrons propagating along different crystal directions to be affected differently by their phonons [78, 92, 110, 117–119]. Indeed, such a scenario of anisotropic e-ph coupling has been already identified theoretically [120] and experimentally in the cuprates, where selective excitations of optical phonons competing with magnons [230] can lead to anisotropic e-ph coupling [122–124]. In 1D cuprates, it has been shown that the coupling strength remains essentially doping independent, which demonstrates an ineffective screening mechanism [125]. In other low dimensional systems like  $\text{CeTe}_3$  and

VO<sub>2</sub>, the anisotropic coupling has been attributed to the formation of collective modes induced by electronic phase transitions [126]. In Ca or K intercalated graphene, anisotropic e-ph coupling was attributed to the nesting condition for intervalley scattering, and showed strong doping dependence [127, 128]. In CdS nanowires, geometrical aspects seem to determine the anisotropy of e-ph coupling [129].

In anatase, the scenario could in principle again be quite different. The dielectric environment of TiO<sub>2</sub> could lead to a polaronic screening mechanism [130, 131] which moderates the effective coupling between an electron and one phonon branch in a directional way. The QP re-normalization would then depend very sensitively on this anisotropy and the in- and out of plane carrier mass ratio  $m_z^*/m_{xy}^*$  could therefore differ significantly from the un-renormalized ratio  $m_z/m_{xy}$ .<sup>1</sup>

Besides the fundamental interest, such a behavior would be of tremendous importance for applications relying on the mobility of carriers typically exploited in applications [134, 135]. Especially if they are based on nanowires which need to transport current essentially along one distinct crystal axis.

To address these questions, high resolution resonant inelastic x-ray scattering (RIXS) measured across the Ti L<sub>3</sub> absorption threshold is a powerful experimental probe. RIXS is known to be very site sensitive and therefore responds to the local symmetry of the absorbing atom. Further, RIXS as a bulk sensitive technique involves the full photon momentum and therefore allows for a study of excitations along all different directions in reciprocal space. Most importantly however, RIXS also can yield - as similar to ARPES - the e-ph coupling strength [136]. For reasonable coupling, we expect the “one phonon line” to be followed by a progression of vibronic satellites. The energy separation of these peaks corresponds to the characteristic phonon energy  $\hbar\omega_0$ , in direct analogy to a generalized Franck-Condon picture in molecules [137]. The relative intensity of these satellites reflect the e-ph coupling strength.<sup>2</sup> RIXS therefore is able to probe the e-ph coupling along different directions of reciprocal space.

### 4.3 Methods

High-quality single crystals of oxygen vacant anatase ( $n_e \sim 10^{18} \text{ cm}^{-3}$ ) TiO<sub>2</sub> were grown by the transport technique described in Ch. 3, section 3.3. This time, single crystals naturally exposed (001) surfaces which were annealed in  $10^{-8}$  mBar of O<sub>2</sub> at 500 K for several hours. This treatment typically results in a well ordered  $2 \times 1$  reconstructed (001) surfaces as independently confirmed by LEED shown in Fig. 3.4.

---

<sup>1</sup>As we saw from Sec. 3.11, ARPES confines the ratio to  $m_z^*/m_{xy}^* \sim 6.7\text{-}15.3$ . Polarized infrared spectroscopy measurements find an anisotropy of the optical effective mass  $m_z^*/m_{xy}^* \sim 3\text{-}6$  [132, 133]. Density functional theory (DFT) in the generalized gradient approximation (GGA) obtain an un-renormalized mass ratio  $m_z/m_{xy} \sim 4.05/0.42 \sim 9.6$  [107].

<sup>2</sup>Unlike in ARPES, the RIXS amplitude of the “one phonon line” remains always dominant, even in the case of very strong e-ph coupling.

RIXS data were taken with the HORNET spectrometer at beam line BL07LSU of the Spring 8 synchrotron, Japan, where an energy resolution of  $\sim 100$  meV was obtained using a combination of focusing elements and high-precision optical gratings [138]. The base pressure of the high-vacuum chamber and the spectrometer was  $10^{-9}$  mBar. Sample temperature was kept below 40 K to suppress the low energetic acoustic phonon background. Total electron yield x-ray absorption (XAS) spectra were taken prior to experiment to calibrate the monochromator. The scattering angle was kept  $90^\circ$ , while the sample was rotated around the  $x$ -axis to change  $\alpha$  and thus the momentum transfer  $q$  (see Fig. 4.2).

Reference spectra to calibrate emission energy, energy resolution and symmetry of the RIXS lineshape were taken before each measurement with photons polarized perpendicular to the horizontal scattering plane ( $\sigma$ -polarization). Spectra shown in this work are summed from several partial measurements, each accumulated for a maximum of 30 min and aligned with respect to the elastic line to minimize possible energy drifts.

#### 4.4 Excitation energy dependence

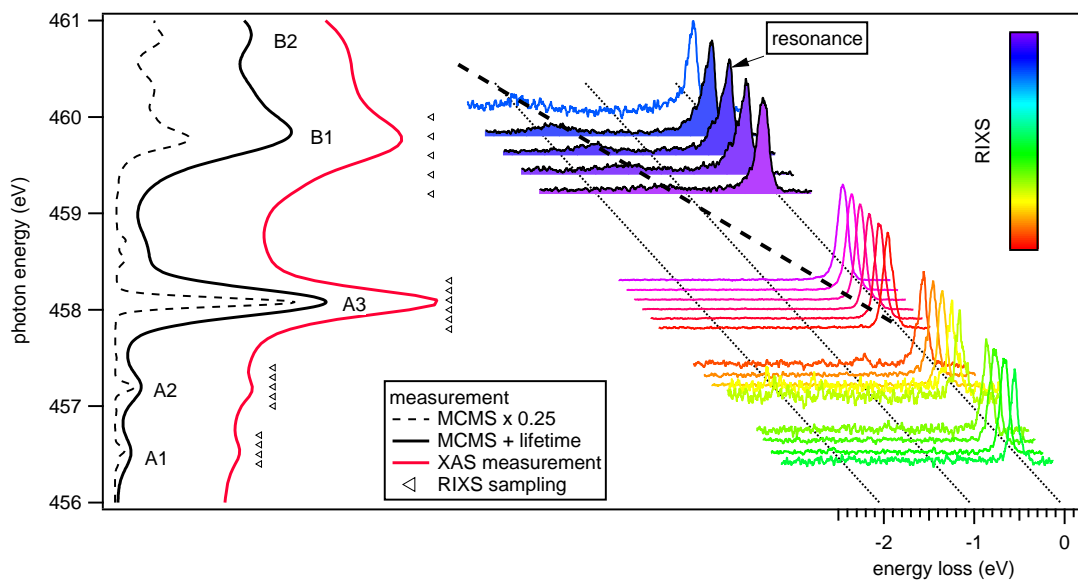


Figure 4.1: **(left)** XAS at the Ti  $L_3$ -edge (**red**) compared to MCMS calculations (**black**). MCMS results are further plotted without taking into account the lifetime broadening of the core hole (**black dashed**), revealing the excitonic character of peaks A1, A2 and A3 as opposed to the delocalized nature of B1 and B2. **(right)** RIXS data obtained at different photon energies are marked by black triangles. Across XAS peak B1, a fluorescence (**black dashed line**) as well as a low energy resonance (**filled spectra**) become visible.

Fig. 4.1 presents an overview of the resonance behavior of  $\text{TiO}_2$  anatase throughout the Ti  $L_3$  absorption threshold. The left part shows our XAS data (red) compared to state of the art multi

channel multiple scattering calculations (MCMS) by Krüger [139]. The total MCMS spectrum is shown with (black solid) and without (black dashed) taking into account the finite core-hole lifetime of the XAS final state. The black dashed spectrum additionally is convoluted by a Gaussian of 0.1 eV FWHM for better visibility of the sharp features.

Whereas the mostly “*t<sub>2g</sub>*” derived absorption peaks A1, A2 and A3 exhibit a linewidth solely determined by this artificial broadening, the “*e<sub>g</sub>*” - derived peaks B1 and B2 exhibit a finite bandwidth, even without taking into account lifetime broadening.<sup>3</sup> This inherent difference underlines the strong excitonic character (core exciton) of features A1, A2 and A3 where the excited electron remains strongly bound to the core hole. This is in contrast to the delocalization of final state carriers probed at peaks B1 and B2, where the width of the features mainly reflects the bandwidth of the conduction band – or in other words the unoccupied density of states (DOS) [140, 141].

The right part of Fig. 4.1 shows energy loss RIXS data obtained for the photon energies  $h\nu$  indicated by black markers. For photon energies  $h\nu$  probing the XAS features A1, A2 and A3, the RIXS spectra exhibit an essentially symmetric elastic lineshape. At XAS peak B1 by contrast, a pronounced feature appears at  $\sim 1.2$  eV energy loss, linearly moving towards higher energy loss as  $h\nu$  increases (black dashed line) – i.e. a typical fluorescence as we will show in the following. Simultaneously to this fluorescence, the elastic peak develops an asymmetric lineshape with a pronounced tail towards the low energy side (filled spectra). This selective appearance of fluorescence and asymmetry, indicates their close relation to the orbital nature of XAS peak B1.

Lets start again from a local Kramers–Heisenberg picture discussed in Ch. 2, where the RIXS amplitude is described as  $F(h\nu, h\nu') = \sum_f \left| \sum_i \frac{\langle f | \hat{T}_2 | i \rangle \langle i | \hat{T}_1 | g \rangle}{E_i - E_g - h\nu - i\Gamma_i} \right|^2 \delta(h\nu - h\nu' + E_g - E_f)$  [51].  $\hat{T}_{1,2}$  is the dipole operator,  $|g\rangle$ ,  $|i\rangle$  and  $|f\rangle$  are the ground, the intermediate and the final state in the RIXS process and  $E_g$ ,  $E_i$  and  $E_f$  their corresponding energies. In Ti L-edge RIXS, a  $2p$  core electron is first excited into the XAS final state  $|i\rangle$ , defined by  $XAS(i) = |\langle i | \hat{T} | g \rangle|^2 \delta(E_i - E_g - h\nu)$ . Like absorption, the RIXS intensity  $F$  recording the overlaps of ground, intermediate and final state will be most pronounced if  $E_i = E_g + h\nu$  – which accentuates the intermediate state selectivity of RIXS – and if absorption *as well as* emission processes are dipole allowed (compare to Ch. 2).

## 4.5 The fluorescence

As already mentioned, MCMS calculations (and atomic multiplet theory [141]) identify the orbital character of peak B1 – location of the low energy resonance and fluorescence – to be predominantly “*e<sub>g</sub>*”-derived. Formally, anatase TiO<sub>2</sub> is a  $d^0$  system and  $dd$  electronic transitions towards “*t<sub>2g</sub>*” orbitals in the RIXS final state are not possible. As we saw however, the bottom of

---

<sup>3</sup>Although the Ti is coordinated tetrahedrally by oxygen, and therefore the proper basisfunctions are the irreducible representations of  $D_{4h} - A_{1g}(d_{z^2})$ ,  $B_{1g}(d_{x^2-y^2})$ ,  $B_{2g}(d_{xy})$  and  $E_g(d_{xz}/d_{yz})$  we will here use the notation of the octahedral pointgroup  $t_{2g}(d_{xy}, d_{xz}/d_{yz})$  and  $e_g(d_{x^2-y^2}/d_{z^2})$  for easier comparison to the literature.

the conduction band in oxygen vacant anatase is populated by electrons, which in principle allows for  $dd$  excitations. For energy losses much smaller than the crystal field,  $dd$  electronic transitions can be safely excluded and we expect no significant electronic-spectator contributions to the RIXS final state. At energy loss energies comparable to the crystal field however,  $dd$  derived spectator processes can become visible where the excitation process is into the “ $e_g$ ” manifold but the de-excitation originates from “ $t_{2g}$ ” derived states [142, 143]. In our spectra, this process appears as marked fluorescence, which extrapolated to zero energy loss closely relates to the main XAS peak A3 (black dashed line), i.e. the “bottom of the conduction band”. We will show in a later section that this fluorescence can be completely suppressed by oxidation of  $\text{Ti}^{3+}$  to  $\text{Ti}^{4+}$  – or in other words by depletion of the “ $t_{2g}$ ” states.

### 4.6 RIXS symmetry selection in anatase

The low energy loss part of the RIXS spectra contains primarily the vibrational excitations of anatase. Thereof, only modes of  $A_{1g}$ ,  $B_{1g}$  and  $E_g$  symmetry are Raman active [144, 145].

At photon energies featuring absorption peaks A1-A3, the nature of the intermediate state according to MCMS is highly excitonic and the excited electron will remain localized close to the core hole. The electron thus efficiently screens the core hole potential and the effective on site charge remains constant. Close to absorption peaks B1 and B2 however, the excited intermediate state electron delocalizes, resulting in an unscreened core hole charge which locally distorts the lattice. In the subsequent de-excitation process, an electron refills the Ti  $2p$  core hole, leaving the lattice in a vibrating state and yielding a progression of phonon emission lines, which form the asymmetry of the elastic peak in RIXS.

In order to get some feeling for the nature of the observed phonon excitations, we start from simple symmetry considerations, as discussed in detail in Ch. 2. Anatase has point group symmetry  $D_{4h}$ , and formally a completely empty conduction band  $d^0$ . The symmetry of the ground state wave function is thus spherical  $A_{1g}$ . In an experimental geometry with  $\pi$ -polarized light, the dipole operator  $T^\pi$  is parallel to the scattering plane  $yz$  (compare to Fig. 4.5) and is thus contained in the irreducible representations  $E_u$  and  $A_{2u}$  of  $D_{4h}$ . Given the weak spin orbit coupling of the Ti  $3d$  carriers and the absence of electronic excitations in the “quasi elastic” response<sup>4</sup> of the low energy loss features, it is safe to assume conservation of polarization in the de-excitation process.<sup>5</sup> The dipole allowed final states are thus contained in  $A_{1g} \otimes (E_u \oplus A_{2u})^2 = A_{1g} \oplus A_{2g} \oplus B_{1g} \oplus B_{2g} \oplus E_g$ . After the RIXS process, the system so can either return into its original ground state  $A_{1g}$  (resonant elastic scattering) or into some excited state of  $A_{1g}$ ,  $A_{2g}$ ,  $B_{1g}$ ,  $B_{2g}$  or  $E_g$  symmetry [56, 146]. We thus can expect all Raman allowed phonon branches  $A_{1g}$ ,  $B_{1g}$  and  $E_g$  in this experimental configuration. In contrast to  $\pi$ -polarization,  $\sigma$ -polarized light  $T^\sigma$  is only contained in the  $E_u$

<sup>4</sup>The term “quasi elastic” means that the electronic quantum numbers are conserved for the low energy excitations. We further neglect electron-hole excitations of the doped in carriers, which is justified by the symmetric lineshape of the elastic peak close to A1, A2 and A3.

<sup>5</sup>This argument is rigorously shown to hold in Ch. 2.

irreducible representation of  $D_{4h}$  and the dipole allowed final states do thus *not* contain the  $E_g$  modes anymore.

A detailed polarization study compared to the model introduced in Ch. 2 is thus absolute prerequisite for a proper identification of the phonon modes observed.

**RIXS angular dependence in  $\sigma$ -polarization**

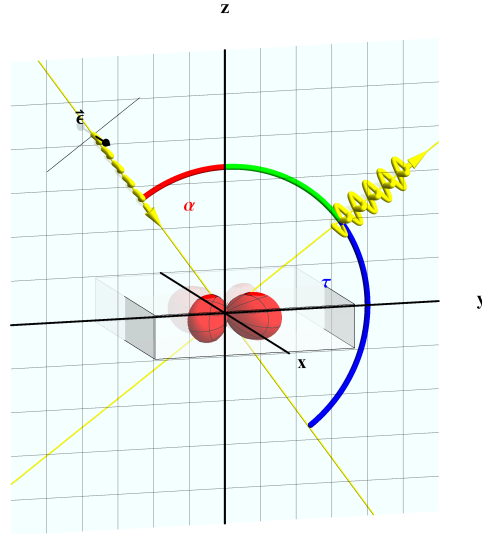


Figure 4.2: RIXS experimental configuration with scattering angle  $\tau = 90^\circ$  in  $\sigma$ -polarization ( $\xi = 0$ ).

We start with an angular dependence study in  $\sigma$  polarization (compare to Fig. 4.2), where we only expect phonon modes  $A_{1g}$  and  $B_{1g}$  to contribute to the low energy RIXS spectral weight – independently of the incident photon angle  $\alpha$  as discussed in Ch. 2. Fig. 4.3 (a) shows RIXS spectra taken at several angles  $\alpha$  between grazing incidence and grazing emission. The data was normalized to integration time and photon flux. For direct comparison, we also plot the Ti L-edge absorption spectrum (pink dashed). Clearly, signal is dominated by elastic Thomson scattering, resulting in the large elastic peak maximizing in specular reflection  $\alpha = 45^\circ$ . A close up of the same data in panel 4.3 (b) reveals a  $p^5d^1$  charge transfer (CT) excitation structure and the fluorescence (F) feature in detail. Except for the data at  $\alpha = 5^\circ$ , the charge transfer structure is essentially  $\alpha$  independent.

The XAS spectrum indicates that absorption of the RIXS spectra in the charge transfer energy region ( $h\nu \sim 450\text{-}455$  eV) is very small and self absorption only affects angles close to grazing emission (compare to Fig. 2.7), as we indeed see in this measurement. In contrast, the fluorescence (here at  $h\nu \sim 458$  eV) is subject to strong absorption and the intensity therefore suppressed almost linearly from grazing incidence towards grazing emission.

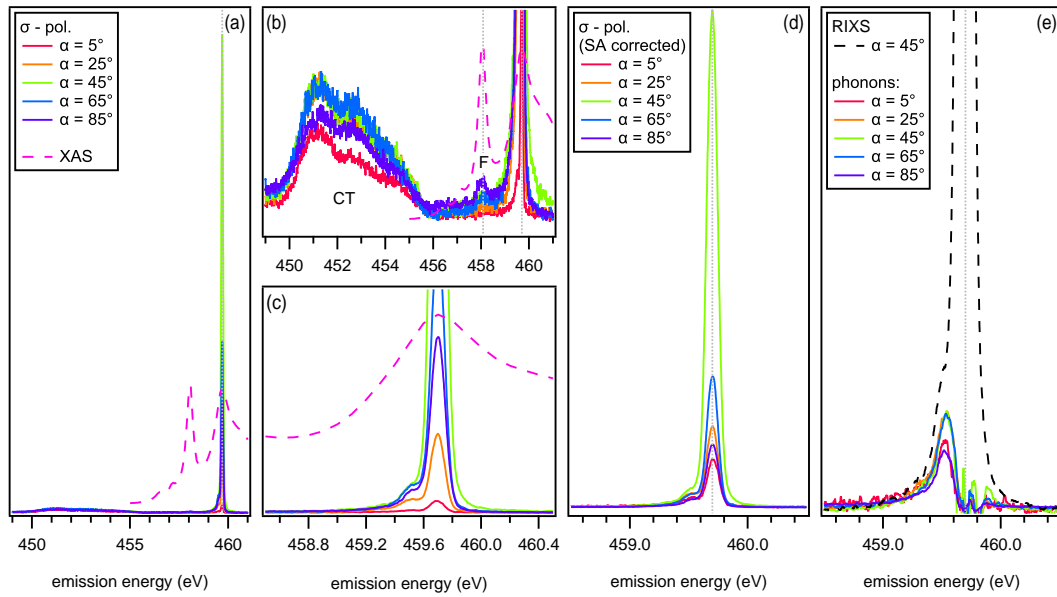


Figure 4.3: RIXS angular dependence in  $\sigma$ -polarization. The pink dashed line indicates the XAS spectrum. **(a)** Data normalized to flux and acquisition time. **(b)** Close up of low intensity part of (a). **(c)** Close up of the low energy loss part of (a). **(d)** Self absorption corrected close up of the low energy loss part. **(e)** Phonon part obtained by subtracting a Voigt profile from the data of (d).

The same accounts for the low energy excitations close to the zero energy loss. A close up of the low energy loss part is shown in panel 4.3 (c). Clearly, the low energy shoulder – as is the elastic peak – is subject to significant intensity variation with  $\alpha$ . Making use of eq. 2.31, we apply a self-absorption correction (SA) and redraw the data in panel 4.3 (d).

The behavior of the elastic line is difficult to analyze quantitatively since resonant processes cooperate with non resonant Thomson scattering. However we see a clear rise of intensity from  $\alpha = 0$  to  $45^\circ$  and a reduction of intensity towards  $85^\circ$ . As shown in Fig. 4.4 (a), elastic intensity is distributed asymmetrically around the specular configuration  $\alpha = 45^\circ$ .<sup>6</sup> The shoulder intensity however is distributed rather symmetrically around the specular angle  $\alpha = 45^\circ$ . To separate out the phonon contributions and to obtain more quantitative information on the phonons' angular dependence, we fit a Voigt profile to the elastic line, subtract it from the data and show the residual in Fig. 4.3 (e). From  $25^\circ$  to  $65^\circ$ , the phonon spectra overlap. This is in agreement with our polarization model of Ch. 2, which suggests spectral weight of Raman allowed phonon modes of  $A_{1g}$  and  $B_{1g}$  to be  $\alpha$  independent.

However, we recognize significant deviations of the phonon intensity at grazing incidence  $\alpha = 85^\circ$  as well as grazing emission  $\alpha = 5^\circ$ . Overall, this can be explained by the large error introduced by subtracting the intense elastic line. At grazing emission, the variation might additionally be due to low statistics and to a large error in the self absorption correction induced

<sup>6</sup>which might just indicate a miscalibration of  $\alpha = 0$

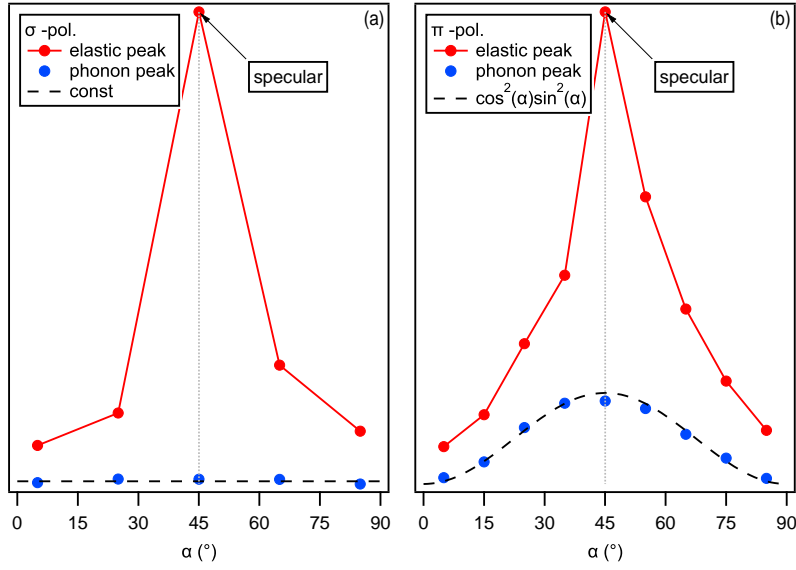


Figure 4.4: Relative angular dependence of RIXS spectral weight associated to elastic and phonon contributions for (a)  $\sigma$ - ( $\xi = 0^\circ$ ) and (b)  $\pi$ -polarization ( $\xi = 90^\circ$ ).

by the uncertainty of  $\alpha$  (compare to Fig. 2.7). The deviation at grazing incidence however can be explained by significant aberration effects due to the elongated beamspot on the surface.

### RIXS angular dependence in $\pi$ -polarization

We now turn our attention to the  $\pi$ -polarized configuration (Fig. 4.5), where according to Ch. 2 all Raman active phonon modes – including  $E_g$  – should be allowed in the RIXS process. Fig. 4.6 (a) shows RIXS spectra taken at several angles  $\alpha$  between grazing incidence and grazing emission. Again, data was normalized to integration time and photon flux.

With respect to the  $\sigma$ -polarized spectra, Thomson scattering diminished considerably and the overall signal is dominated by resonant processes. As before, the charge transfer excitations are largely  $\alpha$  independent, with the two exceptions of grazing incidence and emission. At grazing emission, we assume the self absorption effect again to be the dominant source of suppression whereas aberration effects modify the spectral weight at grazing incidence.

At emission energy  $h\nu' \sim 458$  eV we observe a clear self absorption effect of the fluorescence feature. A similar but less systematic self absorption effect is repeated close to the elastic line. Panel 4.6 (b) presents a close up of self absorption corrected RIXS data. From grazing incidence, elastic as well as inelastic features show a clear intensity rise towards a maximum at the specular angle  $\alpha = 45^\circ$ . From here, intensity again diminishes towards grazing emission. Like in  $\sigma$  polarization, phonon spectral weight is distributed rather symmetrically around the specular angle  $\alpha = 45^\circ$  whereas the elastic scattering strength is distributed slightly asymmetrically. Panel 4.6 (c)



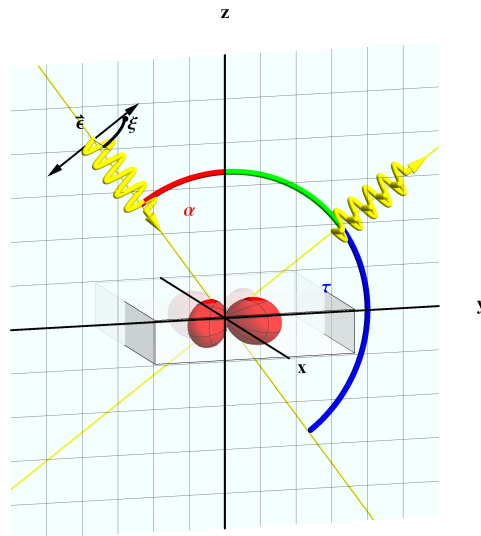


Figure 4.5: RIXS experimental configuration with scattering angle  $\tau = 90^\circ$  in  $\pi$ -polarization ( $\xi = 90^\circ$ ).

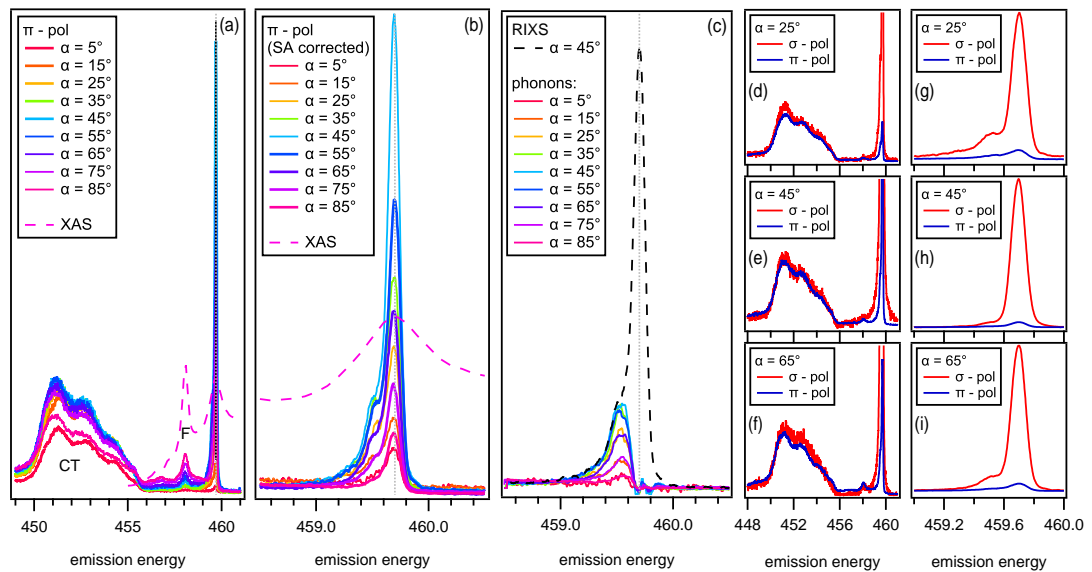


Figure 4.6: RIXS angular dependence in  $\pi$  polarization. **(a)** Data normalized to flux and acquisition time. **(b)** Close up of the self absorption corrected low energy loss part of the data of (a). **(c)** Phonon part obtained by subtracting a Voigt profile from the data of (b). **(d-f)** An absolute comparison of the self absorption corrected data in  $\sigma$  and  $\pi$  polarization shows a good match of the CT peaks. **(g-i)** The same comparison of the low loss energy part shows the phonon cross section for RIXS to be larger in  $\sigma$  polarization.

shows the data subtracted by a Voigt profile in order to isolate the phonon excitations. In contrast to data in  $\sigma$ -polarization, the intensity of the phonon background now shows a symmetric rise and fall around  $\alpha = 45^\circ$  as summarized in Fig. 4.4. We therefore once more independently assign the phonon modes to  $A_{1g}$  or  $B_{1g}$  symmetry final states, which according to Fig. 2.5 indeed behave as  $\propto \cos^2 \alpha \sin^2(\alpha)$  in  $\pi$ -polarization.

### $\sigma$ vs $\pi$ -polarization

We now compare the absolute intensity of the RIXS spectra – normalized by acquisition time and photon flux and self absorption corrected – in Fig. 4.6 (d-i). For three angles,  $\alpha = 25^\circ$ ,  $45^\circ$  and  $65^\circ$ , we clearly see that the charge transfer excitations in both polarizations exhibit about the same spectral weight. Same accounts for the fluorescence, which is a good sign for the validity of the self absorption correction. However, the overall spectral weight for the phonon contributions is about a factor 4 lower in  $\pi$  with respect to  $\sigma$ -polarization. At  $25^\circ$  and  $65^\circ$ , this factor is even higher as we indeed expect from the polarization model of Ch. 2.

We conclude that despite its simplicity, the local model introduced in Ch. 2 can give an “educated guess” of which final states to expect in which experimental geometry. This model therefore may be useful for the experimentalist investigating an a priori unknown system with a known ground state symmetry.

## 4.7 Doping dependence of the elastic contributions

We now turn to the doping dependence of the phonon resonance. Fig. 4.7 summarizes spectra measured at the resonance  $h\nu = 459.6$  eV (B1) and in  $\pi$  polarization. We chose two different experimental configurations, with ( $\alpha = 68^\circ$ ) and without ( $\alpha = 45^\circ$ ) a momentum transfer component  $q_{\parallel}$  within the 001 plane as outlined in Fig. 4.8. In both configurations, spectra were measured with (blue) and without (red) exposure to a small oxygen partial pressure. An overview of the normalized and self absorption corrected data is shown in panel 4.7 (a).

Clearly, exposure to O<sub>2</sub> enhances the elastic line while it suppresses the fluorescence. Nevertheless, the fluorescence peaks in  $\alpha = 45$  and  $68^\circ$  configuration are nicely aligned, respectively, demonstrating again the validity of the self absorption correction. A close up of the zero energy loss region is shown in Fig. 4.7 (b). All spectra exhibit a clear shoulder to the high energy side of the elastic scattering peak. As expected, the relative elastic contribution is significantly enhanced for samples in  $\alpha = 45^\circ$  specular geometry.

The observed oxygen pressure dependence is a direct consequence of the surface and subsurface stoichiometry: as demonstrated in the ARPES study of Ch. 3, soft x-rays of sufficient flux create oxygen vacancies and populate the bottom of the conduction band. If simultaneously exposed to oxygen, a dynamic equilibrium between defect creation and re-oxidation can reduce the free charge carrier concentration from  $\sim 10^{20}$  cm<sup>-3</sup> to  $\sim 10^{18}$  cm<sup>-3</sup>. This net decrease of free charge

## 4.7. Doping dependence of the elastic contributions

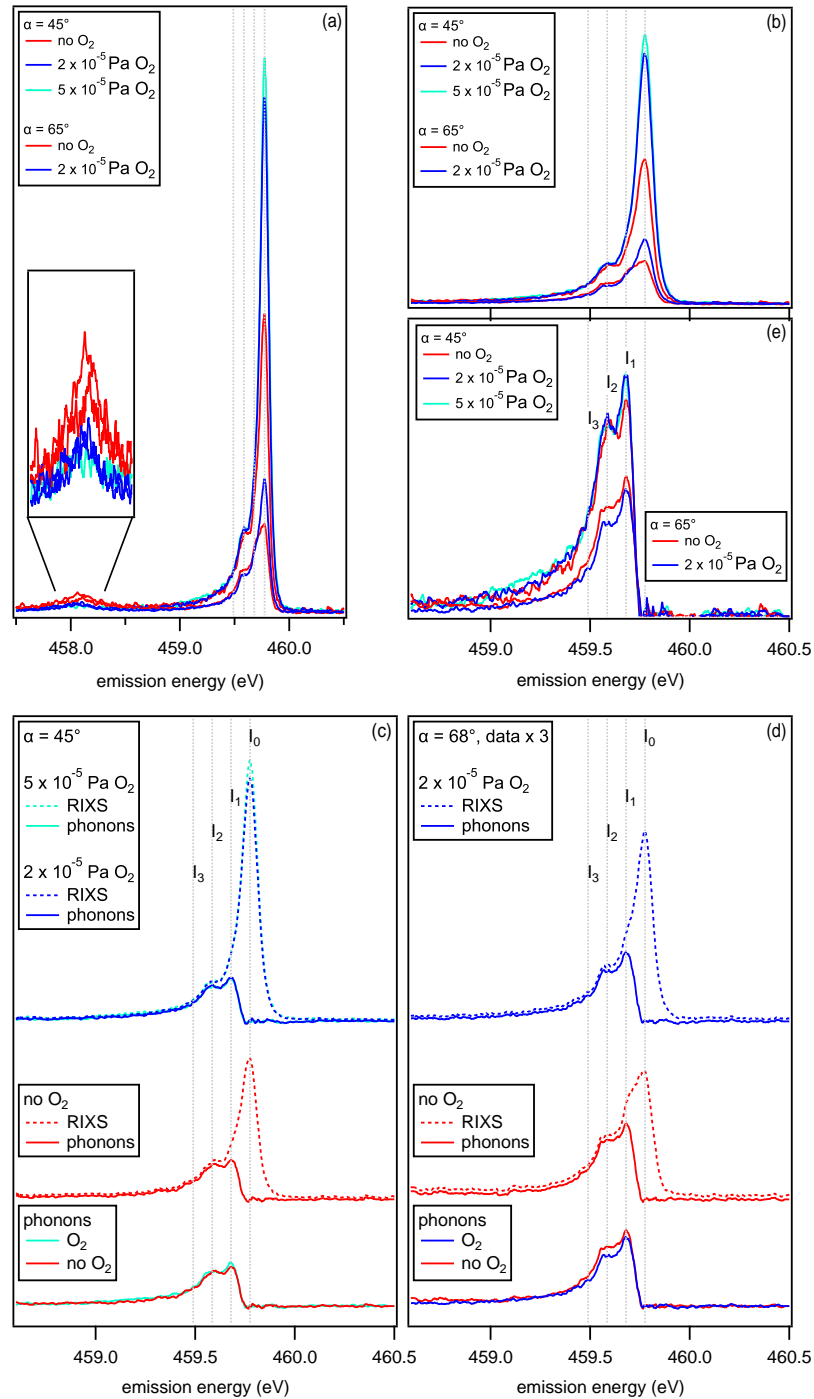


Figure 4.7: RIXS data taken with  $h\nu = 459.6$  eV and  $\pi$ -polarized light with **(blue)** and without **(red)** an oxygen partial pressure. Spectra were acquired in two scattering geometries with ( $\alpha = 68^\circ$ ) and without ( $\alpha = 45^\circ$ ) a component of the in plane momentum transfer  $q_{\parallel}$ . **(a)** Samples treated with oxygen develop a larger elastic line but a lower fluorescence. **(b)** Close up of the data in (a). The elastic line is strongly  $O_2$  pressure dependent, the phonon lines are not. **(c)** Analysis of the data at  $\alpha = 68^\circ$ . The phonon contributions are equivalent with and without  $O_2$ . **(d)** Analysis of the data at  $\alpha = 45^\circ$ . The phonon contributions are equivalent with and without  $O_2$ . **(e)** Absolute comparison of the phonon lineshape.

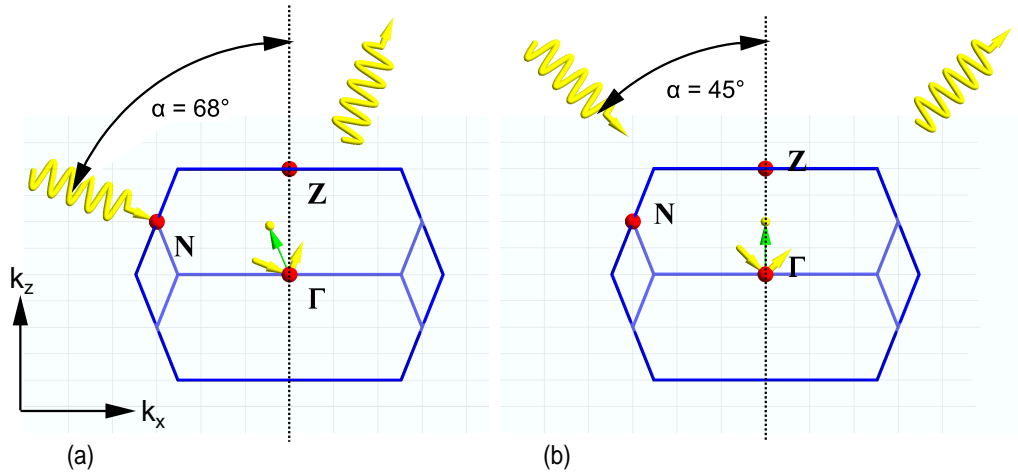


Figure 4.8: RIXS experimental configuration with scattering angle  $\tau = 90^\circ$  in  $\pi$ -polarization ( $\xi = 90^\circ$ ). The blue lines show the projections of the 3D BZ of anatase onto the  $k_y = 0$  plane **(a)**  $\alpha = 68^\circ$  contains a small in plane component  $q_{||}$  of the momentum transfer. **(b)**  $\alpha = 45^\circ$  contains no plane component of the momentum transfer and  $q_{||} = 0$ .

is marginal with respect to the gross number of electrons in the system. Non-resonant Thomson scattering – probing mostly the total charge density and typically enhanced by defects – so is *not* at the origin of the elastic line modulation.

However, the elastic peak is affected by resonant scattering processes which are sensitive to the number of inelastic decay channels from the intermediate state  $|i\rangle$  [147]. An increasing amount of oxygen defects – corresponding to an increasing number of free conduction band carriers – will thus reduce the elastic scattering intensity in favor of alternative processes like Coster-Kronig decay from the lower conduction band, which is expressed in the increase of fluorescence. The fluorescence  $I_f$  – described by a transition  $|2p\rangle \rightarrow |k\rangle$  followed by  $|d_{xy}\rangle \rightarrow |2p\rangle$ , where  $|k\rangle$  is an occupied  $3d t_{2g}$ -band state above  $E_F$  – will rise with the number of  $d_{xy}$  electrons, i.e. the number of oxygen defects. Furthermore, the elastic scattering intensity is reduced in favor of an elastic resonant photoemission channel which will be shown in a further publication [148]. Interestingly, such an oxygen pressure dependence is absent at the O K-edge, which is discussed in section 4.10.

## 4.8 Doping dependence and nature of the phonons

We focus now solely on the low energy excitations, i.e. the phonon contributions. The top part of Fig. 4.7 (c-d) repeat the spectra of samples exposed to oxygen from panel 4.7 (b). Additionally, we plot the difference spectra obtained by subtracting a Voigt profile from the data - the net phonon contribution. The middle part of the graphs plot the corresponding spectra without oxygen

exposure. In the bottom part, an absolute comparison of the phonon contribution for spectra with and without oxygen is shown. Apart from slight deviations resulting from the Voigt fits – especially what concerns the  $\alpha = 68^\circ$  configuration – the phonon contributions are strikingly similar. Analogous to a generalized Franck-Condon picture in molecules [137], the “one phonon” line  $I_1$  at  $\hbar\omega_0 \sim 95$  meV is followed by two vibronic satellites  $I_2$  and  $I_3$ , successively separated by the energy of one phonon mode  $\hbar\omega_0$ .

As shown in detail in Ref. 136 and mentioned in the introduction, the relative intensity of the “two phonon” line  $I_2/I_1$  gives a direct measure of the e-ph coupling constant. Unlike in ARPES however, the RIXS amplitude of  $I_1$  would remain dominant even in the case of very strong e-ph coupling.

Indeed, first principle calculations have obtained a phonon branch of  $A_{1g}$ ,  $B_{1g}$  and  $E_g$  symmetry in between  $\hbar\omega = 65$  and 85 meV [145, 149]. These modes were further confirmed by Raman experiments to be  $\hbar\omega_{B_{1g}} = 64.3$  meV,  $\hbar\omega_{A_{1g}} = 63.6$  meV and  $\hbar\omega_{E_g} = 79.2$  meV [110]. These values are significantly lower than the ones observed by RIXS, a fact that we do not completely understand to this point. RIXS is probing the phonon far away from the BZ center. Thus one could speculate that the phonon dispersion leads to this deviation. More importantly, the parity is not well defined at k-points away from  $\Gamma$  and odd phonon modes could contribute significantly to the signal. One has to bear in mind however that RIXS most likely probes also a sum over much lower energy phonons, which certainly contribute to the observed lineshape.

Fig. 4.7 (e) summarizes all phonon modes and compares their absolute spectral weight. Despite the matrixelement suppression at  $68^\circ$  discussed in Ch. 2, the spectral lineshapes are very similar. Within the accuracy of the experiment we therefore neither resolve a directionality nor a real doping dependence of the e-ph coupling strength.

## 4.9 A generalized Franck Condon model

The spectra can be reproduced by a simple model described in detail in Ref. 136 by Ament et al. Starting from the Fröhlich Hamiltonian of one longitudinal optical Einstein phonon mode  $\hbar\omega_0$

$$H = \sum_R M d_R^\dagger d_R (b_R^\dagger + b_R) + \sum_R \omega_0 b_R^\dagger b_R, \quad (4.1)$$

an analytic solution for the RIXS amplitude in the Kramer Heisenberg picture was found to be

$$A_{Einstein} = \sum \frac{B_{\max(n,n'), \min(n',n)}(g) B_{n,0}(g)}{z + (g - n)\omega_0}, \quad (4.2)$$

where  $g = M^2/\omega_0^2$  encrypts the e-ph coupling strength and  $z = \omega_{det} + i\Gamma$  covers core hole lifetime  $\Gamma$  and the detuning energy from the L-edge resonance  $\omega_{det}$ .  $B_{m,n}(g)$  are Franck Condon overlap factors expressed as

$$B_{m,n} = (-1)^m \sqrt{e^{-g} m! n!} \sum_{l=0}^n \frac{(-g)^l \sqrt{g}^{m-n}}{(n-l)! l! (m-n+l)!}. \quad (4.3)$$

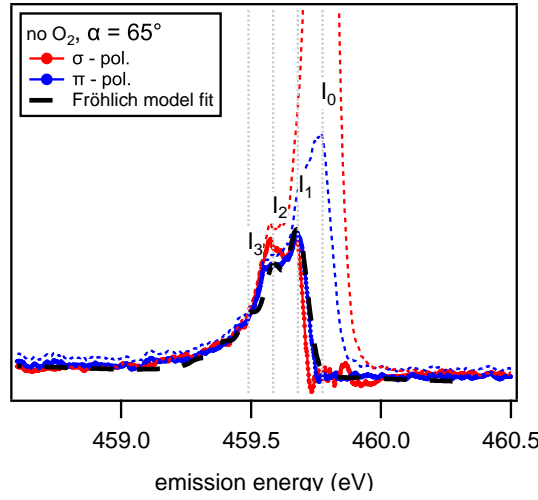


Figure 4.9: Representative phonon lineshapes obtained in  $\sigma$  (red) and  $\pi$ -polarization (blue). For completeness we also plot the self absorption corrected RIXS data (blue/red dashed). The phonon lines are fit by the model obtained by L. Ament et al. (black dashed) for  $\hbar\omega_0 = 95$  meV and  $\Gamma = 0.75$  eV [136]

Fig. 4.9 shows representative phonon spectra in  $\pi$ - and  $\sigma$ -polarization. The fact that these spectra are exhibiting essentially identical lineshapes once more justifies the assignment to  $A_{1g}$  and  $B_{1g}$ , since  $E_g$  components – potentially allowed in  $\pi$ -polarization – do not contribute significantly to the lineshape.

We further superpose a fit of  $|A|^2$  calculated with parameters  $\Gamma = 375$  meV,  $\omega_0 = 95$  meV,  $\omega_{det} = 0$  and  $M = 130$  meV.<sup>7</sup> This result of  $M$  is in nice agreement with the value of  $M_0$  obtained by ARPES and demonstrates the validity of the local model. In an independent approximation,  $M$  can be estimated from the height ratio of the “two” to the “one-phonon line”:  $A_2/A_1 = M/z^2$ . With  $I_2/I_1 = (A_2/A_1)^2 \sim 0.78\dots 0.94$  extracted from the data, we find  $M \sim 125\dots 136$  meV, in good agreement with above value. One always has to keep in mind however that these values are very sensitive to the self absorption correction and the Voigt fit procedure isolating the phonon modes.

<sup>7</sup> $\Gamma = 375$  meV was obtained from a Gaussian fit of the XPS data in Fig. 3.8.

## 4.10 Phonons at the oxygen K-edge

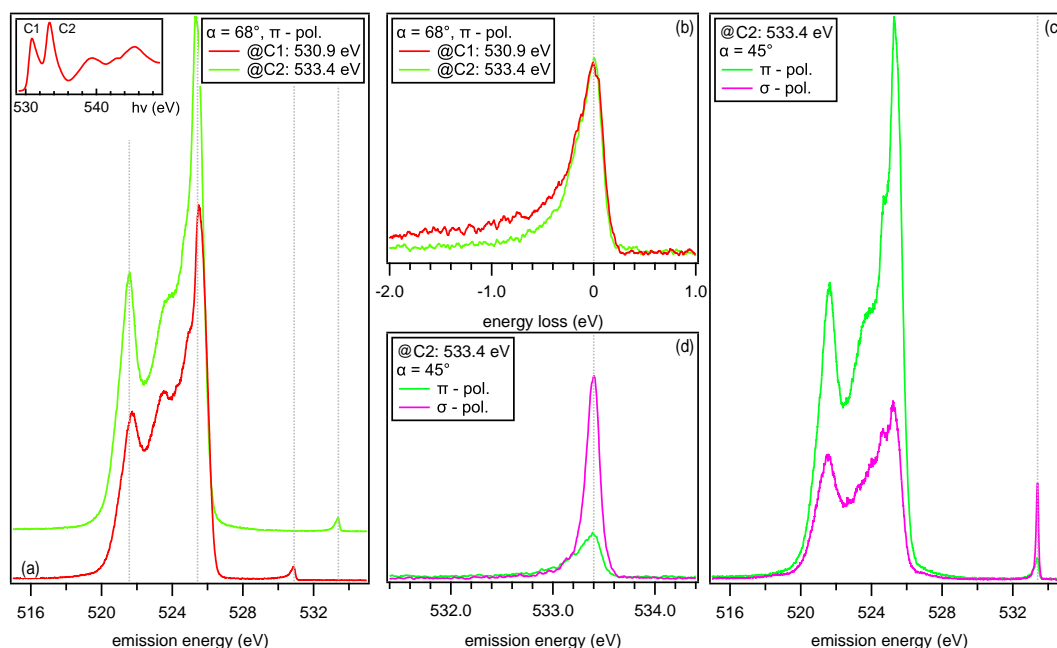


Figure 4.10: RIXS data at obtained at the oxygen K-edge. The spectrum is dominated by an intense fluorescence. **(a)** RIXS data at peaks C1 and C2 of the (inset) absorption spectrum. **(b)** The low loss energy part is largely excitation energy independent. **(c)** While the fluorescence dominates in  $\pi$  polarization, the elastic line dominates in  $\sigma$  polarization **(d)**.

Having shown the clear presence of multi phonon excitations at the Ti L-edge, we finally will turn to the resonance behavior at the oxygen K-edge.

Fig. 4.10 (a) shows RIXS data acquired at 530.9 eV and 533.4 eV photon energy, corresponding to peaks C1 and C2 of the related XAS (inset). The data was acquired in  $\pi$ -polarized light and  $\alpha = 68^\circ$ , normalized to flux and acquisition time and further self absorption corrected. We identify a very intense feature centered at  $h\nu' \sim 524$  eV. Its energy position is clearly independent of the excitation energy and it consequently can be attributed to a strong fluorescence related to the dominating charge transfer processes at the oxygen K-edge. Panel 4.10 (b) shows a closeup of the elastic feature, which exhibits an asymmetric lineshape. In contrast to RIXS at the Ti L-edge, this asymmetry seems largely excitation energy independent.

The reason for this energy independence is found in the fundamental difference of the underlying absorption process [150, 151]. The ground state configuration is  $1s^2 2s^2 2p^6$  and the  $1s \rightarrow 2p$  channel is formally closed. The O  $2p$ -states therefore are only visible as result of the covalent bonding of O  $2p$  with Ti  $3d$  states. Due to negligible Coulomb interaction between core hole and excited electron, multiplet effects are rather weak and the XAS spectrum to a large extent represents the unoccupied density of states of the Ti  $3d$  manifold with core hole [78, 91]. The first

two peaks C1 and C2 correspond respectively the empty “ $t_{2g}$ ” and “ $e_g$ ” states of the 3d conduction band, whereas the higher energy structures are related to the titanium 4s- and 4p-bands. The delocalization effect throughout the entire intermediate regime will thus allow vibronic excitations throughout the absorption threshold, as discussed in detail for the Ti L-edge in section 4.6.

Formally, the absorption process needs to consider an O 1s to O 2p transition and in symmetry terms, there is an approximately equal amount of oxygen 2p character in the “ $t_{2g}$ ” band as in the “ $e_g$ ” band. Thus – similar to the Ti L-edge, no strict intermediate state selection rule applies. We thus expect all Raman allowed phonon branches  $A_{1g}$ ,  $B_{1g}$  and  $E_g$  in  $\pi$  polarization, whereas the  $E_g$  mode is suppressed in  $\sigma$  polarization.

Fig. 4.10 (c) shows two spectra measured with  $\alpha = 68^\circ$  at XAS peak C2, comparing  $\sigma$  and  $\pi$  polarizations. As we discussed at the Ti L-edge,  $\sigma$  polarization results in a stronger elastic line, whereas its fluorescence seems to be largely suppressed. As shown in the close up of panel 4.10 (d), the phonon tail however seems – despite the influence of the elastic line – of equal spectral weight.

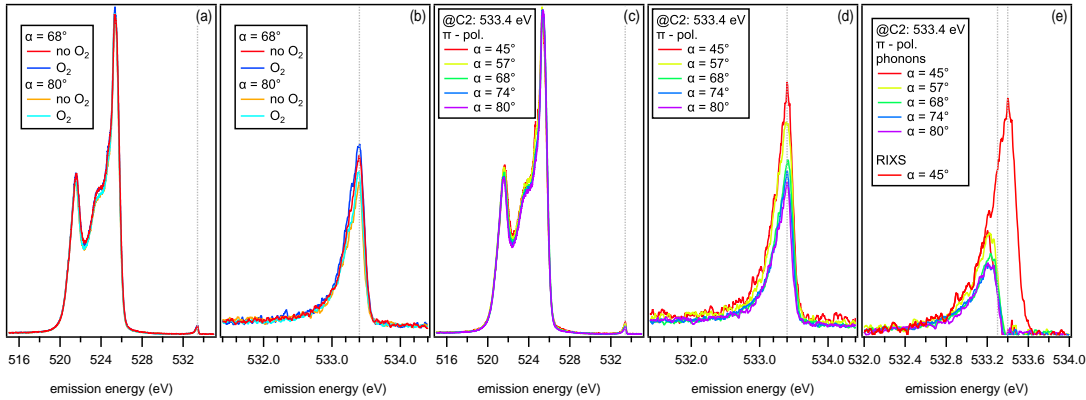


Figure 4.11: Doping dependence of self absorption corrected RIXS data at the oxygen K-edge measured at C2. Both the fluorescence (a) and the elastic feature (b) are only slightly affected geometry and oxygen exposure. (c) The fluorescence is essentially  $\alpha$  independent whereas inelastic peak (d) and phonons (e) vary according to the expectations for  $A_{1g}$  and  $B_{1g}$  final states.

Fig. 4.11 (a-b) show the oxygen vacancy doping dependence. Exposure to oxygen here only has a slight effect on the intensity of the elastic peak and the fluorescence, respectively. The angular dependence of panel 4.11 (c) shows the fluorescence to be quite independent of  $\alpha$ , whereas a continuous suppression of phonons and elastic line towards grazing incidence is noticed in panel 4.11 (d). The isolated phonon part in panel 4.11 (e) shows the same suppression, as expected for the  $A_{1g}$  and  $B_{1g}$  modes in  $\pi$  polarization.

With respect to spectra taken at the Ti L-edge, the oxygen K-edge data is rather featureless. Besides, spectra are independent on the oxygen partial pressure as well as on the experimental geometry. We conclude that several oxygen derived phonon modes build up the RIXS spec-



#### 4.10. Phonons at the oxygen K-edge

---

tral weight. Their insensitivity to the formation of oxygen vacancies suggests a dominating contribution of the centro-symmetric oxygen breathing modes [144].



# 5 T-CuO – a 2D edge-sharing cuprate investigated by ARPES

## 5.1 Summary

In this chapter, we introduce a new cuprate – tetragonal CuO – and reveal its electronic band structure by means of in situ ARPES. Data interpretation in the framework of the extended t-J model reveals the Zhang Rice Singlet nature of the first ionization state. These findings constitute the first observation of the ZRS on a model 2D *edge-sharing* cuprate system. Based on our observation, a prediction on the electronic structure in the doped system is given.

## 5.2 Motivation

Since the discovery of the high temperature superconducting cuprates (HTSC), there has been an ongoing quest to understand the underlying physics and to synthesize new materials with higher and higher transition temperature [152–156]. Soon it was realized that the correlated electron physics in the two dimensional CuO<sub>2</sub> planes was probably responsible for the unusual properties of these new materials. Binary CuO therefore was studied as a prototypical insulating parent compound in view of its simpler stoichiometry.

However, CuO only crystallizes in a monoclinic crystal structure called tenorite which – in contrast to the cuprates – does not contain the archetypical CuO<sub>2</sub> plane with perfect Cu-O-Cu bond angle of 180°. Due to the low symmetry, CuO strongly deviates from the physical trends extrapolated from the lower group transition metal monoxides.

In 2009, Siemons et al. have shown that a higher-symmetry tetragonal phase of CuO (T-CuO) can be obtained as thin films epitaxially grown on top of SrTiO<sub>3</sub> (001) substrates by means of PLD with a crystallographic structure much closer to the one of the cuprates [157, 158]. Most importantly, an extremely stable Néel ground state with transition temperatures up to 800 K has been predicted in Refs. 159 and 160 and  $T_N \sim 600$  K has been claimed experimentally in Ref. 161.

These findings identify T-CuO as new cuprate with presumably peculiar electronic properties in the insulating phase. In the doped compound, this might even lead to new phases of high temperature superconductivity.

### 5.3 Methods

Sample growth and ARPES experiments were performed at the electronic structure factory endstation at beamline 7 of the Advanced Light Source, Lawrence Berkeley National Laboratory. T-CuO was grown as in Refs. [157] and [158] by PLD on a 0.5% Nb-doped (001) SrTiO<sub>3</sub> (STO) substrate. During the deposition, the substrate was kept at 550°C in  $1.3 \times 10^{-3}$  mBar 93.4 % O<sub>2</sub> / 6.6 % O<sub>3</sub> atmosphere. The epitaxial film growth was monitored by *in situ* reflection high energy electron diffraction (RHEED). After deposition, the sample was cooled down to room temperature in the same ozone atmosphere. Fig. 5.1 shows the RHEED images measured before (a) and after the film growth (b). T-CuO clearly adopts the lateral lattice constant of STO (001)  $a = 3.905$  Å. Moreover, the RHEED image does not show any superstructure corresponding to a possible surface reconstruction. Samples were then transferred in UHV ( $p < 10^{-10}$  mbar) to the ARPES chamber, where they were cooled down to 60 K before the measurements. Due to the thinness of the insulating films, no charging effects were observed.

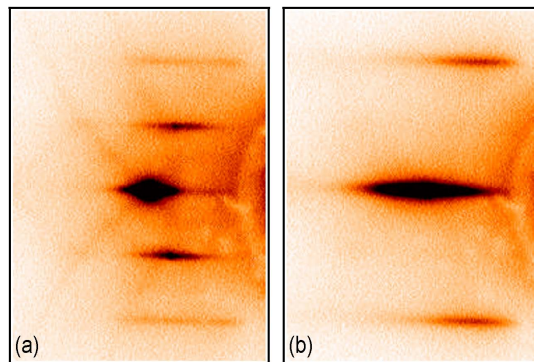


Figure 5.1: RHEED image of (a) clean STO(001), and (b) a thin film of T-CuO.

### 5.4 Film characterization

The lattice parameters of the T-CuO thin films were determined *in situ* by x-ray photoelectron diffraction (XPD) and *ex situ* by x-ray diffraction (XRD) measurements. XPD data at the O 1s threshold was taken with 980 eV, data at the Cu 3p<sub>3/2</sub> threshold with 530 eV photon energy. The measurements show excellent agreement with multiple scattering calculations for  $c = 5.3$  Å from Ref. 157 (Fig. 5.2). Besides the fourfold symmetry, the data reproduce the detailed interference structure predicted by theory.

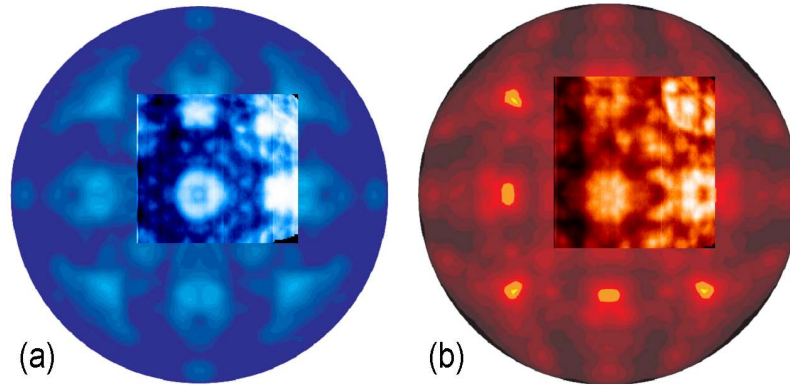


Figure 5.2: In situ XPD of T-CuO (a) for the O  $1s$  and (b) the Cu  $2p_{3/2}$  levels. The regions outside the rectangular inlays reproduce the calculated patterns from Ref. 157.

The XRD measurements were performed after the sample had been exposed for several weeks to atmosphere. A  $\theta - 2\theta$  scan (Fig. 5.3 (a)) yielded a lattice constant  $c = 5.340 \pm 0.002$  Å. Fig. 5.3 (b) is a close-up of the CuO (004) peak, which is  $\sim 10\times$  less intense than the (002) peak, as expected for a  $bct2$  lattice. A film thickness of 6 unit cells was estimated from the RHEED oscillations, as well as from low-angle reflectometry<sup>1</sup> and from a line shape analysis of the (002) XRD peak.<sup>2</sup>

## 5.5 From tenorite to T-CuO

Placing copper and oxygen atoms alternating on the vertices of a cubic lattice would – by symmetry – result in degenerate  $e_g(d_{x^2-y^2}, d_{z^2})$  bands. Since the electron valency is  $3d^9$  these bands would be  $3/4$  occupied. Due to the strong Coulomb repulsion however, such an occupancy is energetically unfavorable and Jahn Teller distortion forces the lattice towards lower symmetry, lifting the orbital degeneracy and reducing the total energy [159, 160, 162]. In contrast to most members of the transition metal monoxide family, this tendency to leave the cubic phase is very pronounced, and CuO naturally is found in the highly asymmetric monoclinic phase tenorite of  $C_{2/c}$  symmetry with lattice parameters,  $a = 4.6837$  Å,  $b = 3.4226$  Å,  $c = 5.1288$  Å,  $\beta = 99.54^\circ$  and bond lengths  $d_{Cu-Cu} = 2.9$  Å,  $d_{Cu-O} = 1.95$  Å and  $d_{O-O} = 2.62$  Å. Though still a “classic” ‘charge transfer insulator, the Cu-O-Cu bond angle of  $146^\circ$  strongly deviates from  $180^\circ$ . According to Fig. 5.4 this reduces the exchange interaction parameter  $J$  and causes

<sup>1</sup> The low angle reflection signal obtained in XRD can be fitted by the Parratt model (e.g. program bocfit) and allows for an independent determination of thickness and roughness of the thin films. We yield a film thickness  $d \sim 27 \pm 3$  Å  $\sim (5.1 \pm 0.6) c$  and a surface roughness of about  $\sim 0.5$  Å which may explain why RHEED oscillations were particularly weak.

<sup>2</sup>The FWHM of the diffraction peak can be used to estimate the approximate film thickness via the Scherrer equation  $d = K\lambda_{h\nu}/FWHM \cos \theta$ , where  $K$  is the shape factor,  $\lambda_{h\nu}$  is the x-ray wavelength, and  $\theta$  is the Bragg angle. Assuming a typical shape factor of  $K \sim 1.1 \pm 0.3$ , we extract  $d \sim 38 \pm 11$  Å  $\sim (7.1 \pm 2.1) c$ .

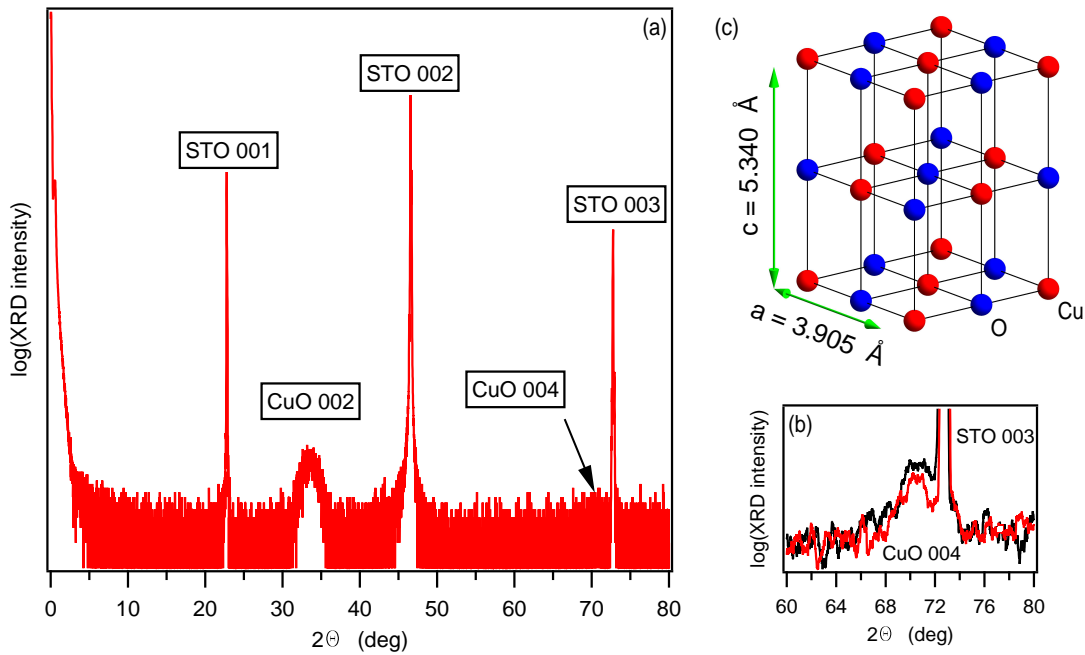


Figure 5.3: (a) Ex situ XRD on T-CuO. The absence of the (001) and (003) peaks indicate a  $bct2$  crystal structure. The lattice constant  $c$  can be determined from analysis of the (002) and (004) peaks in (b). The resulting crystal structure is shown in (c).

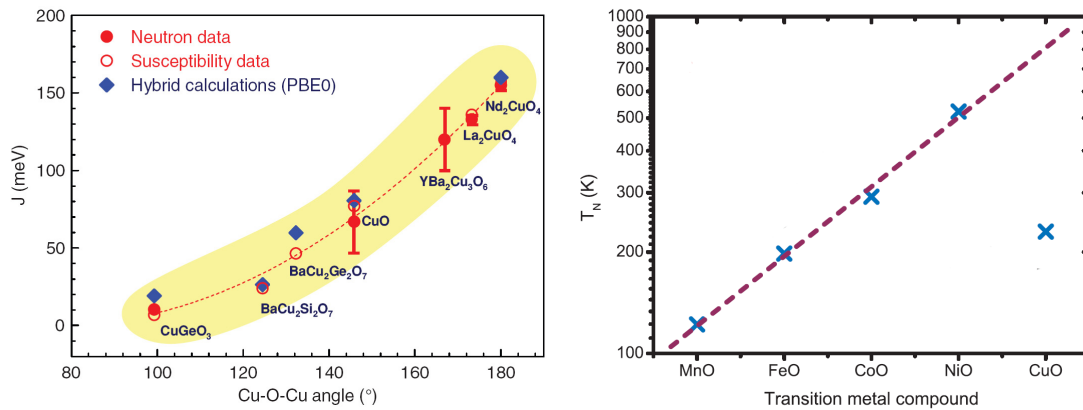


Figure 5.4: (left) Superexchange interaction  $J$  as a function of the Cu-O-Cu bond angle for various low-dimensional cuprates. The experimentally extracted data are compared to calculations. This figure was taken from Rocquefelte et al. [167] (right) Overview of  $T_N$  for transition metal monoxides with a rocksalt structure. Monoclinic CuO does not follow the exponential trend. This figure was taken with slight alteration from Siemons et al. [157].

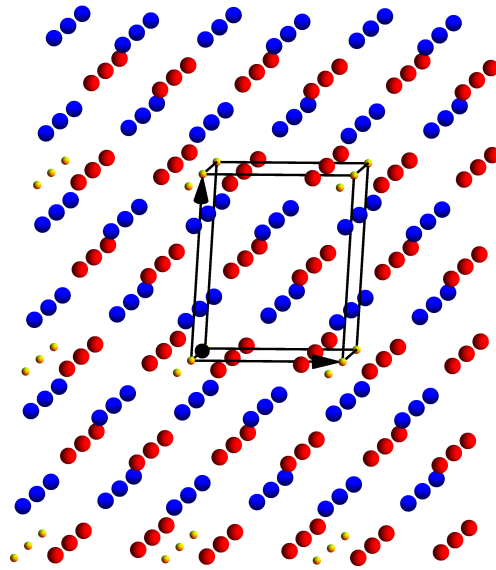
## 5.5. From tenorite to T-CuO

a deviation from some physical trends extrapolated from MnO, FeO, CoO and NiO, e.g. by a relatively low Néel temperature of 230 K [157, 163–171].

It is instructive to imagine how the atoms have to be rearranged such that a more symmetric tetragonal structure can be recovered from this strongly deformed system.

- i. We start from the monoclinic unit cell (unit cell: black, lattice points: yellow) with 4 copper (red) and 4 oxygen atoms (blue). The atomic coordinates  $(x, y, z)$  within the cell are [172]:

Atom	x	y	z	Atoms/cell
Cu <sub>1</sub>	1/4	1/4	0	1/2 + 1/2
Cu <sub>2</sub>	3/4	3/4	0	1/2 + 1/2
Cu <sub>3</sub>	1/4	3/4	1/2	1
Cu <sub>4</sub>	3/4	1/4	1/2	1
O <sub>1</sub>	0	0.41840	1/4	1/2 + 1/2
O <sub>2</sub>	1/2	0.91840	1/4	1
O <sub>3</sub>	0	0.58160	3/4	1/2 + 1/2
O <sub>4</sub>	1/2	0.08160	3/4	1

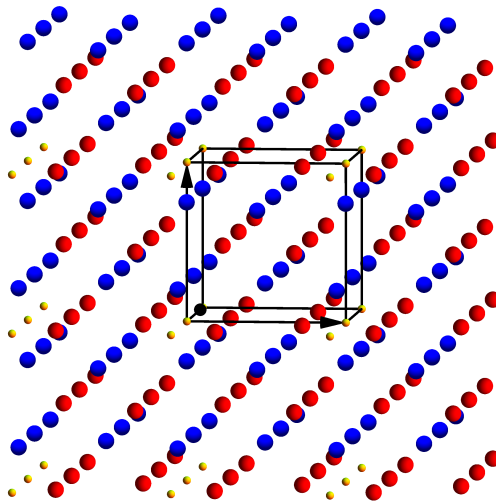


- ii. Now we bend  $\beta$  to  $90^\circ$  and stretch all lattice parameters such that  $a = b = c$ . We arrive in a simple cubic crystal structure

## Chapter 5. T-CuO – a 2D edge-sharing cuprate investigated by ARPES

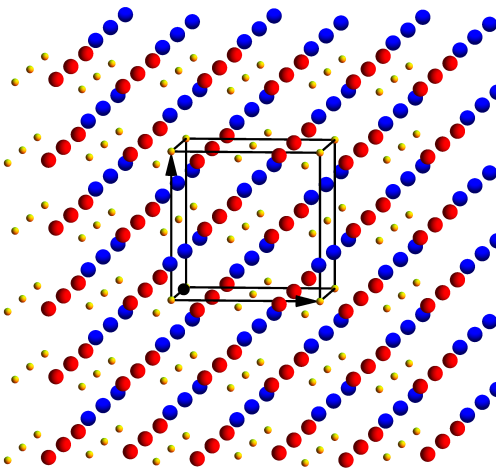
iii. Within this cube, we now we shift oxygen atoms  $O_3$  and  $O_4$  and obtain

Atom	x	y	z	Atoms/cell
Cu <sub>1</sub>	1/4	1/4	0	1/2+1/2
Cu <sub>2</sub>	3/4	3/4	0	1/2+1/2
Cu <sub>3</sub>	1/4	3/4	1/2	1
Cu <sub>4</sub>	3/4	1/4	1/2	1
O <sub>1</sub>	0	0.41840	1/4	1/2+1/2
O <sub>2</sub>	1/2	0.91840	1/4	1
O <sub>3</sub>	0	0.91840	3/4	1/2+1/2
O <sub>4</sub>	1/2	0.41840	3/4	1



iv. This structure now is more appropriately represented by a face centered cubic *fcc* structure with additional Bravais lattice points at  $(1/2, 1/2, 0)$ ,  $(0, 1/2, 1/2)$  and  $(1/2, 0, 1/2)$  (yellow). The atomic coordinates within this fcc lattice are now:

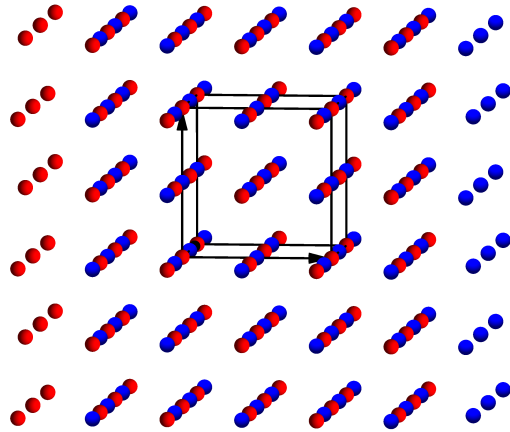
Atom	x	y	z	Atoms/cell
Cu	1/4	1/4	0	$4 \times 1/2 + 2 \times 1$
O	1/2	0.41840	1/4	$4 \times 1/2 + 2 \times 1$



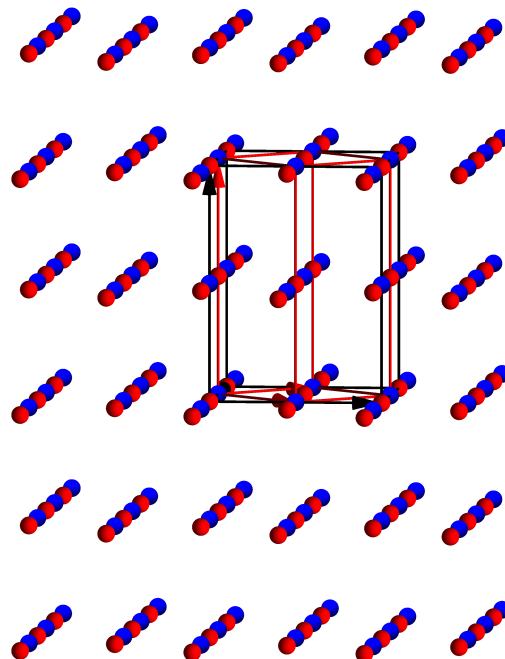


v. We shift these atoms within its *fcc* unit cell and obtain

Atom	x	y	z	Atoms/cell
Cu	0	0	0	$8 \times 1/8 + 6 \times 1/2$
O	1/2	0	0	$4 \times 1/2 + 2 \times 1$



vi. Now, we stretch the lattice parameters to  $a = 3.905 \text{ \AA}$  and  $c = 5.240 \text{ \AA}$  and yield the elongated *fcc* structure of ( $a = 3.905 \text{ \AA}$ ,  $c = 5.340 \text{ \AA}$ ,  $c/a = 1.37$ ,  $V = 79.90 \text{ \AA}^3$ ) displayed in Fig 5.3 (c), which is more properly represented by an elongated *bcc* structure, in other words a body centered tetragonal *bct2* Bravais lattice ( $a = 2.7613 \text{ \AA}$ ,  $c = 5.340 \text{ \AA}$ ,  $V = 40.72 \text{ \AA}^3$ ,  $c/a = 1.93$ ). Clearly, tenorite CuO can be continuously transformed to T-CuO and the topology of both systems is equivalent.



## 5.6 The electronic structure of cuprates

The important structural unit in the high-temperature cuprate superconductors is the ubiquitous two dimensional  $\text{CuO}_2$  plane, with Cu  $3d_{x^2-y^2}$  and O  $2p_{x,y}$  orbitals forming the backbone of its low energy electronic structure [173–175]. The surrounding matrix in this respect is believed to only serve as a charge carrier reservoir, tuning the system away from half filling.

In the cuprates, the copper has a nominal valence of  $\text{Cu}^{2+}$  and formally a  $3d^9$  electron configuration. As a consequence of the tetrahedral crystal field, the single hole mostly occupies the  $d_{x^2-y^2}$  orbitals of copper but to some extent also the ligand oxygen  $p$  orbitals, resulting in a groundstate  $c_1 d^9 + c_2 d^{10} \underline{L}$ .<sup>3</sup> Given the large Hubbard  $U \sim 9$  eV of the  $3d$  orbitals, placing a second hole on the Cu site – e.g via chemical doping – would require a large amount of energy, which leads to a preferential occupation of the ligand O  $2p$  orbital resulting in  $d^9 \underline{L}$  [173, 175]. Remaining strongly coupled via exchange interaction, these two holes gain energy by forming a quasi bound state of singlet character and  $^1A_1$  symmetry – which energetically is preferred to the  $^3B_1$  Hund’s rule ground state and propagates as an effective one particle entity – the Zhang Rice Singlet (ZRS) [176]. This state is formally constructed from the  $d^9$  hole occupying the Cu  $B_{1g}(d_{x^2-y^2})$  orbital and the ligand hole  $\underline{L}$  on a linear combination of the four surrounding oxygen  $p_{x/y}$ -orbitals with equivalently  $B_{1g}$  symmetry [175]. In  $D_{4h}$ , this results in a total symmetry of the ZRS wavefunction  $B_1 \otimes B_1 = A_1$ .

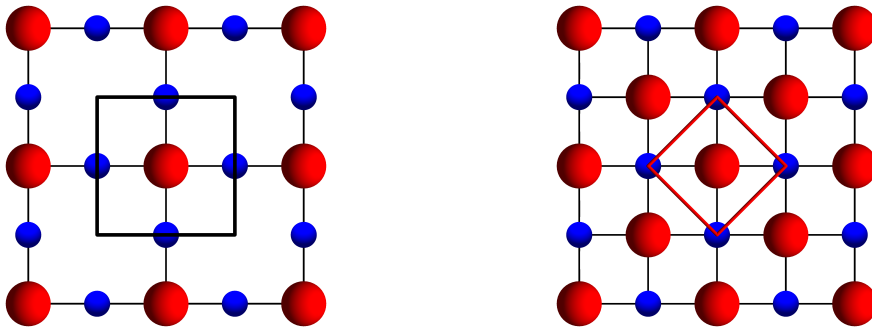


Figure 5.5: Corner-sharing CuO plane (**left**) vs edge-sharing CuO plane (**right**). Red balls indicate copper atoms, blue balls oxygen. The primitive 2D unit cells are marked by a square. The red square (**right**) at the same time outlines one  $\text{CuO}_4$  plaquette, which shares its edges with the neighboring plaquettes.

However, there are two main structural differences of the  $\text{CuO}_2$  plane in the HTSC and T-CuO. First, T-CuO has a three dimensional crystal structure. As can be inferred by the 3D structure of Fig. 5.3 (c), the  $\text{CuO}$  planes are electronically interconnected by Cu  $d_{xz}$ ,  $d_{yz}$ ,  $d_{z^2}$  and O  $p_z$  orbitals. Due to a pronounced elongation along the  $c$ -axis however, tetrahedral crystal field splitting can be expected to energetically separate these orbitals from the important  $d_{x^2-y^2}$  and

<sup>3</sup> $\underline{L}$  implies the hole sitting on the Ligand O  $p$  orbitals.  $c_1$  and  $c_2$  are constants.

$p_{x,y}$  states.

Second, the in-plane structure of T-CuO is different, i.e. the CuO plaquettes are coordinated in an edge-sharing geometry. As shown in Fig. 5.5 the CuO plane of T-CuO has one additional Cu atom with respect to the corner sharing CuO<sub>2</sub> plane in the HTSC and consequently a smaller unit cell.<sup>4</sup> It is due to these structural differences, that we start from a careful comparison of the basic electronic structure of T-CuO with respect to typical cuprate systems.

## 5.7 Core level spectra

Due to its already mentioned relevance as a proxy structure for the HTSCs, monoclinic CuO has been thoroughly studied by photoemission techniques in the past. Spin resolved photoemission experiments on tenorite even provided direct prove of the ZRS in this compound [177]. Core level spectroscopy is a useful tool to identify CuO as a charge transfer insulator and to extract critical parameters like the charge transfer energy  $\Delta = E(d^{10}\underline{L}) - E(d^9)$  and transfer integral  $T = \langle d^9 | H | d^{10}\underline{L} \rangle$ .

A spectrum of the Cu  $2p$  level of T-CuO measured at 1010 eV photon energy is shown in Fig. 5.6. Due to the core hole spin orbit interaction, the spectrum splits in two pairs belonging to the Cu  $2p_{1/2}$  and Cu  $2p_{3/2}$  final states. For each of these hole final states, the valence hole can either remain on the copper site, giving rise to  $2p^5 3d^9$ , or can move to the ligand site resulting in  $2p^5 3d^{10}\underline{L}$ . The energy separation of these configurations consequently will be determined by the charge transfer energy  $\Delta$ , by the hybridization energy  $T$  and by the core-hole  $3d$  interaction.

Following a method by Ghijsen et al. [174], we extract  $\Delta$  and  $T$  from the weighted distance (7.81 eV) and the integrated intensity ratio (0.61) of the  $2p_{3/2}^5 3d^9$  and  $2p_{3/2}^5 3d^{10}\underline{L}$  peaks. We obtain a charge transfer energy  $\Delta \sim 3.6$  eV and a transfer integral  $T \sim 2.8$  eV, respectively. These values, somewhat larger than in monoclinic CuO ( $\Delta \sim 2.75$  eV,  $T \sim 2.5$  eV), reflect a larger band gap of T-CuO and indicate that the ZRS in T-CuO can be stabilized [173, 175, 179, 180].

A local multiplet calculation (software CTM4XAS [178]) is put side by side with our data. The model assumes that the final state in the photoemission process can be properly described by a linear combination of  $p^5 d^9$  and  $p^5 d^{10}\underline{L}$  states in a tetrahedral crystal field, affected by Coulomb interaction with the core hole. The only valence orbitals taken into account are consequently O  $2p$  and Cu  $3d$  states and the important geometry is the CuO<sub>4</sub> plaquette shown in Fig. 5.7. The one hole groundstates are defined by the  $B_{1g}(d_{x^2-y^2})$ ,  $A_{1g}(d_{z^2})$ ,  $B_{2g}(d_{xy})$  and  $E_g(d_{xz,yz})$  components of the square planar symmetry group  $D_{4h}$ .

This model – described in detail in Ref. 141 – is too simplistic to correctly reproduce the intensity ratio of the peaks but can still give some rough estimates. We use a typical crystal field

<sup>4</sup>The term “corner/edge sharing” applies to CuO<sub>4</sub> plaquette. If two neighboring plaquettes share only one oxygen atoms, we refer to a corner sharing geometry. If two neighboring plaquettes share two oxygen atoms, we refer to edge sharing.

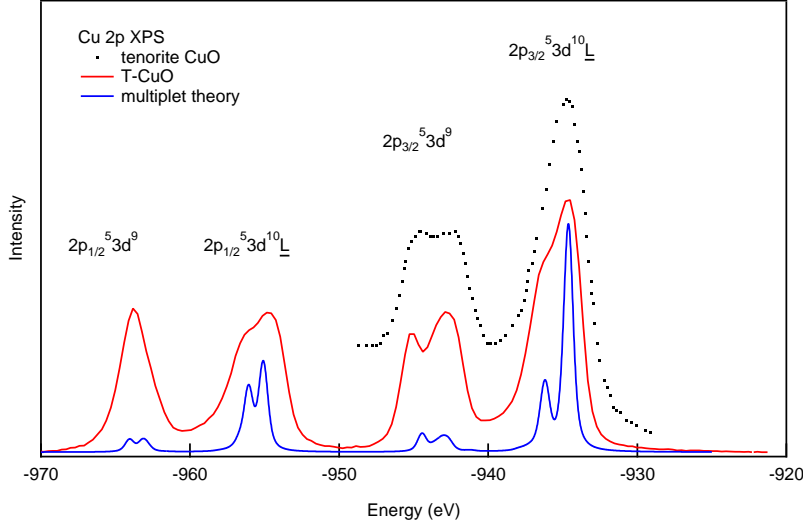


Figure 5.6: The Cu 2p spectrum of T-CuO ( $h\nu = 1010$  eV) is compared with that of monoclinic CuO ( $h\nu = 1486$  eV) from Ref. 174. Additionally we plot the results of a multiplet calculation [178]

splitting of  $10Dq = 0.3$  eV and the charge transfer energy  $\Delta = 3.6$  eV obtained above [141]. For the  $3d$ - $3d$ -correlation we use  $U_{dd} = 8.8$  eV, slightly larger than the core-hole potential  $U_{pd} = -6$  eV [179].

Via Slater-Koster theory, the effective hopping terms can be estimated from the hybridization strength  $V$  of the atomic orbitals as  $T_{pp} = V_{pp}^{\sigma} - V_{pp}^{\pi}$ ,  $T_{pd}(B_{1g}) = \sqrt{3}V_{pd}^{\sigma}$ ,  $T_{pd}(A_{1g}) = V_{pd}^{\sigma}$ ,  $T_{pd}(B_{2g}) = 2V_{pd}^{\pi}$  and  $T_{pd}(E_g) = \sqrt{2}V_{pd}^{\pi}$  [175]. For a “good correspondence” to the XPS data, we use typical values of  $T_{pp} \sim 1.3$ ,  $T_{pd}(B_{1g}) \sim 3.8$  eV,  $T_{pd}(A_{1g}) \sim 2.2$  eV,  $T_{pd}(B_{2g}) \sim -1.5$  eV and,  $T_{pd}(E_g) \sim -1$  eV which yields reasonable values of  $V_{pd}^{\sigma} \sim 2.2$  eV and  $V_{pd}^{\pi} \sim -0.7$  eV.

From the effective hopping terms, we can further estimate the energy difference in between the ZRS and the band of itinerant oxygen states (the band  $\beta$  described in detail in Sec. 5.12), i.e. the ground state hybridization energy  $\delta = (\Delta - T_{pp})/2 - \sqrt{T_{pd}(B_{1g})^2 + (\Delta - T_{pp})^2/4} = -2.1$  eV, which is a good indicator that the ZRS indeed is stable in T-CuO [179]. Further, we obtain a rough estimate of the gap energy  $\sim \Delta - T_{pp} \sim 2.3$  eV.

As shown later, these rough estimates are in good agreement with our ARPES data despite the simplicity of this model. The basic message of this exercise is however that the values obtained for T-CuO are consistent with the values of typical cuprate compounds and T-CuO belongs to the class of the charge transfer insulators.

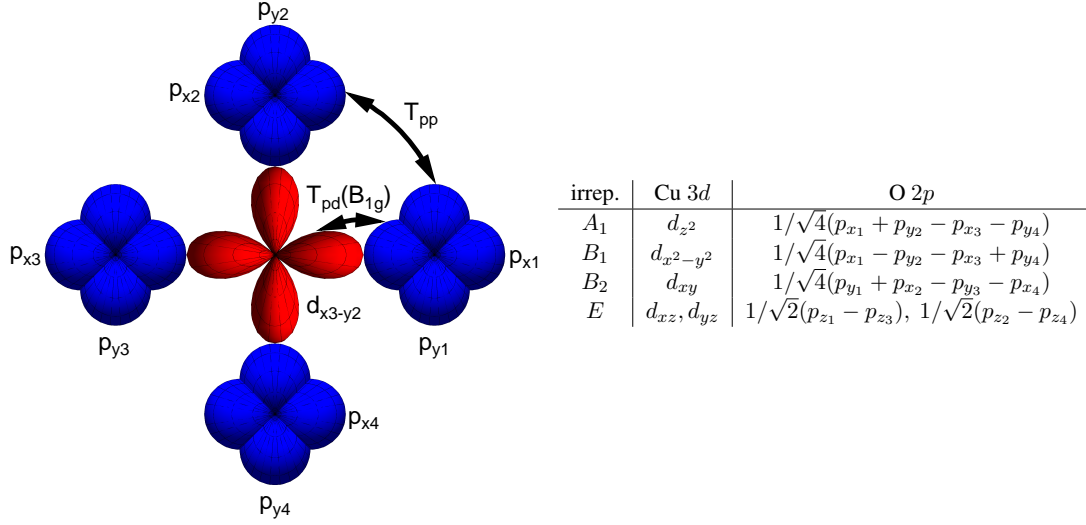


Figure 5.7: **(left)** The  $\text{CuO}_4$  plaquette. The most important orbitals Cu  $d_{x^2-y^2}$  and O  $p_x, p_y$  are shown and the effective hopping terms defined. **(right)** Copper and oxygen basis functions on the square planar  $\text{CuO}_4$  plaquette. E.g.  $p_{x1}$  labels a  $p_x$  orbital centered at point 1.

## 5.8 Valence band spectra

Analogous to chemical doping, the photoemission process can remove an electron from the  $d^9$  valence band. It is therefore a useful probe to investigate the possible two-hole states in this material.

Fig. 5.8 shows angle integrated photoemission spectra of T-CuO, acquired across the Cu  $L_3$  ( $2p \rightarrow 3d$ ) absorption edge, from 929 to 932 eV photon energy. The photoemission cross section ratio O  $2p/\text{Cu } 3d$  is  $\sim 0.03$  at 930 eV, which implies a high sensitivity for states of predominantly copper character [181]. Analogous to a study on tenorite CuO, final states of mainly  $d^8$  character, at 10-15 eV binding energy, are strongly enhanced by the  $d^9 \rightarrow p^5 d^{10} \rightarrow d^8$  resonance [182]. These states form the lower Hubbard band. The low cross section of oxygen states implies that states of  $d^{10} \underline{L}$  character will have only a weak signature. Moreover, they do not resonate due to the closed  $d$  shell.<sup>5</sup>

The right part of Fig. 5.8 shows similar spectra acquired at the Cu  $M_{2,3}$  ( $3p \rightarrow 3d$ ) edge, from 72 to 78 eV photon energy. This time, the cross section ratio O  $2p/\text{Cu } 3d$  is  $\sim 0.27$  at 74 eV [181]. Again, the  $d^8$  states, (10-15 eV binding energy, peaks 1-3), are enhanced by the resonance. Due to the higher cross section of oxygen states, we now also identify the (mainly)  $d^9 \underline{L}$  band at 2-8 eV binding energy (peaks 4-6). From 74 to 78 eV spectral weight is transferred from peak 4 to peak 5, revealing a larger  $d^8$  component in peak 5. Besides, we see a first indicator of the

<sup>5</sup>Above the resonance, an  $L_3VV$  Auger peak contributes to the photoemission signal, seemingly shifting the main peak towards higher energies. [182]

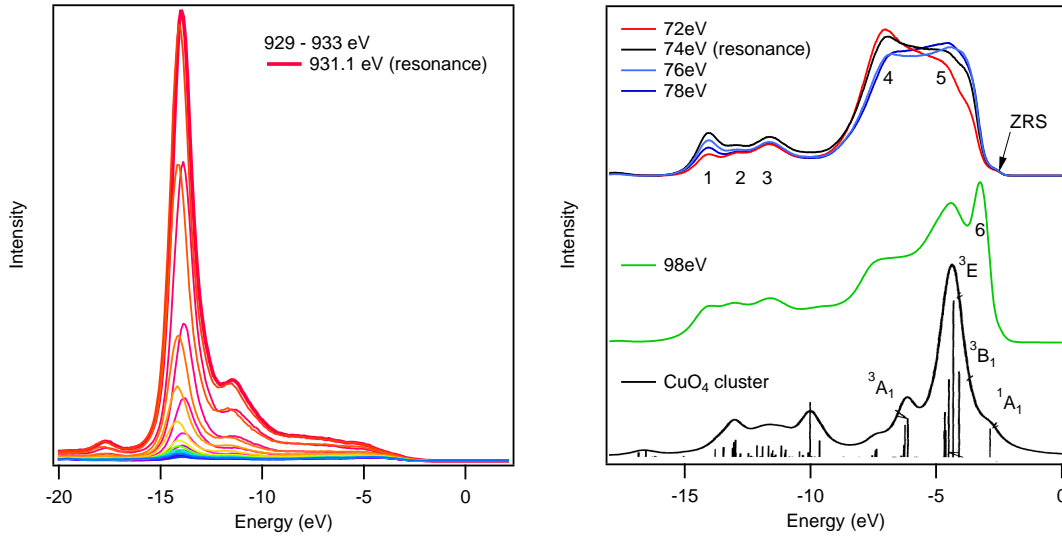


Figure 5.8: **(left)** Integrated photoemission spectra measured at the Cu  $L_3$  resonance at 931 eV. **(right)** Integrated photoemission spectra measured at the Cu  $M_{2,3}$  resonance at 74 eV, and off-resonance at 98 eV. The data is compared to Cu  $3d$  spectral weight obtained from a  $\text{CuO}_4$  cluster calculation by Eskes et al [179]. The parameters used in the calculation were similar to the ones determined for T-CuO in Sec. 5.7.

ZRS band – which is the main object of this study – as a tiny shoulder to the low binding energy shoulder of peak 6.

Off resonance at 98 eV photon energy (green curve), the cross section ratio  $\text{O } 2p/\text{Cu } 3d$  diminishes slightly to  $\sim 0.16$  and the spectrum contains more Cu  $3d$  weight [181]. Peak 6 – which corresponds to the band labeled  $\beta$  discussed in Sec. 5.12 – is now more pronounced. The intensity of peak 4 on the other hand is significantly suppressed, which underlines its strong oxygen character. The spectral weight of peak 5 remains largely unaffected, which points towards a balanced contribution of copper and oxygen states.

Additionally, we show a cluster calculation on the  $\text{CuO}_4$  plaquette shown in Fig. 5.7 by Eskes et al. [179]. The simple model identifies the first excitation state as  $^1A_1$ , which is composed of one Cu  $d_{x^2-y^2}$  hole and a second hole on a linear combination of  $p_x/p_y$  orbitals with  $x^2 - y^2$  symmetry as defined in Fig. 5.7. The higher energy states are triplets of  $^3B_{1g}$  and  $^3E_g$  symmetry, i.e. with one hole on the Cu  $d_{x^2-y^2}$  orbital and the second hole on a linear combination of oxygen  $p$ -orbitals with respectively  $A_1(d_{z^2})$  and  $E(d_{xz}/d_{yz})$  symmetry.

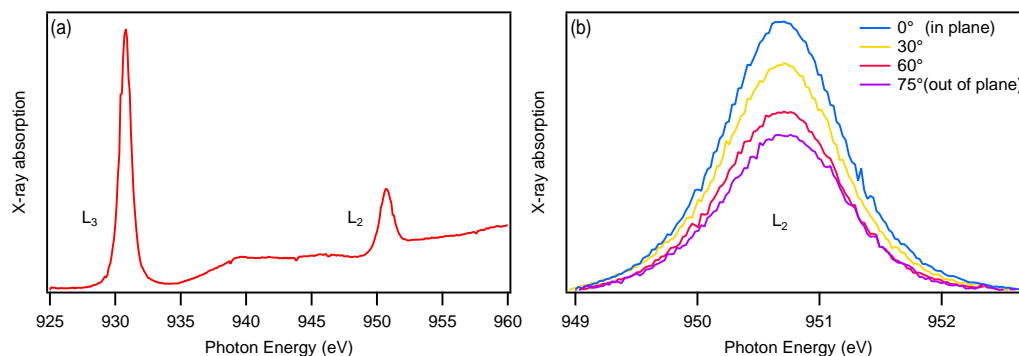


Figure 5.9: (a) Cu  $L_{2,3}$  XAS of T-CuO. Panel (b) shows the polarization dependence of the Cu  $L_2$  white line.

## 5.9 X-ray absorption

Fig. 5.9 (a) shows the Cu  $L_{2,3}$  x-ray absorption (XAS) spectrum of T-CuO. The two ( $2p \rightarrow 3d$ ) peaks (“white lines”) are separated by the large  $2p$  spin-orbit splitting. Fig. 5.10 (b) shows the dependence of the  $L_2$  peak on the angle between the polarization vector of the (linearly polarized) x-rays and the CuO plane. The observed polarization dependence confirms that the Cu  $3d$  hole has predominantly in-plane character.<sup>6</sup>

In summary, the core level data obtained from CuO is consistent with data obtained from monoclinic CuO and the corner sharing cuprates. Integrated photoemission hints towards the existence of the ZRS, which is confirmed in the following paper [183].

<sup>6</sup>The reason why we did not use the  $L_3$  line with much higher intensity is simple: the experiment at the time was not intended to show a dichroism effect.

## 5.10 ARPES overview

### Tetragonal CuO: a quasi two-dimensional cuprate with novel intralayer coupling

S. Moser,<sup>1,2,\*</sup> L. Moreschini,<sup>2,\*</sup> H.-Y. Yang,<sup>3</sup> D. Innocenti,<sup>4</sup> F. Fuchs,<sup>5</sup> N. H. Hansen,<sup>5,6</sup> Y.

J. Chang,<sup>2,7</sup> K. S. Kim,<sup>2</sup> A. L. Walter,<sup>2</sup> A. Bostwick,<sup>2</sup> E. Rotenberg,<sup>2</sup> F. Mila,<sup>3</sup> and M. Grioni<sup>1</sup>

<sup>1</sup>*Ecole Polytechnique Fédérale de Lausanne (EPFL), Institut de Physique des Nanostructures, CH-1015 Lausanne, Switzerland*

<sup>2</sup>*Advanced Light Source (ALS), Berkeley, California 94720, USA*

<sup>3</sup>*Institute of Theoretical Physics, Ecole Polytechnique Fédérale de Lausanne, CH-1015 Lausanne, Switzerland*

<sup>4</sup>*Dipartimento di Ingegneria Meccanica, Università di Roma Tor Vergata, I-00133 Roma, Italy*

<sup>5</sup>*Experimental Physics VI, Julius-Maximilian University of Würzburg, 97074 Würzburg, Germany*

<sup>6</sup>*ZAE Bayern, Am Hubland, 97074 Würzburg, Germany*

<sup>7</sup>*Department of Physics, University of Seoul, Seoul, 130-743, Korea*

(Dated: August 15, 2014)

We investigate by angle resolved photoemission (ARPES) the electronic structure of in-situ grown tetragonal CuO, a synthetic quasi two-dimensional edge-sharing cuprate. We show that, in spite of the very different nature of the copper oxide layers, with twice as many Cu in the CuO layers of tetragonal CuO as compared to the CuO<sub>2</sub> layers of the high-T<sub>c</sub> cuprates, the low-energy electronic excitations are surprisingly similar, with a Zhang-Rice singlet dispersing on weakly-coupled cuprate-like sublattices. This system should thus be considered as a member of the high-T<sub>c</sub> cuprate family, with however interesting differences due to the intra-layer coupling between the cuprate-like sublattices.

The physics of cuprates is remarkably rich, ranging from high-temperature superconductors (HTS) [1, 2] to spin ladders [3, 4]. Their properties derive from the structure of the copper oxide layers, which evolves from CuO<sub>2</sub> in HTS to Cu<sub>2</sub>O<sub>3</sub> in spin ladders by fitting more and more coppers into the layers, as in the family Sr<sub>n-1</sub>Cu<sub>n+1</sub>O<sub>2n</sub> ( $n = 3, 5, \dots$ ) [5]. Synthesizing systems with pure two-dimensional (2D) CuO layers would be fascinating, but this goal has remained elusive. Interestingly, CuO – which has been studied as a model parent compound for the HTS cuprates due to its simple stoichiometry [6, 7] – does not contain copper oxide layers. Its low-symmetry monoclinic tenorite structure consists of crossed ribbons of edge-sharing CuO<sub>4</sub> plaquettes [8], and its magnetic excitations have 1D character (spinons) [9, 10].

A tetragonal (elongated rocksalt) structure, much closer to that of the HTS cuprates, can be stabilized up to a thickness of several unit cells [12, 13] when CuO is grown epitaxially on a SrTiO<sub>3</sub> (001) substrate [11]. In tetragonal CuO (T-CuO), the Cu ions are at the center of edge-sharing elongated CuO<sub>6</sub> octahedra, which form infinite CuO planes stacked along the *c* axis. The ratio of the apical- to in-plane Cu-O distances is large (1.37), which reduces the inter-plane coupling. The inset of Fig. 1 (a) illustrates the structure of a CuO plane, paved by edge-sharing CuO<sub>4</sub> plaquettes. The red square, which outlines one plaquette, is also the 2D unit cell, and *a* is the side of the 3D tetragonal unit cell. In this structure, copper atoms form a square lattice, but the oxygens are *not* between nearest neighbour (NN) coppers, as in the CuO<sub>2</sub> layers of the cuprates, but between next-NNs. As a consequence, the hopping and exchange parameters are expected to be quite small between NN coppers. Indeed, the Sr<sub>n-1</sub>Cu<sub>n+1</sub>O<sub>2n</sub> family consists of essentially decoupled spin ladders because the exchange coupling between NNs located in edge-sharing CuO<sub>4</sub> plaquettes is very small [3, 4]. To which extent the electronic properties of the CuO layers are related to those of the CuO<sub>2</sub> layers of the cuprate parent compounds is one of the important

questions addressed by the present work. Some basic information about the electronic structure of T-CuO has been obtained by first-principles density functional [14, 15] and by LDA+*U* calculations [16], but the band structure has not been discussed or measured yet. The interest in this new material also stems from its predicted magnetic properties. An extrapolation from the behavior of other 3*d* transition metal monoxides, from MnO to NiO, suggests that the Néel temperature T<sub>N</sub> of T-CuO could be as high as 700 – 800 K [12]. A very recent experiment finds T<sub>N</sub> = 600 K [17]. Such enhanced AFM coupling would open the way to new practical applications, but would also be quite interesting for scenarios of HTS based on magnetic fluctuations [18].

Figure 1 gives an overview of the ARPES results on a thin film (6 unit cells) T-CuO sample. Fig. 1(a) is a composite *k<sub>x</sub>* vs. *k<sub>y</sub>* ARPES constant energy map measured at the top of the valence band *E<sub>V</sub>*. The ARPES features in an energy window of at least 1 eV below *E<sub>V</sub>* do not disperse as a function of the perpendicular wave vector *k<sub>z</sub>* [11], i.e. they have nearly 2D character. The map shows four strong intensity maxima, offset by 90°, in the 1st Brillouin zone (BZ), outlined by the red square in Fig. 1(a), corresponding to the crystallographic surface unit cell. The fourfold pattern can be recognized in all adjacent BZs, outlined by dashed red squares, even if intensities are modulated by ARPES matrix elements. Namely, the signal is suppressed along the lines *k<sub>x</sub>* = ±*k<sub>y</sub>*, crossing at (0, 0), reflecting the scattering geometry and the symmetry of the Cu *d<sub>x<sup>2</sup>-y<sup>2</sup></sub>* orbitals [11]. A closer inspection however reveals weaker replicas of this pattern in both the *k<sub>x</sub>* and *k<sub>y</sub>* directions, leading to an overall periodicity which is that of a two times smaller Wigner-Seitz cell in reciprocal space, rotated by 45° and shown in black. It is the BZ of a *c*(2 × 2) unit cell (shown in black in the inset) containing two Cu ions. It would be the relevant BZ if the layer were divided into two non-interacting sublattices, since it would correspond to the primitive unit cell of each sublattice. This is the first exper-



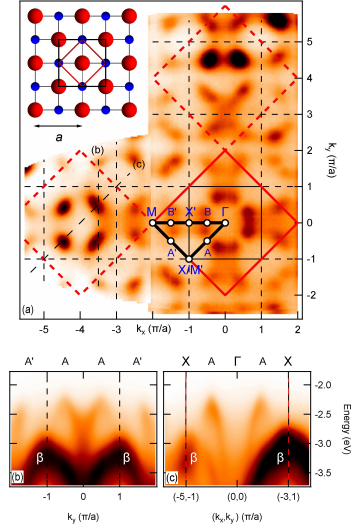


FIG. 1. (Color online) (a) Constant energy map at  $E_V$ , measured at  $\hbar\nu = 120.5$  eV and  $T = 90$  K. It is a composite of two data sets, one centered at  $k_x = -4\pi/a$ , the other at  $k_x = 0$  ( $\Gamma M = 2\pi/a = 1.61 \text{ \AA}^{-1}$ ,  $\Gamma X = \sqrt{2}\pi/a = 1.14 \text{ \AA}^{-1}$ ). The red and black squares are the BZs corresponding to the unit cells defined in the inset. (inset) The structure of a CuO plane: Cu (O) ions are indicated in red (blue). The red square is the 2D unit cell, which coincides with a  $\text{CuO}_4$  plaquette; ‘ $a$ ’ is the length of the side of the 3D tetragonal unit cell. The black square is the non-primitive  $c(2 \times 2)$  unit cell. (b) and (c) show the  $E$  vs.  $k$  dispersion along lines (b) and (c) in panel (a).

imental indication that the coupling between the two sublattices through the interaction between NN copper atoms must be small.

The band dispersion is illustrated in Figs. 1 (b) and (c). To avoid complications due to the intensity suppression along the diagonals  $k_x = \pm k_y$ , here and in the following we will discuss data collected from the BZ centered at  $(-4\pi, 0)$ . In addition to the usual  $\Gamma$ ,  $X$  and  $M$  points, it will prove useful to define the mid-point  $X'$  between  $\Gamma$  and  $M$  (the  $X$  point of the small BZ), and pairs of points  $A, A'$ , and  $B, B'$ , symmetric with respect to the  $XX'$  line. If the two sublattices were completely decoupled, the pairs of points  $(\Gamma, M)$ ,  $(A, A')$  and  $(B, B')$  would be equivalent. Fig. 1 (b,c) presents two  $E$  vs.  $k_{\parallel}$  cuts along the lines marked (b) and (c) in Fig. 1 (a). Cut (b) shows a band with maxima at  $E = -2.35$  eV at the  $A$  points of the BZ, in correspondence of the intensity maxima of Fig. 1(a). This sets a lower limit to the band gap of T-CuO, which is therefore larger than in bulk CuO (1.35 eV [19]). The secondary maxima at  $E = -2.5$  eV at the  $A'$  points, coincide with the replica features. The dispersion outlines the momentum dependence of the first ionization state of an edge-sharing CuO plane. As further discussed below, this is the Zhang-Rice singlet (ZRS) band [20], typical of the 2D corner-sharing cuprates, i.e. a

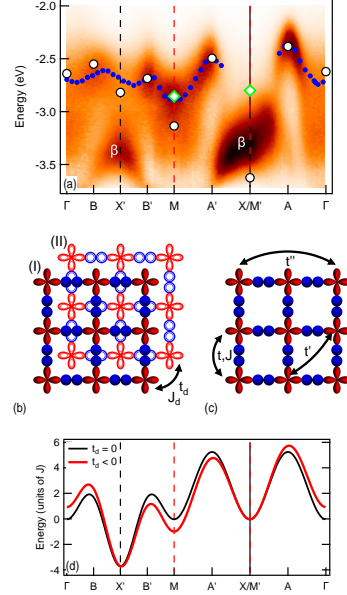


FIG. 2. (Color online) (a) ARPES dispersion along a triangular contour equivalent to that of Fig. 1 (a), in the BZ centered at  $(-4\pi, 0)$ . The data have been normalized to the same integrated intensity for all  $k$  values, after subtraction of an integral (Shirley) background. Filled (blue) symbols outline the experimental dispersion of the ZRS band. Empty circles (diamonds) mark the peak positions calculated by an extended  $t$ - $J$  model, whose parameters are defined in panels (b-c). The CuO plane is seen as the superposition of two corner-sharing sublattices (I) and (II). (d) Dispersions of the lower Hubbard band from Ref. 21 (black line), and illustration of the degeneracy lifting induced by a finite hopping  $t_d = -0.03$  eV between the two sublattices.

band with  $^1A_1$  symmetry, mainly  $d^9 \underline{L}$  character, with both holes in wave-functions with  $b_{1g}$  symmetry (one in the  $d_{x^2-y^2}$  orbital of Cu, the other one in an appropriate linear combination of  $p$  orbitals of neighbouring oxygens). It merges around  $-3$  eV with a more intense band (labelled  $\beta$ ) with a maximum at the  $X$  point. By analogy with the 2D corner-sharing cuprates, we assign the latter to a manifold of  $d^9 \underline{L}$  states of different orbital symmetries [7].

Figure 2 (a) illustrates the experimental band structure measured along a  $\Gamma M X \Gamma$  contour, equivalent to the triangular contour of Fig. 1(a), in the BZ centered at  $(-4\pi, 0)$ . For the ZRS band, blue circles outline the dispersion of the ARPES peak. Along the  $A' X A$  path the broad line shape (see below) prevents a reliable determination of the peak position. The emergent symmetry suggested by the intensity map is still partially reflected in these data, but not fully since the pairs  $(\Gamma, M)$ ,  $(A, A')$  and  $(B, B')$  are not strictly equivalent. As a first step to interpret the experimental data, we have plotted in

Fig. 2 (d) the dispersion for the lower Hubbard band:

$$E(k) = -4t'[\cos(k_x a) \cdot \cos(k_y a)] - 2t''[\cos(2k_x a) + \cos(2k_y a)] - J[\cos(k_x a) + \cos(k_y a)]^2,$$

with  $t' = -0.12$  eV,  $t'' = 0.08$  eV and  $J = 0.125$  eV used to fit the ARPES data for a single hole in the AFM background of the corner-sharing insulating cuprate  $\text{Ca}_2\text{CuOCl}_2$  [21]. This dispersion should be a good starting point if the CuO plane is seen as the superposition of the two interpenetrating corner-sharing sublattices (I) and (II) of Fig. 2 (b), as long as they are weakly coupled. It qualitatively captures the main features of the experimental dispersion, namely the location of the band maxima and minima, but of course cannot quantitatively reproduce the energy difference between the pairs ( $A, A'$ ), ( $B, B'$ ), and ( $\Gamma, M$ ). Adding a “diagonal” hopping  $t_d$  between the two lattices, the dispersion becomes:

$$E'(k) = E(k) - 4t_d[\cos(k_x a/2) \cdot \cos(k_y a/2)],$$

which yields the red line in Fig. 2 (d). The symmetry of the original lattice, corresponding to the larger (red) BZ in Fig. 1 (a), is qualitatively recovered. The  $A, A', B, B'$ , and  $\Gamma, M$  pairs of points are no longer equivalent, and the degeneracies are lifted, in qualitative agreement with the experiment, where  $E(\Gamma) - E(M) = 180$  meV,  $E(A) - E(A') = 140$  meV and  $E(B) - E(B') = 60$  meV.

The model of Fig. 2 (d), which consists in just adding a diagonal hopping to the dispersion of the excitations on the underlying sublattices, has mainly a pedagogical value, and cannot fully describe the complex dynamics of a strongly correlated hole propagating in the AFM background of the edge-sharing CuO plane. As a further step, we consider a generalized  $t$ - $J$  model [22, 23]:

$$\begin{aligned} \tilde{H}_{t,J} = & J \sum_{i,j} \vec{S}_i \cdot \vec{S}_j - t \sum_{i,j,\sigma} \hat{c}_{i,\sigma}^\dagger \hat{c}_{j,\sigma} - t' \sum_{i,j',\sigma} \hat{c}_{i,\sigma}^\dagger \hat{c}_{j',\sigma} \\ & - t'' \sum_{i,j'',\sigma} \hat{c}_{i,\sigma}^\dagger \hat{c}_{j'',\sigma} + J_d \sum_{i,m} \vec{S}_i \cdot \vec{S}_m - t_d \sum_{i,m,\sigma} \hat{c}_{i,\sigma}^\dagger \hat{c}_{m,\sigma}. \end{aligned}$$

Unprimed, primed and double-primed indices refer to first-, second- and third- NNs on the same sublattice;  $m$  indicates NNs on the whole lattice.

Since the local geometry of the corresponding bonds is very similar to that of cuprates, we have adopted for  $t, t', t''$  and  $J$  typical values for cuprate superconductors taken from Ref. 24. The diagonal hopping and exchange terms have been determined from a  $\text{Cu}_2\text{O}_6$  cluster along the lines of Ref. 25. The coupling terms  $t_d$  and  $J_d$  reflect the  $\text{Cu}(I)d_{x^2-y^2}-\text{O}(I)p_{x,y}-\text{O}(II)p_{x,y}-\text{Cu}(II)d_{x^2-y^2}$  orbitals overlap. We found a small but non-negligible  $t_d \sim -t/4 = -100$  meV and a very weak antiferromagnetic (AFM) exchange:  $J_d = 6$  meV. We then performed an exact diagonalization of  $\tilde{H}_{t,J}$  on a 32 site cluster to calculate the hole spectral function  $A(\vec{k}, \hbar\omega)$  (Fig. 3, right column). For our 32-site cluster,  $A(\vec{k}, \hbar\omega)$  is only defined at a small number of  $k$ -points. The corresponding spectra are shown in the left column of Fig. 3, normalized to the same

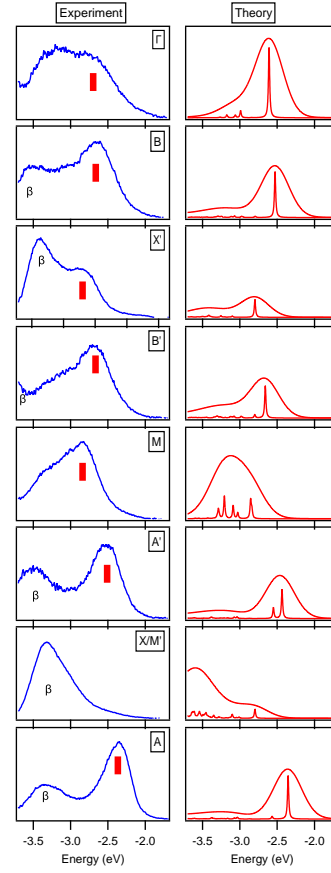


FIG. 3. (Color online) (Left) ARPES spectra extracted from Fig. 2 (a). Red tags mark the energy of a prominent ARPES dispersing feature (blue circles in Fig. 2 (a)) and do not always coincide with the energy of the excitations. (Right) Calculated spectral function of our cluster model with and without a 500 meV broadening.

total integrated intensity. For each  $k$ -point the lowest-energy peak represents the coherent spectral weight. Those at higher energies belong to the incoherent spectral weight, which reflects dressing by electronic and magnetic excitations. The incoherent weight varies strongly from point to point. It is never small, and even becomes dominant at the  $M$  and  $X$  points, reflecting strong and  $k$ -dependent correlations. To enable a comparison with the ARPES spectra shown in the left column, a 500 meV gaussian broadening was applied to the calculated spectra. This is much larger than the experimental energy resolution (30 meV), but typical of ARPES data from insulating cuprates [21]. The peak energies of the broadened spectra are shown as empty circles in Fig. 2 (a). For the  $M$  and  $X$  points the peak energies are clearly not representative of the energy of the excitations, which are then separately in-

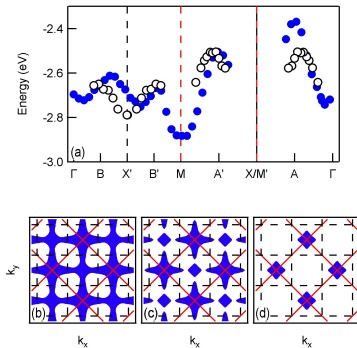


FIG. 4. (Color online) (a) The experimental dispersion of the first ionization state in T-CuO (full symbols) is compared with that of the ZRS band in  $\text{Sr}_2\text{CuO}_2\text{Cl}_2$  (empty symbols) [28], along the same triangular contour as in Fig. 2. (Bottom) Calculated Fermi surface of T-CuO for various hole dopings  $n$ : (b)  $n = 0.07$ ; (c)  $n = 0.37$ ; (d)  $n = 0.80$  holes/Cu ion. Details of the calculations are in Ref. 11.

indicated by empty diamonds. The theory describes the overall ZRS dispersion very well, and captures the inequivalence of the pairs of points  $(A, A')$ ,  $(B, B')$ , and  $(\Gamma, M)$ . The finite size of the cluster leads to a discretization and an underestimation of the incoherent spectral weight. Nevertheless, the experimental spectra are well reproduced, namely the double peak structures at  $\Gamma$  and  $M$ , and especially the suppression of the coherent spectral weight around  $X$ . Let us emphasize that, on the basis of the present data and calculation, a determination through fitting of all hopping parameters is not possible. This is why we have adopted parameters typical of cuprates for  $t, t', t''$ . However, the experimental results seriously constrain the value of the intra-layer coupling  $t_d$  between the sublattices. In particular, the splitting between the peaks at  $A$  and  $A'$  is proportional to  $t_d$  with a coefficient that depends only weakly on the other parameters, and the experimental splitting of 140 meV imposes a value of  $t_d \sim -100$  meV to a good accuracy.

We can now compare the electronic structure of edge-sharing T-CuO with that of a representative corner-sharing cuprate. Figure 4 (a) shows the first ionization state of T-CuO, and the ZRS band of  $\text{Sr}_2\text{CuO}_2\text{Cl}_2$  [28]. The energies of the two bands have been aligned at the  $A'$  point maximum. The two dispersions are quite similar, notwithstanding the already discussed asymmetry of the conjugated points in T-CuO. This conclusively supports the assignment of the topmost band in CuO to the ZRS. The observation of a sharp kink in the momentum-dependent spectral weight distribution [11] reinforces the similarity with the electronic structure of the HTS parent compounds.

Our ARPES data indicate that the CuO layers of T-CuO are best understood as weakly coupled cuprate-like sublattices. Accordingly, the electronic and magnetic properties can be

expected to be very similar. However, as we will now briefly discuss, the weak coupling between the cuprate-like sublattices can induce qualitative differences for some properties. At half filling, which is the case of the samples available so far, the system is a charge-transfer insulator, and in the limit of an infinite stack, it is expected to develop AFM order, with potentially a very high Néel temperature due to the stronger interlayer coupling than in high  $T_c$  cuprates, an expectation very recently confirmed [17]. This is not the whole story however. Since each layer consists of two weakly coupled copies of the AF Heisenberg model on a square lattice, the ordering can take place with wave-vector  $(0, \pi)$  or  $(\pi, 0)$  in the plane, leading to an additional Ising order parameter [29–31]. According to a recent study [32], there are two scenarios for the phase transition. If the interlayer coupling is large the system will either undergo a *first-order* transition to a low-temperature phase where both the Ising and the Néel order parameter acquire a finite value, while for small interlayer coupling there should be a sequence of two phase transitions first to a phase with Ising order (fluctuations choose between  $(0, \pi)$  or  $(\pi, 0)$ ), then to a phase with 3D AFM order. Although the results of Ref. 17 point to a single transition, further experimental investigations of the ordering process are necessary to fully clarify its nature.

Doping T-CuO away from half filling cannot be achieved chemically without introducing disorder in the CuO layers, but it may be realized in principle by a field effect approach employing ionic liquids [33]. This is a real challenge, and we will only briefly discuss this possibility here. By analogy to e.g. Na-doped  $\text{Ca}_2\text{CuO}_2\text{Cl}_2$  [26, 27], the system can be expected to develop superconductivity upon doping. The two-sublattice structure has an interesting consequence however. As shown in Fig. 4, when the Fermi surface changes from hole-like to electron-like, two types of electron pockets with different numbers of carriers would appear before another change of topology takes place that leads to a single type of electron pocket. This should be contrasted to the case of the high- $T_c$  cuprates where there is always only one type of pocket for both electron and hole-like Fermi surface. The consequences on superconductivity are left for future investigation.

We acknowledge support by the Swiss NSF, namely through Grant N PA00P21-36420 (L.M.). We thank C. Proust, B. Vignolle, J. Denlinger, A. Damascelli, S. Nemsak and C. Tournier-Colletta for valuable discussions. The Advanced Light Source is supported by the Director, Office of Science, Office of Basic Energy Sciences, of the U.S. Department of Energy under Contract No. DE-AC02-05CH11231. S.M. and L.M. contributed equally to this work.

\* Equally contributed to this work

[1] J. G. Bednorz and K. A. Müller, *Z. Physik, B* **64**, 189 (1986).  
[2] M. K. Wu *et al.*, *Phys. Rev. Lett.* **58**, 908 (1987).

- [3] E. Dagotto and T.M. Rice, *Science* **271**, 618 (1996).
- [4] M. Azuma, Z. Hiroi, M. Takano, K. Ishida, and Y. Kitaoka, *Phys. Rev. Lett.* **73**, 3463 (1994).
- [5] Z. Hiroi, M. Azuma, M. Takano, and Y. Bando, *J. Solid State Chem.* **95**, 230 (1991).
- [6] J. Zaanen, G.A. Sawatzky, and J.W. Allen, *Phys. Rev. Lett.* **55**, 418 (1985).
- [7] H. Eskes, L.H. Tjeng, and G.A. Sawatzky, *Phys. Rev. B* **41**, 288 (1990).
- [8] S. Åsbrink and L.J. Norrby, *Acta Cryst. B* **26**, 8 (1970).
- [9] A.T. Boothroyd *et al.*, *Physica B* **234**, 731 (1997).
- [10] S.-H. Jung *et al.*, *Phys. Rev. B* **80**, 140516(R) (2009).
- [11] See Supplemental Material at <http://link.aps.org/supplemental/xxxx> for sample growth, supplementary ARPES data, a discussion of ARPES intensities, and details on the model.
- [12] W. Siemons, G. Koster, D.H.A. Blank, R.H. Hammond, T.H. Geballe, and M.R. Beasley, *Phys. Rev. B* **79**, 195122 (2009).
- [13] D. Samal *et al.*, *Euro Phys. Lett* **105**, 17003 (2014).
- [14] G. Peralta, D. Puggioni, A. Filippetti, and V. Fiorentini, *Phys. Rev. B* **80**, 140408(R) (2009).
- [15] X.-Q. Chen, C.L. Fu, C. Franchini, and R. Podloucky, *Phys. Rev. B* **80**, 094527 (2009).
- [16] P.M. Grant, *J. Phys.: Conf. Ser.* **129**, 012042 (2008).
- [17] K.S. Rabinovich, L.L. Samollenko, A.S. Zhuravleva, and A.G. Shneider, *Appl. Phys. Lett.* **104**, 182406 (2014).
- [18] A. Abanov, A. Chubukov, and A.V. Schmalian, *Adv. Phys.* **52**, 119 (2003).
- [19] F.P. Koffyberg and F.A. Benko, *J. Appl. Phys.* **53**, 1173 (1982).
- [20] F.C. Zhang and T.M. Rice, *Phys. Rev. B* **37**, 3759 (1988).
- [21] F. Ronning *et al.*, *Science* **282**, 2067 (1998).
- [22] M. Ogata and H. Fukuyama, *Rep. Prog. Phys.* **71**, 036501 (2008).
- [23] T. Tohyama and S. Maekawa, *Superc. Sci. Technol.* **13**, R17 (2000).
- [24] J.-Y.P. Delannoy, M.J.P. Gingras, P.C.W. Holdsworth, and A.-M.S. Tremblay, *Phys. Rev. B* **79**, 235130 (2009).
- [25] H. Eskes and G.A. Sawatzky, *Phys. Rev. B* **44**, 9656 (1991).
- [26] Y. Kohsaka *et al.*, *J. Am. Chem. Soc.* **124**, 12275 (2002).
- [27] K.M. Shen *et al.*, *Phys. Rev. Lett.* **93**, 267002 (2004).
- [28] B.O. Wells *et al.*, *Phys. Rev. Lett.* **74**, 964 (1995).
- [29] C.L. Henley, *Phys. Rev. Lett.* **62**, 2056 (1989).
- [30] P. Chandra, P. Coleman, and A.I. Larkin, *Phys. Rev. Lett.* **64**, 88 (1990).
- [31] C. Weber *et al.*, *Phys. Rev. Lett.* **91**, 177202 (2003).
- [32] Y. Kamiya, N. Kawashima, and C. D. Batista, *Phys. Rev. B* **84**, 214429 (2011).
- [33] A.T. Bollinger *et al.*, *Nature (London)* **472**, 458 (2011).

## 5.11 *c*-axis dispersion

To show the quasi two dimensional nature of the first excitation ZRS state in T-CuO, we mapped the high symmetry directions as a function of photon energy. The photon energies were chosen in the interval {84.6 -160} eV and in such a way as to maintain a constant stepsize  $\Delta k_z = \frac{\partial k_z}{\partial h\nu} \Delta h\nu$ , where  $k_z = \frac{1}{\hbar} \sqrt{2m(E_{kin} \cos^2(\theta) + V_0)}$  and  $E_{kin} = h\nu - \Phi - |E_b|$  with the binding energy  $|E_b|$ . For simplicity, the measurement was done in an experimental configuration  $\theta = 0$ . This implies the intensity suppression of the ZRS band along the  $k_x = \pm k_y$  diagonal as discussed in Sec. 5.13.

For each photon energy  $h\nu$ , a complete  $\{k_x, k_y, E_{kin}\}$  data set was acquired in the entire 1st BZ. The 4D  $\{h\nu, k_x, k_y, E_{kin}\}$  data set was then converted to  $\{k_z, k_x, k_y, E_b\}$  with an inner potential  $V_0 = 15.3$  eV, determined self consistently by adjusting the  $k_z$  dispersion of band  $\beta$  to the  $4\pi/c$  periodicity of the 3D BZ.

Two  $\{k_{||}, k_z\}$  cuts for  $E_b = 2.5$  eV and  $E_b = 3.5$  eV, along the high symmetry path  $\Gamma\text{MX}\Gamma$ , are shown in Fig. 5.13. The traces of the ZRS ( $E_b = 2.5$  eV; Fig. 5.10 (a)) are vertical straight lines, consistent with a nearly two dimensional character of that band. Due to the suppression of the ZRS spectral weight along the  $k_x = \pm k_y$  diagonal, the intensity is unequally distributed around momenta A and A' as well as B and B'. By contrast, band  $\beta$  ( $E_b = 3.5$  eV; Fig. 5.13 (b)) shows a clear  $k_z$  dispersion, suggesting a mixed Cu  $d_{x^2-y^2}$  and O  $p_z$  character.

## 5.12 Angle resolved photoemission - beyond the ZRS

In the discussion of the paper in Sec. 5.10., we focussed mainly on the dispersion of the ZRS and its propagation on and in between corner sharing sublattices. However, we did not scratch the physics of the higher binding energy bands building the backbone of the non-bonding  $d^9\bar{L}$  manifold.

Although the ZRS band is mostly split off the higher binding energy states  $\beta$ , there are still some k-points of slight overlap between the ZRS and  $\beta$  as e.g. close to X' and X. At these points,  $\beta$  masks the incoherent spectral weight of the ZRS.

Fig. 5.11 presents an ARPES intensity map over a large binding energy window along  $\Gamma\text{MX}\Gamma$ . Three band features are visible. Towards low binding energy, the ZRS state appears faintly. It is dominated by two more intense bands. The first one – labeled  $\beta$  – has a maximum at around 3.25 eV binding energy and a band width of approximately 500 meV. These are the states building up peak 6 in the integrated photoemission spectra of Fig. 5.8 and have been claimed to be of mostly  ${}^3B_1$  symmetry (one hole on the Cu  $B_{1g}(d_{x^2-y^2})$  orbital, one on a linear combination of O  $p$  orbitals with  $A_{1g}(d_{z^2})$  symmetry:  $B_{1g} \otimes A_{1g} = B_{1g}$ ) [175, 179]. Likely to be influenced by apical oxygen states, band  $\beta$  shows enhanced  $k_z$  dependence (i.e. photon energy dependence) of the ARPES signal at higher binding energies (compare to Sec. 5.11).

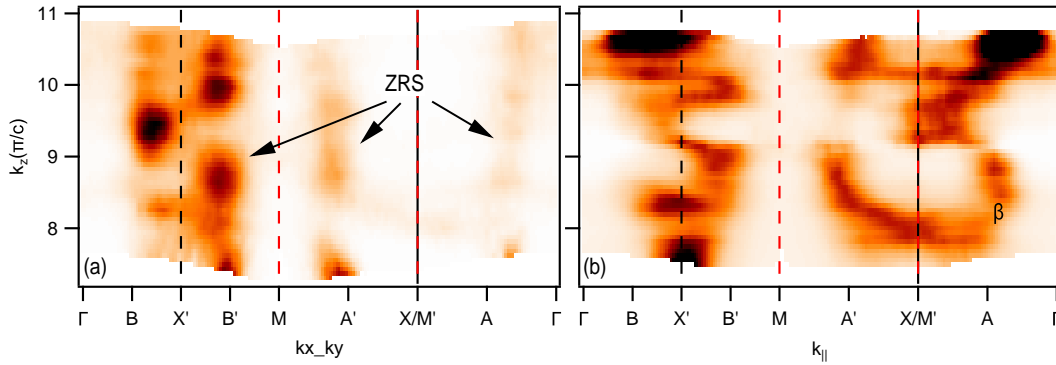


Figure 5.10: (a)  $k_x k_z$  CE map of the ZRS at 2.5 eV binding energy. The out of plane dispersion of this state is negligible and only subject to intensity modulation due to matrix element effects. (b) same for band  $\beta$  at 3.5 eV binding energy. The  $k_z$  dispersion is not negligible anymore, suggesting significant intermixing of out of plane orbitals.

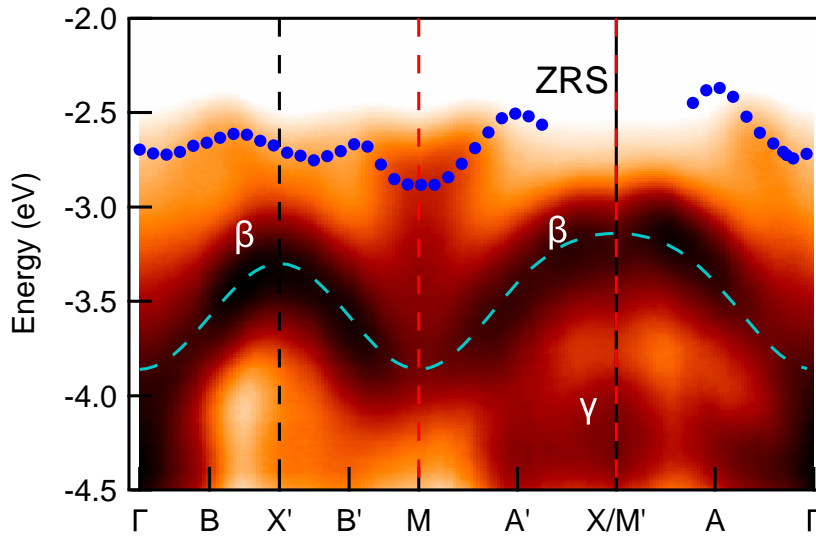


Figure 5.11: The dispersion of band  $\beta$  measured with 120 eV photonenergy. This state is extremely pronounced with respect to the ZRS (blue balls) and can be modeled by a simple tight binding dispersion with effective hopping terms  $t = 90$  meV and  $t' = 25$  meV (blue dashed). A third band  $\gamma$  of low dispersion appears at about -4.2 eV.

At fixed photon energy  $h\nu = 120$  eV, we can fit band  $\beta$  to a 2D tight binding dispersion  $\varepsilon_{\mathbf{k}} \sim -2t[\cos(ak_x) + \cos(ak_y)] - 4t' \cos(ak_x) \cos(ak_y) - 3.4$  eV with  $t = 90$  meV and  $t' = 25$  meV.

States  $\beta$  are followed by a hardly dispersing but broad band  $\gamma$  at around 4.2 eV binding energy corresponding to peak 5 in Fig. 5.8 and mostly of unhybridized oxygen  $2p$  character.

### 5.13 Matricelements in T-CuO

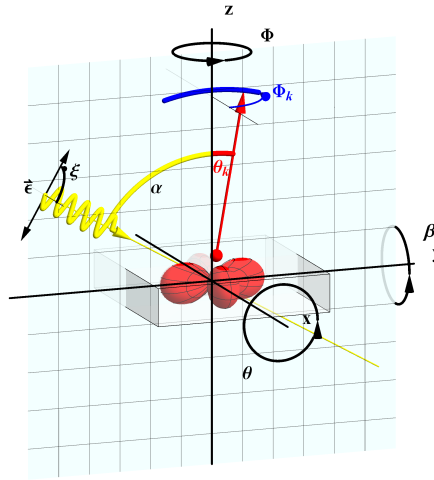


Figure 5.12: Experimental geometry at BL07 of the ALS. The sample can be rotated around  $x$ ,  $y$  and  $z$  axis by angles  $\theta$ ,  $\beta$  and  $\phi$ . The polarization is fixed in the scattering plane  $\xi = \pi/2$ . So is the orientation of the analyzer slit  $\phi_k = \pi/2$  (blue bow).

In our experimental geometry (Fig. 5.12), the scattering plane  $yz$  is fixed and contains the polarization vector  $\epsilon$  as well as the analyzer slits ( $\phi_k = \pi/2$ ). The angle between the incident light and the spectrometer's axis ( $z$ -axis) is  $\alpha = 60^\circ$ . Photoelectrons are collected within an angular range  $-15^\circ < \theta_k < 15^\circ$ . Mapping of  $k$ -space is performed by rotating the sample by angles  $\theta$ ,  $\beta$  and  $\phi$  around the  $x$ -,  $y$ - and  $z$ -axis, respectively. At normal emission,  $\theta = \beta = \phi = 0$  and the sample normal coincides with the  $z$  axis. The rotation is described by the rotation matrix  $\mathcal{R}(\theta, \phi, \beta)$ . In the  $k_x k_y$  ARPES measurement,  $\beta$  is changed, while  $\theta$  and  $\phi$  remain constant.

As discussed above, the lowest energy two-hole state in CuO is a ZRS of  ${}^1A_1$  symmetry. This state is constructed from one hole occupying the Cu  $B_{1g}(d_{x^2-y^2})$  orbital and another hole on an linear combination of the four surrounding oxygen  $p_{x/y}$ -orbitals with equally  $B_{1g}(x^2 - y^2)$  symmetry. The basis functions are defined in Fig. 5.7 [175]. In  $D_{4h}$ , this results in a total final state symmetry of  $B_1 \otimes B_1 = A_1$ .

The one-hole ground state of CuO is well described By a linear combination  $c_1 d^9 + c_2 d^{10} \underline{L}$ , where  $c_1/c_2 \sim \mathcal{O}(1)$ . The photoemission signal building the ZRS spectral weight consequently results from an emitting orbital of  $x^2 - y^2$  symmetry, either from Cu  $3d_{x^2-y^2}$  or from the linear combination  $1/\sqrt{4}(p_{x1} - p_{y2} - p_{x3} + p_{y4})$  of oxygen orbitals as defined in Fig. 5.7.

The angular part of the Cu  $3d_{x^2-y^2}$  orbital can be written as

$$|d_{x^2-y^2}\rangle = \frac{1}{\sqrt{2}}(|2, 2\rangle + |2, -2\rangle) . \quad (5.1)$$

According to Eq. 1.45 the matrix element so becomes

$$\begin{aligned} M^{d_{x^2-y^2}}(\mathbf{k}_f, \theta, \phi, \beta) &\propto \frac{1}{\sqrt{2}} \sum_{m'=-2}^2 \left( D_{m',2}^2(\theta, \phi, \beta) M^{2m'}(\mathbf{k}_f) + D_{m',-2}^2(\theta, \phi, \beta) M^{2m'}(\mathbf{k}_f) \right) \\ &= \frac{1}{\sqrt{2}} \sum_{m'=-2}^2 M^{2m'}(\mathbf{k}_f) \left( D_{m',2}^2(\theta, \phi, \beta) + D_{m',-2}^2(\theta, \beta, \phi) \right) . \end{aligned} \quad (5.2)$$

The matrix element of the  $B_1$  oxygen state is a little more complex as it involves a linear combination  $\sum_n c_n \phi(\mathbf{r} - \mathbf{R}_n)$  of off-centered orbitals. According to Eq. 1.32 the matrix element of the  $p_{x^2-y^2} := 1/\sqrt{4}(p_{x1} - p_{y2} - p_{x3} + p_{y4})$  orbital becomes

$$\begin{aligned} M^{p_{x^2-y^2}}(\mathbf{k}_f) &= \frac{1}{\sqrt{4}} \left[ e^{-iak_{fx}/2} M_{p_x} - e^{-iak_{fy}/2} M_{p_y} - e^{iak_{fx}/2} M_{p_{xf}} + e^{iak_{fy}/2} M_{p_{yf}} \right] \\ &= \frac{2i}{\sqrt{4}} \left[ \sin(ak_{fx}/2) M_{p_x} - \sin(ak_{fy}/2) M_{p_y} \right] \\ &= \frac{i}{\sqrt{2}} \sin(ak_{fx}/2) [M^{11} - M^{1-1}] - \frac{1}{\sqrt{2}} \sin(ak_{fy}/2) [M^{11} + M^{1-1}] \\ &= \frac{1}{\sqrt{2}} \left( [i \sin(ak_{fx}/2) - \sin(ak_{fy}/2)] M^{11} \right. \\ &\quad \left. - [i \sin(ak_{fx}/2) + \sin(ak_{fy}/2)] M^{1-1} \right) . \end{aligned} \quad (5.3)$$

Rotating the orbitals now involves an additional transformation of the phasefactor  $\mathbf{k}'_f = \mathcal{R}\mathbf{k}_f$  and we obtain as a final result



$$\begin{aligned}
 M^{p_{x^2-y^2}}(\mathbf{k}_f, \theta, \phi, \beta) &= \frac{1}{\sqrt{2}} \sum_{m'=-1}^1 M^{1m'} ([i \sin(ak'_{fx}/2) - \sin(ak'_{fy}/2)] D_{m',1}^1(\theta, \phi, \beta) \\
 &\quad - [i \sin(ak'_{fx}/2) + \sin(ak'_{fy}/2)] D_{m',-1}^1(\theta, \phi, \beta)) . \quad (5.4)
 \end{aligned}$$

To simulate the spectral function of the ZRS, we use a phenomenological SDW dispersion  $\varepsilon_{\mathbf{k}} = -4t' \cos(ak_x) \cos(ak_y) - 2t''(\cos(2ak_x) + \cos(2ak_y)) - J(\cos(ak_x) + \cos(ak_y))^2 - 4t_d \cos(ak_x/2) \cos(ak_y/2)$  with  $t' = -40$  meV,  $t'' = 12$  meV,  $J = 120$  meV and  $t_d = -40$  meV which fits our QP dispersion well. We further approximate the spectral function of Eq. 1.13 as a Gaussian function

$$A(\mathbf{k}, E) \propto \frac{1}{\sqrt{2\pi}\sigma} e^{-\frac{(E-\varepsilon_{\mathbf{k}})^2}{2\sigma^2}} . \quad (5.5)$$

with broadening  $\sigma \sim 1$  eV.

Fig. 5.13 illustrates the effect of the matrix elements on the ZRS band and can be compared directly to Fig. 1 (a) of the paper in Sec. 5.10. Figs. 5.13 (a1) and (b1) show two calculated  $k_x k_y$  intensity maps, around  $k_x = 0 \text{ \AA}^{-1}$  ( $\theta = 0^\circ$ ) and  $k_x = -3 \text{ \AA}^{-1}$  ( $\theta = 36^\circ$ ), respectively. They reproduce the spectral function of Eq. 5.5, without matrix elements. The same intensity maps, multiplied by the angle-dependent matrix elements of the  $\text{Cu}d_{x^2-y^2}$  orbital, are shown in Figs. 5.13 (a2) and (b2). One observes a general reduction of intensity around normal emission ( $k_x = 0$ ;  $k_y = 0$ ). Intensity is also suppressed along the diagonals  $k_x = k_y$  – but *not* along the diagonals of a generic BZ – consistent with the experimental observations. Figs. 5.13 (a3) and (b3) take into account the matrix elements of the linear combination of O  $p$  states  $M^{p_{x^2-y^2}}$ . Clearly, spectral weight is again suppressed towards normal emission. The suppression along the diagonal however remains obsolete. We thus conclude our observation to stem mostly from Cu  $d_{x^2-y^2}$  states, which in view of a cross section ratio O  $2p$ /Cu  $3d \sim 0.16$  is not surprising.

Notice that since the left and right parts of the composite map of Fig. 1 (a) of the paper in Sec. 5.10. were collected in different scattering geometries  $\theta$ , intensities do not connect smoothly at their boundary.

## 5.14 The generalized $t$ - $J$ model

Following the method of Eskes and Sawatzky [179], Mila and Yang have performed a  $\text{Cu}_2\text{O}_6$  cluster calculation to estimate the effective hopping  $t_d$  and exchange parameter  $J_d$  of the gen-

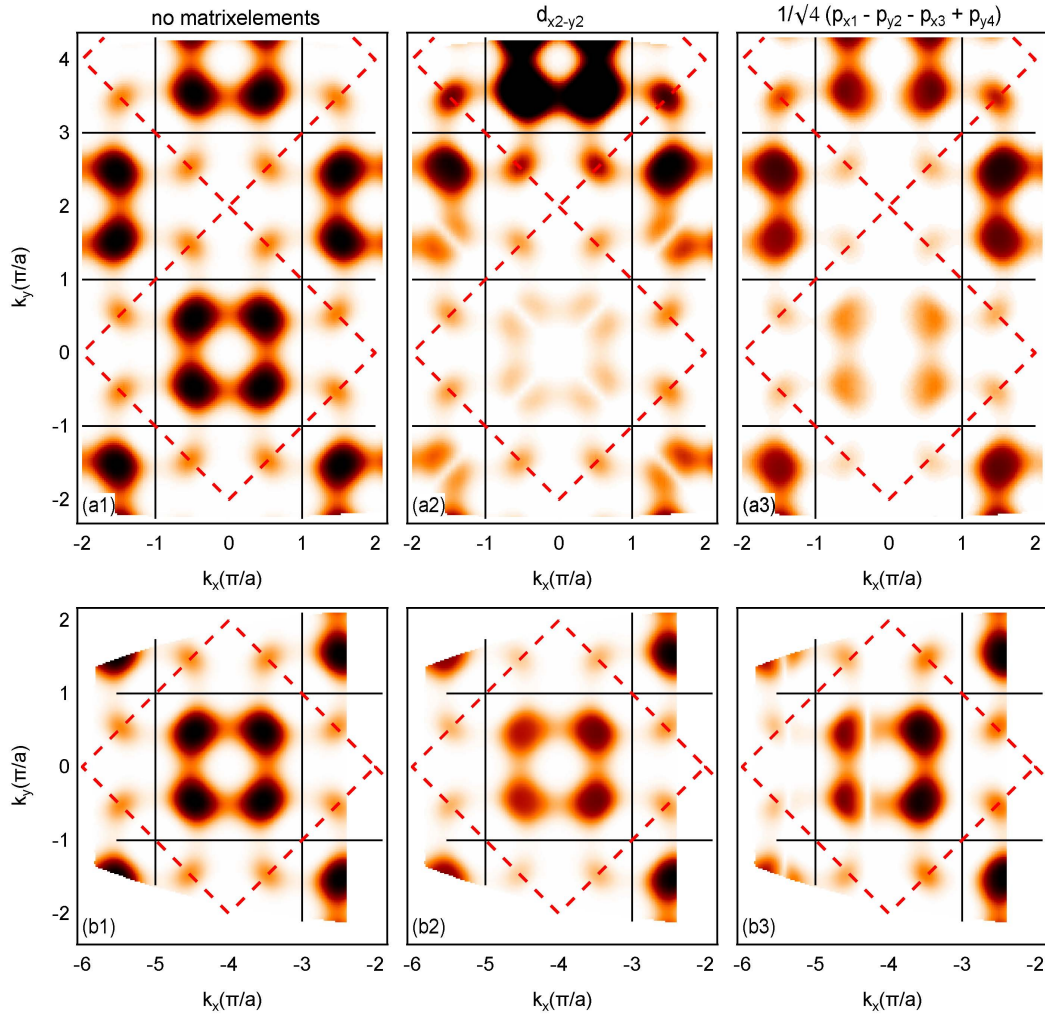


Figure 5.13: Simulated ARPES constant energy maps at 120 eV photon energy. Column **(1)** shows the simulated spectral function. Column **(2)** takes into account matrix elements of the  $\text{Cu}d_{x^2-y^2}$  orbital. Column **(3)** takes into account matrix elements of the oxygen state  $1/\sqrt{4}(p_{x1} - p_{y2} - p_{x3} + p_{y4})$ . Panels **(a1/2/3)** are calculated for  $\theta = 0$ , panels **(b1/2/3)** for  $\theta = 36^\circ$ . These configurations correspond to the  $\beta$ -scans taken in Fig. 1 of the paper in Sec. 5.10.

eralized  $t$ - $J$  model. The values for the Cu-O and O-O hybridization strengths  $V_{pd}^\sigma = 1.5$  eV,  $V_{pd}^\pi = -0.7$  eV,  $V_{pp}^\sigma = -1.0$  eV and  $V_{pp}^\pi = 0.3$  eV, as well as for the on-site correlation parameters  $U_{dd} = 8.8$  eV and  $U_{pd} = -6$  eV, were adopted from [179]. For the charge transfer energy, the experimental estimate  $\Delta = 3.6$  eV of Sec. 5.7 was used.

To estimate the diagonal coupling terms between two corner-sharing sublattices, the three-band Hubbard model on  $\text{Cu}_2\text{O}_6$  (shown in Fig. 5.14) with two and three hole configurations was diagonalized exactly, and the lowest energy states were mapped onto the corresponding states of the  $t$ - $J$  model. This yields a diagonal hopping  $t_d \sim -0.1$  eV, and a very small diagonal exchange coupling  $J_d = 0.006$  eV. The diagonal coupling terms originate mostly from hopping between oxygen  $p_x p_y$  orbitals and have little dependence on the Cu-O hybridization strengths  $V_{pd}^\sigma$  or  $V_{pd}^\pi$ . These terms also change very little when repulsion and exchange terms between Cu and O atoms are added to the model. Inside corner-sharing sublattices, typical parameters for cuprates  $t = 0.42$  eV,  $t' = -0.14$  eV,  $t'' = 0.06$  eV and  $U = 3.34$  eV were adopted from Ref. 184. The exchange term  $J = 0.21$  eV is then estimated from  $4t^2/U$ .

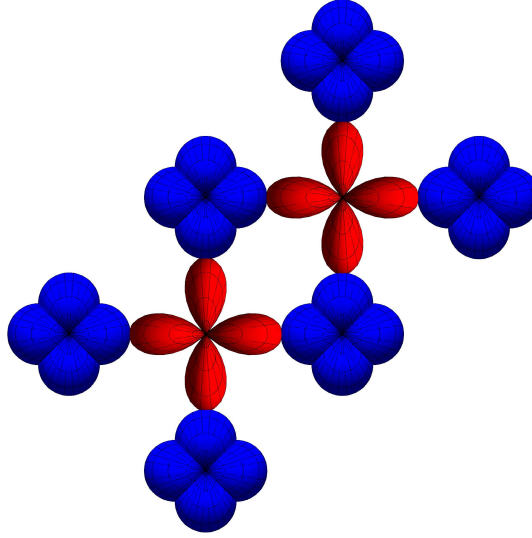


Figure 5.14:  $\text{Cu}_2\text{O}_6$  cluster.

We then consider an extended  $t$ - $J$  model defined as:

$$\begin{aligned} \tilde{H}_{tJ} = & J \sum_{i,j} \mathbf{S}_i \cdot \mathbf{S}_j - t \sum_{i,j,\sigma} \hat{c}_{i,\sigma}^\dagger \hat{c}_{j,\sigma} - t' \sum_{i,j',\sigma} \hat{c}_{i,\sigma}^\dagger \hat{c}_{j',\sigma} \\ & - t'' \sum_{i,j'',\sigma} \hat{c}_{i,\sigma}^\dagger \hat{c}_{j'',\sigma} + J_d \sum_{i,m} \mathbf{S}_i \cdot \mathbf{S}_m - t_d \sum_{i,m,\sigma} \hat{c}_{i,\sigma}^\dagger \hat{c}_{m,\sigma} . \end{aligned}$$

The  $t$ - $J$  model has proven to provide an accurate description of the low energy physics of the corner sharing  $\text{CuO}_2$  plane when taking into account the higher order hopping terms  $t'$  and  $t''$ . The additional Cu atom at the center of the edge-sharing CuO plaquette (compare Fig. 5.5) now gives rise to the hopping term  $t_d \sim -t/4$  which mainly governs the energy separation of quasi-equivalent  $k$ -points shown in Fig. 3 of the paper in Sec. 5.10.

$\tilde{H}_{t,J}$  was exactly diagonalized on a 32 site cluster to calculate the hole spectral function  $A(\mathbf{k}, \hbar\omega)$ , which is proportional to the ARPES electron-removal spectrum:

$$A(\mathbf{k}, \omega) = \sum_f |\langle \Psi_f^{N-1} | \hat{c}_{\mathbf{k},\sigma} | \Psi_0^N \rangle|^2 \delta(\hbar\omega - E_0^N + E_n^{N-1}(\mathbf{k})). \quad (5.6)$$

$\Psi_0^N$  is the  $N$ -particle many-body ground state, with energy  $E_0^N$ , and  $\Psi_n^{N-1}$  are the  $(N-1)$ -particle eigenstates, with energies  $E_n^{N-1}$ . For our 32-site cluster,  $A(\mathbf{k}, \omega)$  is only defined at a small number of  $k$ -points.

The wavefunction  $\Psi_0^N$  was initially calculated for half filling by the Lanczos algorithm. Applying the fermion destruction operator onto  $\Psi_0^N$ , yields a one hole state that is appropriate to initialize the Lanczos algorithm a second time. After 350 Lanczos cycles we calculated the spectral function with the standard continued fraction technique. To mimic the typically broad line shapes of our ARPES data, the results were convoluted by a gaussian of FWHM= 500 meV.

## 5.15 Speculations about the doped system

Various attempts to dope T-CuO by chemical means during the PLD growth process failed so far, indicating that it is hard for this highly strained system to incorporate substitutional or interstitial impurities.<sup>7</sup> Nevertheless it is instructive to get a feeling of how the electronic structure could look like in the doped system.

As a “first guess”, one can assume that the Fermi surface of doped T-CuO – as typically the case for the doped corner sharing cuprates – is well approximated by the tight binding dispersion

$$\begin{aligned} \varepsilon_{\mathbf{k}} = & -4t_d [\cos(ak_x/2) \cos(ak_y/2)] - 2t [\cos(ak_x) + \cos(ak_y)] \\ & -4t' [\cos(k_x a) \cos(k_y a)] - 2t'' [\cos(2k_x a) + \cos(2k_y a)]. \end{aligned} \quad (5.7)$$

Both the corresponding unit cell and the Brillouin zone are marked by red squares in Fig. 1 (a) of the paper in Sec. 5.10. For a given hole concentration  $n = \#\text{holes}/\text{Cu}$ , the Fermi energy  $E_F$  is

---

<sup>7</sup>Substitutional doping attempts by Ni and Zn led to a collapse of the tetragonal structure. Surface doping by alkali metals such as Na and Li did not show any effect on the electronic structure.

obtained by solving the equation

$$\frac{1}{2}(1 - n) = \frac{1}{4\pi^2} \int_{BZ} \Theta(E_F - \varepsilon_{\mathbf{k}}) d^3\mathbf{k}, \quad (5.8)$$

where  $\Theta(E)$  is the Heaviside step function.

The tight binding dispersion  $\varepsilon_{\mathbf{k}}$  using the values obtained in our cluster calculation  $t'/t = -0.327$ ,  $t_d/t = -0.237$  and  $t''/t = 0.154$  is plotted in Fig. 5.15. Additionally, the dispersion is cut at energies corresponding to solutions of Eq. 5.8 for three different hole doping levels of (a)  $n = 0.07$ , (b)  $n = 0.37$  and (c)  $n = 0.80$ . The topology of the corresponding Fermi surfaces obviously changes by varying the doping level away from half filling, i.e. there are two types of pockets when the Fermi surface becomes electron-like as discussed in Fig. 4 (b-d) of the paper in Sec. 5.10.

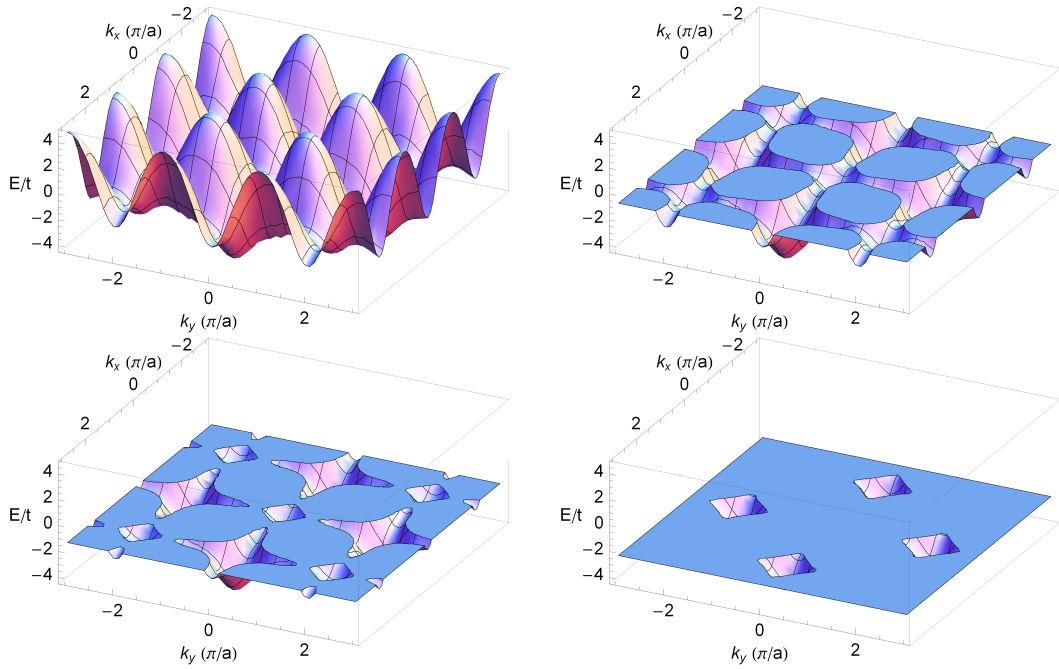


Figure 5.15: Tight binding dispersion (**top left**) and Fermi sea for hole doping levels  $n = 0.07$  (**top right**),  $n = 0.37$  (**bottom left**) and  $n = 0.80$  (**bottom right**).



# 6 T-CuO – a 2D edge-sharing cuprate investigated by RIXS

## 6.1 Summary

In the last chapter we will give some perspectives on the magnetic ground state and the spin excitations in T-CuO. A peculiar signature of ARPES spectral weight in T-CuO and other cuprates suggests particle scattering with bosonic spin excitations. RIXS data at the Cu  $L_3$  edge however are at surprising variance to what is known from the *corner-sharing* cuprates which leaves T-CuO an open field for future investigations.

## 6.2 Motivation

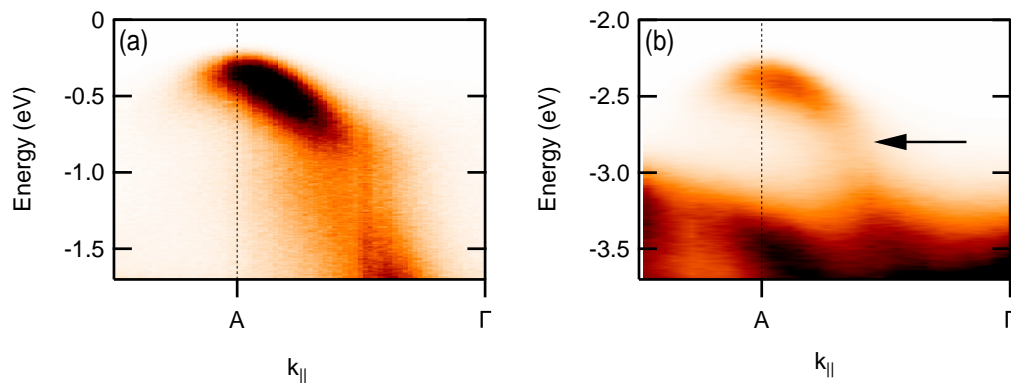


Figure 6.1: ARPES dispersion for (a)  $\text{Ca}_2\text{CuO}_2\text{Cl}_2$  (from Ref. 185) and (b) for T-CuO. The arrow marks the position of the characteristic kink in the dispersion.

One typical aspect of the ARPES data in the corner-sharing cuprates is the sharp steepening of the ARPES band dispersion between  $\Gamma$  and A, that occurs roughly 0.5 eV below the top of the valence band. Fig. 6.1 (a) shows a typical example of such a high-energy anomaly for insulating  $\text{Ca}_2\text{CuO}_2\text{Cl}_2$  [185]. The apparent sudden change of the band velocity is due to a transfer of spectral weight from the coherent to the incoherent part of the spectral function.

Fig. 6.1 (b) shows a remarkably similar anomaly for T-CuO. Even if the nature of this “waterfall”-structure is still matter of debate [186–199], the effect is suggestive of coupling of the particles to a bosonic collective mode with an energy close to the energy of zone-boundary magnons (0.3 – 0.4 eV) [52, 122, 200, 201].

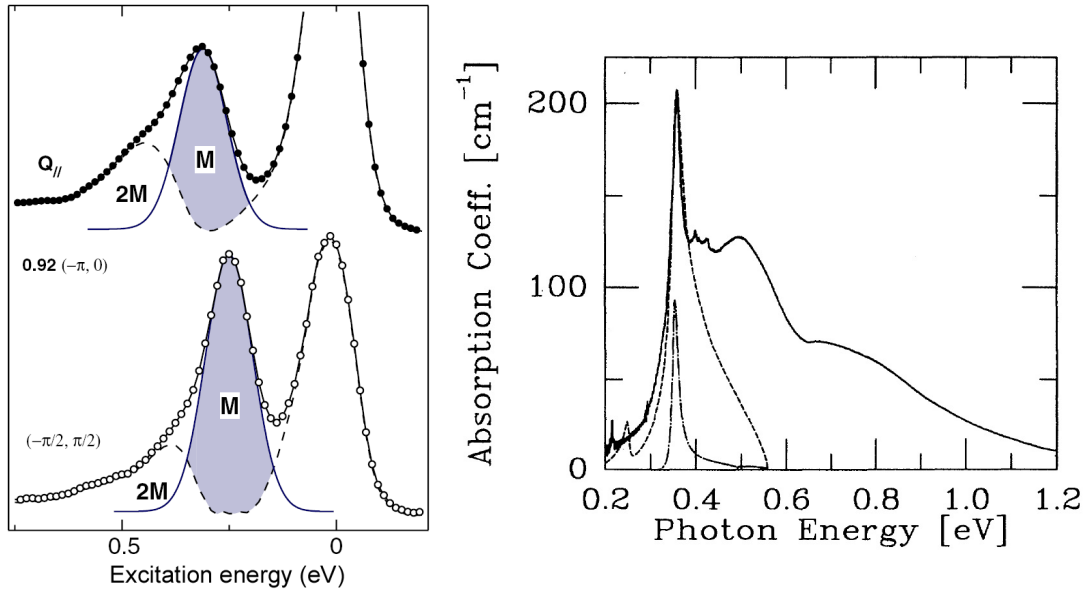


Figure 6.2: **(left)** RIXS spectra at  $(-\pi/a, 0)$  and  $(-\pi/2a, -\pi/2a)$  measured with  $\sigma$  polarization. The single magnon contribution M is followed by a bimagnon peak 2M and a multimagnon tail. This figure was taken from Ref. 52 and slightly altered. **(right)** Experimental data from Ref. 202 (solid line) and theoretical line shape for two-magnon absorption from Ref. 203 (dashed line) in  $\text{Sr}_2\text{CuO}_2\text{Cl}_2$ . The dashed dotted line peaked at  $\sim 350$  meV is the contribution to the line shape from the bimagnon at  $(\pi/a, 0)$ . The tail towards higher energies indicates contributions of multimagnon features. This figure was taken from Ref. 203.

Indeed, there is some theoretical research on the one- and three band Hubbard model which claims the incoherent contributions of the ZRS to identify with so called string excitations [192, 204, 205]. The idea behind these models is based on the assumption that holes propagating within an antiferromagnetic background leave a trace of local spin frustration (compare Fig. 6.3). Naively estimated, each frustrated spin increases the total energy of the system by  $\sim \mathcal{O}(2J)$ . Consequently, the total energy caused by the frustration will increase the further the hole moves. This potential consequently reduces the mobility of the hole and leads to the formation of a so called “spin polaron particle” [206]. However, adjacent frustrated spins can regain their antiferromagnetic coordination by simply exchanging position, thus releasing an energy on the order of  $\sim \mathcal{O}(4J)$ .

It is interesting to note that the energy scale of the kink-structure (500 meV) coincides well with typical multimagnon excitations as observed by means of RIXS and RAMAN spectroscopy in some cuprates and depicted in Fig. 6.2 [52, 207, 208]. Further, optical reflectivity data identified



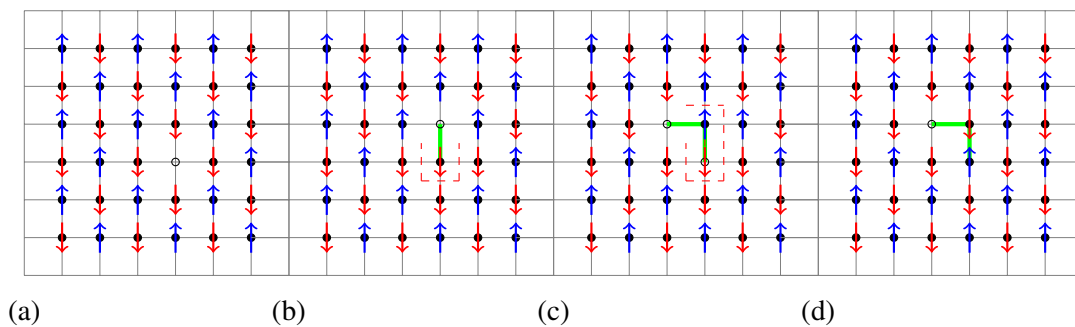


Figure 6.3: Concept of a spin polaron: (a) Creation of a hole in an antiferromagnetic spin background. (b) The hole exchanges place with a neighboring spin, causing a trace (green) of local frustration (red dashed). (c) A second exchange of place results in adjacent frustrated spin pairs  $\uparrow\uparrow\downarrow\downarrow$ . (d) Position exchange of two spins results in a relaxed configuration  $\uparrow\uparrow\downarrow\downarrow \rightarrow \uparrow\downarrow\uparrow\downarrow$ .

the existence of the so called Lorenzana Sawatzky mechanism [202, 203, 209], which allows for the emission of multimagnon excitations supported by phonons. Based on these speculations, one can estimate the exchange interaction in T-CuO.  $J \sim 180$  meV from the Hubbard [210–214], and  $J \sim 146$  meV from the Heisenberg model [215, 216]. These values compare reasonably well to a theoretical estimate of 160 meV as obtained by density functional theory [160] and to typical cuprate values [184].

One way to test the validity of these speculations is to search for spin excitations in T-CuO and compare them to the ARPES results. Due to the small film thickness, T-CuO is probably out of reach for inelastic neutron scattering experiments. Resonant inelastic x-ray scattering on the other hand has been successful in probing spin waves in various cuprates and thanks to its resonant enhancement very sensitive to small probing volumes [52, 53, 201, 215, 217, 230, 231].

## 6.3 Methods

RIXS data were taken at the SAXES spectrometer of the ADDRESS beam line, Swiss Light Source, Switzerland, where an energy resolution of  $\sim 100$  meV was obtained using a combination of focusing elements and high-precision optical gratings [219]. The base pressure of the high-vacuum chamber and the spectrometer was below  $10^{-9}$  mBar. Sample temperature was kept below 20 K. Total electron yield x-ray absorption (XAS) spectra were taken prior to experiment to calibrate the monochromator. According to Fig. 6.4, the scattering angle was kept at  $\tau = 130^\circ$ , while the sample was rotated around  $\alpha$ . The momentum transfer as a function of  $\alpha$  was calculated from Eq. 2.13.

If not otherwise indicated, RIXS spectra were measured with light linearly polarized perpendicular to the scattering plane ( $\sigma$ -polarization) to be less sensitive to dichroism in absorption. Reference spectra to calibrate emission energy, energy resolution and symmetry of the RIXS lineshape

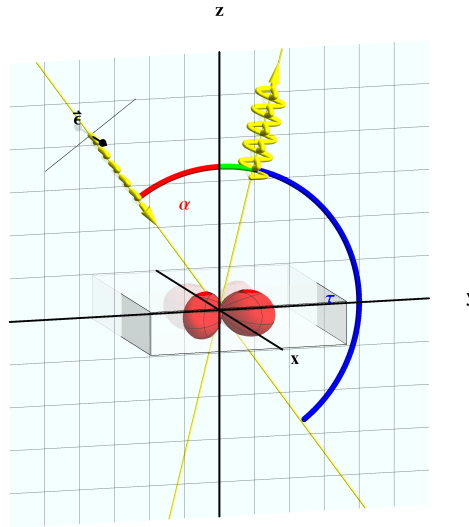


Figure 6.4: RIXS setup of SAXES at the SLS. The sample is represented by its natural coordinate system. The scattering angle  $\tau = 130^\circ$  is kept fixed while the momentum transfer direction is varied by changing  $\alpha$ . If not otherwise indicated,  $\sigma$ -polarized ( $\xi = 0$ ) light was used.

were taken for every sample prior to measurement. Spectra shown in this work are summed from several partial measurements, each accumulated for a maximum of 10 min and aligned with respect to the elastic line to minimize possible energy drifts.

## 6.4 RIXS along $\Gamma X$

Fig. 6.5 summarizes RIXS data obtained along the  $\Gamma X$  direction of T-CuO in  $\sigma$ -polarization. Panel 6.5 (a) shows the data normalized to acquisition time and photon flux. We observe three major contributions to the RIXS signal. A pronounced elastic feature at zero energy loss is followed by a structureless  $dd$  excitation peak at  $-1.5$  eV and a broad featureless plateau between  $-2$  and  $-8$  eV attributed to charge transfer (CT) excitations [220–222]. Clearly, the RIXS signal is subject to large intensity suppression away from grazing incidence ( $\alpha = 90^\circ$ ).

In panel 6.5 (b), we plot the absolute intensity of the elastic as well as the  $dd$  excitation peak. Towards grazing incidence, both features clearly exhibit a similar rise whereas towards grazing emission, the signal saturates at low intensity. The only exception to this trend is presented by the sharp signal rise of the elastic feature close to the specular reflection at  $\alpha = 25^\circ$ . This trend is indicative of a typical self absorption effect in thin films as discussed in Fig. 2.8, which is determined by the normalized film thickness  $d \times \mu(h\nu)$  rather than the absorption ratio  $\mu(h\nu')/\mu(h\nu)$  of out and ingoing beam. The data was therefore normalized to the intensity of the  $dd$  excitation peak and plotted in panel 6.5 (c).

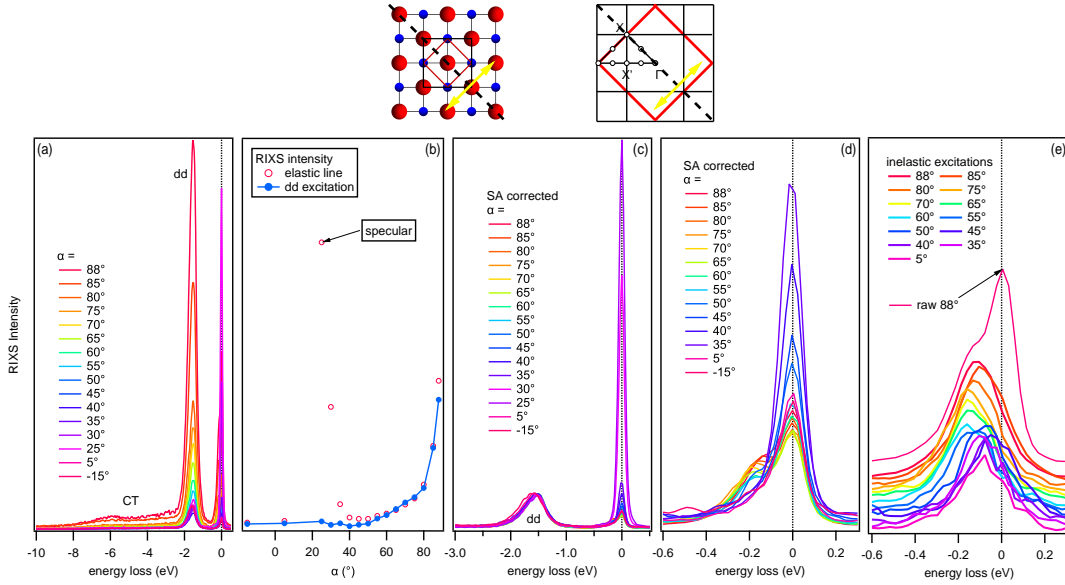


Figure 6.5: RIXS of T-CuO along  $\Gamma X'$  measured with  $\sigma$ -polarized light. **(a)** Normalized data. **(b)** Angular distribution of elastic and  $dd$ -excitation peak. **(c)** Data normalized to  $dd$ -excitation peak. **(d)** Close up of the low energy loss region. **(e)** Data subtracted by a Voigt profile exposes the low energy excitations.

In panel 6.5 (d) we show a close up of the low energy loss region and see the elastic peak to be accompanied by a distinct shoulder.<sup>1</sup> In order to isolate the inelastic contributions, we subtract a Voigt profile to account for the elastic peak and show the residual in panel 6.5 (e). Starting from grazing incidence  $\alpha = 90^\circ$ , the remaining feature disperses towards higher energy loss, with a maximum at  $\alpha \sim 70^\circ$ . From here this feature disperses again towards zero energy loss, loses spectral weight and disappears in the dominant inelastic peak. A reliable detection is again possible at  $\alpha = 5^\circ$ , where self absorption however reduces signal statistics.

## 6.5 RIXS along $\Gamma X'$

RIXS measurements along the  $\Gamma X'$  direction are summarized in Fig. 6.6 (a). Whereas the CT structure remains unchanged, we now observe a pronounced double peak structure  $dd1/dd2$  in the  $dd$  excitation regime.  $dd1$  is located at  $\sim -1.5$  eV and can be identified with the  $dd$  excitation observed along  $\Gamma X$ , where  $dd2$  was not observed.

The intensity ratio of peaks  $dd1$  and  $dd2$  varies as a function of  $\alpha$ . Panel 6.6 (b) plots the absolute intensity of the  $dd$ - and the elastic peak. The discrepancy of  $dd1$  and  $dd2$  becomes most obvious close to grazing incidence, where both  $dd1$  and the elastic peak seem to be equally enhanced in comparison to  $dd2$ . Thus, we again use  $dd1$  to normalize our data.

<sup>1</sup>Due to the dominance of Thomson scattering, the curves measured at  $\alpha = 30$  and  $25^\circ$  are not shown here.

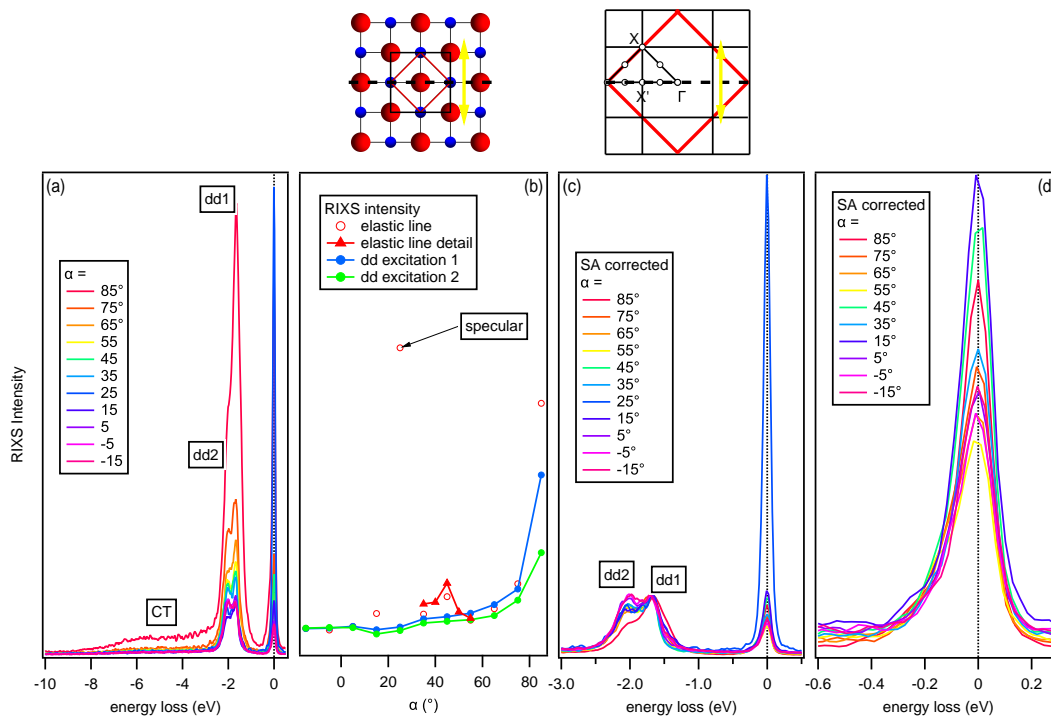


Figure 6.6: RIXS of T-CuO along  $\Gamma X'$ . **(a)** Normalized data. **(b)** Angular distribution of elastic and  $dd$ -excitation peaks. A peculiar resonance at  $\alpha = 45^\circ$  is observed. **(c)** Self absorption corrected data. **(d)** Close up of the low energy loss region. We resolve no distinct inelastic excitation.

The relative intensity variation along  $\Gamma X'$  is very similar to what has been observed for  $\text{La}_2\text{CuO}_4$  and  $\text{Sr}_2\text{CuO}_2\text{Cl}_2$ , where  $dd1$  was attributed to excitations of  $d_{xy}$ ,  $dd2$  to excitations of  $d_{xz}/d_{yz}$  electrons [222]. The large suppression of  $dd2$  along  $\Gamma X$  however is at surprising variance to these cuprates.

The angular dependence of the elastic peak exhibits an interesting feature. In specular configuration  $\alpha = 25^\circ$ , we find the expected intensity maximum of non-resonant Thomson scattering. Additionally, we observe a second, much weaker local maximum at  $\alpha \sim (45^\circ \pm 3^\circ)$ . The in plane momentum transfer corresponding to this angle is  $q_{\parallel} \sim (0.29 \pm 0.04) \text{ \AA}^{-1} \sim (0.36 \pm 0.05) \pi/a$ . Interestingly, a similar peak has been observed before in the underdoped cuprates at  $q_{\parallel} \sim 0.31 \pi/a$  and interpreted as resonant scattering of a charge density wave instability, believed to compete with high temperature superconductivity [223–225].

Panel 6.6 (c) plots the data normalized to the intensity of  $dd1$  and panel 6.6 (d) shows a close up of the low energy part. With respect to the  $\Gamma X$  direction, spectral weight of low energy excitations is now clearly suppressed, and a line shape analysis insignificant.

## 6.6 $\sigma$ vs $\pi$ -polarization

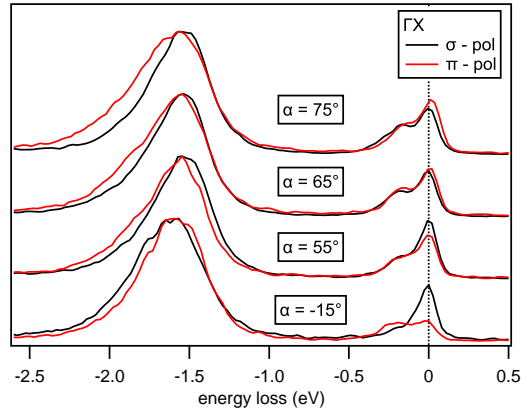


Figure 6.7: Polarization study of RIXS spectral weight measured in  $\sigma$  and  $\pi$  polarization.

In order to make sure certain excitations did not escape through a geometry imposed selection rule, we show spectra along  $\Gamma X$  over a wide range of  $\alpha$  for  $\sigma$  and  $\pi$  polarized light in Fig. 6.7. Even though nonresonant Thomson scattering can largely be suppressed in the  $\pi$  polarized configuration, the inelastic spectral weight stays largely the same. In  $\pi$ -polarization, we observe a slight broadening of the  $dd$  excitation peak. This is due to the additional  $z$  component of the polarization vector causing additional transitions in the RIXS process. The data shown so far thus indeed is representative of RIXS on T-CuO.

## 6.7 Comparison to the antiferromagnetic cuprates

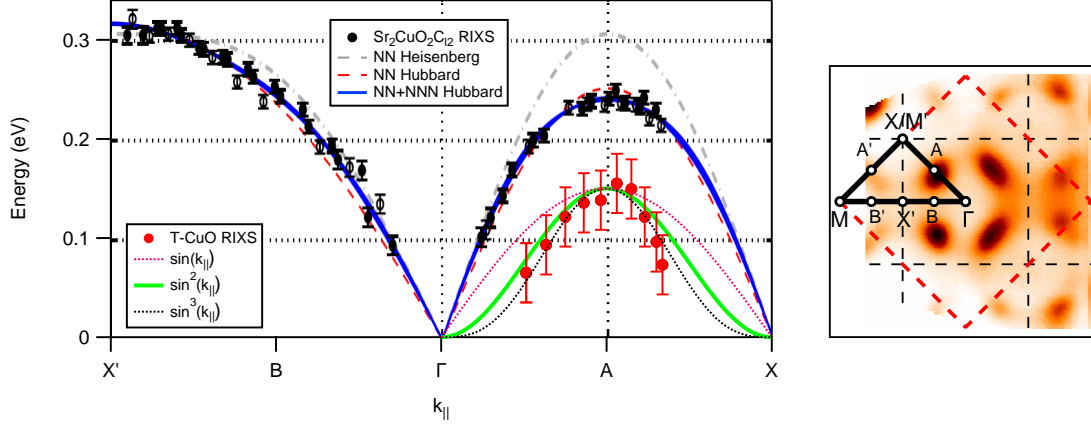


Figure 6.8: **(left)** Magnon energies from  $\text{Sr}_2\text{CuO}_2\text{Cl}_2$  taken from Ref. 52 compared to our RIXS data of T-CuO along the  $X'\Gamma X$  high symmetry path.  $\text{Sr}_2\text{CuO}_2\text{Cl}_2$  shows the typical signature of a magnon, compatible with a NN Heisenberg model with  $J = 130$  meV (**gray dashed**) a NN Hubbard model fit for  $t = 0.261$  eV and  $U = 1.59$  eV and a further-neighbor Hubbard model (**blue solid**). RIXS data from T-CuO (**red dots**) shows a detectable excitation of much lower energy along the  $\Gamma X$  direction, with a dispersion  $\sim \sin^2 k_{\parallel}$ . **(right)** BZ of T-CuO and definition of high symmetry path. For better orientation, we plot also the ARPES data of Ch. 5

As we saw, RIXS on T-CuO shows a distinct low energy inelastic feature along  $\Gamma X$  which is significantly suppressed along  $\Gamma X'$ . In Fig. 6.8, we compare the dispersion along  $\Gamma X$  extracted from the data of Fig. 6.5 (e) with magnon excitation spectra in  $\text{Sr}_2\text{CuO}_2\text{Cl}_2$  from Ref. [52]. The in plane momentum transfer of  $q_{\parallel}$  was calculated according to Eq. 2.13.

Clearly, the magnon energy in  $\text{Sr}_2\text{CuO}_2\text{Cl}_2$  is on the order of  $\mathcal{O}(2J)$ , as predicted by both the Hubbard and Heisenberg model. Despite the fact that there is no reliable sign of a dispersion along  $\Gamma X'$ , the representative excitation energy along the  $\Gamma X$  direction of T-CuO is about 30% smaller than in  $\text{Sr}_2\text{CuO}_2\text{Cl}_2$ , but still much larger than expected for typical vibrational excitations. Phenomenologically, the dispersion can be described by a  $\sin^2$  function with an amplitude of  $\sim 150$  meV, a value which is in surprising agreement with neutron diffraction experiments on the 1D spinon system tenorite (147 meV) [232]. We can therefore assume that the observed excitations are of magnetic origin.

## 6.8 What's next

In the last section we found no marked sign of spectral weight in the  $\sim 500$  meV regime which would relate to multimagnon excitations. The interpretation of the “high energy anomaly” in the framework of electron-multimagnon scattering can therefore not be confirmed so far. To some

extent, this discrepancy however could have been expected:

In contrast to the antiferromagnetic corner sharing cuprates, T-CuO involves a small additional exchange coupling term  $J_d$ . Such a term is known to spontaneously break the fourfold symmetry as the system undergoes an Ising transition at finite temperature through the order by disorder effect discussed in Ch. 5 [226–228]. From this point of view, it is questionable if the spin excitation spectra should still be analogous to the ones observed in the corner sharing cuprates. The system should be rather approximated by the  $J_1$ - $J_2$  Heisenberg Model, where the standard linear spin-wave theory predicts the dispersion relation to be [227, 229]

$$\hbar\omega \sim 2J \sqrt{\left(1 + \frac{J_d}{2J} \cos k_x\right)^2 - \cos^2 k_y \left(\cos k_x + \frac{J_d}{2J}\right)}. \quad (6.1)$$

This dispersion relation again yields magnon energies on the order of  $\mathcal{O}(2J) \sim 0.3$ - $0.4$  eV along  $\Gamma X$  and  $\Gamma X'$ , in clear discrepancy to our RIXS results on T-CuO.

In summary, our preliminary RIXS investigation of T-CuO by RIXS yields low energy excitations of presumably magnetic origin of an energy scale comparable to what was observed in tenorite. The data is further incompatible with the typical magnon dispersion of the cuprates. We further observe a peculiar resonant scattering feature which might point towards charge ordering but might as well be an artefact.

These exciting observations leave T-CuO a playground for further studies. Its magnetic excitations and their interplay with the elastic resonance must be studied by further experiments – but beamtime for a detailed RIXS measurement has already been granted...





# A Iridates – spin-orbit induced Mott insulators investigated by ARPES

Crossing the periodic system from low to high periods, spin-orbit coupling increases as electron-electron correlation effects decrease. Whereas the interplay of band filling and correlation can lead to complex electronic groundstates in the  $3d$  perovskite compounds, the  $4d$  systems are typically weakly correlated metals governed by Hund's rule coupling [234].

In the  $5d$  systems, where spin-orbit- and Hubbard energy are of the same order, the situation can change radically. A cooperation of spin orbit coupling and orbital polarization due to crystal field splitting (1-3 eV) can reorder the  $t_{2g}$ -bands into a four-fold degenerate and mostly filled  $j_{eff} = 3/2$  and a narrow two-fold degenerate and nearly half-filled  $j_{eff} = 1/2$  band close to the Fermi energy. The band-width of the latter is small enough to lift its degeneracy in the presence of correlation ( $\sim \mathcal{O}(500)$  meV) and to open a gap. This type of transition metal oxides can be classified as a spin-orbit induced Mott insulators with typically antiferromagnetic (AF) ground [235,236].

The most prominent example of a SOI-MI is the perovskite iridate  $\text{Sr}_2\text{IrO}_4$ , a layered compound with a structure similar to the one of the cuprates, where  $\text{IrO}_6$  octahedra form quasi two dimensional corner sharing planes, well separated from each other by the strontium atoms [235,236]. To maintain the favorable Ir-O bond length within this crystal structure, the octahedra are canted with respect to the  $c$ -axis, which lowers the symmetry and mixes  $d_{xy}$  with  $d_{x^2-y^2}$  orbitals. The result is an antiferromagnetic SOI-MI with residual in-plane ferromagnetic moment at temperatures below 100 K.

## A.1 Monolayer perovskite iridate $\text{Ba}_2\text{IrO}_4$

Within the scope of this thesis work, a sister compound of  $\text{Sr}_2\text{IrO}_4$ , the system  $\text{Ba}_2\text{IrO}_4$  was investigated. The canting effect and subsequent orbital polarization is absent in this compound due to the larger barium radius [233]. As shown in the following publication, the magnetic as well as electronic properties are however quite insensitive to these structural differences [237].

## New Journal of Physics

The open access journal at the forefront of physics

Deutsche Physikalische Gesellschaft  DPG | IOP Institute of Physics

### The electronic structure of the high-symmetry perovskite iridate $\text{Ba}_2\text{IrO}_4$

S Moser<sup>1,2,6</sup>, L Moreschini<sup>2</sup>, A Ebrahimi<sup>1</sup>, B Dalla Piazza<sup>1</sup>, M Isobe<sup>3</sup>,  
H Okabe<sup>3</sup>, J Akimitsu<sup>4</sup>, V V Mazurenko<sup>5</sup>, K S Kim<sup>2</sup>, A Bostwick<sup>2</sup>,  
E Rotenberg<sup>2</sup>, J Chang<sup>1</sup>, H M Rønnow<sup>1</sup>  
and M Grioni<sup>1</sup>

<sup>1</sup> Institute of Condensed Matter Physics (ICMP), Ecole Polytechnique Fédérale de Lausanne (EPFL), CH-1015 Lausanne, Switzerland

<sup>2</sup> Advanced Light Source (ALS), Lawrence Berkeley National Laboratory, Berkeley, CA 94720, USA

<sup>3</sup> National Institute for Materials Science (NIMS), 1-1 Namiki, Tsukuba, Ibaraki 305-0044, Japan

<sup>4</sup> Department of Physics and Mathematics, Aoyama Gakuin University, 5-10-1 Fuchinobe, Chuo-ku, Sagami-hara, Kanagawa 252-5258, Japan

<sup>5</sup> Theoretical Physics and Applied Mathematics Department, Ural Federal University, Mira Street 19, 620002 Ekaterinburg, Russia

E-mail: [simon.moser@epfl.ch](mailto:simon.moser@epfl.ch)

Received 4 October 2013, revised 27 November 2013

Accepted for publication 2 December 2013

Published 9 January 2014

*New Journal of Physics* **16** (2014) 013008

doi:[10.1088/1367-2630/16/1/013008](https://doi.org/10.1088/1367-2630/16/1/013008)

#### Abstract

We report angle-resolved photoemission (ARPES) measurements, density functional and model tight-binding calculations on  $\text{Ba}_2\text{IrO}_4$  (Ba-214), an antiferromagnetic ( $T_N = 230$  K) insulator. Ba-214 does not exhibit the rotational distortion of the  $\text{IrO}_6$  octahedra that is present in its sister compound  $\text{Sr}_2\text{IrO}_4$  (Sr-214), and is therefore an attractive reference material to study the electronic structure of layered iridates. We find that the band structures of Ba-214 and Sr-214 are qualitatively similar, hinting at the predominant role of the spin-orbit interaction in these materials. Temperature-dependent ARPES data show that the energy gap persists well above  $T_N$ , and favor a Mott over a Slater scenario for this compound.

<sup>6</sup> Author to whom any correspondence should be addressed.



Content from this work may be used under the terms of the [Creative Commons Attribution 3.0 licence](https://creativecommons.org/licenses/by/3.0/).

Any further distribution of this work must maintain attribution to the author(s) and the title of the work, journal citation and DOI.

*New Journal of Physics* **16** (2014) 013008  
1367-2630/14/013008+13\$33.00

© 2014 IOP Publishing Ltd and Deutsche Physikalische Gesellschaft

## 1. Introduction

The iridates are a new family of strongly correlated materials, with fascinating physical properties [1–12]. Unlike 3d transition metal oxides (TMOs), dominated by the Coulomb interaction, or 4d TMOs, where Hund’s rule coupling plays a major role [13], the electronic structure of the 5d iridates reflects the coexistence of similar Coulomb, crystal-field (CEF) and spin–orbit (SO) coupling energy scales. As a result, Mott physics and local magnetic moments can emerge in the iridates for values of the Coulomb interaction that are one order of magnitude smaller than in the 3d series.

The layered perovskite Sr<sub>2</sub>IrO<sub>4</sub> (Sr-214) has attracted considerable attention because of intriguing similarities with the cuprate parent compound La<sub>2</sub>CuO<sub>4</sub> (LCO). Structurally, it exhibits weakly coupled IrO<sub>2</sub> square-lattice planes built from corner-sharing IrO<sub>4</sub> plaquettes, analogous to the characteristic CuO<sub>4</sub> building blocks of the cuprates [4, 5, 14–16]. The electronic structure is shaped by strong SO coupling, which splits the Ir 5d  $t_{2g}^5$  manifold, so that the highest occupied state is a narrow, half-filled  $j_{\text{eff}} = 1/2$  band. The Ir spins order into an antiferromagnetic (AFM) state below  $T_N = 230\text{--}240$  K. According to the leading scenario, Sr-214 is an insulator because a Mott gap  $\Delta \sim 0.06$  eV opens within this band, but the actual origin of the gap is still being debated. An alternative Slater picture, coupling the onset of magnetic order with the opening of a gap [17, 18], has been advocated by susceptibility, time-resolved optical conductivity and scanning tunneling spectroscopy data [19, 20, 23, 24].

One may speculate that Sr-214 could be turned into a superconductor by doping, similarly to LCO. However, superconductivity is hindered by weak in-plane ferromagnetism, attributed to the Dzyaloshinsky–Moriya interaction, which arises from a rotational distortion of the IrO<sub>6</sub> octahedra (figure 1(a)). Recently, the sister compound Ba<sub>2</sub>IrO<sub>4</sub> (Ba-214), with similar physical properties (table 1), was synthesized using high pressure methods [20] (figure 2(b)). Due to the larger Ba radius, Ba-214 does not exhibit the rotational distortion, and is therefore a more promising parent compound for possible iridate superconductors. Ba-214 also offers the possibility of studying the electronic structure of an undistorted IrO<sub>2</sub> square lattice.

We present here an investigation of Ba-214 by angle-resolved photoelectron spectroscopy (ARPES). We analyze the experimental data with the help of first-principles density functional theory (DFT) and model tight-binding (TB) band structure calculations. We find that the band structure of Ba-214 is quite similar to that of Sr-214, and is therefore rather insensitive to the presence of the rotational distortion. We also observe a backfolding of the band structure corresponding to a larger  $c(2 \times 2)$  in-plane unit cell, that coincides with the AFM unit cell. ARPES data collected over a broad temperature range do not give evidence for a temperature-dependent gap, and therefore are more consistent with a Mott than with a Slater scenario.

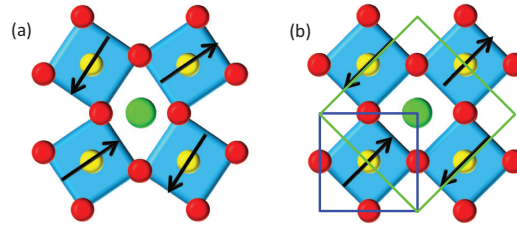
## 2. Methods

Samples of Ba-214 were grown as in [20] in the form of dense, black polycrystalline pellets. The pellets were broken into clusters of  $\sim 1$  mm<sup>3</sup> size, and then dipped in 1% hydrofluoric acid for 1 min. After rinsing in deionized water, single crystals of  $\sim 400$   $\mu\text{m}$  lateral size could be extracted. Crystals naturally exposing the (001) surface were selected under an optical microscope and mounted on ceramic pins.

The ARPES measurements were performed at the electronic structure factory end station of beam line 7 of the Advanced Light Source, Lawrence Berkeley National Laboratory. The

**Table 1.** Comparison of structural, magnetic and electronic properties in  $\text{Ba}_2\text{IrO}_4$  and  $\text{Sr}_2\text{IrO}_4$ .  $d_b$  and  $d_{ap}$  are the in-plane and apical Ir–O distances.

	$d_b$ (Å)	$d_{ap}$ (Å)	$\theta_{\text{tilt}}$	$T_N$ (K)	$\mu$ ( $\mu_B$ )	$E_a$ (meV)	Ref.
$\text{Ba}_2\text{IrO}_4$	2.01	2.15	$0^\circ$	230	0.34	70	[20]
$\text{Sr}_2\text{IrO}_4$	1.98	2.06	$11^\circ$	230–240	0.33	60	[2, 14, 16]


**Figure 1.** (a)  $\text{Sr}_2\text{IrO}_4$  structure, projected on the  $ab$  plane (red = O; green = Sr; and yellow = Ir). Apical oxygen atoms are not shown. Each  $\text{IrO}_6$  octahedron is rotated by  $11^\circ$  around the perpendicular  $c$ -axis with respect to the ideal  $\text{K}_2\text{NiF}_4$  structure, yielding a larger  $c(2 \times 2)$  unit cell. The distortion is absent in  $\text{Ba}_2\text{IrO}_4$  (b) (green = Ba). The arrows illustrate the Ir spin arrangement in the AFM phase. Blue and green squares are the primitive and magnetic unit cell [21, 22].

combined energy resolution of the monochromator and of the Scienta R4000 hemispherical analyzer was  $\sim 30$  meV. Samples were cleaved at  $T \sim 100$  K at a pressure  $< 10^{-10}$  mbar. The Fermi level reference was measured on polycrystalline copper in good electrical equilibrium with the sample. Sample charging hindered measurements below  $\sim 80$  K. All data presented here were collected at  $T \geq 120$  K, where the effect was smaller and under control. The data were subsequently corrected for the residual energy shift, which was estimated from a comparison with data measured in a low-filling mode of the storage ring, with a photon intensity reduced by almost two orders of magnitude.

### 3. Angle-resolved photoemission results

#### 3.1. Band structure

Figure 2(a) presents an ARPES constant energy (CE) map of Ba-214, measured at  $E = -0.1$  eV, near the top of the valence band. The map is extracted from a dataset measured at photon energy  $h\nu = 155$  eV, and  $T = 130$  K. The blue square is the surface Brillouin zone (BZ) corresponding to the crystallographic unit cell of figure 1(b) [20]. The map shows intense round features ( $\alpha$  features in the following) at the  $M$  points, the corners of the BZ. A second set of features ( $\beta$  features), with fourfold symmetry, is observed at the  $X$  points. Both  $\alpha$  and  $\beta$  features are repeated in all BZs of the map. A closer inspection reveals also a weaker, round contour ( $\alpha^*$ ) at all  $\Gamma$  points. It will be clear in the following that  $\alpha^*$  is a signature of band folding into the smaller  $c(2 \times 2)$  BZ (green square).

Figures 2(b)–(d) show the experimental  $E$  versus  $k_{\parallel}$  dispersion along high-symmetry lines marked (b), (c) and (d) in figure 2(a). Along  $M\Gamma M$ , figure 2(b) shows a prominent band with a maximum at the  $M$  point, where it gives rise to the  $\alpha$  contour. As discussed below, this

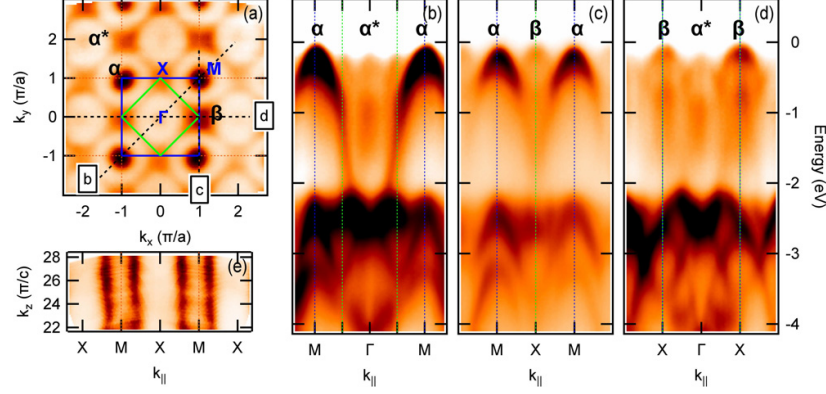


**Figure 2.** (a) ARPES  $k_x$  versus  $k_y$  CE map of Ba-214, measured at  $E = -0.1$  eV with  $h\nu = 155$  eV at  $T = 130$  K. It shows intense features centered at the  $M$  and  $X$  points of the surface BZ (blue square), and a weaker replica of the former at  $\Gamma$ . The green square is the  $c(2 \times 2)$  BZ. (b)–(d)  $E$  versus  $k_{\parallel}$  cuts along the high symmetry directions indicated as (b), (c) and (d) in panel (a). Blue and green vertical lines indicate the boundaries of the  $(1 \times 1)$  and of the  $c(2 \times 2)$  BZs. (e) ARPES  $k_x$  versus  $k_z$  CE map at  $E = -0.4$  eV and  $k_y = \pi/a$ , extracted from a photon energy scan between 95 and 162 eV, assuming an inner potential  $V_0 = 10$  eV. It shows negligible dispersion along the  $c$ -axis.  $\Gamma X = \pi/a = 0.78 \text{ \AA}^{-1}$ ;  $\Gamma Z = \pi/c = 0.24 \text{ \AA}^{-1}$ . In all panels, the darkest features correspond to the largest intensity.

band corresponds primarily to Ir states of  $j_{\text{eff}} = 3/2$  character. It merges around  $-2$  eV with a manifold of O 2p-derived states. The same band is seen to disperse downwards along the  $MXM$  direction in figure 2(c). A second band, with a maximum at the  $X$  point, generates the  $\beta$  contour. In the Mott scenario, it is assigned to the Ir-derived lower-Hubbard band of  $j_{\text{eff}} = 1/2$  character. The maxima of this band are more visible along the  $X\Gamma X$  direction in figure 2(d), which also shows a dispersive feature with a maximum at  $\Gamma$ , associated with the  $\alpha^*$  contour. Figure 2(e) shows a  $k_x$  versus  $k_z$  CE map for  $E = -0.4$  eV and  $k_y = \pi/a$ . It is extracted from ARPES measurements with photon energies in the range  $h\nu = 95$ – $162$  eV, assuming an inner potential  $V_0 = 10$  eV. Apart from slight intensity variations with photon energy, the data are essentially independent of  $k_z$ . Namely, the absence of wiggling contours indicates that the  $k_z$  dispersion at the top of the valence band (VB), and the interplane coupling for these states, are quite small.

Representative spectra for the  $\Gamma$ ,  $M$  and  $X$  points of the BZ are shown in figure 3. They exhibit rather broad peaks, with maxima at  $-0.37$  eV (at  $\Gamma$ ),  $-0.26$  eV (at  $M$ ), and  $-0.21$  eV (at  $X$ ), which places the VB maximum at the  $X$  point. The peak energy at the VB maximum should yield a lower limit for the energy gap, the actual value depending on the separation between the Fermi level and the conduction band minimum, which cannot be accessed by ARPES. However, the peak binding energy at  $X$  (0.21 eV) is already larger than the gap value  $\Delta_g \simeq 2E_a \sim 140$  meV, estimated from the activation energy  $E_a = 70$  meV of the electrical resistivity [20]. This discrepancy, and the broad line shapes, suggest unresolved overlapping features in the spectra of figure 3. This hypothesis is supported by the first-principles calculations of section 4.1. It also explains the different peak energies measured at

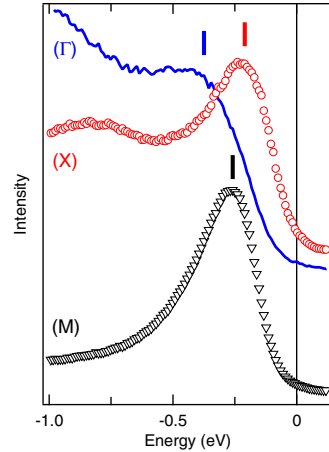


**Figure 3.** ARPES spectra of Ba-214, measured at three high symmetry points of the BZ. The corresponding peak positions are indicated by vertical lines.

the top of the band at the  $M$  point, and at its backfolded replica at  $\Gamma$ , since the underlying components can be differently modulated by matrix elements.

We now compare the electronic structure of Ba-214 and Sr-214. Figure 4(a) reproduces ARPES data on Sr-214 from [4]. The spectra are measured along the  $\Gamma M' X'$  contour in the  $c(2 \times 2)$  BZ, indicated by a yellow triangle in the top panel. Our results for Ba-214, extracted from the dataset of figure 2, are shown for the same triangular contour in figure 4(b). Data measured along the same triangular contour in the adjacent  $c(2 \times 2)$  BZ are also shown in figure 4(c). Two conclusions can be drawn from the figure. Firstly, there is a good overall correspondence between the band structure of the two compounds. Secondly, while the relative intensities of the Ba-214  $j_{\text{eff}} = 3/2$  and  $1/2$  bands in figures 4(b) and (c) are different, their dispersions are identical. The triangular contours in figures 4(b) and (c) are equivalent for the  $c(2 \times 2)$  BZ, but clearly not for the structural BZ (blue square). This shows that—similarly to the case of Sr-214 [4]—the band structure of Ba-214 is folded into the smaller BZ. The smaller intensity of the  $\alpha^*$  manifold in figure 4(b), compared with that of the  $\alpha$  manifold in figure 4(c), is consistent with band folding from a superlattice potential that is substantially weaker than the primary lattice potential [25]. The different intensities in the two contours can be exploited to disentangle the two bands. We find that in Ba-214 the width of the  $j_{\text{eff}} = 1/2$  band ( $\sim 0.8$  eV) is somewhat larger than in Sr-214 ( $\sim 0.5$  eV) [4], and is considerably smaller than the width of the  $j_{\text{eff}} = 3/2$  band ( $\sim 2.5$  eV). The maxima of the  $j_{\text{eff}} = 1/2$  band at  $X$  ( $-0.21$  eV) and of the  $j_{\text{eff}} = 3/2$  band at  $M$  ( $-0.26$  eV) in Ba-214 are shallower than those ( $-0.25$  eV and, respectively  $-0.45$  eV) of the corresponding bands in Sr-214. Their energy separation is also smaller (0.05 versus 0.2 eV) in Ba-214.

### 3.2. Temperature evolution

We now address the issue, raised in the introduction, of the persistence of the energy gap above  $T_N \sim 240$  K. Previous theoretical and experimental studies [18, 23, 24] have claimed significant Slater-type contributions to the stability of the gap, which should then collapse in

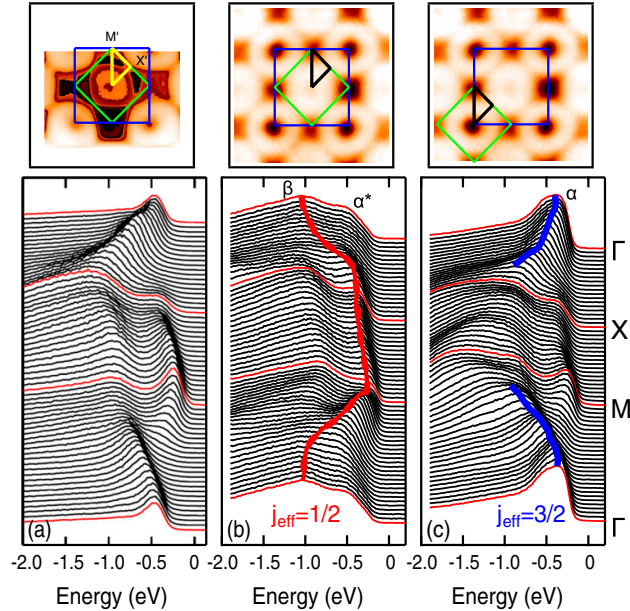


**Figure 4.** (a) ARPES spectra of Sr-214, measured along the  $\Gamma M' X'$  contour (yellow triangle) in the  $c(2 \times 2)$  BZ (green square), from [4]. Data for Ba-214, extracted from figure 2, are shown along the same contour in (b), and for an equivalent contour in an adjacent  $c(2 \times 2)$  BZ in (c). Spectra corresponding to the high-symmetry points are in red. Matrix elements enhance the signal from  $j_{\text{eff}} = 1/2$  states in (b), and from  $j_{\text{eff}} = 3/2$  states in (c). Thick red (b) and blue (c) curves outline their dispersion.

the paramagnetic phase. We collected data over a broad temperature range, from well below (120 K) to well above (300 K)  $T_N$ . Figure 5 displays temperature-dependent ARPES spectra measured at the  $\Gamma$  and  $M$  points of the BZ. The leading edge of the spectra exhibits a trivial thermal broadening, but no indications that the gap closes at  $T_N$ . The energy gap appears to be robust even in the absence of long-range magnetic order. Therefore, the ARPES data do not support a Slater picture, at least in its simplest form.

## 4. Electronic structure calculations

### 4.1. First-principles calculations

We performed a local density approximation (LDA) calculation including the on-site Coulomb and SO interactions (LDA +  $U$  + SO) [29]. For this purpose, the linear muffin-tin orbital approach in the atomic sphere approximation (Stuttgart LMTO47 code) [30] was used, with crystal structure data taken from [20]. We include Ba(6s,6p,5d), Ir(6s,6p,5d) and O(2s,2p) states in the orbital basis set. Both the ferromagnetic (FM) and AFM configurations were simulated for different sets of on-site Ir 5d Coulomb repulsion  $U$  and intra-atomic exchange interaction  $J_H$ . The FM configuration is calculated with one Ir atom per unit cell. In order to reproduce the AFM order observed in  $\text{Ba}_2\text{IrO}_4$ , we have used a supercell containing four Ir atoms. The



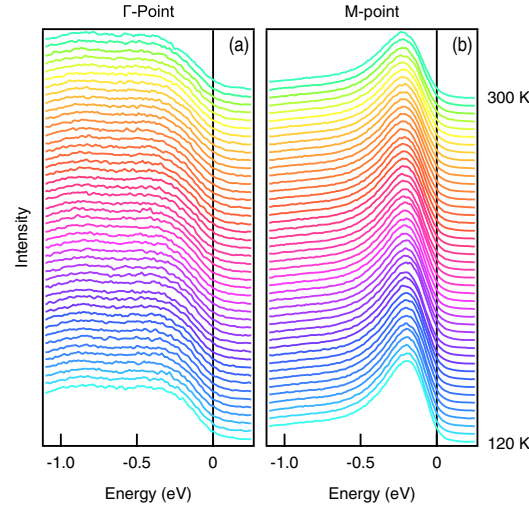


**Figure 5.** Temperature-dependent ARPES spectra of Ba-214 from  $T = 120$  to  $300$  K, measured at (a) the  $\Gamma$ , and (b) the  $M$  points of the BZ.

primitive lattice vectors in units of  $a = 4.03 \text{ \AA}$  are  $(0, 2, 0)$ ,  $(2, 0, 0)$  and  $(0.5, 0.5, -1.65)$ . In the AFM configuration,  $U = 3 \text{ eV}$  and  $J_H = 0.4 \text{ eV}$  produced the correct energy gap value of  $140 \text{ meV}$ . The same values were recently used in [12].

The calculated band structure is illustrated in figure 6(a), superimposed on the ARPES data. Overall, DFT yields many more states than ARPES can individually resolve, which probably explains the absence of sharp quasiparticle features in the spectra. The partial densities of states of figure 6(b) show that Ir 5d and 2p in-plane oxygen states are strongly hybridized at the top of the valence band, while the bottom of the conduction band is mainly formed by Ir 5d electrons. The 2p states of the apical oxygen atoms are confined between  $-1$  and  $-2 \text{ eV}$ , due to a limited overlap with the Ir 5d orbitals. These states have a non-negligible dispersion along the  $c$ -axis. The band observed in ARPES around  $-3 \text{ eV}$  corresponds to in-plane 2p oxygen states.

We now briefly discuss the implications of the DFT results for the magnetic properties of Ba-214. Firstly, we emphasize that the occupied states close to the gap at the  $\Gamma$  and  $M$  points strongly depend on the specific magnetic configuration. For instance, in the FM state the top of the valence band is found at  $E \simeq -0.7 \text{ eV}$  (not shown). Moreover, a FM insulating ground state with the correct energy gap could only be obtained for unreasonably large values of  $U$  and  $J_H$ . Therefore, the inter-site exchange interaction plays a decisive role in determining the band structure close to the Fermi level.

Within the LDA +  $U$  + SO approximation [29] the electronic Hamiltonian matrix and the corresponding occupation matrix of the system can be defined in the  $\{LS\}$  basis (the eigenfunctions of both spin and orbital moment operators) or  $\{jm_j\}$  basis (the total moment operator eigenfunctions). They correspond to  $LS$  (Russell–Saunders) or  $jj$  coupling schemes. The basis choice becomes important when one calculates the expectation value of the magnetic moment to compare it with experimental data. In this case, either the  $LS$  coupling scheme or the  $jj$  coupling scheme should be chosen, depending on the strength of the SO coupling. However, when the SO coupling and the intra-atomic exchange interaction are comparable, neither the



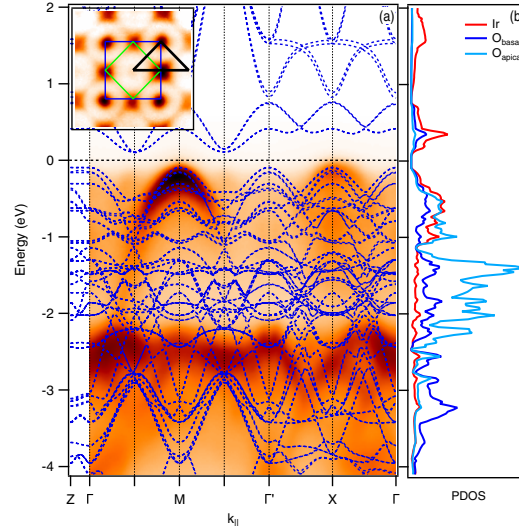


**Figure 6.** (a) The LDA +  $U$  + SO band structure is superimposed on an ARPES intensity map, where an integral Shirley background has been subtracted. The bands were calculated for the AFM configuration with  $U = 3$  eV and  $J_H = 0.4$  eV. Apical oxygen states between  $-1$  and  $-2$  eV are not resolved in the experiment. (b) Partial densities of states. Red, dark and light blue lines correspond to Ir 5d, in-plane oxygen 2p and apical oxygen 2p states, respectively.

$LS$  nor the  $jj$  scheme are valid, and an intermediate coupling theory should be developed [29]. Practically, it means that the occupation matrix is neither diagonal in the  $\{LS\}$  nor in  $\{jm_j\}$  orbital basis. Such a situation is realized in Ba-214, where the SO strength  $\lambda \sim 0.48$  eV and  $J_H \sim 0.4$  eV.

Within an  $\{LS\}$  eigenstates basis we obtain for the spin and orbital magnetic moments  $M_S = 0.12 \mu_B$  and  $M_L = 0.33 \mu_B$ , respectively. The resulting total magnetic moment is therefore  $M_{LS} = (2M_S + M_L) = 0.57 \mu_B$ , in reasonable agreement with the value  $M = 0.36 \mu_B$  from magnetic susceptibility measurements [20]. The total magnetic moment calculated within a  $\{jm_j\}$  basis is equal to  $M_J = 0.43 \mu_B$ , in better agreement with the experimental value. However, one should note that in both basis sets there are large non-diagonal elements of the occupation matrix that do not contribute to the expectation value of the magnetic moment. Therefore, an intermediate coupling scheme should be used to correctly describe the magnetism of Ba-214. We leave such a consideration for a future investigation.

The performed first-principles calculations have demonstrated a complicated band structure depending on the metal–ligand hybridization, on-site Coulomb interaction, SO coupling, intra- and inter-atomic exchange interactions. The agreement between all-electron LDA +  $U$  + SO and experimental ARPES spectra is not enough to determine the exact microscopic mechanisms that are responsible for forming the electronic structure of  $\text{Ba}_2\text{IrO}_4$ . To solve this problem below we propose a tight-binding model with a minimal set of orbitals.

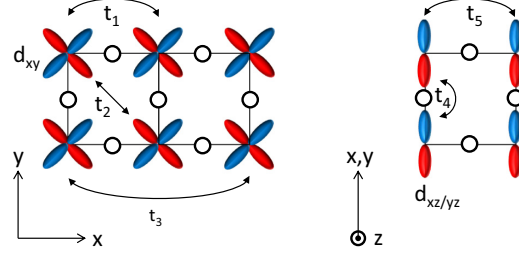


**Figure 7.** Effective hopping terms for the Ir  $t_{2g}$  states used in the TB model: (a)  $d_{xy}$  orbitals and (b)  $d_{xz/yz}$  orbitals. Empty circles represent oxygen ions.

#### 4.2. Tight binding approach

In order to gain more direct insight in the interplay of orbital ordering, SOC and correlation effects, we also performed a model TB calculation, along the lines of [27, 28]. We included the whole Ir 5d  $t_{2g}$  and  $e_g$  manifolds, and a set of effective hopping terms describing the hybridization between the Ir 5d and O 2p electrons, as illustrated in figure 7. The tight binding Hamiltonian is

$$H = H_0 + H_{SO}. \quad (1)$$

$H_0$  includes the kinetic term  $T = \sum_{k,v} \varepsilon_v(k) c_{kv}^\dagger c_{kv}$ , where  $c_k^\dagger$  and  $c_k$  are the fermion creation and annihilation operators and  $v$  spans the Ir 5d manifold, and an octahedral CEF parameterized by  $10Dq = E(e_g) - E(t_{2g})$ . Since we are primarily interested in the occupied states for a comparison with ARPES, we focus on the  $t_{2g}$  levels. The relevant hopping terms are schematically illustrated in figure 7. The form of the  $\varepsilon_v$ 's is dictated by the symmetry of the system [27]:

$$\begin{aligned} \varepsilon_{xy} &= -2t_1(\cos k_x + \cos k_y) - 2t_2 \cos k_x \cos k_y - 2t_3(\cos 2k_x + \cos 2k_y), \\ \varepsilon_{xz} &= -2t_4 \cos k_x - 2t_5 \cos k_y, \\ \varepsilon_{yz} &= -2t_5 \cos k_x - 2t_4 \cos k_y. \end{aligned} \quad (2)$$

The SO coupling term for the 5d orbitals is:  $H_{SO} = \lambda_{5d} \vec{L} \cdot \vec{S}$ . We introduce electron correlations in the model in a phenomenological way, by imposing AFM order. This is achieved by an additional Zeeman term with an in-plane staggered magnetic field

$$H_{AFM} = B \sum_{i,v} e^{i\vec{Q} \cdot \vec{r}_i} \left( c_{iv\uparrow}^\dagger c_{iv\downarrow} + c_{iv\downarrow}^\dagger c_{iv\uparrow} \right), \quad (3)$$

where  $\vec{Q} = (\pi, \pi)$  is the AFM ordering vector, and the sum is over the Ir sites  $i$  and the three  $t_{2g}$  orbitals. The effect of  $H_{AF}$  is to fold all bands into the smaller  $c(2 \times 2)$  BZ, and to open gaps at the AFM zone boundaries.

The band structures produced by the various terms of the hamiltonian are plotted in figure 8(a)–(c), along the same  $\Gamma X'M'\Gamma$  contour of figures 4(a) and (b). The parameters of the model are summarized in table 2. Figures 8(a')–(c') schematically illustrate the local electronic structure at the Ir site. Figure 8(a) shows the band dispersion in the presence of the octahedral CEF. The empty  $e_g$  and the partially filled  $t_{2g}$  manifolds are well separated by  $10Dq$ , and the

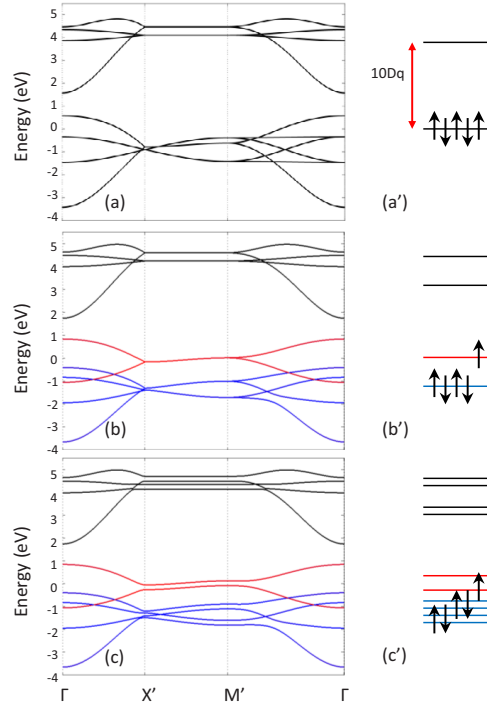


**Figure 8.** The calculated TB band structure is shown in (a) in the presence of an octahedral CEF. In (b) the addition of SO coupling rearranges the bands into  $j_{\text{eff}} = 3/2$  (blue) and  $j_{\text{eff}} = 1/2$  (red) states. A staggered magnetic field splits all states in (c), namely within the half-filled  $j_{\text{eff}} = 1/2$  band, simulating the opening of the Mott gap. Panels (a'–c') are corresponding schematic pictures of the local electronic structure at the Ir sites.

**Table 2.** The set of parameters (in eV) of the TB model used for the calculated band structure of figures 8 and 9.

$\lambda_{5d}$	$t_1$	$t_2$	$t_3$	$t_4$	$t_5$	$B$
0.7	0.5	0.1	0.03	0.27	0.01	0.1

system is metallic. Adding the SO interaction, in figures 8(b) and (b'), mixes the CEF states. The  $t_{2g}$  states are split into a four-fold degenerate, fully occupied  $j_{\text{eff}} = 3/2$  (blue), and a doubly degenerate, half-filled,  $j_{\text{eff}} = 1/2$  manifold (red), but the system remains metallic. Figures 8(c) and (c') illustrate the further band splitting induced by  $H_{\text{AFM}}$ , namely of the  $j_{\text{eff}} = 1/2$  band into  $m_j = -1/2$  and  $1/2$  subbands, which effectively simulates the opening of a correlation gap between an occupied lower Hubbard band and an empty upper Hubbard band.

The calculated TB band structure is compared with the ARPES data in figure 9 for the set of parameters of table 2. Although the TB parameters, namely the external magnetic field, should not be taken too literally, they do provide a useful description of the electronic structure.

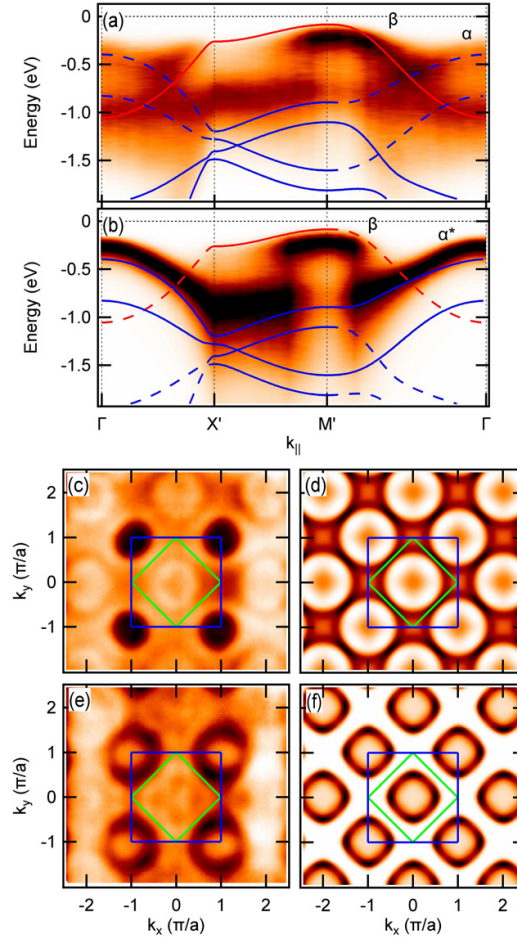


**Figure 9.** The calculated TB band structure is superimposed on the experimental ARPES data, along two equivalent contours in the first (a) and in an adjacent (b)  $c(2 \times 2)$  BZ, as in figure 4(b), (c). Folded bands are indicated by dashed lines. The color code is the same as in figure 8. Panels (c), (d) show the experimental (c) and calculated (d) CE maps for  $E = -0.35$  eV. The corresponding CE maps for  $E = -0.7$  eV are shown in (e), (f).

Figures 9(a) and (b) show data along equivalent contours in the first and in the adjacent  $c(2 \times 2)$  BZs, as in figures 4(b) and (c). Folded bands are indicated by dashed lines. The good agreement with the data substantiates the description of the bands given in section 3, namely the assignment of the top of the valence band to states of  $j_{\text{eff}} = 1/2$  character. The good agreement of the TB model with the experiment is confirmed by a comparison of the experimental and calculated CE maps shown in figures 9(c) and (d) and figures 9(e) and (f), for  $E = -0.35$  eV (c, d) and  $E = -0.7$  eV (e, f). The experimental  $\alpha$  ( $\alpha^*$ ) and  $\beta$  features are well reproduced. Of course, the TB model does not yield any information on the spectral weight, and therefore all  $c(2 \times 2)$  BZs are equivalent.

## 5. Summary

We have measured the electronic structure of the perovskite iridate Ba<sub>2</sub>IrO<sub>4</sub> (Ba-214) by ARPES on high-quality single crystal samples grown under high pressure. A comparison of spectra measured at non-equivalent locations of reciprocal space allows us to unambiguously identify the  $j_{\text{eff}} = 3/2$  and  $1/2$  subbands into which the Ir 5d  $t_{2g}$  manifold is split by the SO interaction. The experimental data are well reproduced by an LDA +  $U$  + SO calculation for an AFM configuration. A satisfactory agreement is also achieved by a simple empirical tight-binding model. The overall band dispersion is similar to that of the sister compound Sr-214. The electronic structure is therefore rather insensitive to the rotational distortion of the IrO<sub>6</sub> octahedra, which is present in Sr-214 but not in Ba-214. This observation contrasts with the behavior of 3d TM perovskites, such as the rare earth nickelates RNiO<sub>3</sub>, where the tilting of the octahedra, which affects the orbital overlap, strongly influences the band dispersion, as well as transport and magnetic properties [31]. This lends support to a proposed scenario for the iridates, where the effective hopping parameters are less sensitive to the distortion due to the strong mixing of  $d_{xy}$ ,  $d_{xz}$  and  $d_{yz}$  orbital characters induced by the SO interaction [26].

We have also found that the bands measured by ARPES are folded, with reduced intensity, into a smaller  $c(2 \times 2)$  BZ, producing a characteristic checkerboard intensity distribution. Band folding has also been observed in Sr-214 [4], and attributed to the effect of the structural distortion. Very sensitive x-ray diffraction measurements with synchrotron radiation rule out a structural distortion in the bulk of Ba-214 [32]. Our results are consistent with the periodicity of the AFM structure, and could indicate scattering of the quasiparticles by the corresponding superlattice potential. However, we cannot exclude that a structural distortion develops at the surface, which has indeed been suggested by low-energy electron diffraction measurements on thin film samples [33]. Accurate surface x-ray diffraction experiments are necessary to determine the surface structure of Ba-214, and resolve this issue.

Finally, we have studied the evolution with temperature of the energy gap, and found no notable variations, namely around the magnetic ordering temperature  $T_N = 230$  K. The gap remains open well into the paramagnetic phase. The ARPES data are therefore more consistent with a Mott than with a Slater scenario, even if our calculations indicate a clear influence of magnetic order on the size of the gap.

## Acknowledgments

We gratefully acknowledge insightful discussions with V I Anisimov, A O Shorikov, B J Kim, D F McMorro, S Boseggia and C Tournier-Colletta. Special thanks are due to K M Shen for sharing with us his unpublished data. The work at Lausanne is supported by the Swiss NSF LM was supported by the Swiss NSF Grant N PA00P21-36420. The work of VVM is supported by the grant program of President of Russian Federation MK-5565.2013.2 and the contract of the Ministry of Education and Science of Russia N 14.A18.21.0076. The Advanced Light Source is supported by the Director, Office of Science, Office of Basic Energy Sciences, of the US Department of Energy under contract no. DE-AC02-05CH11231.

## References

- [1] Cao G, Bolivar J, McCall S, Crow J E and Guertin R P 1998 *Phys. Rev. B* **57** 11039
- [2] Kini N S, Strydom A M, Jeevan H S, Geibel C and Ramakrishnan S 2006 *J. Phys.: Condens. Matter* **18** 8205

- [3] Moon S J *et al* 2008 *Phys. Rev. Lett.* **101** 226402
- [4] Kim B J *et al* 2008 *Phys. Rev. Lett.* **101** 076402
- [5] Kim B J, Ohsumi H, Komesu T, Sakai S, Morita T, Takagi H and Arima T 2009 *Science* **323** 1329
- [6] Ge M, Qi T F, Korneta O B, De Long L E, Schlottmann P, Crummet W P and Cao G 2011 *Phys. Rev. B* **84** 100402
- [7] Qi T F, Korneta O B, Chikara S, Ge M, Parkin S, De Long L E, Schlottmann P and Cao G 2011 *J. Appl. Phys.* **109** 07D906
- [8] Wang F and Senthil T 2011 *Phys. Rev. Lett.* **106** 136402
- [9] Fujiyama S, Ohsumi H, Komesu T, Matsuno J, Kim B J, Takata M, Arima T and Takagi H 2012 *Phys. Rev. Lett.* **108** 247212
- [10] Haskel D, Fabbri G, Zhernenkov M, Kong P P, Jin C Q, Cao G and van Veenendaal M 2012 *Phys. Rev. Lett.* **109** 027204
- [11] Cetin M F, Lemmens P, Gnezdilov V, Wulferding D, Menzel D, Takayama T, Ohashi K and Takagi H 2012 *Phys. Rev. B* **85** 195148
- [12] Comin R *et al* 2012 *Phys. Rev. Lett.* **109** 226406
- [13] Georges A, de' Medici L and Mravlje J 2013 *Annu. Rev. Condens. Matter Phys.* **4** 137
- [14] Crawford M K, Subramanian M A, Harlow R L, Fernandez-Baca J A, Wang Z R and Johnston D C 1994 *Phys. Rev. B* **49** 9198
- [15] Kim J, Casa D, Upton M H, Gog T, Kim Y J, Mitchell J F, van Veenendaal M, Daghofer M, van den Brink J and Khaliullin G 2012 *Phys. Rev. Lett.* **108** 177003
- [16] Shimura T, Inaguma Y, Nakamura T, Itoh M and Morii Y 1995 *Phys. Rev. B* **52** 9143
- [17] Gebhard F 1997 *The Mott Metal–Insulator Transition: Models and Methods* (Heidelberg: Springer)
- [18] Arita R, Kunes J, Kozhevnikov A V, Eguluz A G and Imada M 2012 *Phys. Rev. Lett.* **108** 086403
- [19] Moon S J, Jin H, Choi W S, Lee J S, Seo S S A, Yu J, Cao G, Noh T W and Lee Y S 2009 *Phys. Rev. B* **80** 195110
- [20] Okabe H, Isobe M, Takayama-Muromachi E, Koda A, Takeshita S, Hiraishi M, Miyazaki M, Kadono R, Miyake A and Akimitsu J 2011 *Phys. Rev. B* **83** 155118
- [21] Boseggia S, Walker H C, Vale J, Springell R, Feng Z, Perry R S, Moretti Sala M, Rønnow H M, Collins S P and McMorro D F 2013 *J. Phys.: Condens. Matter* **25** 422202
- [22] Boseggia S, Springell R, Walker H C, Rønnow H M, Rüegg Ch, Okabe H, Isobe M, Perry R S, Collins S P and McMorro D F 2013 *Phys. Rev. Lett.* **110** 117207
- [23] Hsieh D, Mahmood F, Torchinsky D H, Cao G and Gedik N 2012 *Phys. Rev. B* **86** 035128
- [24] Li Q *et al* 2013 arXiv:1303.7265
- [25] Voit J, Perfetti L, Zwick F, Berger H, Margaritondo G, Grüner G, Höchst H and Grioni M 2000 *Science* **290** 501
- [26] Katukuri V M, Stoll H, van den Brink J and Hozoi L 2012 *Phys. Rev. B* **85** 220402
- [27] Watanabe H, Shirakawa T and Yunoki S 2010 *Phys. Rev. Lett.* **105** 216410
- [28] Martins C, Aichorn M, Vaugier L and Biermann S 2011 *Phys. Rev. Lett.* **107** 266404
- [29] Shorikov A O, Lukoyanov A V, Korotin M A and Anisimov A I 2005 *Phys. Rev. B* **72** 024458
- [30] Andersen O K 1975 *Phys. Rev. B* **12** 3060
- [31] Torrance J B, Lacorre P, Nazzari A I, Ansaldo E J and Niedermayer C 1992 *Phys. Rev. B* **45** 8209
- [32] McMorro D F private communication
- [33] Shen K M private communication

## A.2 Bilayer perovskite iridate $\text{Sr}_3\text{Ir}_2\text{O}_7$

Another type of SOI-MI that was studied within the scope of this thesis is the bilayer version of  $\text{Sr}_2\text{IrO}_4$ , i.e.  $\text{Sr}_3\text{Ir}_2\text{O}_7$ . Like the atoms in a hydrogen molecule, the electronic states resulting from each of the layers hybridize and effectively increase the bandwidth of the nearly half-filled  $j_{eff} = 1/2$  band close to the Fermi energy. The following ARPES study shows that this considerably reduces, but not completely closes, the spin orbit induced Mott gap [238].



**Bilayer splitting and wave functions symmetry in Sr<sub>3</sub>Ir<sub>2</sub>O<sub>7</sub>**L. Moreschini,<sup>1,\*</sup> S. Moser,<sup>2</sup> A. Ebrahimi,<sup>2</sup> B. Dalla Piazza,<sup>2</sup> K. S. Kim,<sup>1,3,4</sup> S. Boseggia,<sup>5,6</sup> D. F. McMorrow,<sup>5</sup> H. M. Rønnow,<sup>2</sup> J. Chang,<sup>2</sup> D. Prabhakaran,<sup>7</sup> A. T. Boothroyd,<sup>7</sup> E. Rotenberg,<sup>1</sup> A. Bostwick,<sup>1</sup> and M. Grioni<sup>2</sup><sup>1</sup>Advanced Light Source (ALS), Lawrence Berkeley National Laboratory, Berkeley, California 94720, USA<sup>2</sup>Institute of Condensed Matter Physics (ICMP), Ecole Polytechnique Fédérale de Lausanne (EPFL), CH-1015 Lausanne, Switzerland<sup>3</sup>Department of Physics, Pohang University of Science and Technology, Pohang 790-784, Korea<sup>4</sup>Center for Artificial Low Dimensional Electronic Systems, Institute for Basic Science, Pohang 790-784, Korea<sup>5</sup>London Centre for Nanotechnology, University College London, London WC1E 6BT, United Kingdom<sup>6</sup>Diamond Light Source Ltd., Harwell Science and Innovation Campus, Didcot, Oxfordshire OX11 0DE, United Kingdom<sup>7</sup>Clarendon Laboratory, Department of Physics, University of Oxford, Parks Road, Oxford OX1 3PU, United Kingdom

(Received 23 February 2014; revised manuscript received 2 May 2014; published 23 May 2014)

The influence of dimensionality on the electronic properties of layered perovskite materials remains an outstanding issue. We address it here for Sr<sub>3</sub>Ir<sub>2</sub>O<sub>7</sub>, the bilayer compound of the iridate Sr<sub>n+1</sub>Ir<sub>n</sub>O<sub>3n+1</sub> series. By angle-resolved photoemission spectroscopy we show that in this material the interlayer coupling is large and that the intercell coupling is, conversely, negligible. From a detailed mapping of the bilayer splitting, and from the intensity modulation of the bonding and antibonding bands with photon energy, we establish differences and similarities with the prominent case of the bilayer superconducting cuprates.

DOI: 10.1103/PhysRevB.89.201114

PACS number(s): 71.20.-b, 71.30.+h, 79.60.-i

Iridium oxides are generating increasing attention [1–13]. In these materials, the entanglement of the spin and orbital degrees of freedom induces a reorganization of the electronic energy levels, described by an effective total angular momentum  $J_{\text{eff}}$ . This is different from the case of 3d and 4d oxides, governed by Coulomb interactions and, respectively, Hund's coupling [14]. The interaction between such composite moments strongly depends on the symmetry of the Ir-O covalent bonds [10,15]. In spite of such differences, iridates built from corner sharing IrO<sub>6</sub> octahedra, such as Sr<sub>2</sub>IrO<sub>4</sub>, show surprising analogies with the isostructural cuprate compounds, namely, a single band at the Fermi level [2] and a similar magnetic structure [1,4,6]. This motivates a search for connections between iridates and cuprates and, quite naturally, most studies have been performed on the Ruddlesden-Popper series Sr<sub>n+1</sub>Ir<sub>n</sub>O<sub>3n+1</sub>, which shows a close similarity with the layered cuprates housing high-temperature superconductivity.

Experimental efforts have been so far oriented to the stoichiometric “parent compounds”, and to the role of structural distortions and of dimensionality in determining both the electronic and the magnetic properties. Insight into the former is gained by substituting Sr with, e.g., Ba, which enhances the tetragonal distortion and prevents the rotation of the IrO<sub>6</sub> octahedra [16]. The effect of dimensionality can be assessed by comparing the compounds of the series from  $n=1$ , the two-dimensional (2D) limit, to  $n \rightarrow \infty$ , the three-dimensional (3D) one. Early optical data showed an evolution from a Mott insulator (Sr<sub>2</sub>IrO<sub>4</sub>) to a correlated metal (SrIrO<sub>3</sub>), which was attributed to interlayer coupling and a consequent increase of the bandwidth  $W$  [3]. A similar evolution is observed in cuprates where, e.g., La<sub>2</sub>CuO<sub>4</sub> is a charge transfer insulator [17], whereas LaCuO<sub>3</sub> is a poor metal [18,19].

In between these two extremes, Sr<sub>3</sub>Ir<sub>2</sub>O<sub>7</sub> is notable, as a small electronic gap seems to indicate that it lies very

close to the critical point marking the metal-to-insulator transition. Its band structure has been mapped for the first time with laser-based angle-resolved photoemission spectroscopy (ARPES) [20], and refined more recently [21,22]. Reference [21] suggests a polaronic ground state with a vanishing quasiparticle pole close to the Fermi level, another possible similarity to the cuprates [23]. Alternatively, Ref. [22] ascribes the reduced gap to the intercell coupling, which would cause a sizable dispersion in the direction perpendicular to the IrO layers and mark a departure from the 2D physics already for  $n = 2$ . Our results suggest a different scenario. We measure a bilayer splitting between bonding and antibonding bands as large as 0.2 eV, which indicates that the interlayer coupling cannot be treated simply as a perturbative term to the electronic structure of the monolayer counterpart. From the intensity modulation of these states with photon energy, we infer the reflection symmetry properties of the corresponding wave functions. We find that the lowest energy state is antisymmetric, opposite to the much studied case of the bilayer cuprates.

Single crystals of Sr<sub>3</sub>Ir<sub>2</sub>O<sub>7</sub> were grown using the self-flux technique, as described elsewhere [24], and characterized by magnetization measurements, x-ray diffraction, x-ray resonant magnetic scattering, and resonant inelastic scattering. All the ARPES data were measured at beamline 7.0.1 of the Advanced Light Source with a Scienta analyzer, and the momentum and energy resolution were 0.1° and 30 meV at  $h\nu = 100$  eV, respectively. The light was linearly polarized in the horizontal plane containing the  $k_x$  axis of the sample and the analyzer slits ( $p$  scattering geometry), and the angular scans were obtained by rotating the sample about  $k_x$ , in steps of  $k_y$ . The measurements were performed at  $T = 30$  K and no charging effects were observed at this temperature.

Figure 1 shows an overview of the band topology of Sr<sub>3</sub>Ir<sub>2</sub>O<sub>7</sub>. The crystal structure has recently been refined from tetragonal to orthorhombic [25] but, as common practice in these layered iridates, we discuss the data with reference to a square surface Brillouin zone (BZ), as shown in Fig. 1(a). As we will show later, this choice is certainly justified for

\*lmoeschini@lbl.gov



L. MORESCHINI *et al.*

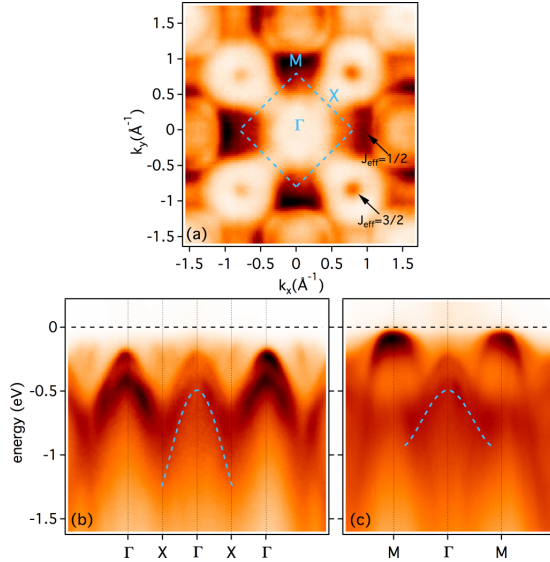
 PHYSICAL REVIEW B **89**, 201114(R) (2014)


FIG. 1. (Color online) (a) ARPES constant energy cut taken at  $E = -180$  meV, near the top of the  $J_{\text{eff}} = 3/2$  states. The square indicates the surface BZ, determined by the in-plane rotation of the  $\text{IrO}_6$  octahedra and the G-type antiferromagnetic ordering. The characteristic contours of the distinct  $J_{\text{eff}}$  bands are indicated by arrows. (b) and (c) show the band dispersion along the two high-symmetry directions through  $\Gamma$ . Note in (b) the intensity modulation due to the folding potential generated by the structural distortion. The dashed curves outline the dispersion along the same directions for the monolayer compound  $\text{Sr}_2\text{IrO}_4$ , as reported in Ref. [2]. The relevant dimensions are  $\Gamma M = 0.78 \text{ \AA}^{-1}$  and  $\Gamma X = 0.55 \text{ \AA}^{-1}$ .

our bilayer compound. The dispersion shown in Figs. 1(b) and 1(c) is in general agreement with previous reports [20–22]. The intensity in the first eV below the Fermi level is due to two manifolds of holelike bands. The lowest energy state has maximum at  $-90$  meV, i.e.,  $90$  meV below the Fermi level  $E_F$ , at the  $M$  point. A second manifold has maximum at the  $\Gamma$  point at  $-0.23$  eV. The experimental band dispersion shows marked similarities with that of  $\text{Sr}_2\text{IrO}_4$ , where the states are assigned to  $J_{\text{eff}} = 1/2$  and  $J_{\text{eff}} = 3/2$  character as indicated by the arrows in Fig. 1(a), but each band is further split into a bonding and an antibonding branch. While significant hybridization between these two manifolds is expected here, we keep the same labeling for simplicity. Such assignment of the bands to a specific  $J_{\text{eff}}$  character remains accurate near the  $\Gamma$  and  $M$  high-symmetry points, where hybridization is negligible [26]. The dashed curves in Figs. 1(b) and 1(c) indicate the measured dispersion of the  $J_{\text{eff}} = 3/2$  band in  $\text{Sr}_2\text{IrO}_4$  [2]. As noted in a recent comparative ARPES study [22], the monolayer bands are clearly not in the center of the split states of the bilayer, as expected if the interaction between states on the two Ir-O planes were small with respect to the other relevant energy scales.

It was argued [22] that this energy shift could be ascribed to the interaction between two adjacent unit cells along the  $z$

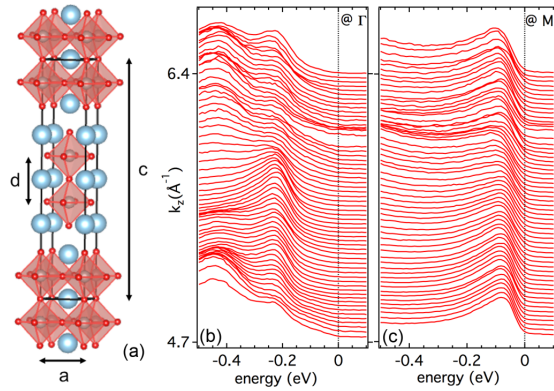


FIG. 2. (Color online) (a) The crystal structure of  $\text{Sr}_3\text{Ir}_2\text{O}_7$ , where the  $\text{IrO}_6$  octahedra are colored and the large spheres indicate Sr atoms;  $a$  and  $c$  are the lattice constants parallel and normal to the Ir-O layers, respectively, and  $d$  is the bilayer spacing. (b) and (c) show stacks of spectra measured for varying photon energy at  $\Gamma$  and  $M$ , where the intensity is normalized to the lowest binding energy peak, at  $-0.23$  and  $-0.09$  eV, respectively. The slight irregularity in the measured intensity around  $k_z = 6 \text{ \AA}^{-1}$  is due to the Sr  $3d$  doublet generated by second order radiation from the monochromator. The  $k_z$  values are calculated assuming an inner potential  $V_0 = 10$  eV. Note that due to the lack of a measurable  $k_z$  periodicity a precise extraction of  $V_0$  is not possible. However, it can be approximately set to  $10$  eV through analysis of the photoemission intensity modulation (see text).

axis, and therefore to the increased dimensionality from the almost ideal 2D case of  $\text{Sr}_2\text{IrO}_4$ . In Figs. 2(b) and 2(c) we show the evolution of the spectra with photon energy, which probes the  $c$ -axis dispersion, at the  $\Gamma$  and  $M$  points, respectively. The spectra are normalized by the lowest energy peak intensity. The lattice constant in the direction perpendicular to the Ir-O layers,  $c$  in Fig. 2(a), is  $\sim 20.9 \text{ \AA}$ . For a tetragonal unit cell, the expected  $k_z$  periodicity is  $4\pi/c \simeq 0.6 \text{ \AA}^{-1}$ . The range shown in Figs. 2(b) and 2(c) covers almost three BZs, with no detectable dispersion comparable with an  $80$  meV shift of the leading edge at the  $M$  point, reported in Ref. [22].

A possible explanation for these seemingly contradictory results is offered by the analysis of Fig. 3(a), which shows as a color plot the  $k_z$  dependence of the ARPES signal at the  $\Gamma$  point as in Fig. 2(b), but this time without any normalization, except for that by the photon flux. The spectral weight of the bonding and antibonding bands in a bilayer system is expected to have a markedly different, and in fact nearly opposite, dependence on the excitation energy, due to the opposite reflection symmetry of the states with respect to the intermediate plane between the two layers. We use a simple model, accounting only for the phase difference between the wave functions and considering a free electron final state. For a multilayer system of transverse periodicity  $d$ , the  $k_z$  dependence of the matrix elements essentially follows a sine wave of period  $2\pi/d$ , dampened with increasing energy [27]. This behavior has been observed for surface states [28], quantum well states [29], and, more recently, for multilayer graphene [30]. The observed intensity modulation of Fig. 3(a) indeed shows good agreement with the

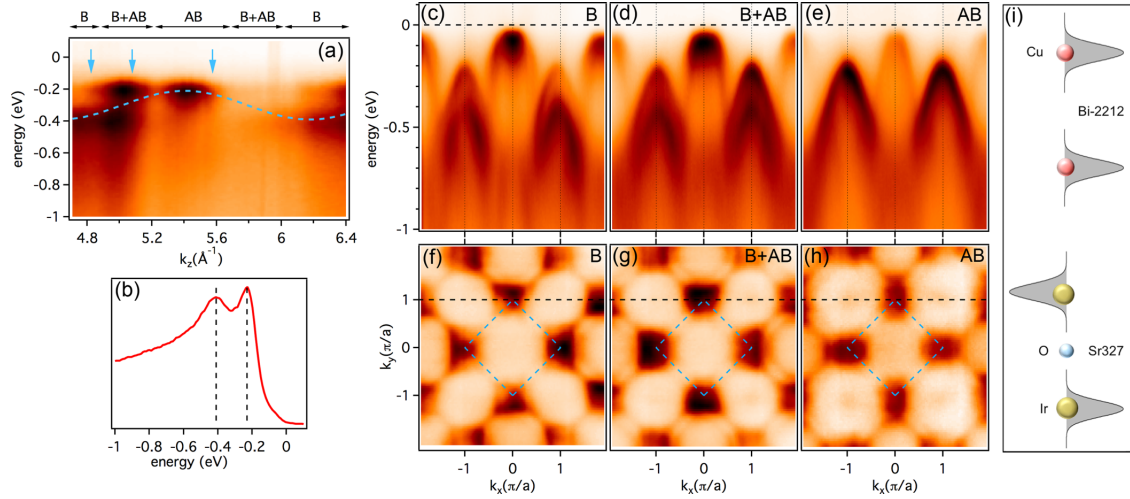


FIG. 3. (Color online) (a) The spectra of Fig. 2(b) are shown as an image plot and with no intensity normalization. The dashed line is a sine wave of period  $10\pi/c$ . The intervals defined above the panel indicate the approximate ranges where the intensity of either the bonding (B) or antibonding (AB) branch of the  $J_{\text{eff}} = 3/2$  states is dominant. (b) Energy distribution curve measured at  $\Gamma$  and  $h\nu = 96$  eV, in the second BZ. (c)–(e) Band dispersion along a  $\Gamma M \Gamma$  line at  $k_y = \pi/a$ , measured at  $h\nu = 85, 96,$  and  $113$  eV, respectively, corresponding to the arrows in (a); the corresponding constant energy cuts at  $E = -90$  meV are shown in (f)–(h). In reference to the intervals in (a), (c), (f): B; (d), (g): B + AB; (e), (h): AB. (i) Pictorial representations of the initial state bonding wave functions for Bi-2212 and for  $\text{Sr}_3\text{Ir}_2\text{O}_7$ .

predictions of this simple approach. In  $\text{Sr}_3\text{Ir}_2\text{O}_7$   $d \simeq c/5$ , and a sine wave of period  $k = 2\pi/(c/5) = 10\pi/c$  (dashed curve) convincingly tracks the transfer of spectral weight between the two branches of the bilayer dispersion.

By choosing the photon energy so that either one or the other of the states are suppressed, the bonding and antibonding bands can almost be mapped separately. Figures 3(c)–3(e) illustrate the dispersion along  $\Gamma M \Gamma$  at  $k_y = \pi/a$  [dashed lines in panels (f)–(h)], measured for the three photon energies corresponding to the arrows in Fig. 3(a). At the  $\Gamma$  point, the three panels show for the  $J_{\text{eff}} = 3/2$  states mainly the bonding band (c), both bands with comparable intensity (d), or only the antibonding band (e). The spectrum measured at  $\Gamma$  and  $h\nu = 96$  eV, shown in panel (b), clearly shows two peaks, separated by 0.18 eV, corresponding to the bonding and antibonding bands. The distinction is less clear for the  $J_{\text{eff}} = 1/2$  bands close to  $M$ , but signatures of the splitting are visible in panels (f)–(h), which present constant energy cuts at  $E = -90$  meV, at the top of the valence band. The corresponding intensity patterns are different, as they map in fact different states. Namely, the rectangular contours at the  $M$  points are elongated along different directions in (f) and (h), and are nearly square in (g). Notice that the transfer of spectral weight between the two bands could be misinterpreted as an energy dispersion, which may be the origin of the report of transverse dispersion of Ref. [22].

A further analysis of the intensity modulation of Fig. 3(a) reveals an interesting difference with the related case of the bilayer cuprates. The intensity of the bonding and antibonding bands evolves exactly in antiphase with respect to the case of  $\text{Bi}_2\text{Sr}_2\text{CaCu}_2\text{O}_{8+\delta}$  (Bi-2212) [27,31]. This is the result of a crucial difference in the structure of the two compounds

along the  $c$  axis. Namely, a bridging oxygen is present within the bilayer between two Ir ions in  $\text{Sr}_3\text{Ir}_2\text{O}_7$ , but not in Bi-2212. As a consequence, the wave function of the (bonding) lowest energy state is symmetric in Bi-2212, but antisymmetric in  $\text{Sr}_3\text{Ir}_2\text{O}_7$ , as shown in the cartoon of Fig. 3(i). In pictorial terms, the oxygen-mediated bond between Ir atoms favors a configuration with an increased  $5d$  charge density outside of the bilayer. Since  $V_0$  is evaluated by matching the smooth variation of the photoemission intensity with the expected matrix element modulation, it has a considerable uncertainty which we estimate to be  $\sim 5$  eV. However, this does not translate into any ambiguity in the assignment of the phase of the wave functions. At these photon energies, an unphysical value of  $V_0 > 30$  eV would be needed to translate the data by half a period of the sine wave of Fig. 3(a).

We notice in passing an interesting link between these conclusions and the band structure of  $\text{SrIrO}_3$ , the  $n \rightarrow \infty$  limit (3D) compound of the series, which remains unavailable.  $\text{Sr}_3\text{Ir}_2\text{O}_7$  provides indeed an  $n = 2$  sampling of the band structure of  $\text{SrIrO}_3$ . Given the cubic or nearly cubic structure of  $\text{SrIrO}_3$  the bands are expected to show a similar, holelike, dispersion along the  $c$  axis, as they do in the plane. Therefore, the top of the  $J_{\text{eff}} = 3/2$  manifold is expected at the  $\Gamma$  point, where the (totally symmetric) wave function has the same phase on adjacent layers, and the bottom at  $Z$ , where the phase is reversed on each adjacent layer. This is consistent with the previous considerations about the relative energy of the symmetric and antisymmetric states in  $\text{Sr}_3\text{Ir}_2\text{O}_7$ .

Figure 4(a) presents the measured band dispersion in the second BZ, where the  $J_{\text{eff}} = 3/2$  intensity is higher, for

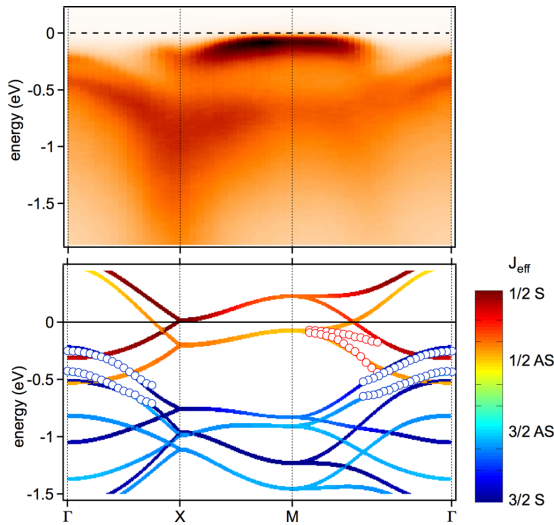


FIG. 4. (Color online) (a) Band dispersion along a  $\Gamma XM\Gamma$  path in the second BZ. (b) The peak energies extracted from the experimental data are superposed to the calculated bands of a TB model. The calculation follows Ref. [26], but neglects for simplicity the in-plane octahedra rotation. Colors represent the projected weights of each band on a fourfold bilayer basis set. Intermediate colors indicate mixed character.

$h\nu = 96$  eV, as in Figs. 3(d) and 3(g). Since the line shapes are rather broad, as typical for insulators, for the quantitative analysis of the splitting we used the curvature method, which is known to accurately yield the peak positions [32]. The latter are superimposed in Fig. 4(b) to the result of a tight-binding (TB) model. The calculation is structured as in Ref. [26] and, with respect to our previous work on  $\text{Ba}_2\text{IrO}_4$  [33], it includes additional interlayer hopping terms, which produce a  $k$ -dependent splitting of all bands. The parameters have been slightly adjusted in order to suppress the  $k$  offset between the  $J_{\text{eff}} = 1/2$  band maximum and the  $M$  point [26], consistent with the experimental data. More details are available in Ref. [34]. The projected weights of each band on a fourfold bilayer basis set [symmetric (S), antisymmetric (AS);  $J_{\text{eff}} = 1/2, 3/2$ ] is encoded in the color scale. For simplicity,

we do not consider the staggered tilting of the octahedra and neglect electronic correlations, which are essential to capture hybridization and avoided crossings, and therefore to reproduce the observed energy gap. As a consequence, the results, namely, for the  $J_{\text{eff}} = 1/2$  manifold, should be considered with caution in the vicinity of the Fermi level. Nevertheless the agreement is excellent further away from  $E_F$ .

A comparison of the experimental peak positions with the calculated bands in Fig. 4(b) confirms that the bilayer splitting of the  $J_{\text{eff}} = 3/2$  states is as large as  $\sim 0.2$  eV. As a term of comparison, the separation between bonding and antibonding states is only  $\sim 0.09$  eV in  $\text{Bi-2212}$  [27,31]. There, the bilayer splitting is directly related to a relevant interlayer hopping term  $t_{\perp}$ , and the energy splitting  $\Delta E$  is simply  $2t_{\perp}$ , at least in a TB approach [35]. In  $\text{Sr}_3\text{Ir}_2\text{O}_7$  the  $t_{2g}$  states are not orbitally ordered, so that the measured ARPES intensity does not exhibit the dramatic matrix element suppression characteristic of the cuprates. On the other hand, the presence of two interacting states and of comparable energy scales makes the link to the perpendicular hopping term less straightforward [26,36]. What is more important, in  $\text{Sr}_3\text{Ir}_2\text{O}_7$  the interlayer hopping is comparable to all other other relevant energy scales, i.e., the in-plane hopping terms [26] and the magnetic exchange terms [5]. Therefore, it cannot be treated as a simple perturbative term to the electronic structure of the monolayer counterpart  $\text{Sr}_2\text{IrO}_4$ .

In summary, a thorough ARPES  $k$ -space survey of the electronic structure of the bilayer iridate  $\text{Sr}_3\text{Ir}_2\text{O}_7$  reveals a very large splitting of the bonding and antibonding states of mainly  $J_{\text{eff}} = 3/2$  character. Moreover, the  $k_z$ -dependent transfer of spectral weight between these two bands shows that the bonding state has antisymmetric character, opposite to the much studied case of  $\text{Bi-2212}$ , a typical bilayer cuprate.

L.M. and S.M. equally contributed to this work. We gratefully acknowledge discussions with B. J. Kim, Yeonkwon Kim, and Y. Cao. We acknowledge support by the Swiss NSF, namely, through Grant No. PA00P21-36420 (L.M.) and the Sinergia network on Mott Physics Beyond the Heisenberg Model (MPBH). The Advanced Light Source is supported by the Director, Office of Science, Office of Basic Energy Sciences, of the U.S. Department of Energy under Contract No. DE-AC02-05CH11231. Work in the UK was supported by EPSRC.

- [1] B. J. Kim, H. Ohsumi, T. Komesu, S. Sakai, T. Morita, H. Takagi, and T. Arima, *Science* **323**, 1329 (2009).
- [2] B. J. Kim, H. Jin, S. J. Moon, J.-Y. Kim, B.-G. Park, C. S. Leem, J. Yu, T. W. Noh, C. Kim, S.-J. Oh *et al.*, *Phys. Rev. Lett.* **101**, 076402 (2008).
- [3] S. J. Moon, H. Jin, K. W. Kim, W. S. Choi, Y. S. Lee, J. Yu, G. Cao, A. Sumi, H. Funakubo, C. Bernhard *et al.*, *Phys. Rev. Lett.* **101**, 226402 (2008).
- [4] S. Fujiiyama, H. Ohsumi, T. Komesu, J. Matsuno, B. J. Kim, M. Takata, T. Arima, and H. Takagi, *Phys. Rev. Lett.* **108**, 247212 (2012).
- [5] J. Kim, A. H. Said, D. Casa, M. H. Upton, T. Gog, M. Daghofer, G. Jackeli, J. van den Brink, G. Khaliullin, and B. J. Kim, *Phys. Rev. Lett.* **109**, 157402 (2012).
- [6] J. Kim, D. Casa, M. H. Upton, T. Gog, Y.-J. Kim, J. F. Mitchell, M. van Veenendaal, M. Daghofer, J. van den Brink, G. Khaliullin *et al.*, *Phys. Rev. Lett.* **108**, 177003 (2012).
- [7] J. W. Kim, Y. Choi, J. Kim, J. F. Mitchell, G. Jackeli, M. Daghofer, J. van den Brink, G. Khaliullin, and B. J. Kim, *Phys. Rev. Lett.* **109**, 037204 (2012).

- [8] S. Boseggia, R. Springell, H. C. Walker, H. M. Rønnow, C. Rüegg, H. Okabe, M. Isobe, R. S. Perry, S. P. Collins, and D. F. McMorrow, *Phys. Rev. Lett.* **110**, 117207 (2013).
- [9] D. Hsieh, F. Mahmood, D. H. Torchinsky, G. Cao, and N. Gedik, *Phys. Rev. B* **86**, 035128 (2012).
- [10] G. Jackeli and G. Khaliullin, *Phys. Rev. Lett.* **102**, 017205 (2009).
- [11] F. Wang and T. Senthil, *Phys. Rev. Lett.* **106**, 136402 (2011).
- [12] H. Watanabe, T. Shirakawa, and S. Yunoki, *Phys. Rev. Lett.* **105**, 216410 (2010).
- [13] C. Martins, M. Aichhorn, L. Vaugier, and S. Biermann, *Phys. Rev. Lett.* **107**, 266404 (2011).
- [14] A. Georges, L. de' Medici, and J. Mravlje, *Ann. Rev. Condens. Matter Phys.* **4**, 137 (2013).
- [15] V. M. Katukuri, H. Stoll, J. van den Brink, and L. Hozoi, *Phys. Rev. B* **85**, 220402 (2012).
- [16] H. Okabe, M. Isobe, E. Takayama-Muromachi, A. Koda, S. Takeshita, M. Hiraishi, M. Miyazaki, R. Kadono, Y. Miyake, and J. Akimitsu, *Phys. Rev. B* **83**, 155118 (2011).
- [17] A. Ino, C. Kim, M. Nakamura, T. Yoshida, T. Mizokawa, Z.-X. Shen, A. Fujimori, T. Kakeshita, H. Eisaki, and S. Uchida, *Phys. Rev. B* **62**, 4137 (2000).
- [18] J. F. Bringley, B. A. Scott, S. J. La Placa, T. R. McGuire, F. Mehran, M. W. McElfresh, and D. E. Cox, *Phys. Rev. B* **47**, 15269 (1993).
- [19] T. Mizokawa, A. Fujimori, H. Namatame, Y. Takeda, and M. Takano, *Phys. Rev. B* **57**, 9550 (1998).
- [20] B. M. Wojek, M. H. Berntsen, S. Boseggia, A. T. Boothroyd, D. Prabhakaran, D. F. McMorrow, H. M. Rønnow, J. Chang, and O. Tjernberg, *J. Phys.: Condens. Matter* **24**, 415602 (2012).
- [21] P. D. C. King, T. Takayama, A. Tamai, E. Rozbicki, S. M. Walker, M. Shi, L. Patthey, R. G. Moore, D. Lu, K. M. Shen *et al.*, *Phys. Rev. B* **87**, 241106 (2013).
- [22] Q. Wang, Y. Cao, J. A. Waugh, S. R. Park, T. F. Qi, O. B. Korneta, G. Cao, and D. S. Dessau, *Phys. Rev. B* **87**, 245109 (2013).
- [23] K. M. Shen, F. Ronning, D. H. Lu, W. S. Lee, N. J. C. Ingle, W. Meevasana, F. Baumberger, A. Damascelli, N. P. Armitage, L. L. Miller *et al.*, *Phys. Rev. Lett.* **93**, 267002 (2004).
- [24] S. Boseggia, R. Springell, H. C. Walker, A. T. Boothroyd, D. Prabhakaran, D. Wermeille, L. Bouchenoire, S. P. Collins, and D. F. McMorrow, *Phys. Rev. B* **85**, 184432 (2012).
- [25] G. Cao, Y. Xin, C. S. Alexander, J. E. Crow, P. Schlottmann, M. K. Crawford, R. L. Harlow, and W. Marshall, *Phys. Rev. B* **66**, 214412 (2002).
- [26] J.-M. Carter and H.-Y. Kee, *Phys. Rev. B* **87**, 014433 (2013).
- [27] D. L. Feng, C. Kim, H. Eisaki, D. H. Lu, A. Damascelli, K. M. Shen, F. Ronning, N. P. Armitage, N. Kaneko, M. Greven *et al.*, *Phys. Rev. B* **65**, 220501 (2002).
- [28] S. G. Louie, P. Thiry, R. Pinchaux, Y. Pétrouff, D. Chandross, and J. Lecante, *Phys. Rev. Lett.* **44**, 549 (1980).
- [29] A. Mugarza, J. E. Ortega, A. Mascaraque, E. G. Michel, K. N. Altmann, and F. J. Himpsel, *Phys. Rev. B* **62**, 12672 (2000).
- [30] T. Ohta, A. Bostwick, J. L. McChesney, T. Seyller, K. Horn, and E. Rotenberg, *Phys. Rev. Lett.* **98**, 206802 (2007).
- [31] A. A. Kordyuk, S. V. Borisenko, T. K. Kim, K. A. Nenkov, M. Knupfer, J. Fink, M. S. Golden, H. Berger, and R. Follath, *Phys. Rev. Lett.* **89**, 077003 (2002).
- [32] P. Zhang, P. Richard, T. Qian, Y.-M. Xu, X. Dai, and H. Ding, *Rev. Sci. Instrum.* **82**, 043712 (2011).
- [33] S. Moser, L. Moreschini, A. Ebrahimi, B. D. Piazza, M. Isobe, H. Okabe, J. Akimitsu, V. V. Mazurenko, K. S. Kim, A. Bostwick *et al.*, *New J. Phys.* **16**, 013008 (2014).
- [34] See Supplemental Material at <http://link.aps.org/supplemental/10.1103/PhysRevB.89.201114> for details on the tight-binding model used.
- [35] A. I. Liechtenstein, O. Gunnarsson, O. K. Andersen, and R. M. Martin, *Phys. Rev. B* **54**, 12505 (1996).
- [36] Several hopping terms between the two IrO layers affect the band dispersion (five in Ref. [26]). In this qualitative discussion,  $t_{\perp}$  embodies an effective hopping term responsible for the size of the splitting between bonding and antibonding branch.

# Bibliography

- [1] H. Lesch, Frag' den Lesch 144, Energie: Die Grenzen des Wachstums, TV Broadcast Second German Television ZDF (2014).
- [2] M. Wagner, G. Franken, N. Martin, F. Melcher, J. Vasters, Zertifizierte Handelsketten im Bereich mineralischer Rohstoffe, Deutsche Bundesanstalt für Geowissenschaften und Rohstoffe, Projektstudie (2007).
- [3] S. Behrendt, M. Scharp, W. Kahlenborn, M. Feil, C. Dereje, R. Bleischwitz and R. Delzeit Seltene Metalle Maßnahmen und Konzepte zur Lösung des Problems konfliktverschärfender Rohstoffausbeutung am Beispiel Coltan, Umweltforschungsplan des deutschen Bundesministeriums für Umwelt, Naturschutz und Reaktorsicherheit, Forschungsbericht 363 01 124 (2007).
- [4] Deutsche Bundesregierung, Zwischenbilanz der Rohstoffaktivitäten der deutschen Bundesregierung – Schwerpunkt nichtenergetische Rohstoffe (2008).
- [5] US Department of Energy, Complex Systems: Science for the 21st Century, Lawrence Berkeley National Laboratory (1999).
- [6] US Department of Energy, Nanoscale Science, Technology and Research Directions, Oak Ridge National Laboratory (1999).
- [7] US Department of Energy, Basic Research Needs for the Hydrogen Economy, Rockville (2003).
- [8] US Department of Energy, Basic Energy Research Needs for Superconductivity, Washington DC (2006).
- [9] US Department of Energy, Opportunities for Discovery: Theory and Computation in Basic Energy Sciences (2005).
- [10] US Department of Energy, Basic Research Needs for Solar Energy Utilization, Bethesda (2005).
- [11] E. Rotenberg, *Many-Body Interactions in Nanoscale Materials by Angle - Resolved Photoemission Spectroscopy in X-Rays in Nanoscience: Spectroscopy, Spectromicroscopy, and Scattering Techniques*, Wiley-VCH, Weinheim, Germany (2010).

## Bibliography

---

- [12] S. Hüfner, *Photoelectron Spectroscopy: Principles and Applications*, Springer, Berlin/Heidelberg/New York, 2nd edn. (1995).
- [13] S. D. Kevan, *Angle-Resolved Photoemission: Theory and Current Applications*, Elsevier, Amsterdam (1992).
- [14] T. Valla, A. V. Fedorov, P. D. Johnson and S. L. Hulbert, Many-body effects in angle-resolved photoemission: quasiparticle energy and lifetime of a Mo(110) surface state, *Phys. Rev. Lett.* **83**, 2085 (1999).
- [15] M. Hengsberger, D. Purdie, P. Segovia, M. Garnier and Y. Baer, Photoemission study of a strongly coupled electron-phonon system, *Phys. Rev. Lett.* **83**, 592 (1999).
- [16] T. Valla, A.V. Fedorov, P.D. Johnson, B.O. Wells, S.L. Hulbert, Q. Li, G.D. Gu and N. Koshizuka, Evidence for quantum critical behavior in the optimally doped cuprate,  $\text{Bi}_2\text{Sr}_2\text{CaCu}_2\text{O}_{8+d}$ , *Science* **285**, 2110 (1999).
- [17] S. LaShell, E. Jensen and T. Balasubramanian, Nonquasiparticle structure in the photoemission spectra from the Be(0001) surface and determination of the electron self energy, *Phys. Rev. B* **61**, 2371 (2000).
- [18] A. Lanzara, P. V. Bogdanov, X. J. Zhou, S. A. Kellar, D. L. Feng, E. D. Lu, T. Yoshida, H. Eisaki, A. Fujimori, K. Kishio, J.-I. Shimoyama, T. Noda, S. Uchida, Z. Hussain and Z.-X. Shen, Evidence for ubiquitous strong electron-phonon coupling in high-temperature superconductors, *Nature* **412**, 510 (2001).
- [19] Y.-D. Chuang, A. D. Gromko, D. S. Dessau, T. Kimura and Y. Tokura Fermi surface nesting and nanoscale fluctuating charge/orbital ordering in colossal magnetoresistive oxides, *Science* **292**, 1509 (2001).
- [20] E. Rotenberg and S.D. Kevan, Electron-phonon coupling in W(110)-(1 × 1), *J. Electron Spectrosc. Relat. Phenom.* **126**, 125 (2002).
- [21] A. Damascelli, Z. Hussain and Z.X. Shen, Angle-resolved photoemission studies of the cuprate superconductors, *Rev. Mod. Phys.* **75**, 473 (2003).
- [22] J. Shi, S.-J. Tang, B. Wu, P. T. Sprunger, W. L. Yang, V. Brouet, X. J. Zhou, Z. Hussain, Z.-X. Shen, Z. Zhang and E. W. Plummer, Direct extraction of the Eliashberg function for electron-phonon coupling: a case study of Be(10-10), *Phys. Rev. Lett.* **92**, 186401 (2004).
- [23] A. Einstein, Concerning an heuristic point of view toward the emission and transformation of light, *Ann. Phys.* **17**, 132 (1905).
- [24] A. Damascelli, Probing the electronic structure of complex systems by ARPES, *Phys. Scripta* **T109**, 61 (2004).

- [25] G. Bian, L. Zhang, Y. Liu, T. Miller and T.-C. Chiang, Illuminating the surface spin texture of the giant-Rashba quantum-well system Bi/Ag(111) by circularly polarized photoemission, *Phys. Rev. Lett.* **108**, 186403 (2012).
- [26] G. D. Mahan *Many-particle physics* Plenum, New York, N.Y., 2nd edn. (1993).
- [27] G. D. Mahan, Theory of photoemission in simple metals, *Phys. Rev. B* **2**, 11 (1970).
- [28] J. W. Gadzuk, Surface molecules and chemisorption. II. Photoemission angular distributions, *Phys. Rev. B* **10**, 12 (1974).
- [29] J. W. Gadzuk, Angular distributions of electrons photoemitted from chemisorbed atoms, *Solid State Commun.* **15**, 1011 (1974).
- [30] J. W. Gadzuk, Angle-resolved photoemission from crystal-field split  $d$  shells of adsorbed atoms *Phys. Rev. B* **12**, 12 (1975).
- [31] L. Schaich and N. W. Ashcroft, Model calculations in the theory of photoemission, *Phys. Rev. B* **3**, 8 (1971).
- [32] S. M. Goldberg, C. S. Fadley and S. Kono, Photoionization cross-sections for atomic orbitals with random and fixed spatial orientation, *J. Electron Spectrosc. Relat. Phenom.* **21**, 285 (1981).
- [33] X.-P. Wang, P. Richard, Y.-B. Huang, H. Miao, L. Cevey, N. Xu, Y.-J. Sun, T. Qian, Y.-M. Xu, M. Shi, J.-P. Hu, X. Dai and H. Ding, Orbital characters determined from Fermi surface intensity patterns using angle-resolved photoemission spectroscopy, *Phys. Rev. B* **85**, 214518 (2012).
- [34] V. Brouet, M. F. Jensen, P.-H. Lin, A. Taleb-Ibrahimi, P. Le Fèvre, F. Bertran, C.-H. Lin, W. Ku, A. Forget and D. Colson, Impact of the two Fe unit cell on the electronic structure measured by ARPES in iron pnictides, *Phys. Rev. B* **86**, 075123 (2012).
- [35] Y. Zi-Rong, Z. Yan, X. Bin-Ping and F. Dong-Lai Angle-resolved photoemission spectroscopy study on iron-based superconductors, *Chin. Phys. B* **22**, 8 (2013).
- [36] L. Moreschini, P.-H. Lin, C.-H. Lin, W. Ku, D. Innocenti, Y. J. Chang, A. L. Walter, V. Brouet, E. Rotenberg, A. Bostwick and M. Grioni, Direct evidence of broken translational symmetry in ARPES: the case of  $\text{ReTe}_x\text{Se}_{1-x}$ , *Phys. Rev. Lett.* **112**, 087602 (2014).
- [37] N. Marzari, A. A. Mostofi, J. R. Yates, I. Souza and D. Vanderbilt, Maximally localized Wannier functions: theory and applications, *Rev. Mod. Phys.* **84**, 1419 (2012).
- [38] D.A. Shirley, High-resolution x-ray photoemission spectrum of the valence bands of gold, *Phys. Rev.* **B5**, 4709 (1972).
- [39] G. Panati and A. Pisante, Bloch bundles, Marzari-Vanderbilt functional and maximally localized Wannier functions, *Commun. Math. Phys.* **322**, 835 (2013).



## Bibliography

---

- [40] M.P. Seah and W.A. Dench, Quantitative electron spectroscopy of surfaces: a standard data base for electron inelastic mean free paths in solids, *Surf. Interface Anal.* **1**, 2 (1979).
- [41] Y. Liao, Electron inelastic mean free path of elements and compounds in practical electron microscopy and database, Retrieved from <http://www.globalsino.com/EM/page4809.html> (2013).
- [42] B. Podolsky and L. Pauling, The momentum distribution in hydrogen-like atoms, *Phys. Rev.* **34**, 109 (1929).
- [43] J. W. Cooper, Photoionization from outer atomic subshells. A model study, *Phys. Rev.* **128**, 681 (1962).
- [44] D. Eberly, Euler angle formulas, Retrieved from <http://www.geometrictools.com> (1998).
- [45] J. J. P. Stewart, Generic (non-trigonometric) rotation of atomic orbitals, Retrieved from [http://openmopac.net/manual/rotate\\_atomic\\_orbitals\\_generic.html](http://openmopac.net/manual/rotate_atomic_orbitals_generic.html) (2007).
- [46] L.J.P. Ament, M. van Veenendaal, T. P. Devereaux, J. P. Hill and J. van den Brink, Resonant inelastic x-ray scattering studies of elementary excitations, *Rev. Mod. Phys.* **83**, 705 (2011).
- [47] I. Jarrige, D. Arena, A. Baron, Y. Cai, Y.-D. Chuang, F. de Groot, J. Guo, J.P. Hill, S. Hulbert, C. McGuinness, R. Reininger, J.E. Rubenson, C. Sanchez-Hanke, T. Schmitt and K. Smith, Soft inelastic x-ray scattering (SIX) Accepted Proposal, National Synchrotron Light Source II, Retrieved from <http://www.bnl.gov/nsls2/beamlines/2010BeamlineProposal-Approved.asp>, Brookhaven National Laboratory (2010).
- [48] Address user information Retrieved from <http://www.psi.ch/sls/adress/user-information>, Swiss Light Source (2014).
- [49] W. Schülke, *Electron dynamics by inelastic x-ray scattering*, Oxford University Press, New York, N.Y., (2007).
- [50] M. Altarelli, Resonant x-ray scattering: a theoretical introduction, *Lect. Notes Phys.* **697**, 201 (2006).
- [51] M. Blume, Magnetic scattering of x rays, *J. Appl. Phys.* **57**, 3615 (1985).
- [52] M. Guarise, B. Dalla Piazza, M. Moretti Sala, G. Ghiringhelli, L. Braicovich, H. Berger, J. N. Hancock, D. van der Marel, T. Schmitt, V. N. Strocov, L. J. P. Ament, J. van den Brink, P.-H. Lin, P. Xu, H. M. Rønnow and M. Grioni, Measurement of magnetic excitations in the two-dimensional antiferromagnetic  $\text{Sr}_2\text{CuO}_2\text{Cl}_2$  insulator using resonant x-ray scattering: evidence for extended interactions, *Phys. Rev. Lett.* **105**, 157006 (2010).
- [53] L. Braicovich, L. J. P. Ament, V. Bisogni, F. Forte, C. Aruta, G. Balestrino, N. B. Brookes, G. M. De Luca, P. G. Medaglia, F. Miletto Granozio, M. Radovic, M. Salluzzo, J. van den Brink and G. Ghiringhelli, Dispersion of magnetic excitations in the cuprate  $\text{La}_2\text{CuO}_4$  and  $\text{CaCuO}_2$  compounds measured using resonant x-ray scattering, *Phys. Rev. Lett.* **102**, 167401 (2009).



- [54] G.F. Koster, J. O. Dimmock, R. W. Wheeler and H. Statz, *Properties of the thirty-two point groups*, M.I.T. Press, Cambridge, M.A. (1963).
- [55] J. S. Griffith, *The irreducible tensor method for molecular symmetry groups*, Englewood Cliffs: Prentice-Hall, N.J. (1962).
- [56] M. Matsubara, T. Uozumi, A. Kotani, Y. Harada and S. Shin, Polarization dependence of resonant x-ray emission spectra in early transition metal compounds, *J. Phys. Soc. Japan* **69**, 1558 (2000).
- [57] M. Nakazawa, H. Ogasawara and A. Kotani, Theory of polarization dependence in resonant x-ray emission spectroscopy of Ce compounds, *J. Phys. Soc. Japan* **69**, 4071 (2000).
- [58] M. Matsubara, T. Uozumi, A. Kotani, Y. Harada and S. Shin, Polarization dependence of resonant x-ray emission spectra in  $3d^n$  transition metal compounds with  $n = 0, 1, 2, 3$ , *J. Phys. Soc. Japan* **71**, 347 (2002).
- [59] H. Ogasawara, K. Fukui and M. Matsubara, Polarization dependence of x-ray emission spectroscopy *J. Electron Spectrosc. Relat. Phenom.* **136**, 161 (2004).
- [60] Y. Tanabe and S. Sugano, On the Absorption Spectra of Complex Ions, *J. Physic. Soc. Japan* **9**, 753 (1954).
- [61] Y. Tanabe and H. Kamimura, On the absorption spectra of complex ions IV. the effect of the spin-orbit interaction and the field of lower symmetry on  $d$  electrons in cubic field, *J. Physic. Soc. Japan* **13**, 394 (1958).
- [62] U. Fano, G. Racah, *Irreducible tensorial sets*, Academic Press, New York, N.Y. (1959).
- [63] D. W. Snoke, *32 Point Groups*, Retrieved from <http://www.phyast.pitt.edu/snoke/resources/resources.html> (2008).
- [64] J. N. Kotzev and M. I. Aroyo, Clebsch-Gordan coefficients for the corepresentations of Shubnikov point groups, *J. Phys. A: Math. Gen.* **13**, 2275 (1980).
- [65] J. N. Kotzev and M. I. Aroyo, Clebsch-Gordan coefficients for the corepresentations of Shubnikov point groups. II. cubic groups, *J. Phys. A: Math. Gen.* **14**, 1543 (1981).
- [66] J. N. Kotzev and M. I. Aroyo, Clebsch-Gordan coefficients for the corepresentations of Shubnikov point groups. III. groups of tetragonal, orthorhombic, monoclinic and triclinic crystal systems, *J. Phys. A: Math. Gen.* **15**, 711 (1982).
- [67] J. N. Kotzev and M. I. Aroyo, Clebsch-Gordan coefficients for the corepresentations of Shubnikov point groups. IV. groups of hexagonal and trigonal systems *J. Phys. A: Math. Gen.* **15**, 725 (1982).
- [68] A. P. Cracknell and M. R. Daniel, Magnetic point groups, selection rules and the antiferromagnetic phase transition in  $\text{UO}_2$ , *Proc. Phys. Soc.* **92**, 705 (1967).

## Bibliography

---

- [69] M. van Veenendaal, Polarization dependence of *L*- and *M*- edge resonant inelastic x-ray scattering on transition metal compounds, *Phys. Rev. Lett.* **96**, 117404 (2006).
- [70] L. J. P. Ament, G. Ghiringhelli, M. M. Sala, L. Braicovich and J. van den Brink Theoretical demonstration of how the dispersion of magnetic excitations in cuprate compounds can be determined using resonant inelastic x-ray scattering, *Phys. Rev. Lett.* **103**, 117003 (2009).
- [71] M. Guarise, Electronic and magnetic resonant inelastic x-ray study of cuprates, PhD-Thesis, EPFL (2012).
- [72] R. Asahi, T. Morikawa, T. Ohwaki, K. Aoki and Y. Taga, Visible-light photocatalysis in nitrogen-doped titanium oxides, *Science* **293**, 269 (2001).
- [73] Y. He, A. Tilocca, O. Dulub, A. Selloni and U. Diebold, Local ordering and electronic signatures of submonolayer water on anatase TiO<sub>2</sub>(101), *Nature Mater.* **8**, 585 (2009).
- [74] A. Fujishima and K. Honda, Electrochemical photolysis of water at a semiconductor electrode, *Nature* **238**, 37 (1972).
- [75] B. O'Regan and M. Grätzel, A low-cost, high-efficiency solar-cell based on dye-sensitized colloidal TiO<sub>2</sub> films, *Nature* **353**, 737 (1991).
- [76] D. Kuang, J. Brillet, P. Chen, M. Takata, S. Uchida, H. Miura, K. Sumioka, S. M. Za-keeruddin and M. Grätzel, Application of highly ordered TiO<sub>2</sub> nanotube arrays in flexible dye-sensitized solar cells, *Acs Nano* **2**, 1113 (2008).
- [77] O. K. Varghese, M. Paulose and C. A. Grimes, Long vertically aligned titania nanotubes on transparent conducting oxide for highly efficient solar cells, *Nat. Nanotechnol.* **4**, 592 (2009).
- [78] R. Asahi, Y. Taga, W. Mannstadt and A. J. Freeman, Electronic and optical properties of anatase TiO<sub>2</sub>, *Phys. Rev. B* **61**, 7459 (2000).
- [79] H. Tang, H. Berger, P.E. Schmid, F. Levy and G. Burri, Photoluminescence in TiO<sub>2</sub> anatase single-crystals, *Solid State Commun.* **87**, 847 (1993).
- [80] J. Jaćimović, C. Vaju, A. Magrez, H. Berger, L. Forró, R. Gaál, V. Cerovski and R. Žikić, Pressure dependence of the large-polaron transport in anatase TiO<sub>2</sub> single crystals, *Europhys. Lett.* **99**, 57005 (2012).
- [81] L. Forró, O. Chauvet, D. Emin, L. Zuppiroli, H. Berger and F. Lévy, High-mobility n-type charge-carriers in large single-crystals of anatase (TiO<sub>2</sub>), *J. Appl. Phys.* **75**, 633 (1994).
- [82] S. D. Yoon, Y. Chen, A. Yang, T. L. Goodrich, X. Zuo, D. A. Arena, K. Ziemer, C. Vittoria and V. G. Harris, Oxygen-defect-induced magnetism to 880 K in semiconducting anatase TiO<sub>2</sub>-delta films. *J. Phys.: Condens. Matter* **18**, L355 (2006).

- [83] S. Mohri, Y. Hirose, S. Nakao, N. Yamada, T. Shimada and T. Hasegawa, Transparent conductivity of fluorine-doped anatase TiO<sub>2</sub> epitaxial thin films, *J. Appl. Phys.* **111**, 093528 (2012).
- [84] A. Kitada, S. Kasahara, T. Terashima, K. Yoshimura, Y. Kobayashi and H. Kageyama Highly reduced anatase TiO<sub>2-δ</sub> thin films obtained via low-temperature reduction, *Appl. Phys. Express* **4**, 035801 (2011).
- [85] J. K. Burdett, T. Hughbanks, G. J. Miller, J. W. Richardson and J. V. Smith, Structural-electronic relationships in inorganic solids: powder neutron diffraction studies of the rutile and anatase polymorphs of titanium dioxide at 15 and 295 K, *J. Am. Chem. Soc.* **109**, 3639 (1987).
- [86] H. Berger, H. Tang and F. Lévy, Growth and Raman spectroscopic characterization of TiO<sub>2</sub> anatase single crystals, *J. Cryst. Growth* **130**, 108 (1993).
- [87] R. Hengerer, B. Bolliger, M. Erbudak and M. Grätzel, Structure and stability of the anatase TiO<sub>2</sub> (101) and (001) surfaces, *Surf. Sci.* **460**, 162 (2000).
- [88] Y. Liang, S. Gan and S. A. Chambers, Surface structure of anatase TiO<sub>2</sub>(001): Reconstruction, atomic steps and domains, *Phys. Rev. B* **63**, 235402 (2001)
- [89] U. Diebold, The surface science of titanium dioxide, *Surf. Sci. Rep.* **48**, 53 (2002).
- [90] S. Moser, L. Moreschini, J. Jaćimović, O. S. Barišić, H. Berger, A. Magrez, Y. J. Chang, K. S. Kim, A. Bostwick, E. Rotenberg, L. Forró and M. Grioni, Tunable polaronic conduction in anatase TiO<sub>2</sub>, *Phys. Rev. Lett* **110**, 196403 (2013).
- [91] Z. Cheng, T. Liu, C. Yang, H. Gan, F. Zhang and J. Chen, Study on the electronic structures of the reduced anatase TiO<sub>2</sub> by the first-principle calculation, *J. Phys. Chem. Solids* **73**, 302 (2012).
- [92] L. Chiodo, J. M. García-Lastra, A. Iacomino, S. Ossicini, J. Zhao, H. Petek and A. Rubio, Self-energy and excitonic effects in the electronic and optical properties of TiO<sub>2</sub> crystalline phases, *Phys. Rev. B* **82**, 045207 (2010).
- [93] M. Mikami, S. Nakamura, O. Kitao, H. Arakawa and X. Gonze, First-principles study of titanium dioxide: rutile and anatase, *Jpn. J. Appl. Phys.* **39**, 847 (2000).
- [94] M. Calatayud, P. Mori-Sánchez, A. Beltrán, A. Martín Pendás, E. Francisco, J. Andrés and J. M. Recio, Quantum-mechanical analysis of the equation of state of anatase TiO<sub>2</sub>, *Phys. Rev. B* **64**, 184113 (2001).
- [95] H. Cheng and A. Selloni, Surface and subsurface oxygen vacancies in anatase TiO<sub>2</sub> and differences with rutile, *Phys. Rev. B* **79**, 092101 (2009).

## Bibliography

---

- [96] M. Emori, M. Sugita, K. Ozawa and H. Sakama, Electronic structure of epitaxial anatase TiO<sub>2</sub> films: Angle-resolved photoelectron spectroscopy study, *Phys. Rev. B* **85**, 035129 (2012).
- [97] M. L. Knotek and P. J. Feibelman, Ion desorption by core-hole Auger decay, *Phys. Rev. Lett.* **40**, 14 (1978).
- [98] P. Scheiber, M. Fidler, O. Dulub, M. Schmid, U. Diebold, W. Hou, U. Aschauer and A. Selloni, (Sub)surface mobility of oxygen vacancies at the TiO<sub>2</sub> anatase (101) surface, *Phys. Rev. Lett.* **109**, 136103 (2012).
- [99] S. Moser, L. Moreschini and E. Rotenberg, Lithographic patterning of insulating or semi-conducting solid state material in crystalline form, International Patent Application n° PCT/IB2013/060328 (2012).
- [100] R. Ciancio, E. Carlino, G. Rossi, C. Aruta, U. Scotti di Uccio, A. Vittadini and A. Selloni, Magnéli-like phases in epitaxial anatase TiO<sub>2</sub> thin films, *Phys. Rev. B* **86**, 104110 (2012).
- [101] T. Holstein, Theory of transport phenomena in an electron-phonon gas, *Ann. Phys.* **29**, 410 (1964).
- [102] R.E. Prange and L.P.Kadanoff, Transport theory for electron-phonon interactions in metals, *Phys. Rev.* **134**, 566 (1964).
- [103] P.B. Allen and W.W. Schulz, Bloch-Boltzmann analysis of electrical transport in inter-metallic compounds: ReO<sub>3</sub>, BaPbO<sub>3</sub>, CoSi<sub>2</sub> and Pd<sub>2</sub>Si, *Phys. Rev. B* **47**, 14434 (1993).
- [104] C.J. Howard, T.M. Sabine and F. Dickson, Structural and thermal parameters for rutile and anatase, *Acta Crystallogr., Sect. B: Struct. Sci* **47**, 462 (1991).
- [105] Y. Furubayashi, T. Hitosugi, Y. Yamamoto, K. Inaba, G. Kinoda and Y. Hirose, T. Shimada and T. Hasegawa, A transparent metal: Nb-doped anatase TiO<sub>2</sub>, *Appl. Phys. Lett.* **86**, 252101 (2005).
- [106] A.S. Alexandrov, Theory of superconductivity: from weak to strong coupling, IOP publishing (2003).
- [107] T. Hitosugi, H. Kamisaka, K. Yamashita, H. Nogawa, Y. Furubayashi, S. Nakao, N. Yamada, A. Chikamatsu, H. Kumigashira, M. Oshima, Y. Hirose, T. Shimada and T. Hasegawa, Electronic band structure of transparent conductor: Nb-doped anatase TiO<sub>2</sub>, *Appl. Phys. Express* **1**, 111203 (2008).
- [108] C.N. Veenstra, G.L. Goodvin, M. Berciu and A. Damascelli, Elusive electron-phonon coupling in quantitative analyses of the spectral function, *Phys. Rev. B* **82**, 012504 (2010).
- [109] Y. Furubayashi, N. Yamada, Y. Hirose, Y. Yamamoto, M. Otani, T. Hitosugi, T. Shimada and T. Hasegawa, Transport properties of *d*-electron-based transparent conducting oxide: Anatase Ti<sub>1-x</sub>Nb<sub>x</sub>O<sub>2</sub>, *J. Appl. Phys.* **101**, 093705 (2007).

- [110] R. J. Gonzalez, R. Zallen and H. Berger, Infrared reflectivity and lattice fundamentals in anatase  $\text{TiO}_2$ , *Phys. Rev. B* **55**, 7014 (1997).
- [111] A. S. Mishchenko, N. Nagaosa, N. V. Prokof'ev, A. Sakamoto and B. V. Svistunov, Optical conductivity of the Fröhlich polaron, *Phys. Rev. Lett.* **91**, 23 (2003).
- [112] A. S. Mishchenko, N. V. Prokof'ev, A. Sakamoto and B. V. Svistunov, Diagrammatic quantum Monte Carlo study of the Fröhlich polaron, *Phys. Rev. B* **62**, 10 (2000).
- [113] L.D. Landau and S.I. Pekar, Effective mass of a polaron, *Zh. Eksp. Teor. Fiz.* **18**, 419 (1948).
- [114] L. N. Cooper, Bound electron pairs in a degenerate Fermi gas, *Phys. Rev.* **104**, 1189 (1956).
- [115] J. Bardeen, L. N. Cooper and J. R. Schrieffer, Microscopic theory of superconductivity, *Phys. Rev.* **106**, 162 (1957).
- [116] J. Bardeen, L. N. Cooper and J. R. Schrieffer, Theory of Superconductivity, *Phys. Rev.* **108**, 1175 (1957).
- [117] P. Déak, B. Aradi and T. Frauenheim Polaronic effects in  $\text{TiO}_2$  calculated by the HSE06 hybrid functional: Dopant passivation by carrier self-trapping *Phys. Rev. B* **83**, 155207 (2011).
- [118] W. Kang and M. S. Hybertsen, Quasiparticle and optical properties of rutile and anatase  $\text{TiO}_2$ , *Phys. Rev. B* **82**, 085203 (2010).
- [119] R. Shirley and M. Kraft, Electronic and optical properties of aluminium-doped anatase and rutile  $\text{TiO}_2$  from ab initio calculations, *Phys. Rev. B* **81**, 075111 (2010).
- [120] M. Berciu and G. A. Sawatzky, Light polarons and bipolarons for a highly inhomogeneous electron-boson coupling, *Euro Phys. Lett.*, **81**, 57008 (2008).
- [121] L. Braicovich, J. van den Brink, V. Bisogni, M. Moretti Sala, L. J. P. Ament, N. B. Brookes, G. M. De Luca, M. Salluzzo, T. Schmitt, V. N. Strocov and G. Ghiringhelli, Magnetic excitations and phase separation in the underdoped  $\text{La}_{2-x}\text{Sr}_x\text{CuO}_4$  superconductor measured by resonant inelastic x-ray scattering, *Phys. Rev. Lett.* **104**, 077002 (2010).
- [122] T. Cuk, D. H. Lu, X. J. Zhou, Z. X. Shen, T. P. Devereaux and N. Nagaosa, A review of electron-phonon coupling seen in the high- $T_c$  superconductors by angle-resolved photoemission studies (ARPES), *Phys. Stat. Sol.* **242**, 11 (2005).
- [123] T. P. Devereaux, T. Cuk, Z.-X. Shen and N. Nagaosa, Anisotropic electron-phonon interaction in the cuprates, *Phys. Rev. Lett.* **93**, 117004 (2004).
- [124] Fabrizio Carbone, Ding-Shyue Yang, Enrico Giannini and Ahmed H. Zewail, Direct role of structural dynamics in electron-lattice coupling of superconducting cuprates, *PNAS* **105**, 20161 (2008).

## Bibliography

---

- [125] W. S. Lee, S. Johnston, B. Moritz, J. Lee, M. Yi, K. J. Zhou, T. Schmitt, L. Patthey, V. Strocov, K. Kudo, Y. Koike, J. van den Brink, T. P. Devereaux and Z. X. Shen, Role of lattice coupling in establishing electronic and magnetic properties in quasi-one-dimensional cuprates, *Phys. Rev. Lett* **110**, 265502 (2013).
- [126] Z. Tao, T.-R. T. Han and C.-Y. Ruan, Anisotropic electron-phonon coupling investigated by ultrafast electron crystallography: three-temperature model, *Phys. Rev. B* **87**, 235124 (2013).
- [127] T. Valla, J. Camacho, Z.-H. Pan, A.V. Fedorov, A. C. Walters, C. A. Howard and M. Ellerby, Anisotropic electron-phonon coupling and dynamical nesting on the graphene sheets in superconducting  $\text{CaC}_6$  using angle-resolved photoemission spectroscopy, *Phys. Rev. Lett.* **102**, 107007 (2009).
- [128] D. Haberer, L. Petaccia, A. V. Fedorov, C. S. Praveen, S. Fabris, S. Piccinin, O. Vilkov, D. V. Vyalikh, A. Preobrajenski, N. I. Verbitskiy, H. Shiozawa, J. Fink, M. Knupfer, B. Büchner and A. Grüneis, Anisotropic Eliashberg function and electron-phonon coupling in doped graphene, *Phys. Rev. B* **88**, 081401(R) (2013).
- [129] H. M. Fan, Z. H. Ni, Y. P. Feng, X. F. Fan, J. L. Kuo, Z. X. Shen and B. S. Zou, Anisotropy of electron-phonon coupling in single wurtzite CdS nanowires, *Appl. Phys. Lett.* **91**, 171911 (2007).
- [130] C. Persson and A. Ferreira da Silva, Strong polaronic effects on rutile  $\text{TiO}_2$  electronic band edges, *Appl. Phys. Lett.* **86**, 231912 (2005).
- [131] J. P. Hague, P. E. Kornilovitch, A. S. Alexandrov and J. H. Samson, Effects of lattice geometry and interaction range on polaron dynamics, *Phys. Rev B* **73**, 054303 (2006).
- [132] Y. Hirose, N. Yamada, S. Nakao, T. Hitosugi, T. Shimada and T. Hasegawa, Large electron mass anisotropy in a  $d$ -electron-based transparent conducting oxide: Nb-doped anatase  $\text{TiO}_2$  epitaxial films, *Phys. Rev. B* **79**, 165108 (2009).
- [133] H. A. Huy, B. Aradi, T. Frauenheim and P. Déak, Calculation of carrier-concentration-dependent effective mass in Nb-doped anatase crystals of  $\text{TiO}_2$ , *Phys. Rev. B* **83**, 155201 (2011).
- [134] P. E. Kornilovitch, Path-integral approach to lattice polarons, *J. Phys.: Condens. Matter* **19**, 255213 (2007).
- [135] P. E. Spencer, J. H. Samson, P. E. Kornilovitch and A. S. Alexandrov Effect of electron-phonon interaction range on lattice polaron dynamics: A continuous-time quantum Monte Carlo study, *Phys. Rev. B* **71**, 184310 (2005).
- [136] L. J. P. Ament, M. van Veenendaal and J. van den Brink, Determining the electron-phonon coupling strength from resonant inelastic x-ray scattering at transition metal L-edges, *Euro Phys. Lett.*, **95**, 27008 (2011).

- [137] Y. Harada, T. Tokushima, Y. Horikawa, O. Takahashi, H. Niwa, M. Kobayashi, M. Oshima, Y. Senba, H. Ohashi, K. T. Wikfeldt, A. Nilsson, L. G. M. Pettersson and S. Shin, Selective probing of the OH or OD stretch vibration in liquid water using resonant inelastic soft-x-ray scattering, *Phys. Rev. Lett.* **111**, 193001 (2013).
- [138] Y. Harada, M. Kobayashi, H. Niwa, Y. Senba, H. Ohashi, T. Tokushima, Y. Horikawa, S. Shin, M. Oshima, Ultrahigh resolution soft x-ray emission spectrometer at BL07LSU in SPring-8, *Rev. Sci. Instrum.* **83**, 013116 (2012).
- [139] P. Krüger, Multichannel multiple scattering calculation of  $L_{2,3}$ -edge spectra of  $TiO_2$  and  $SrTiO_3$ : importance of multiplet coupling and band structure, *Phys. Rev. B* **81**, 125121 (2010).
- [140] J. P. Crocombette and F. Jollet, Ti  $2p$  x-ray absorption in titanium dioxides ( $TiO_2$ ): the influence of the cation site environment, *J. Phys.: Condens. Matter* **6**, 10811 (1994).
- [141] F. de Groot and A. Kotani, *Core Level Spectroscopy of Solids*, CRC Press, London, UK (2008).
- [142] K.-J. Zhou, M. Radovic, J. Schlappa, V. Strocov, R. Frison, J. Mesot, L. Patthey and T. Schmitt, Localized and delocalized Ti  $3d$  carriers in  $LaAlO_3/SrTiO_3$  superlattices revealed by resonant inelastic x-ray scattering, *Phys. Rev. B* **83**, 201402(R) (2011).
- [143] A. Augustsson, A. Henningsson, S. M. Butorin, H. Siegbahn, J. Nordgren and J.-H. Guo, Lithium ion insertion in nanoporous anatase  $TiO_2$  studied with RIXS, *J. Chem. Phys.* **119**, 3983 (2003).
- [144] O. Frank, M. Zikalova, B. Laskova, J. Kürti, J. Koltaib and L. Kavan, Raman spectra of titanium dioxide (anatase, rutile) with identified oxygen isotopes (16, 17, 18), *Phys. Chem. Chem. Phys.* **14**, 14567 (2012).
- [145] M. Mikami, S. Nakamura, O. Kitao and H. Arakawa, Lattice dynamics and dielectric properties of  $TiO_2$  anatase: a first-principles study, *Phys. Rev. B* **66**, 155213 (2002).
- [146] M. Tinkham, *Group Theory and Quantum Mechanics*, McGraw-Hill, New York, N.Y. (1964).
- [147] J. Fink, E. Schierle, E. Weschke and J. Geck, Resonant elastic soft x-ray scattering, *Rep. Prog. Phys.* **76**, 05650 (2013).
- [148] S. Moser, L. Moreschini, P. Krüger, H. Berger, P. Bugnon, A. Magrez, Y. J. Chang, K. S. Kim, A. Bostwick, E. Rotenberg and M. Grioni, Orbital selective resonance of conduction carriers at the Ti L-edge of anatase  $TiO_2$ , in preparation
- [149] E. Shojaei and M. R. Mohammadzadeh, First-principles elastic and thermal properties of  $TiO_2$ : a phonon approach, *J. Phys.: Condens. Matter* **22**, 015401 (2010).

## Bibliography

---

- [150] F. M.F. de Groot, High-resolution x-ray emission and x-ray absorption spectroscopy, *Chem. Rev.* **101**, 1779 (2001).
- [151] F.M.F. de Groot, Ligand and metal x-ray absorption in transition metal complexes, *Inorganica Chimica Acta* **361**, 850 (2008).
- [152] J. G. Bednorz and K. A. Müller, Possible high  $T_c$  superconductivity in the Ba-La-Cu-O system, *Z. Physik, B* **64**, 189 (1986).
- [153] M. K. Wu, J. R. Ashburn, C. J. Torng, P. H. Hor, R. L. Meng, L. Gao, Z. J. Huang, Y. Q. Wang and C. W. Chu, Superconductivity at 93 K in a new mixed-phase Y-Ba-Cu-O compound system at ambient pressure, *Phys. Rev. Lett.* **58**, 908 (1987).
- [154] Z. Hiroi, M. Azuma, M. Takano and Y. Bando, A new homologous series  $\text{Sr}_{n-1}\text{Cu}_{n+1}\text{O}_{2n}$  found in the SrO-CuO system treated under high pressure, *J. Solid State Chem.* **95**, 230 (1991).
- [155] M. Azuma, Z. Hiroi, M. Takano, K. Ishida and Y. Kitaoka, Observation of a spin gap in  $\text{SrCu}_2\text{O}_3$  comprising spin-1/2 quasi-1D two-leg ladders, *Phys. Rev. Lett.* **73**, 3463 (1994).
- [156] E. Dagotto and T.M. Rice, Surprises on the way from one- to two-dimensional quantum magnets: the ladder materials, *Science* **271**, 618 (1996).
- [157] W. Siemons, G. Koster, D.H.A. Blank, R.H. Hammond, T.H. Geballe and M.R. Beasley, Tetragonal CuO: end member of the  $3d$  transition metal monoxides, *Phys. Rev. B* **79**, 195122 (2009).
- [158] D. Samal, H. Tan, Y. Takamura, W. Siemons, J. Verbeeck, G. van Tendeloo, E. Arenholz, C. A. Jenkins, G. Rijnders and G. Koster, Direct structural and spectroscopic investigation of ultrathin films of tetragonal CuO: six-fold coordinated copper, *Euro Phys. Lett.* **105**, 17003 (2014).
- [159] G. Peralta, D. Puggioni, A. Filippetti and V. Fiorentini, Jahn-Teller stabilization of magnetic and orbital ordering in rocksalt CuO, *Phys. Rev. B* **80**, 140408(R) (2009).
- [160] X.-Q. Chen, C.L. Fu, C. Franchini and R. Podloucky, Hybrid density-functional calculation of the electronic and magnetic structures of tetragonal CuO, *Phys. Rev. B* **80**, 094527 (2009).
- [161] K. S. Rabinovich, L. L. Samoilenko, A. S. Zhuravleva and A. G. Shneider, Magnetic properties of high-symmetry CuO, *Appl. Phys. Lett.* **104**, 182406 (2014).
- [162] A. Filippetti and V. Fiorentini Magnetic Ordering in CuO from First Principles: a cuprate antiferromagnet with fully three-dimensional exchange interactions, *Phys. Rev. Lett* **95**, 086405 (2005).
- [163] P. W. Anderson, Antiferromagnetism. Theory of superexchange interaction, *Phys. Rev.* **79**, 350 (1950).



- [164] J. B. Goodenough, Theory of the role of covalence in the perovskite-type manganites  $[\text{La}, M(\text{II})]\text{MnO}_3$ , *Phys. Rev.* **100**, 564 (1955).
- [165] J. B. Goodenough, An interpretation of the magnetic properties of the perovskite-type mixed crystals  $\text{La}_{1-x}\text{Sr}_x\text{CoO}_{3-\lambda}$ , *J. Phys. Chem. Solids* **6**, 287 (1958).
- [166] J. Kanamori, Superexchange interaction and symmetry properties of electron orbitals, *J. Phys. Chem. Solids* **10**, 87 (1959).
- [167] X. Rocquefelte, K. Schwarz and P. Blaha, Theoretical investigation of the magnetic exchange interactions in copper(II) oxides under chemical and physical pressures, *Sci. Rep.* **2**, 759 (2012).
- [168] L.F. Mattheiss, Electronic structure of the  $3d$  transition-metal monoxides I. energy-band results, *Phys. Rev. B* **5**, 290 (1972).
- [169] K. Terakura, T. Oguchi, A. R. Williams and J. Kübler, Band theory of insulating transition-metal monoxides: band-structure calculations, *Phys. Rev. B* **30**, 4734 (1984).
- [170] W. A. Harrison, Heisenberg exchange in the magnetic monoxides, *Phys. Rev. B* **76**, 054417 (2007).
- [171] J. Zaanen and G. A. Sawatzky, The electronic structure and superexchange interactions in transition-metal compounds, *Can. J. Phys.* **65**, 1262 (1987).
- [172] S. Åsbrink and L.J. Norrby, A refinement of the crystal structure of copper(II) oxide with a discussion of some exceptional e.s.fl.'s, *Acta Cryst. B* **26**, 8 (1970).
- [173] J. Zaanen, G.A. Sawatzky and J.W. Allen, Band gaps and electronic structure of transition-metal compounds, *Phys. Rev. Lett.* **55**, 418 (1985).
- [174] J. Ghijsen, L. H. Tjeng, J. van Elp, H. Eskes, J. Westerink and G. A. Sawatzky, Electronic structure of  $\text{Cu}_2\text{O}$  and  $\text{CuO}$ , *Phys. Rev. B* **38**, 11322 (1988).
- [175] H. Eskes, L.H. Tjeng and G.A. Sawatzky, Cluster-model calculation of the electronic structure of  $\text{CuO}$ : a model material for the high-T, superconductors, *Phys. Rev. B* **41**, 288 (1990).
- [176] F. Zhang and T. Rice, Effective Hamiltonian for the superconducting Cu oxides, *Phys. Rev. B* **37**, 3759 (1988).
- [177] L. H. Tjeng, B. Sinkovic, N. B. Brookes, J. B. Goedkoop, R. Hesper, E. Pellegrin, F. M. F. deGroot, S. Altieri, S. L. Hulbert, E. Shekel and G. A. Sawatzky, Spin-resolved photoemission on anti-ferromagnets: direct observation of Zhang-Rice singlets in  $\text{CuO}$ , *Phys. Rev. Lett.* **78**, 1126 (1997).
- [178] E. Stavitski and F. M. F. de Groot, The CTM4XAS program for EELS and XAS spectral shape analysis of transition metal L edges, *Micron* **41**, 687 (2010).

## Bibliography

---

- [179] H. Eskes and G. A. Sawatzky, Single-, triple-, or multiple-band Hubbard models, *Phys. Rev. B* **44**, 9656 (1991).
- [180] A. E. Bocquet and A. Fujimori, Predictions for core-level x-ray photoemission spectra of divalent and trivalent  $3d$  transition-metal compounds, *J. Electron Spectrosc. Relat. Phenom.* **82**, 87 (1996).
- [181] J.J. Yeh and I. Lindau, Atomic subshell photoionization cross sections and asymmetry parameters:  $1 < Z < 103$ , *At. Data And Nucl. Data Tables* **32**, 1 (1985).
- [182] L. H. Tjeng, C.T. Chen, J. Ghijsen, P. Rudolf and F. Sette, Giant Cu  $2p$  resonances in CuO valence-band photoemission, *Phys. Rev. Lett.* **67**, 501 (1991).
- [183] S. Moser, L. Moreschini, H.-Y. Yang, D. Innocenti, F. Fuchs, N. H. Hansen, Y. J. Chang, K. S. Kim, A. L. Walter, A. Bostwick, E. Rotenberg, F. Mila and M. Grioni, Angle-resolved photoemission spectroscopy of tetragonal CuO: evidence for intralayer coupling between cupratelike sublattices, accepted by *Phys. Rev. Lett* (2014).
- [184] J.-Y.P. Delannoy, M.J.P. Gingras, P.C.W. Holdsworth and A.-M.S. Tremblay, Low-energy theory of the  $t$ - $t'$ - $t''$ - $U$  Hubbard model at half-filling: interaction strengths in cuprate superconductors and an effective spin-only description of  $\text{La}_2\text{CuO}_4$ , *Phys. Rev. B* **79**, 235130 (2009).
- [185] F. Ronning, K. M. Shen, N. P. Armitage, A. Damascelli, D. H. Lu, Z.-X. Shen, L. L. Miller and C. Kim, Anomalous high-energy dispersion in angle-resolved photoemission spectra from the insulating cuprate  $\text{Ca}_2\text{CuO}_2\text{Cl}_2$ , *Phys. Rev. B* **71**, 094518 (2005).
- [186] A. Bansil, S. Basak, T. Das, H. Lin, M. Lindroos, J. Nieminen, I. Suominen and R. S. Markiewicz, Interplay of matrixelement, self-energy and geometric effects in various spectroscopies of the cuprates, *J. Phys. Chem. Solids* **72**, 341 (2011).
- [187] J. Chang, S. Pailh s, M. Shi, M. M nsson, T. Claesson, O. Tjernberg, J. Voigt, V. Perez, L. Patthey, N. Momono, M. Oda, M. Ido, A. Schnyder, C. Mudry and J. Mesot, When low- and high-energy electronic responses meet in cuprate superconductors, *Phys. Rev. B* **75**, 224508 (2007).
- [188] A. Foussats, A. Greco and M. Bejas, Role of dynamical non-double-occupancy excitations on the quasiparticle damping of the  $t$ - $J$  model in the large- $N$  limit, *Phys. Rev. B* **78**, 153110 (2008).
- [189] P. Grete, S. Schmitt, C. Raas, F. B. Anders and G. S. Uhrig, Kinks in the electronic dispersion of the Hubbard model away from half filling, *Phys. Rev. B* **84**, 205104 (2011).
- [190] D. S. Inosov, J. Fink, A. A. Kordyuk, S. V. Borisenko, V. B. Zabolotnyy, R. Schuster, M. Knupfer, B. B chner, R. Follath, H. A. D rr, W. Eberhardt, V. Hinkov, B. Keimer and H. Berger, Momentum and energy dependence of the anomalous high-energy dispersion in the electronic structure of high temperature superconductors, *Phys. Rev. Lett.* **99**, 237002 (2007).

- [191] S. Kar and E. Manousakis, Finite-temperature spectral function of a hole in a quantum antiferromagnet and the role of phonons, *Phys. Rev. B* **78**, (2008).
- [192] D. Katagiri, K. Seki, R. Eder and Y. Ohta, Theory of the waterfall phenomenon in cuprate superconductors, *Phys. Rev. B* **83**, (2011).
- [193] A. Macridin, M. Jarrell, T. Maier and D. J. Scalapino, High-energy kink in the single-particle spectra of the two-dimensional Hubbard model, *Phys. Rev. Lett.* **99**, 237001 (2007).
- [194] K. Matho, Kinks and waterfalls in the dispersion of ARPES features, *J. Electron Spectrosc. Relat. Phenom.* **181**, 2 (2010).
- [195] B. Moritz, S. Johnston and T. P. Devereaux, Insights on the cuprate high energy anomaly observed in ARPES, *J. Electron Spectrosc. Relat. Phenom.* **181**, 31 (2010).
- [196] E. A. Pashitskii and V. I. Pentegov, A high energy “kink” in the quasiparticle spectrum as evidence of the importance of charge density fluctuations in the mechanism for high temperature superconductivity in cuprates, *J. Low Temp. Phys.* **36**, 716 (2010).
- [197] P. Srivastava, S. Ghosh and A. Singh, High-energy kink in the dispersion of a hole in an antiferromagnet: double-occupancy effects on electronic excitations, *Phys. Rev. B* **76**, 184435 (2007).
- [198] F. Tan and Q.-H. Wang, Two-mode variational Monte Carlo study of quasiparticle excitations in cuprate superconductors, *Phys. Rev. Lett.* **100**, 117004 (2008).
- [199] Q. Yin, A. Gordienko, X. Wan and S. Y. Savrasov, Calculated momentum dependence of Zhang-Rice states in transition metal oxides, *Phys. Rev. Lett.* **100**, 066406 (2008).
- [200] N.S. Headings, S.M. Hayden, R. Coldea and T.G. Perring, Anomalous high-energy spin excitations in the High- $T_c$  superconductor-parent antiferromagnet  $\text{La}_2\text{CuO}_4$ , *Phys. Rev. Lett.* **105**, 247001 (2010).
- [201] M. Le Tacon, G. Ghiringhelli, J. Chaloupka, M. Moretti Sala, V. Hinkov, M.W. Haverkort, M. Minola, M. Bakr, K. J. Zhou, S. Blanco-Canosa, C. Monney, Y. T. Song, G. L. Sun, C. T. Lin, G. M. De Luca, M. Salluzzo, G. Khaliullin, T. Schmitt, L. Braicovich and B. Keimer Intense paramagnon excitations in a large family of high-temperature superconductors *Nature Phys.* **7**, 725 (2011).
- [202] D. Perkins, J. M. Graybeal, M. A. Kastner, R. J. Birgeneau, J. P. Falck and M. Greven, Mid-infrared optical absorption in undoped lamellar copper oxides, *Phys. Rev. Lett.* **71**, 1621 (1993).
- [203] J. Lorenzana and G. A. Sawatzky, Theory of phonon-assisted multimagnon optical absorption and bimagnon states in quantum antiferromagnets, *Phys. Rev. B* **52**, 13 (1995).
- [204] P. Wróbel, W. Suleja and R. Eder, Spin-polaron band structure and hole pockets in underdoped cuprates, *Phys. Rev. B* **78**, 064501 (2008).

## Bibliography

---

- [205] E. Manousakis, String excitations of a hole in a quantum antiferromagnet and photoelectron spectroscopy, *Phys. Rev. B* **75**, 035106 (2007).
- [206] B. Lau, M. Berciu and G. A. Sawatzky, High-spin polaron in lightly doped  $\text{CuO}_2$  planes, *Phys. Rev. Lett.* **106**, 036401 (2011).
- [207] Y. Tokura, S. Koshihara, T. Arima, H. Takagi, S. Ishibashi, T. Ido and S. Uchida, Cu-O network dependence of optical charge-transfer gaps and spin-pair excitations in single- $\text{CuO}_2$ -layer compounds, *Phys. Rev. B* **41**, 11657 (1990).
- [208] G. Blumberg, P. Abbamonte, M. V. Klein, W. C. Lee, D. M. Ginsberg, L. L. Miller and A. Zibold, Resonant two-magnon Raman scattering in cuprate antiferromagnetic insulators, *Phys. Rev. B* **53**, 11930 (1996).
- [209] J. Lorenzana and G. A. Sawatzky, Phonon assisted multimagnon optical absorption and long lived two-magnon states in undoped lamellar copper oxides, *Phys. Rev. Lett.* **74**, 10 (1995).
- [210] A. Chubukov and D. Frenkel, Resonant two-magnon Raman scattering in antiferromagnetic insulators, *Phys. Rev. Lett.* **74**, 3057 (1995).
- [211] A. Chubukov and D. Frenkel, Resonant two-magnon Raman scattering in parent compounds of high- $T_c$  superconductors, *Phys. Rev. B* **52**, 9760 (1995).
- [212] B. Shastri and B. Shraiman, Theory of Raman scattering in Mott-Hubbard systems, *Phys. Rev. Lett.* **65**, 1068 (1990).
- [213] I. Kupcic, Resonant two-magnon Raman scattering in high- $T_c$  cuprates, *J. Raman Spectrosc.* **42**, 998 (2011).
- [214] S. Sugai, S. Shamoto and M. Sato, Two-magnon Raman scattering in  $(\text{La}_{1-x}\text{Sr}_x)_2\text{CuO}_4$ , *Phys. Rev. B* **38**, 6436 (1988).
- [215] V. Bisogni, L. Simonelli, L. J. P. Ament, F. Forte, M. M. Sala, M. Minola, S. Huotari, J. van den Brink, G. Ghiringhelli, N. B. Brookes and L. Braicovich, Bimagnon studies in cuprates with resonant inelastic x-ray scattering at the O K edge. I. Assessment on  $\text{La}_2\text{CuO}_4$  and comparison with the excitation at Cu  $L_3$  and Cu K edges, *Phys. Rev. B* **85**, 214527 (2012).
- [216] F. Forte, L. J. P. Ament and J. van den Brink, Magnetic excitations in  $\text{La}_2\text{CuO}_4$  probed by indirect resonant inelastic x-ray scattering, *Phys. Rev. B* **77**, 134428 (2008).
- [217] L. J. P. Ament, G. Ghiringhelli, M. M. Sala, L. Braicovich and J. van den Brink, Theoretical demonstration of how the dispersion of magnetic excitations in cuprate compounds can be determined using resonant inelastic x-ray scattering, *Phys. Rev. Lett.* **103**, 117003 (2009).

- [218] L. Braicovich, J. van den Brink, V. Bisogni, M. Moretti Sala, L. J. P. Ament, N. B. Brookes, G. M. De Luca, M. Salluzzo, T. Schmitt, V. N. Strocov and G. Ghiringhelli, Magnetic excitations and phase separation in the underdoped  $\text{La}_{2-x}\text{Sr}_x\text{CuO}_4$  superconductor measured by resonant inelastic x-ray scattering, *Phys. Rev. Lett.* **104**, 077002 (2010).
- [219] G. Ghiringhelli, A. Piazzalunga, C. Dallera, G. Trezzi and L. Braicovich, SAXES, a high resolution spectrometer for resonant x-ray emission in the 400-1600 eV energy range, *Rev. Sci. Instrum.* **77**, 113108 (2006).
- [220] Pieter Kuiper, J.-H. Guo, Conny Sâthe, L.-C. Duda and Joseph Nordgren, J. J. M. Pothuizen, F. M. F. de Groot and G. A. Sawatzky, Resonant x-Ray Raman spectra of Cu  $dd$  excitations in  $\text{Sr}_2\text{CuO}_2\text{Cl}_2$ , *Phys. Rev. Lett.* **80**, 5204 (1998).
- [221] G. Ghiringhelli, N. B. Brookes, E. Annese, H. Berger, C. Dallera, M. Grioni, L. Perfetti, A. Tagliaferri and L. Braicovich, Low energy electronic excitations in the layered cuprates studied by copper  $L_3$  resonant inelastic x-ray scattering, *Phys. Rev. Lett.* **92**, 117406 (2004).
- [222] M. Moretti Sala, V. Bisogni, C. Aruta, G. Balestrino, H. Berger, N. B. Brookes, G. M. de Luca, D. Di Castro, M. Grioni, M. Guarise, P. G. Medaglia, F. Miletto Granozio, M. Minola, P. Perna, M. Radovic, M. Salluzzo, T. Schmitt, K. J. Zhou, L. Braicovich and G. Ghiringhelli, Energy and symmetry of  $dd$  excitations in undoped layered cuprates measured by Cu  $L_3$  resonant inelastic x-ray scattering, *New J. Phys.* **13**, 043026 (2011).
- [223] G. Ghiringhelli, M. Le Tacon, M. Minola, S. Blanco-Canosa, C. Mazzoli, N. B. Brookes, G. M. De Luca, A. Frano, D. G. Hawthorn, F. He, T. Loew, M. Moretti Sala, D. C. Peets, M. Salluzzo, E. Schierle, R. Sutarto, G. A. Sawatzky, E. Weschke, B. Keimer, L. Braicovich, Long-range incommensurate charge fluctuations in  $(\text{Y,Nd})\text{Ba}_2\text{Cu}_3\text{O}_{6+x}$ , *Science* **337**, 821 (2012).
- [224] E. H. da Silva Neto, P. Aynajian, A. Frano, R. Comin, E. Schierle, E. Weschke, A. Gyenis, J. Wen, J. Schneeloch, Z. Xu, S. Ono, G. Gu, M. Le Tacon and A. Yazdani, Ubiquitous interplay between charge ordering and high-temperature superconductivity in cuprates, *Science* **343**, 393 (2014).
- [225] R. Comin, A. Frano, M. M. Yee, Y. Yoshida, H. Eisaki, E. Schierle, E. Weschke, R. Sutarto, F. He, A. Soumyanarayanan, Yang He, M. Le Tacon, I. S. Elfimov, J. E. Hoffman, G. A. Sawatzky, B. Keimer, A. Damascelli, Charge order driven by Fermi-arc instability in  $\text{Bi}_2\text{Sr}_{2-x}\text{La}_x\text{CuO}_{6+\delta}$ , *Science* **343**, 390 (2014).
- [226] C.L. Henley, Ordering due to disorder in a frustrated vector antiferromagnet, *Phys. Rev. Lett.* **62**, 2056 (1989).
- [227] P. Chandra, P. Coleman and A.I. Larkin, Ising transition in frustrated Heisenberg models, *Phys. Rev. Lett.* **64**, 88 (1990).

## Bibliography

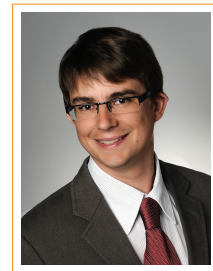
---

- [228] C. Weber, L. Capriotti, G. Misguich, F. Becca, M. Elhajal and F. Mila, Ising transition driven by frustration in a 2D classical model with continuous symmetry, *Phys. Rev. Lett.* **91**, 177202 (2003).
- [229] R. R. P. Singh, W. Zheng, J. Oitmaa, O. P. Sushkov and C. J. Hamer, Symmetry breaking in the collinear phase of the  $J_1$ - $J_2$  Heisenberg model, *Phys. Rev. Lett.* **91**, 1 (2003).
- [230] L. Braicovich, J. van den Brink, V. Bisogni, M. Moretti Sala, L. J. P. Ament, N. B. Brookes, G. M. De Luca, M. Salluzzo, T. Schmitt, V. N. Strocov and G. Ghiringhelli, Magnetic excitations and phase separation in the underdoped  $\text{La}_{2-x}\text{Sr}_x\text{CuO}_4$  superconductor measured by resonant inelastic x-ray scattering, *Phys. Rev. Lett.* **104**, 077002 (2010).
- [231] M. P. M. Dean, R. S. Springell, C. Monney, K. J. Zhou, J. Pereiro, I. Božović, B. Dalla Piazza, H. M. Rønnow, E. Morenzoni, J. van den Brink, T. Schmitt and J. P. Hill, Spin excitations in a single  $\text{La}_2\text{CuO}_4$  layer, *Nat. Mater* **11**, 850 (2012).
- [232] A.T. Boothroyd, A. Mukherjee, S. Fulton, T.G. Perring, R.S. Eccleston, H.A. Mook and B.M. Wanklyn, High-energy magnetic excitations in  $\text{CuO}$ , *Physica B* **234**, 731 (1997).
- [233] H. Okabe, M. Isobe, E. Takayama-Muromachi, A. Koda, S. Takeshita, M. Hiraishi, M. Miyazaki, R. Kadono, A. Miyake and J. Akimitsu,  $\text{Ba}_2\text{IrO}_4$ : A spin-orbit Mott insulating quasi-two-dimensional antiferromagnet, *Phys. Rev. B* **83**, 155118 (2011).
- [234] A. Georges, L. de' Medici and J. Mravlje, Strong correlations from Hund's coupling, *Annu. Rev. Cond. Mat. Phys.* **4**, 137 (2013).
- [235] B.J. Kim, H. Jin, S.J. Moon, J.W. Kim, B.G. Park, C. S. Leem, J. Yu, T.W. Noh, C. Kim, S.J. Oh, J.H. Park, V. Durairaj, G. Cao and E. Rotenberg, Novel  $J_{eff} = 1/2$  Mott state induced by relativistic spin-orbit coupling in  $\text{Sr}_2\text{IrO}_4$ , *Phys. Rev. Lett* **101**, 076402 (2008).
- [236] B.J. Kim, H. Ohsumi, T. Komesu, S. Sakai, T. Morita, H. Takagi and T. Arima, Phase-Sensitive Observation of a Spin-Orbital Mott State in  $\text{Sr}_2\text{IrO}_4$ , *Science* **323**, 1329 (2009).
- [237] S. Moser, L. Moreschini, A. Ebrahimi, B. Dalla Piazza, M. Isobe, H. Okabe, J. Akimitsu, V. V. Mazurenko, K. S. Kim, A. Bostwick, E. Rotenberg, J. Chang, H. M. Rønnow and M. Grioni, The electronic structure of the high-symmetry perovskite iridate  $\text{Ba}_2\text{IrO}_4$ , *New J. Phys.* **16**, 013008 (2014).
- [238] L. Moreschini, S. Moser, A. Ebrahimi, B. Dalla Piazza, K. S. Kim, S. Boseggia, D. F. McMorrow, H. M. Rønnow, J. Chang, D. Prabhakaran, A. T. Boothroyd, E. Rotenberg, A. Bostwick, and M. Grioni, Bilayer splitting and wave functions symmetry in  $\text{Sr}_3\text{Ir}_2\text{O}_7$ , *Phys. Rev. B* **89**, 201114(R) (2014).

# Simon Moser

## Curriculum Vitae

Rue du Simplon 22  
1020 Renens  
☎ +41 (077) 429 7522  
☎ +41 (021) 634 2838  
✉ [simon.moser@epfl.ch](mailto:simon.moser@epfl.ch)  
\* 04.05.1983, Germany



### Education

- 09/2010 – present **PhD in Physics**, *Laboratory of Photoelectron Spectroscopy, Institute of Condensed Matter Physics, Swiss Institute of Technology, Lausanne, Switzerland.*  
Thin **film growth and spectroscopic studies** of CuO, TiO<sub>2</sub>, Ba<sub>2</sub>IrO<sub>4</sub> and Sr<sub>3</sub>Ir<sub>2</sub>O<sub>7</sub> with Prof. Marco Grioni. **Results are published** through international talks and journals (see publication list). One **patent** application is pending.  
09/2011-06/2012 **Visiting Scholar** at the Advanced Light Source, **Berkeley, USA.**
- 10/2004 – 06/2010 **Diploma in Physics**, *Julius Maximilians Universität, Würzburg, Germany, GPA: 1.1 on a scale of 1 to 4 with 1 being the highest.*  
Studies of physics (major), bioinformatics (minor) and neurobiology (optional). Investigation of **Single Molecule Transistors** with Prof. Laurens Molenkamp.  
09/2009 – present: e-fellows scholarship.
- 08/2007 – 08/2008 **Master of Arts in Physics**, *State University of New York, Stony Brook, USA, GPA: 3.860 on a scale of 1 to 4 with 4 being the highest.*  
Studies of physics as part of an **exchange program**. **Detector development** for the **X-ray microscope** at the National Synchrotron Light Source with Prof. Chris Jacobsen.

### Laboratory Experience

- management Proposal, planning and coordination of research projects within international collaborations.
- vacuum Operation and maintenance of various low- and ultra-high- vacuum equipment.
- refrigeration Operation and maintenance of bath-, continuous-flow- and dilution-cryostats.
- lithography UV- and e-beam lithography, pulsed laser deposition and molecular beam epitaxy.
- microscopy Optical-, x-ray-absorption-, scanning electron- and atomic force-microscopy.
- spectroscopy ARPES, XPS, XAS, Raman, RIXS, Auger, LEED, RHEED, beamtimes at various synchrotron facilities (ALS, ELETTRA, NSLS, SLS, SOLEIL, SPRING-8).
- transport Gated and ungated 2-probe, 4-probe and hallbar configuration.

### Skills

- languages German (**native**), English (**fluent**), French (**fluent**), Spanish (**basic**)
- computer Igor, Origin, C, Mathematica, Matlab, Labview, Latex, MS-office, Illustrator
- electronics Design, simulation, fabrication and programming of basic electronic circuits.
- mechanics Design and fabrication of simple parts. Operation of lathe, mill, drill and saw.





# Simon Moser

## Publication List

Rue du Simplon 22  
1020 Renens  
☎ +41 (077) 429 7522  
☎ +41 (021) 693 3399  
✉ simon.moser@epfl.ch

### Peer Reviewed Journals

- in preparation **S. Moser**, S. Fatale, A. Magrez, H. Berger, Y. Harada et al., Probing phonons in anatase TiO<sub>2</sub> by RIXS.
- in preparation **S. Moser**, L. Moreschini, P. Krüger, A. Magrez, H. Berger et al., Orbital selective resonance of conduction carriers at the Ti L-edge of anatase TiO<sub>2</sub>.
- submitted L. Moreschini, G. Autès, A. Crepaldi, **S. Moser**, J. C. Johannsen et al., Bulk and surface band structure of the new family of semiconductors BiTeX (X=I, Br, Cl).
- October 2014 **S. Moser**, L. Moreschini, H.-Y. Yang, D. Innocenti, F. Fuchs et al., Angle-resolved photoemission spectroscopy of tetragonal CuO: evidence for intralayer coupling between cupratelike sublattices. accepted by *Phys. Rev. Lett.*
- May 2014 L. Moreschini, **S. Moser**, A. Ebrahimi, B. Dalla Piazza, M. Isobe et al., Bilayer splitting and wave functions symmetry in Sr<sub>3</sub>Ir<sub>2</sub>O<sub>7</sub>, *Phys. Rev. B* **89**, 201114(R) (2014).
- January 2014 **S. Moser**, L. Moreschini, A. Ebrahimi, B. Dalla Piazza, M. Isobe et al., The electronic structure of the high-symmetry perovskite iridate Ba<sub>2</sub>IrO<sub>4</sub>, *New J. Phys.* **16**, 013008 (2014).
- June 2013 C. Tournier-Colletta, L. Moreschini, G. Autès, **S. Moser**, A. Crepaldi et al., Electronic Instability in a Zero-Gap Semiconductor: The Charge-Density Wave in (TaSe<sub>4</sub>)<sub>2</sub>I, *Phys. Rev. Lett.* **110**, 236401 (2013).
- May 2013 **S. Moser**, L. Moreschini, J. Jaćimović, O. S. Barišić, H. Berger et al., Tunable Polaronic Conduction in Anatase TiO<sub>2</sub>, *Phys. Rev. Lett.* **110** 196403 (2013).
- August 2012 A. Crepaldi, L. Moreschini, G. Autès, C. Tournier-Colletta, **S. Moser** et al., Giant Ambipolar Rashba Effect in the Semiconductor BiTeI, *Phys. Rev. Lett.* **109** 096803 (2012).

### Intellectual Property

- November 2012 **S. Moser**, L. Moreschini, E. Rotenberg, International Patent Application n° PCT/IB2013/060328, *Lithographic patterning of insulating or semiconducting solid state materia in crystalline form.*

### Public Presentations

- October 2014 Invited talk at TCM 2014, Platania, Crete, *Tunable Polaronic Conduction in Anatase TiO<sub>2</sub>.*
- September 2014 Talk at summer school SUCCESS, Les Houches, France, *Tetragonal CuO: a two dimensional cuprate with novel intralayer coupling.*
- May 2014 Seminars at Uni. Chiba and Spring-8, Japan, *Tetragonal CuO: a two dimensional cuprate with novel intralayer coupling.*

- July 2013 Seminar at ELETTRA, Trieste, *Shedding new light on two textbook transition metal oxides: Anatase  $TiO_2$  and tetragonal  $CuO$ .*
- March 2013 Talk at DPG March Meeting, *Tunable Polaronic Conduction in Anatase  $TiO_2$ .*
- March 2013 Poster at DPG March Meeting, *The electronic structure of tetragonal  $CuO$ .*
- October 2012 Seminar at ICMP, EPFL, *The Zhang-Rice Singlets in tetragonal  $CuO$ .*
- February 2012 Talk at APS March Meeting, Boston, USA, *The electronic structure of tetragonal  $CuO$ .*
- October 2011 Seminar at School of Biomedical, Biomolecular and Chemical Sciences, University of Western Australia, *A modern ARPES view of spin-orbit interaction.*
- March/April 2010 Seminars at Néel Institute, Grenoble, at DPMC, University of Geneva and at ICMP, EPFL, *Nanostructures for Transport Measurements in Single Molecule Transistors.*